minerals

Special Issue Reprint

Large Igneous Provinces

Research Frontiers

Edited by
Richard E. Ernst and Hafida El Bilali

mdpi.com/journal/minerals

MDPI

Large Igneous Provinces: Research Frontiers

Large Igneous Provinces: Research Frontiers

Guest Editors

Richard E. Ernst
Hafida El Bilali

MDPI

Basel • Beijing • Wuhan • Barcelona • Belgrade • Novi Sad • Cluj • Manchester

Guest Editors

Richard E. Ernst
Department of Earth Sciences
Carleton University
Ottawa
Canada

Hafida El Bilali
Department of Earth Sciences
Carleton University
Ottawa
Canada

Editorial Office
MDPI AG
Grosspeteranlage 5
4052 Basel, Switzerland

This is a reprint of the Special Issue, published open access by the journal *Minerals* (ISSN 2075-163X), freely accessible at: https://www.mdpi.com/journal/minerals/special_issues/LIPRF.

For citation purposes, cite each article independently as indicated on the article page online and as indicated below:

Lastname, A.A.; Lastname, B.B. Article Title. *Journal Name* **Year**, *Volume Number*, Page Range.

ISBN 978-3-7258-6045-6 (Hbk)
ISBN 978-3-7258-6046-3 (PDF)
https://doi.org/10.3390/books978-3-7258-6046-3

Contents

About the Editors

Richard E. Ernst

Richard E. Ernst is a Scientist in Residence at Carleton University, Ottawa, Canada. His work has been focused on Large Igneous Provinces (LIPs), with nearly 300 refereed publications covering all aspects of LIPs, including their dramatic flood basalts; the 'plumbing system' of mafic/ultramafic dykes; sills and layered intrusions; association with carbonatites, kimberlites, and silicic magmatism; links to supercontinent breakup; catastrophic environmental/climate change including mass extinction events; mineral, metal, and hydrocarbon resource exploration; planetary analogues (particularly Venus); and characterization of the role of mantle plumes in their origin. He is the author of "Large Igneous Provinces", Cambridge University Press (2014), leader of the LIPs Commission of IAVCEI (since 2003), leader of the LIPs and Resource Exploration Program ("LIPs Industry Consortium", since 2010), and co-leader of the International Venus Research Group (IVRG) (since 2021). He received the 2022 Career Achievement Award of the Volcanology and Igneous Petrology Division (VIP) of the Geological Association of Canada, was elected a Fellow of the Geological Society of America (2024), and received the 2025 Natural Sciences and Engineering Research Council of Canada (NSERC) Synergy Award for Innovation.

Hafida El Bilali

Hafida El Bilali is an adjunct Professor at Carleton University. She is co-leader of the international Venus Research Group (IVRG) and Vice President of the Large Igneous Provinces (LIPs) Commission of the International Association of Volcanology and Chemistry of the Earth's Interior (IAVCEI). Her areas of expertise are Planetary Sciences, Volcanology, Isotopic Geochemistry, Paleoclimatology and Time Series Analysis. She has authored and co-authored peer-reviewed articles in international journals such as *Nature Communications*, *Geoscience Frontiers*, *Mathematical Geosciences*, *Paleaeogeography Palaeoclimatology and Palaeoecology*, *Organic Geochemistry*, *Holocene*, *Cretaceous Research*... etc. In addition, she has co-authored book chapters in *Mathematical Geosciences* and AGU Geophysical Monograph 255, the latter on LIPs and climate change.

minerals

MDPI

Editorial

Editorial for the Special Issue "Large Igneous Provinces: Research Frontiers"

Richard E. Ernst * and Hafida El Bilali

Department of Earth Sciences, Carleton University, Ottawa, ON K1S 5B6, Canada; hafidaelbilali@cunet.carleton.ca
* Correspondence: richard.ernst@ernstgeosciences.com

Large Igneous Provinces (LIPs) are vast intraplate magmatic events, typically mafic to ultramafic in composition, with volumes exceeding 0.1 million km^3 (typically proxied by an areal extent greater than 0.1 million km^2), and with significant geodynamic implications, comparable in impact to plate tectonics (e.g., [1–25]). LIPs occur in both continental and oceanic settings and are short-lived, usually lasting under five million years, though some have multiple pulses spanning tens of millions of years. LIPs feature extensive flood basalt volcanism and complex plumbing systems of mafic dykes, sills, and layered intrusions, sometimes accompanied by silicic magmatism (and termed Silicic LIPs when large enough, i.e., of LIP size), carbonatites, and kimberlites. Since the Archean eon, continental LIPs have formed irregularly, with an average recurrence of 20–30 million years. Oceanic LIPs, better preserved over the past 200 million years, occur at similar rates, suggesting a combined LIP recurrence interval of 10–15 million years back to 2.5 Ga. The Archean LIP record has recently been significantly expanded, resulting in the recognition of LIPs back to about 3.5 Ga, with a frequency comparable to that of the Proterozoic–Phanerozoic LIP record [14]. LIP analogs are also present on Venus and Mars. Terrestrial LIPs are closely tied to major geological and environmental phenomena, including continental rifting and breakup, ore deposit formation, sedimentary basin development, and climate perturbations, including those linked to mass extinctions. They are generally linked to mantle plumes, with the largest events being linked to plumes rising from the deep mantle. Other processes can contribute to multiple LIP pulses—most notably decompression melting and lithospheric delamination.

Our goal in producing this Special Issue has been to highlight some recent developments in LIPs research. This Special Issue consists of eight publications, five published in 2023, two in 2024, and one in 2025. They collectively represent a wide thematic range, each representing an important advance in our understanding of plume-generated LIPs. The papers presented in this Special Issue are organized in chronological order (youngest to oldest) with respect to their associated LIPs.

Two papers address aspects of the youngest known LIP, the 17 Ma Columbia River LIP: Streck et al. (2023) [26] consider the geochemical relationship of Picture Gorge Basalts (PGBs) to the lowermost units of Imnaha basalts; and Cahoon et al. (2024) [26] focus on the geochronology and geochemistry of the PGBs.

Streck et al. (2023) [26], in their paper titled "Province-Wide Tapping of a Shallow, Variably Depleted, and Metasomatized Mantle to Generate Earliest Flood Basalt Magmas of the Columbia River Basalt, Northwestern USA," consider the Columbia River Basalt Group (CRBG), the youngest LIP, which began with the Imnaha, Steens, and PGB fed from separate dyke swarms. The PGB, long considered compositionally distinct, shares chemical similarities with the lowermost Imnaha flows. This paper shows that the earliest

CRBG lavas (~17 Ma) were derived from the shallow, variably depleted, subduction-metasomatized mantle across the province. Compositional provinciality reflects regional differences in mantle depletion and subduction overprint, indicating relatively local lava emplacement during initial CRBG activity.

Cahoon et al. (2024) [27], in their paper titled "Mantle Sources and Geochemical Evolution of the Picture Gorge Basalt, Columbia River Basalt Group," focusing on PGB, an early Columbia River Basalt Group (CRBG) unit, provide key insights into mantle sources and plume influence. PGB geochemistry reveals LILE enrichment, HFSE depletion, low $^{87}Sr/^{86}Sr$, and mantle-like $\delta^{18}O$, indicating a metasomatized upper mantle source. Two parental magma types best explain observed variability. Age data indicate that PGB eruptions occurred in two pulses ~0.4 Ma apart (before and during the main-phase CRBG activity). Combined geochemical age evidence suggests progressively greater plume-like mantle input over time.

The next two papers, Chatterjee and Ghose (2023) [28] and Stotz et al. (2025) [29], address the role of plume-generated LIPs in continental breakup. Chatterjee and Ghose (2023) [28] consider the case of the Rajmahal flood basalts, which are linked with the Kerguelen mantle plume; and Stotz et al. (2025) [29] quantitatively analyze the role of plume-generated LIPs in the early Cretaceous opening of the South Atlantic

Chatterjee and Ghose (2023) [28], in their paper titled "Thermobarometry of the Rajmahal Continental Flood Basalts and Their Primary Magmas: Implications for the Magmatic Plumbing System," consider the Late Aptian Rajmahal flood basalts caused by the Kerguelen Plume along India's eastern margin. Thermobarometry indicates crystallization at ~5 kbar/1100–1200 °C (~19 km), while primary melts equilibrated deeper at ~9 kbar/1280 °C (~33 km). These depths match the gravity data, which shows a dense layer at lower the crustal depths, representing anomalous mantle. Magmas ponded beneath an upwarped Moho and rose through transcrustal faults to shallow chambers, where fractional crystallization occurred. This plumbing system reflects plume-driven magmatism and lithospheric erosion during Gondwana breakup.

Stotz et al. (2025) [29], in their paper titled "Continental Rift Driven by Asthenosphere Flow and Lithosphere Weakening by Flood Basalts: South America and Africa Cenozoic Rifting," consider the much-debated mechanism by which LIPs contribute to continental rifting and breakup. It is shown that plume flow quantitatively links LIP magmatism to rifting, supported by the sedimentary record of stratigraphic hiatuses and LIP distribution. During the West Gondwana breakup, the Jurassic plume ascent created dynamic topography, while Cretaceous mafic dykes and sills weakened the lithosphere. Together, plume-driven forces and lithospheric weakening from dyke intrusion localized deformation, facilitating rift initiation and the separation of South America and Africa.

Latyshev et al. (2023) [30], in their paper titled "Reconstruction of the Magma Transport Patterns in the Permian-Triassic Siberian Traps from the Northwestern Siberian Platform on the Basis of Anisotropy of Magnetic Susceptibility Data," propose that understanding magma transport is key to the characterization of LIPs. Producing Anisotropy of Magnetic Susceptibility (AMS) data from >100 sites in lava flows and intrusions, the authors determined the magma flow patterns in the Noril'sk and Kulumbe regions of the northwestern part of the Siberian Traps LIP. The data show a predominant NW–SE lateral magma flow, fed from the Noril'sk–Kharaelakh and Imangda–Letninskiy fault zones. The magma transport geometry in these flows and intrusions contrasts with that determined in their earlier AMS study of the southern part of the Siberian Traps, where the magma-feeding was inferred to be located in the central, most down-warped part of the Angara–Taseeva depression.

Shelepaev et al. (2023) [31], in their chapter titled "Petrology and Age of the Yamaat Uul Mafic Complex, Khangai Mountains, Western Mongolia," consider the petrology and age of a mafic complex in Mongolia that provides some important new information on the poorly understood Khangai LIP of Central Asia. The Yamaat Uul mafic complex in western Mongolia hosts Cu-Ni mineralization and comprises two intrusions: plagioclase–olivine–pyroxene cumulates and monzogabbro—the latter enriched with incompatible elements. U-Pb zircon dating indicates a Late Permian age (~256–263 Ma). Geochemical and isotopic data suggest derivation from a common parental melt without crustal contamination. The low-evolution sulfide melt resembles other Khangai intrusions (Nomgon, Oortsog Uul). As part of the Khangai LIP, Yamaat Uul is a potential PGE-Cu-Ni resource.

Stifeeva et al. (2023) [32], in their paper titled "Timing of Carbonatite Ultramafic Complexes of the Eastern Sayan Alkaline Province, Siberia: U–Pb (ID–TIMS) Geochronology of Ca–Fe Garnets," apply an innovative dating method to units of the Eastern Sayan Alkaline Province (which may represent a portion of a poorly characterized LIP, based on the idea of alkaline suites being frequently associated with LIPs). U–Pb (ID-TIMS) dating of a calcic garnet from the Eastern Sayan alkaline ultramafic complexes constrains magmatism to 619–651 Ma. New ages from Bolshaya Tagna (632 $\pm$ 2 Ma) and Srednaya Zima (624 $\pm$ 5 Ma), combined with Belaya Zima (646 $\pm$ 6 Ma), define the main pulse of magmatic activity. Geochemical variations indicate parental melts derived from distinct chambers during a single mantle melting episode. Results demonstrate garnet U–Pb dating as a precise tool for dating alkaline ultramafic magmaism in large magmatic provinces, including in LIPs.

Yun et al. (2024) [33], in their chapter titled "Origin of Redbeds in the Neoproterozoic Socheong Formation and Their Relation to the Dashigou Large Igneous Province," consider the role of a LIPs in producing hydrothermal fluids affecting sedimentary basins in the Sino–Korean craton (also known as the North China craton). Extensional tectonics in the Sino–Korean Craton produced basins influenced by the Dashigou LIP (ca. 940–890 Ma). This chapter reports Fe-rich redbeds in the Neoproterozoic Socheong Formation (Pyeongnam Basin). Geochemistry reveals basin-wide Fe enrichment from hydrothermal fluids linked to mafic intrusions of the Dashigou LIP. Episodic magmatism generated short-lived anoxia, preserved as ferruginous layers, making these redbeds key markers for stratigraphic correlation and carbon isotope studies across related basins, including the Sangwon, Xu-Huai, and Dalian basins.

We appreciate our authors for their authoritative contributions to this Special Issue, covering a range of LIP themes. All of chapters in this book were peer-reviewed according to journal standards. Our sincere thanks are extended to the many reviewers whose detailed and thoughtful comments helped ensure the scientific quality of the research presented herein. We also appreciate the invaluable role of the staff of *Minerals*, who have been our partners in this journey from conception to the publication of this volume.

Conflicts of Interest: The authors declare no conflict of interest.

References

1. Black, B.A.; Karlstrom, L.; Mather, T.A. The life cycle of large igneous provinces. *Nat. Rev. Earth Environ.* **2021**, *2*, 840–857. [CrossRef]
2. Bryan, S.; Ernst, R.E. Revised definition of Large Igneous Provinces (LIPs). *Earth-Sci. Rev.* **2008**, *86*, 175–202. [CrossRef]
3. Bryan, S.E.; Ferrari, L. Large Igneous Provinces and Silicic Large Igneous Provinces: Progress in our understanding over the last 25 years. *Geol. Soc. Am. Bull.* **2013**, *125*, 1053–1078. [CrossRef]
4. Coffin, M.F.; Eldholm, O. Large igneous provinces: Crustal structure, dimensions, and external consequences. *Rev. Geophys.* **1994**, *32*, 1–36. [CrossRef]
5. Coffin, M.F.; Eldholm, O. Large igneous provinces. In *Encyclopedia of Geology*; Selley, R.C., Cocks, R., Plimer, I.R., Eds.; Elsevier: Oxford, UK, 2005; pp. 315–323.

6. Courtillot, V.; Renne, P.R. On the ages of flood basalt events. *Comptes Rendus Geosci.* **2003**, *335*, 113–140. [CrossRef]
7. Courtillot, V.; Davaille, A.; Besse, J.; Stock, J. Three distinct types of hotspots in the Earth's mantle. *Earth Planet. Sci. Lett.* **2003**, *205*, 295–308. [CrossRef]
8. Dilek, Y.; Ernst, R. Links Between Ophiolites and LIPs in Earth History, Special Issue. *Lithos* **2008**, *100*, 1–354. [CrossRef]
9. Dobretsov, N.L.; Ernst, R.E.; Izokh, A.E. Large Igneous Provinces of Asia, Mantle Plumes, and Metallogeny, Special Issue. *Russ. Geol. Geophys.* **2008**, *49*, 439–556. [CrossRef]
10. Ernst, R.E.; Buchan, K.L. *Mantle Plumes: Their Identification Through Time*; Special Paper 352; Geological Society of America: Boulder, CO, USA, 2001; pp. 1–575.
11. Ernst, R.E.; Söderlund, U.; W Bleeker, W. LIPs and Supercontinents, Special Issue. *Lithos* **2013**, *174*, 1–348. [CrossRef]
12. Ernst, R.E. *Large Igneous Provinces*; Cambridge University Press: Cambridge, UK, 2014.
13. Ernst, R.E.; Dickson, A.J.; Bekker, A. *Large Igneous Provinces: A Driver of Global Environmental and Biotic Changes*; AGU Geophysical Monograph 255; Wiley: Hoboken, NJ, USA, 2021.
14. Ernst, R.E.; El Bilali, H.; Buchan, K.L.; Chamberlain, K.R.; Srivastava, R.K.; Evans, D.A.D. Record of Archean and earliest Proterozoic Large Igneous Provinces (LIPs) and their mafic dyke swarms. In *The Archean Earth*, 2nd Edition of The Precambrian Earth; Homann, M., Lyons, T.W., Ernst, R.E., Heubeck, C., Stüeken, E.E., Webb, A.A.G., Papineau, D., Mason, P.R.D., Mazumder, R., Altermann, W., Eds.; Elsevier: Amsterdam, The Netherlands, 2025; *in press*.
15. Ernst, R.E.; Youbi, N. How Large Igneous Provinces affect global climate, sometimes cause mass extinctions, and represent natural markers in the geological record. *Palaeogeogr. Palaeoclimatol. Palaeoecol.* **2017**, *478*, 30–52. [CrossRef]
16. Kuzmin, M.; Ernst, R.E. Mantle plumes and their role in the formation of lithosphere structure, large igneous provinces, and metallogeny, Special Issue. *Russ. Geol. Geophys.* **2016**, *57*, 637–841. [CrossRef]
17. Mahoney, J.; Coffin, M. *Large Igneous Provinces: Continental, Oceanic, and Planetary Volcanism*; AGU Geophysical Monograph Series; AGU: Washington, DC, USA, 1997; Volume 100, pp. 1–438.
18. Lange, B.; Blichert-Toft, J.; Chakraborty, S.; Sisson, T.; Posner, E. Large Igneous Provinces: Versatile Drivers of Global Change, Special Issue. *Elements* **2023**, *5*, 263–308. [CrossRef]
19. Peng, P.; Ernst, R.E.; Söderlund, U.; Hamilton, M. Dyke Swarms: Keys for Precambrian Paleogeographic Reconstruction, Special Issue. *Precambrian Res.* **2019**, *329*, 1–294. [CrossRef]
20. Percival, L.M.E.; Matsumoto, H.; Callegaro, S.; Erba, E.; Kerr, A.C.; Mutterlose, J.; Suzuki, K. Cretaceous large igneous provinces: From volcanic formation to environmental catastrophes and biological crises. *Geol. Soc. Lond. Spec. Publ.* **2025**, *544*, 299–342. [CrossRef]
21. Söderlund, U.; Klausen, M.; Ernst, R.E.; Bleeker, W. New advances in using Large Igneous Provinces (LIPs) to reconstruct ancient supercontinents, Special Issue. *GFF* **2016**, *138*, 1–275. [CrossRef]
22. Srivastava, R.K.; Ernst, R.; Bleeker, W.; Hamilton, M.A. Precambrian Large Igneous Provinces (LIPs) and their dyke swarms: New insights from high-precision geochronology integrated with paleomagnetism and geochemistry, Special Issue. *Precambrian Res.* **2010**, *183*, 379–668.
23. Srivastava, R.K.; Ernst, R.E.; Peng, P. *Dyke Swarms of the World—A Modern Perspective*; Springer: Berlin/Heidelberg, Germany, 2019; pp. 1–492. [CrossRef]
24. Srivastava, R.K.; Ernst, R.E.; Buchan, K.L.; de Kock, M. *Large Igneous Provinces and Their Plumbing Systems*; Geological Society: London, UK, 2022; Volume 518, pp. 1–600.
25. Stephenson, S.N.; Ball, P.W.; Richards, F.D. Destruction and regrowth of lithospheric mantle beneath large igneous provinces. *Sci. Adv.* **2023**, *9*, eadf6216. [CrossRef]
26. Streck, M.J.; Fredenberg, L.J.; Fox, L.M.; Cahoon, E.B.; Mass, M.J. Province-Wide Tapping of a Shallow, Variably Depleted, and Metasomatized Mantle to Generate Earliest Flood Basalt Magmas of the Columbia River Basalt, Northwestern USA. *Minerals* **2023**, *13*, 1544. [CrossRef]
27. Cahoon, E.B.; Streck, M.J.; Carlson, R.W.; Bindeman, I.N. Mantle Sources and Geochemical Evolution of the Picture Gorge Basalt, Columbia River Basalt Group. *Minerals* **2024**, *14*, 440. [CrossRef]
28. Chatterjee, N.; Ghose, N.C. Thermobarometry of the Rajmahal Continental Flood Basalts and Their Primary Magmas: Implications for the Magmatic Plumbing System. *Minerals* **2023**, *13*, 426. [CrossRef]
29. Stotz, I.L.; Vilacís, B.; Hayek, J.N.; Bunge, H.-P. Continental Rift Driven by Asthenosphere Flow and Lithosphere Weakening by Flood Basalts: South America and Africa Cenozoic Rifting. *Minerals* **2025**, *15*, 644. [CrossRef]
30. Latyshev, A.; Radko, V.; Veselovskiy, R.; Fetisova, A.; Krivolutskaya, N.; Fursova, S. Reconstruction of the Magma Transport Patterns in the Permian- Triassic Siberian Traps from the Northwestern Siberian Platform on the Basis of Anisotropy of Magnetic Susceptibility Data. *Minerals* **2023**, *13*, 446. [CrossRef]
31. Shelepaev, R.; Shapovalova, M.; Egorova, V.; Shelepov, Y.; Oyunchimeg, T.-U.; Tolstykh, N. Petrology and Age of the Yamaat Uul Mafic Complex, Khangai Mountains, Western Mongolia. *Minerals* **2023**, *13*, 833. [CrossRef]

32. Stifeeva, M.V.; Salnikova, E.B.; Savelyeva, V.B.; Kotov, A.B.; Danilova, Y.V.; Bazarova, E.P.; Danilov, B.S. Timing of Carbonatite Ultramafic Complexes of the Eastern Sayan Alkaline Province, Siberia: U–Pb (ID–TIMS) Geochronology of Ca–Fe Garnets. *Minerals* **2023**, *13*, 1086. [CrossRef]
33. Yun, H.; Lee, S.H.; Seo, I. Origin of Redbeds in the Neoproterozoic Socheong Formation and Their Relation to the Dashigou Large Igneous Province. *Minerals* **2024**, *14*, 59. [CrossRef]

minerals

MDPI

Article

Province-Wide Tapping of a Shallow, Variably Depleted, and Metasomatized Mantle to Generate Earliest Flood Basalt Magmas of the Columbia River Basalt, Northwestern USA

Martin J. Streck [1,*], Luke J. Fredenberg [1], Lena M. Fox [1], Emily B. Cahoon [2] and Mary J. Mass [1]

[1] Department of Geology, Portland State University, Portland, OR 97207-0751, USA; ljfredenberg@gmail.com (L.J.F.); lfox@meiser-earl.com (L.M.F.); mjrobbin@pdx.edu (M.J.M.)
[2] College of Earth, Ocean, and Atmospheric Sciences, Oregon State University, Corvallis, OR 97331-5503, USA; emily.cahoon@oregonstate.edu
* Correspondence: streckm@pdx.edu

Abstract: The Miocene Columbia River Basalt Group (CRBG) of the Pacific Northwest of the United States is the world's youngest and smallest large igneous province. Its earliest formations are the Imnaha, Steens, and now the Picture Gorge Basalt (PGB), and they were sourced from three different dike swarms exposed from SE Washington to Nevada to northcentral Oregon. PGB is often viewed to be distinct from the other formations, as its magmas are sourced from a shallow, relatively depleted, and later subduction-induced metasomatized mantle, along with its young stratigraphic position. It has long been known that the lowermost American Bar flows (AB1&2) of the Imnaha Basalt are chemically similar to those of the PGB, yet the Imnaha Basalt is generally thought to carry the strongest plume source component. These opposing aspects motivated us to revisit the compositional relationships between AB1&2 and PGB. Our findings suggest that tapping a shallow, variably depleted, and metasomatized mantle reservoir to produce earliest CRBG lavas occurred across the province, now pinpointed to ~17 Ma. Moreover, compositional provinciality exists indicating regional differences in degree of depletion and subduction overprint that is preserved by regionally distributed lavas, which in turn implies relatively local lava emplacement at this stage.

Keywords: Columbia River Basalt; CRBG; flood basalt; Imnaha Basalt; Picture Gorge Basalt; depleted mantle; metasomatized mantle; LIP

1. Introduction

The Miocene Columbia River Basalt Group (CRBG) of the Pacific Northwest of the United States is the world's youngest and smallest large igneous province (LIP) (e.g., [1,2]) (Figure 1). The Group consists of seven formations (Figures 1 and 2), formally defined by [3] and distinguished on the basis of stratigraphic position, distribution, lithology, and chemical composition [4]. Despite extensive study, numerous questions remain in the collective understanding of the Columbia River Basalts (CRBs). Such questions include: (1) the exact driving force of this magmatism, mantle plume or plate tectonics (e.g., [5–9]), (2) the precise timing of CRBG magmatism [2,10–14], (3) the nature of crustal storage sites prior to eruption [5,15–17]; and (4) chemical variations among lavas and what these imply about mantle sources [18–23].

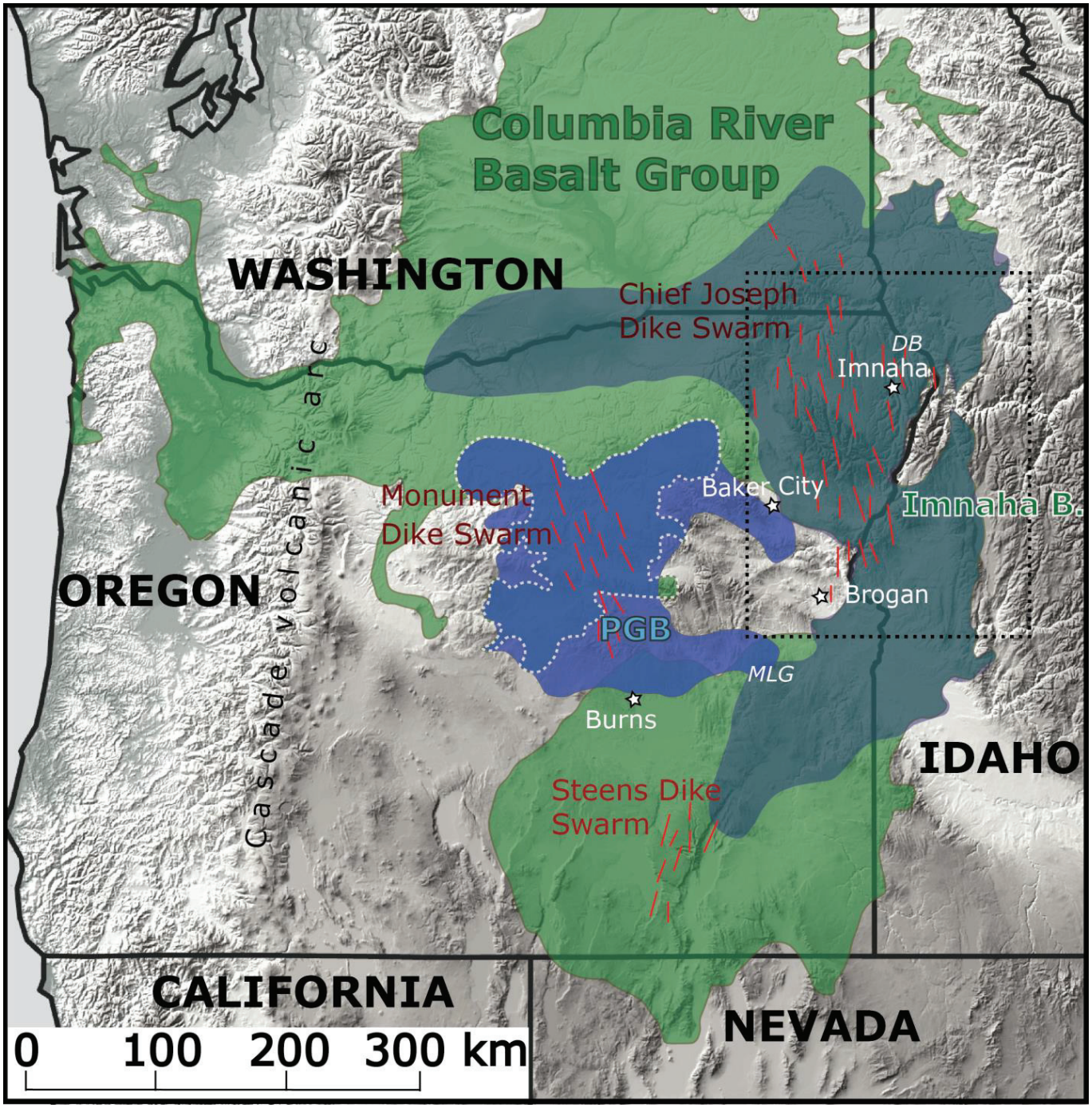

Figure 1. Extent of the Imnaha Basalt and Picture Gorge Basalt within the Columbia River Basalt Group of the Pacific NW, USA. Blue for PGB is the extended distribution of [24]; dashed white line is for original distribution. Distribution of CRBG, original PGB, and Imnaha Basalt taken from [1]; DB = Dug Bar, MLG = Malheur Gorge. Dashed black rectangle indicates coverage of Figure 4.

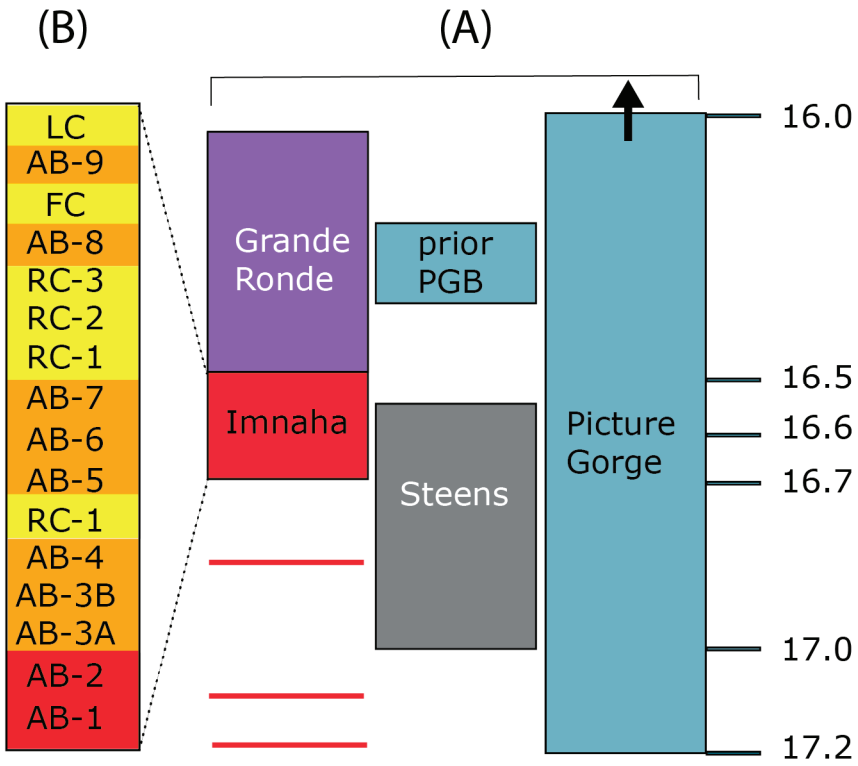

Figure 2. (**A**) Age and stratigraphic relationships of main phase CRBG formations of Imnaha, Grande Ronde, Steens, and Picture Gorge Basalt. Younger (Wanapum, Saddle Mountains) and minor (Prineville) formations are not shown. Ages from [2,12,24,25]; red line for ages of AB1&2 flows of this study; 'prior PGB' = stratigraphic position prior to [2], upward arrow on PGB to indicate youngest age of 15.75 Ma [24] (see text for discussion). (**B**) Flow stratigraphy of Imnaha Basalt after [26]; AB = American Bar, RC = Rock Creek, FC = Fall Creek, and LC = Log Creek subunits.

Current understanding of the stratigraphy and spatio-temporal evolution of the CRBG has evolved over many decades [1,3,26–30], often involving significant revisions to earlier schemes. In early work [27], the name "Picture Gorge Basalt" was applied to the early flow package underlying the Grande Ronde lavas (called "Yakima Basalt" at the time) in the deep canyons of northeastern Oregon, western Idaho, and southeastern Washington, now assigned to the Imnaha Basalt [3,26]. However, the type locality for Picture Gorge Basalt (PGB) is located approximately 150 km to the west and consists of lavas originating from the Monument dike swarm rather than the Chief Joseph swarm, producing the Imnaha Basalt and overlying formations (Figure 1). Chemical and mineralogical differences between the eastern basalts and type Picture Gorge Basalt lavas were recognized and were key to establishing these lavas as their own formation, the Imnaha Basalt [3,26,29]. Nonetheless, strong similarities exist between some Imnaha flows and PGB, but whether they had the same age, came from the same source, and were physically continuous with PGB flows was uncertain [31]. At that same time, however, new radiometric age determination [32] indicated that Picture Gorge Basalt was significantly younger than the Imnaha Basalt and contemporaneous with eruption of the middle of the Grande Ronde Basalt that overlies the Imnaha Basalt (Figure 2). As a result, the most PGB-like, at the base of the whole basalt flow sequence in the region of Imnaha, were grouped with the overlying flows into the Imnaha Basalt [3,26] and this has remained the case ever since. Recent work by [2] extended the PGB formation to the east (Figure 1) and yielded $^{40}Ar/^{39}Ar$ ages that indicate that eruptive activity of the Picture Gorge Basalt started significantly earlier around 17.25 Ma, making the PGB older than or, as a minimum, as old as the earliest CRBG lavas anywhere. The updated timeframe now makes it probable that the lower flows of the Imnaha Basalt and the Picture Gorge Basalt may have erupted synchronously, as originally envisaged

by [3,27]. Ref. [2] also drew attention back to these lowest two flow units of the Imnaha and questioned whether they might be far-travelled PGB flows or erupted more locally where they are exposed. This context provided the impetus for this study, in which we revisit the compositional relationships between the lowest flow units of the Imnaha Basalt and the Picture Gorge Basalt and the other Imnaha lavas that occur stratigraphically higher.

Although our focus is quite specific about lava compositions and stratigraphy of select locations, it is significant for the understanding of temporal and spatial trends of CRBG magmatism across this flood basalt province. PGB magmas have long been viewed as being sourced from a shallow depleted mantle that has been metasomatized in a subduction setting prior to the CRB event [11,19,20,33] whether or not this mantle is lithospheric is controversial [11,20]. PGB-like lavas of the Imnaha as well as the earliest Steens Basalt lavas from the southern CRBG extent (Figure 1) share compositional characteristics with PGB lavas. Hence, it appears that tapping a shallow mantle reservoir gave rise to the earliest CRBG lavas over a much broader area than previously appreciated. Furthermore, the longer eruption duration recently documented for the PGB [2] indicates longer term prevalence of this depleted mantle source, and it also appears there is compositional evidence in the stratigraphy of the Imnaha and Steens Basalt that also record (although muted and more punctuated) the tapping of a depleted yet metasomatized shallow reservoir through time.

2. Geologic Background

2.1. The Imnaha Basalt

The currently accepted stratigraphy of the Imnaha Basalt was established by [26] who subdivided the formation into two main chemical types: the American Bar (AB) and Rock Creek (RC). Within the American Bar type, nine flow units are distinguished, AB1 through AB9, while the Rock Creek type is represented by RC1 through RC3, plus the Fall Creek (FC) flow and the capping Log Creek (LC) flow. AB1 and AB2 are the stratigraphically lowest flows of the Imnaha Basalt. Higher in the composite section, AB and RC flows are intercalated, with AB dominating the lower part of the sequence and RC the upper (Figure 2) [26].

Lavas of Imnaha Basalt, especially the basal flows, are confined to the lowest parts of the greater Hells Canyon area, where they are underlain by accreted terrane rocks and overlain by flows of the Grande Ronde Basalt (Figures 2–4). Ref. [26] noted that stratigraphic correlations between sections are generally good north of the Wallowa Mountain-Seven Devils divide, while less consistent south of it (Figure 4). But even in the north, there are Imnaha sections that start with different flows, and some flows can be missing. Stronger pre-Imnaha paleotopographic relief is likely the main reason for missing lower flows. Upward missing flows could also be explained by lava flowing only into specific paleo drainages.

All Imnaha lavas range from olivine to quartz-normative tholeiites with a concentration of 4.04–7.09 wt.% MgO [11]. Lavas of the Rock Creek type have a range of 48–51 wt.%, and the American Bar type have 51–52.5 wt.% SiO_2 (on 100% volatile free basis); thus, both subtypes can be readily distinguished by silica content (Figure 5) [26]. On average, American Bar lavas have lower Ni content, higher Sc and Ca, and lower abundances of incompatible trace elements than Rock Creek samples, seen most clearly in the two lowest AB flows (AB1&2). Recently, [23] have shown that the differences between the two types can be explained by variable mineralogy in the source mantle; the RC source had a higher pyroxene to olivine ratio than that for AB. The difference is most clearly seen in the Ni contents of olivine from the two types, with AB flows having low-Ni olivine. There is some overlap between the two, and one flow (Log Creek) contains olivine of both types.

Figure 3. Tilted terrane rocks underlying horizontal lavas of Grand Ronde Basalt (horizontal layers in foreground and ridge in shade of background) and of Imnaha Basalt (lower flat bench in middle of picture). Image taken in Imnaha Canyon, 10 km north of the town of Imnaha.

Radiogenic isotope ratios of Imnaha lavas lie at the apex of radiating trends defined by all other CRBG formations, suggesting a mantle source dominated by one component. This enriched component was identified by [18], and attributed to a mantle plume source by [16,20].

2.2. The Picture Gorge Basalt

The PGB, as defined by [3] erupted from the Monument dike swarm in north-central Oregon (Figure 1). Its volume is 3300 km^3 and is relatively small, accounting for only 1.1% of the CRBG as compared to the other major units like the Imnaha Basalt and Grande Ronde Basalt, which comprise 15% and 72% of the CRBG, respectively [1]. However, recent work by [24] has revealed that the extent of PGB lavas is likely larger by ~14,000 km^2 with a total distribution of ~25,000 km^2 (Figure 1), yielding an additional volume ranging from ~3000–8000 km^3 based on using different thickness estimates.

The primary and original outcrop area of PGB flows is the John Day Basin of the Blue Mountains region of north-central Oregon (Figure 1) [34]; this has now been extended to the south and east to reach Malheur Gorge (Figure 1) [24], where Imnaha Basalt, Grande Ronde Basalt, and Steens Basalt interfinger (Figure 1) [30,35]. The northwestern outcrop area of the original PGB was also extended eastward based on new data [24]. Until recently, emplacement of the PGB was thought to have taken place 16.4–15.2 Ma [10]. New data now constrain PGB activity to 17.23–15.76 Ma [2,24].

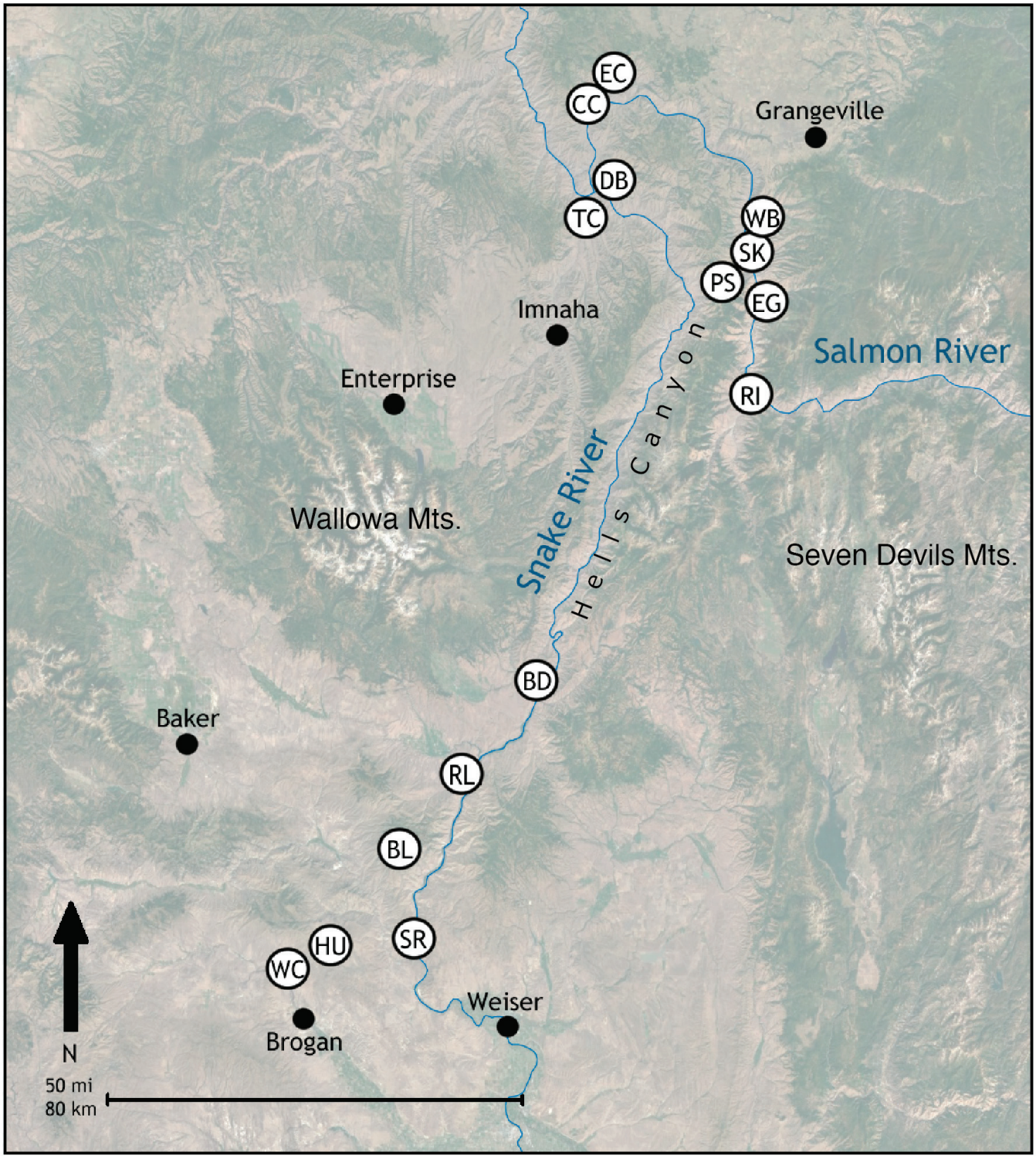

Figure 4. Map of sample locations of this study: BD = Brownlee Dam, BL = south flank of Big Lookout Mountain, CC = China Creek, DB = Dug Bar, EC = Eagle Creek, EG = Eagle Gulch, HU = West of Huntington, PS = Pittsburg Saddle, RI = Riggins, RL = Richland, SK = Skookumchuck, SR = Slaughterhouse Range, TC = Tully Creek, WB = Whitebird, WC = Willow Creek. See Figure 1 for coverage of Figure 4 within the CRBG distribution.

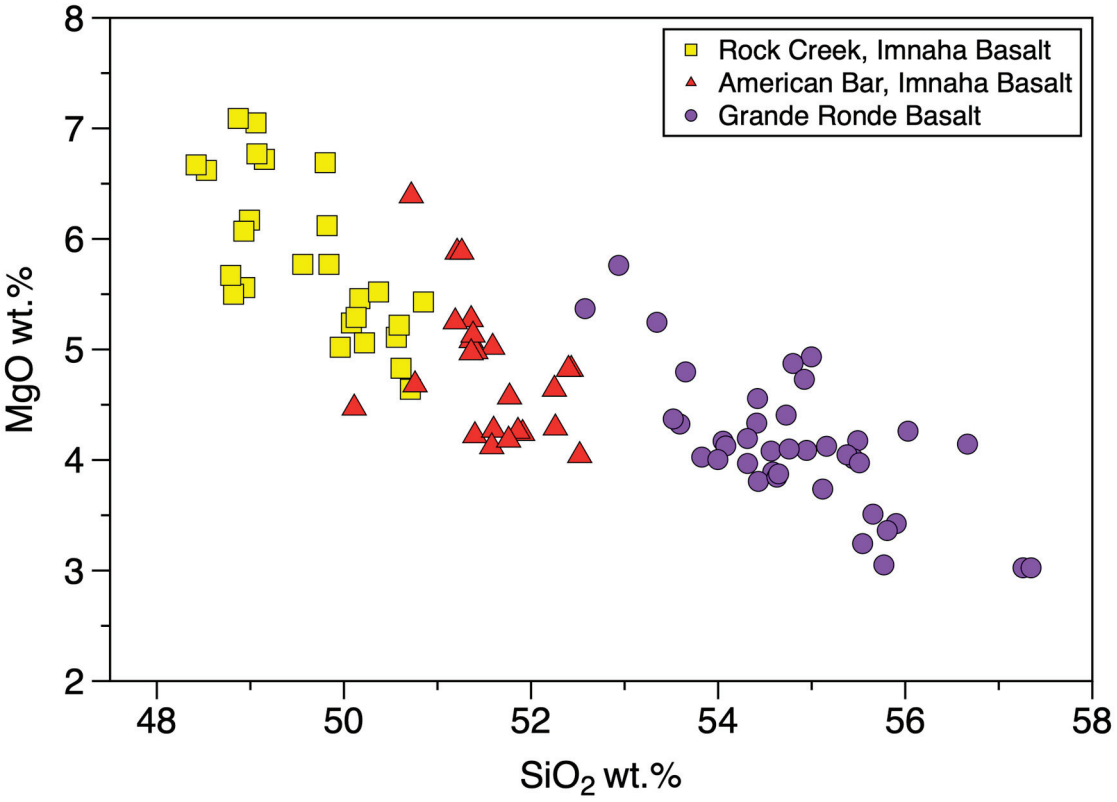

Figure 5. MgO vs. SiO_2 plot displaying data from the American Bar and Rock Creek flows of the Imnaha Basalt and the Grande Ronde Basalt. Data from [16].

Although PGB is generally geochemically similar to main-phase CRBG units in major elements, it is closest in composition to the Steens Basalt with respect to incompatible trace elemental and isotopic compositions [2,11,19,24]. Picture Gorge Basalt shows comparable SiO_2 wt.% ranges of 49–53 wt.% to those of the Steens and Imnaha Basalt, but PGB contains lower concentrations of Th, high field strength elements (HFSEs), light rare earth elements (LREEs) and Zr/Y values [2]. Compatible trace element abundances are however more similar to Imnaha AB than to Steens; this extends to the Ni content of olivines, suggesting that the PGB is derived from a peridotite source similar to AB lavas [23]. The PGB is primarily thought to be the product of a subduction-modified MORB-like source [11,16,19,20,36,37].

2.3. Other Main Phase CRBG Formations: Steens Basalt, Grande Ronde Basalt, and Wanapum Basalt

Here, for the sake of completeness, we briefly summarize these three additional main phase formations without treating each separately as they are less the topic of this paper. Based on previous geochronological work, onset of eruption of lavas of the Steens Basalt slightly predates the ones of the Imnaha Basalt at 16.97 ± 0.06 Ma [25]. All Steens Basalt lavas are thought to have erupted from the Steens dike swarm in southeastern Oregon (Figure 1). Steens Basalt is subdivided into the Upper and Lower Steens, which itself is divided into Lower Steens A and B [25,38]. Lower Steens Basalt generally reflects a relatively primitive composition, characterized by tholeiitic basalts interpreted to represent a homogenous mix of melts derived from depleted and enriched mantle with little contamination from the crust. By contrast, the Upper Steens Basalt is compositionally more alkalic and enriched in incompatible elements compared to the Lower Steens Basalt [25,37]. The Steens Basalt is thought to represent a mix of an enriched, OIB-like plume component and a depleted mantle component [11,22,38]. The compatible element inventory of Steens lavas nonetheless suggests derivation from a pyroxenite source, more similar to that for the Imnaha RC type than PGB [23].

The Grande Ronde Basalt is volumetrically the largest unit of the CRBG, covering 170,000 km^2 and comprising 72% of the CRBG by volume [1]. Eruptions of the Grande Ronde commencing ca. 16.56 Ma [14] from the Chief Joseph dike swarm (Figure 1). In the Hells Canyon region, the Grande Ronde Basalt conformably overlies the Imnaha Basalt. In the field, the Grande Ronde Basalt can be differentiated from the Imnaha Basalt as generally finer-grained and more resistant to erosion; additionally, most flows lack large phenocrysts. Chemically, the Grande Ronde is tholeiitic and more evolved than the Imnaha Basalt, with SiO_2 values generally above 53 wt.% and MgO values generally below 5 wt.% (Figure 5) [1,11,16]. The trace element and isotopic characteristics of the Grande Ronde show the influence of crustal contamination, and their genesis has been attributed to combined assimilation and fractional crystallization of Imnaha-type parental magmas [11,16,18].

The Wanapum Basalt consists of six members which are, in stratigraphic order: Ekler Mountain, Lookinglass, Frenchmen Springs, Shumaker Creek, Roza, and the Priest Rapids member. The Frenchman Springs, Roza, and Priest Rapids are major members, each having volumes >1000 km^3 and SiO_2 contents of ca. 50%, while the more primitive Eckler Mountain and more evolved Lookinglass and Schumaker Creek members are much smaller. Earlier age constraints suggested an activity period from 15.5 to ~15 Ma cf. [1] and hence lavas of the Wanapum Basalt were considered part of the CRBG "waning phase". More recent age dating of intercalated tuffaceous sediments however suggests that earliest Wanapum lavas erupted as early as 16.1 Ma and lavas of the youngest member around 15.9 Ma [12]. The latter age is supported by U-Pb zircon and sanidine $^{40}Ar/^{39}Ar$ ages and tephra correlation of silicic ashes overlying the capping Priest Rapids Member of ~15.8–16.0 Ma [39–42]. Given these new ages, it is reasonable to include the Wanapum Basalt in the "Main Eruptive Phase" cf. [21]. Lavas of the Wanapum Basalt cover about 87,400 km^2 and crop out mostly in Washington state and along the Washington/Oregon state border. Lavas represent a volume of 5.3% of the total CRBG volume [1]. Lava compositions are diverse, ranging from early Eckler Mountain basalts with ~8 wt.% MgO through the major members with typically ~4–5.5 wt.% MgO, to the minor basaltic andesite Schumaker Creek lava with >3 wt.% MgO. Trace element and isotopic variations among the Wanapum lavas suggest an origin involving complex fractionation and interaction between primitive Eckler Mountain-type magma and residues from the preceding Grande Ronde magmatic episode [43].

3. Methods

3.1. Fieldwork

Sampling for this study was carried out in two areas, the northern one encompassing the greater Hells Canyon area located north of the Wallowa–Seven Devils Mountains divide (Figure 4). The northern area has historically received the most attention for investigating Imnaha Basalt and is the basis for establishing the existing stratigraphy and chemical types of the Imnaha Basalt [26]. The second area includes a wide swath from just south of the Wallowa–Seven Devils Mts divide (Figure 4) towards the town of Huntington and the town of Brogan. Lavas of Imnaha Basalt have been reported from this area e.g. [44], and this area constitutes the southeastern-most extent of the Imnaha Basalt (Figure 1). In both areas, lavas of Imnaha Basalt directly overlie rocks of Paleozoic terranes or Cretaceous plutonic (mostly granodioritic) rocks.

Sampling locations in the northern study area were chosen based on stratigraphic columns, sample locations, and compositional data from [26]. A total of nine locations were sampled throughout the greater Hells Canyon area of NE Oregon and western Idaho (Figure 3). We resampled locations studied by [26] that previously indicated exposures of American Bar flows 1 and 2, as these flows are not as uniformly distributed throughout the Hells Canyon area compared to stratigraphically higher American Bar and Rock Creek flows. This is mainly due to the significant pre-existing relief at the time of onset of CRBG eruption in NE Oregon (Figure 3). Resampled locations of [26] include Dug Bar, Eagle Creek, China Creek, Riggins, and Whitebird Creek. Several additional transects were

conducted at locations proximal to terrane rock–basalt boundaries, in the northern area these sites being Eagle Creek and Tully Creek; south of the Wallowa Mountains, additional transects were performed at Richland, Slaughterhouse Range, and Willow Creek. Lastly, one or two flows near terrane boundaries were sampled at Skookumchuck, Brownlee Dam, Big Lookout Mountain Road, and Huntington Road (Figure 4).

3.2. Analytical Work

The majority of samples collected in the field were analyzed for their major and trace element compositions by X-ray fluorescence (XRF) and inductively coupled plasma mass spectrometry (ICP-MS) analyses at the Peter Hooper GeoAnalytical Laboratory at Washington State University, Pullman. Samples were first chipped and further prepared according to laboratory standards, depending on the type of analysis. Major and trace element data were determined with a ThermoARL X-ray fluorescence spectrometer, and trace elements and REEs were analyzed with an Agilent 7700 ICP-MS. More detailed descriptions of analytical methods and precision can be found in [45] for XRF and [46] for ICP-MS, available at https://environment.wsu.edu/facilities/geoanalytical-lab/technical-notes/ (accessed 20 February 2021).

Petrographic thin sections were prepared by Spectrum Petrographic. Thin sections were examined to determine mineral phases and relative abundances.

Three samples from the southern sector of the study area were chosen for age dating. New high-precision $^{40}Ar/^{39}Ar$ ages (Table 1) were obtained by incremental heating methods using the ARGUS-VI mass spectrometer housed at the Oregon State Geochronology Lab. Samples were irradiated for 6 hours (Irradiation 15-OSU-07) in the TRIGA CLICIT nuclear reactor at Oregon State University, along with the FCT sanidine (28.201 $\pm$ 0.023 Ma, 1σ) flux monitor [47]. Detailed analytical procedures, geochronological methods, and data are included in the Supplemental Material (S4, S5).

Table 1. Summary Table of $^{40}Ar/^{39}Ar$ Ages for Imnaha Basalt.

Sample Location	Sample Name	Phase	Age (Ma)	Error (±2σ)	MSWD	$^{40}Ar/^{36}Ar$ Intercept	No. Steps
Richland section	MM-CRB-32	plagioclase	17.11	0.15	1.60	295.11	9
Richland section	LF-21-54	groundmass	17.18 *	0.07	1.76	303.10	13
Willow Creek section	LMF-19-80	groundmass	16.84 *	0.07	4.43	296.16	7

Plateau ages are within error of their inverse isochron age unless otherwise specified

* = Mini plateau.

3.3. Assignment of Imnaha Chemical Types

As our sampling targeted the stratigraphic lowest part of the Imnaha Basalt, our evaluation focused on determining if collected samples fall into the following categories: (1) they represent lavas of American Bar flow 1 and 2 (AB1&2); (2) they represent middle to higher American Bar flows (AB3+), or (3) they represent flows of the Rock Creek type (RC). In our comparison, we initially excluded data from the stratigraphically highest Rock Creek flows, the Fall Creek and Log Creek chemical types, as both of these types exhibit chemical systematics overlapping with lower Imnaha flows, yet our stratigraphic focus on the basal Imnaha flows falls clearly below where Fall or Log Creek flows are exposed. Where we sampled all the way up to the overlaying Grande Ronde Basalt flows (Richland section), we specifically address whether or not flows of these two types were sampled there. However, we will revisit the top Imnaha flow units later in the discussion.

The chemical data and flow classifications from [16,26] were used to compare the data of this study to determine the likely flow designation of samples collected. We used a combination of major and incompatible trace elements to designate the chemical affinity of our samples. Examples are shown in Figures 6 and 7. Plots for all sample locations as well as additional plots used for assigning a unit identity can be found in the Supplemental Material (S1, S2, S3).

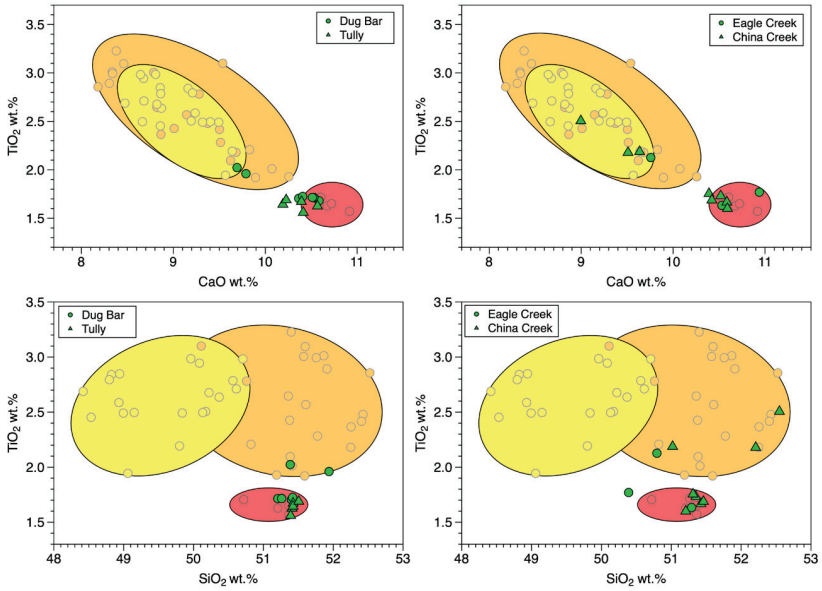

Figure 6. Compositional fields for AB1&2 (red), AB3+ (i.e., AB3-9) (orange), and RC flows (yellow) (except for uppermost two flows, Fall Creek and Log Creek) [16]. New data of this study in green. These diagrams illustrate how samples of four of our field sites from this study compare to published data [16]. This method, along with other compositional fields on bivariant plots and normalized incompatible element diagrams (see Figure 7) were used to assign our samples a flow identity of either AB1&2, AB3+, or RC (see text).

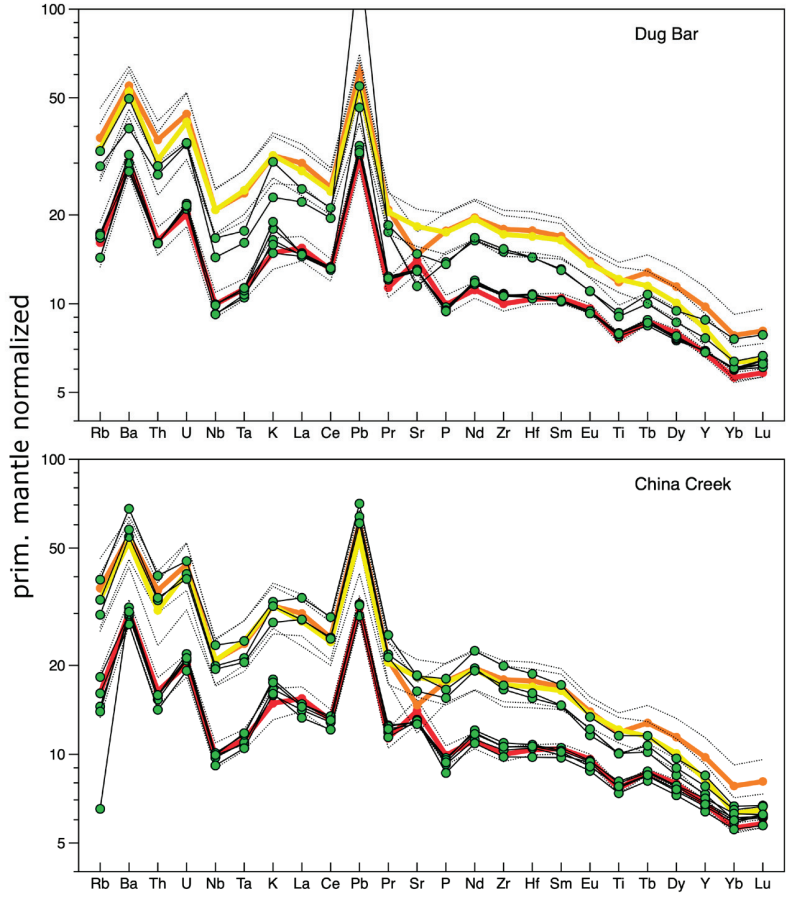

Figure 7. Primitive mantle-normalized incompatible elemental diagrams (normalization values taken from [48] of average AB1&2 (red), AB3+ (orange), and RC (yellow) compositions of data by [16]

with 1 sigma envelopes (dashed lines) and samples of our study (green circles) from two sites, illustrating how normalized incompatible elemental diagrams were used to assign our samples a flow identity of either AB1&2, AB3+, or RC (see text).

4. Results

4.1. Dug Bar

Dug Bar is the type locality for the Imnaha Basalt [26]. Here, the Snake River incised through around a kilometer of basalt flows to the current water level. On the northern and southern margins of Dug Bar, the Imnaha Basalt is underlain by accreted terrane rocks comprised of granodiorites, metasedimentary, and metavolcanic rocks of the Wallowa terrane. Directly across the river from the sample location, the basalts form a series of colonnades and entablatures indicative of differential cooling directions [49].

The seven samples, likely representing multiple flows (up to seven) collected at Dug Bar are porphyritic, containing elongate plagioclase phenocrysts ranging from 5 mm to 20 mm in length within a fine plagioclase groundmass with pyroxene and minor olivine and pyroxene phases [49] (S1 Supplemental Material).

All seven samples were selected for bulk rock analysis. These samples have SiO_2 values that range from 51.2 to 51.9. The five samples from the stratigraphically lowest flows are nearly indistinguishable, while the two uppermost are compositionally distinct (Figure 6, S2, S3 Supplemental Material). For example, the elemental range of these five for TiO_2, CaO, La, and Zr are, respectively: 1.68–1.72 wt.%, 10.36–10.58 wt.%, 9.9–10.2 ppm, and 118 to 121 ppm. The values for the same elements for the stratigraphically highest two samples are: 1.96–2.02 wt.%, 9.68–9.79 wt.%, 15.2–16.8 ppm, and 168–172 ppm. All samples possess Mg numbers of 46, with the exception of the two stratigraphically highest samples with values of 40 and 43. The five lower samples all fall within the envelope representing the spread of samples classified as American Bar 1 and 2 by [26], while the higher pair plot in diagnostic major element space (TiO_2 vs. SiO_2 or TiO_2 vs. CaO) into the American Bar 3+ field (Figure 6). The silica values for all of the Dug Bar samples reported are too high to represent Rock Creek flows [26].

The trends of samples from Dug Bar seen on normalized incompatible element diagrams ('spidergrams') are consistent with the grouping based on major elements (Figure 7). The majority of the samples plot more closely to the AB1&2 average values. Samples LF-20-05 and LF-21-40 (the "two higher" units), while not quite as enriched, are most similar to the AB3+ pattern. This is most noticeable with the negative Sr and Ti anomaly observable in the average AB3+ curve that is not present in RC flows, while a positive Sr spike appears in the first two AB flows.

All samples have peaks in Ba and Pb, with sample LF-20-05 being enriched in Pb by nearly an order of magnitude. Additionally, all samples from Dug Bar have a relatively distinct Nb-Ta trough that is present throughout the Imnaha Basalt.

4.2. Tully Creek

Five samples were collected along the west bank of the Imnaha River proximal to Tully Creek, located approximately 10 km south-southwest of Dug Bar (Figure 4), and all are near the same stratigraphic level (S1 Supplemental Material). Like the exposures at Dug Bar, the basalt outcrops at Tully Creek form entablatures underlain and capped by colonnades. The basalts are again porphyritic, with elongate 5 to 25 mm twinned plagioclase phenocrysts in a fine plagioclase-pyroxene matrix with minor olivine, pyroxene, and opaque phases [49].

The samples from Tully Creek all plot tightly together (e.g., with SiO_2 values of 51.39 to 51.51 and TiO_2 values of 1.56–1.69 wt.%). Observed concentrations are consistent with values for samples of American Bar 1 and 2 (S2 Supplemental Material). The incompatible element patterns for the Tully Creek samples also most closely resemble those of the lowest American Bar flows 1 and 2 (S3 Supplemental Material). The only readily discernible differences between the average AB1&2 values and the values of Tully Creek samples are

the marginally elevated concentrations in the most incompatible elements and a small positive K anomaly likely reflecting weathering effects.

4.3. Eagle Creek

Eagle Creek is the northernmost location visited during our sampling campaign. Three samples were collected at this location along a creek bed that drains into the Salmon River (S1 Supplemental Material). Outcrops are not as pronounced along Eagle Creek, with many being eroded and buried by weathered basalt colluvium, yet samples were taken from progressively higher stratigraphic levels. Samples collected at Eagle Creek once again exhibit large plagioclase phenocrysts typical of the lower basalt flows throughout Hells Canyon [49].

Major element values for these samples are more variable than reported for the previous locations. Silica values range from 50.4 wt.% to 51.3 wt.%, and TiO_2 ranges from two values around 1.7 to one with 2.1 wt.%. Lower TiO_2 but higher CaO in two samples compared to the third sample correspond well with incompatible element concentrations (S2, S3 Supplemental Material), suggesting that these two samples correlate with AB1&2 compositions while the third sample reflects a AB3+ composition rather than a Rock Creek flow.

Sample LF-21-29 is somewhat anomalous, in that is has a relatively low Rb value compared to the average values for the other Imnaha Basalt flows. The sample also possesses a negative K anomaly, indicating that this is likely the result of post-eruption alteration rather than representative of the original composition.

4.4. China Creek

China Creek is located roughly 3.5 km to the west of Eagle Creek. At this location we were able to collect samples across a stratigraphic transect of flows proximal to the Salmon River. We collected eight samples sequentially from the lowest exposed basalt (LF-91-27) towards progressively higher stratigraphic levels (S1 Supplemental Material). As at Eagle Creek, basalt exposures here are partially covered by colluvium and weathered basalt. Basalts are all porphyritic, with large 1 to 2 cm elongate plagioclase phenocrysts in a fine groundmass [49].

In major element space of TiO_2 vs. CaO and TiO_2 vs. SiO_2, it is evident that five samples fall into or very close to the AB1&2 field, as they have low TiO_2 and high CaO and SiO_2, comparable to AB1&2 samples. Three samples are clearly different and fall into the AB3+ field and Rock Creek field in the TiO_2 vs. CaO plot. However, the TiO_2 vs. SiO_2 identifies them clearly as AB3+ samples (S2 Supplemental Material).

Incompatible element compositions of the lowest five China Creek samples are consistent with findings based on major elements, as their elemental pattern plots on top of the average AB1&2 curve. The remaining three uppermost samples closely match the patterns for Rock Creek and AB3+, yet the higher silica values suggest that they belong to the latter (S3 Supplemental Material).

4.5. Riggins and Eagle Gulch

The Riggins sample, LF-21-03, was collected from the colonnade near the town of Riggins [49]. Samples LF-21-01 and LF-21-02 were collected to the north at Eagle Gulch.

The major element plots show the Riggins sample plotting close to AB1&2. The other two samples are more ambiguous, with silica concentrations midway between average Rock Creek and AB averages and Mg numbers closest to AB3+ (S2 Supplemental Material). The low CaO and high TiO_2 values seen in these samples are closest to Rock Creek samples.

The incompatible element pattern for the sample from Riggins is most similar to the AB1&2 average (S3 Supplemental Material). The other two samples from Eagle Gulch are at the high end of the sigma 1+ envelope of avg. AB3+ and Rock Creek samples. The steeper elemental patterns from P through Lu suggest they are rather Rock Creek compositions, but the Sr trough resembles AB3+. Overall higher incompatible elements and lower Sr would

be however consistent if they represent slightly more fractionated Rock Creek compositions. Mg# values at the lower end of Rock Creek composition would also be compatible with this. Taken all together, we group these two samples with the Rock Creek unit.

4.6. Pittsburg Saddle

The Pittsburg Saddle sampling location site is unique in that it is stratigraphically removed from other nearby sampling locations by thrust faulting that occurred directly to the east of the sample site, uplifting these exposures [50]. All samples collected at this location plot most closely to the AB1&2 compositions, with average values around 51.5 wt.% silica and low TiO_2 concentrations. CaO and TiO_2 values cluster closely together, around 10.3 wt.% CaO and 1.67 wt.% TiO_2 (S1, S2 Supplemental Material).

The incompatible element patterns for the Pittsburg Saddle samples plot close to one another and along the upper sigma 1+ envelope to the average AB1&2 values. Hence, major and trace elements are consistent to group them with AB1&2 (S3 Supplemental Material).

4.7. Skookumchuck Creek

Three samples were collected from a cliff face proximal to Skookumchuck Creek, with the lower two samples likely sampling bottom and top of a lower flow and the third sampling the overlying flow [49]. The basalts at this location also form colonnades and contain large plagioclase grains in a fine-grained plagioclase matrix.

These samples exhibit major element data which are most similar to the average values for the Rock Creek flows, ranging from 49.5 to 50.5 wt.% silica. Major elements CaO and TiO_2 values display a similar distribution with samples plotting near the Rock Creek and AB3+ average values, with CaO values ranging from 8.7 wt.% to 9.7 wt.% and TiO_2 values of 2.8 wt.% (S2 Supplemental Material).

Considering the low silica content and incompatible element patterns, these samples are most similar to Rock Creek. Samples LF-21-04, and LF-21-06 to a lesser extent, have substantial Rb depletions. Both samples have a negative K anomaly as well, likely indicators of secondary alteration, as Rb and K are both fluid-mobile elements (S3 Supplemental Material).

4.8. Whitebird Creek

Five samples were collected along a short transect south of the town of Whitebird (S1 Supplemental Material). Two samples, LF-21-14 and LF-21-15, most closely resemble the average values for AB3+, while the remaining samples, LF-21-16, 18, and 19, are most similar to Rock Creek (S2 Supplemental Material). Silica values are distributed in two groups; the three samples taken higher in stratigraphy contain around 49–50 wt.% silica, while the lower two samples contain 51.5 wt.% silica. A similar pattern can be seen with TiO_2, where the stratigraphically lowest samples contain lower TiO_2, around 2.1 wt.%, while the three higher samples all contain just over 3.0 wt.%. The lowest samples also contain slightly higher CaO than the samples from higher flows.

All samples collected from Whitebird are most similar to the normalization patterns representing the average AB3+ and Rock Creek flows (S3 Supplemental Material). The stratigraphically lower samples, LF-21-14 and 14, both have incompatible element values slightly below those of the average values of AB3+, while the stratigraphically higher samples are all slightly enriched compared to the average values of Rock Creek. Samples LF-21-16, 18, and 19 may have experienced some loss of K due to slight weathering, leading to lower than expected normalized K values in element patterns of these samples. All samples collected at this location possess negative Sr anomalies. With that in mind, samples LF-21-16, 18, and 19 resemble Rock Creek samples from Riggins, where we suggest negative Sr anomalies with plotting along upper envelope of Rock Creek indicates more fractionated Rock Creek compositions. The Whitebird Rock Creek samples also indicate lower Mg#.

4.9. Richland

Ten samples were collected along a transect to the southeast of Richland, Oregon (S1 Supplemental Material). One additional sample was taken ~300 m up the road from the transect location. The Richland location is roughly 130 km south from the sites sampled to the north, and is the second northernmost location of our second sampling area located south of the Wallowa–Seven Devils Mountains divide (Figure 4). The basal CRBG flow here directly overlies Burnt River schist that crops out ~50 m down the road from the transect location and that represents accreted terrane rocks. The lower flows of this outcrop are partially covered in colluvium. The basalts are slightly vesicular and contain cm-scale plagioclase phenocrysts similar to the basalts found at the sample sites to the north. About midway in the section, some parts are more friable as they are more vesiculated and some are brecciated, representing flow tops or bottoms. The uppermost flows, near the top two samples, are finer-grained, dense and are phenocryst-poor to aphyric. Lithological variations along this transect by itself suggest that the lower two-thirds along the transect are Imnaha flows while the uppermost part of the transect and the overlying towering cliffs are lavas of the Grande Ronde Basalt [49].

The samples collected along this transect show an array of compositions, some unique compared to those documented for the sample locations of the northern area. Seven samples possess CaO, TiO_2 (with the exception of LF-21-54; (S2, S6 Supplemental Material)) and incompatible element patterns very similar to AB1&2, yet have SiO_2 and Mg# that resemble those of Rock Creek lavas, except LF-21-50 that has a SiO_2 content of 50.8 wt.%, matching AB1&2 values (S6 Supplemental Material). LF-21-51, -52, are most similar to Grande Ronde Basalt, in line with their aphyric texture. Sample LP-21-53 is texturally like these two and is our stratigraphically highest sample. It has a SiO_2 content of 52.2 wt.%, which is not typical for Grande Ronde Basalt. The remaining samples appear most similar to the AB3+ subset.

Incompatible element patterns reveal that the stratigraphically lowest five samples, the seventh sample (LF-21-50), and the sample collected further up the road (MM-CRB-32) plot closer to the average AB1&2 value, with two samples, LF-21-47 and MM-CRB-32, plotting substantially below. All these samples have a Nb-Ta trough and have also notably stronger Ba and Sr peaks (S3 Supplemental Material). While we group these samples as AB1&2, we recognize that there are distinct differences to our AB1&2 samples of our northern area that will be addressed below.

4.10. Slaughterhouse Range

A subset of eight samples were selected for analysis from a sample transect about 8 km east of Huntington, OR (S1 Supplemental Material). Accreted terrane rocks also underlie this section. Basalts are all porphyritic with ~10% phenocrysts of plagioclase and a coarse-grained groundmass, except for the most SiO_2-rich sample, LMF-19-73, which is fine-grained with only small and few phenocrysts (<5%), and the highest sample LM-19-76 which has also few phenocrysts [51]. Similar to the Richland samples, compositions observed here are diverse and somewhat deviate from what was observed in the northern sampling area. The two stratigraphically lowest samples (LMF-19-70, -71) and the fifth sample LMF-19-74 are overall best matched with lower American Bar (i.e., AB1&2) compositions, yet significant differences exist (S2 Supplemental Material). The strongest evidence for this association is seen in mantle-normalized incompatible element patterns (S3 Supplemental Material). All three samples plot on top of AB1&2 average or close to the +1 sigma envelope. In terms of major elements, low TiO_2 and higher Mg# on plots vs. SiO_2 similarly suggest that, although the compositional field is scattered around the actual AB1&2 field. The other samples overall fit best with AB3+ compositions. Among these, two samples are notable; the first one is LMF-19-73 with a 53.3 wt.% SiO_2, 8 wt.% CaO, and a Mg# of only 32. Typically, such evolved compositions along with elevated incompatible elements are only observed in Grande Ronde Basalt and lavas of the upper Steens Basalt cf. [24], yet this sample is intercalated among flows with AB1&2 as well as

AB3+ characteristics. Also notable is the sample from the stratigraphically highest lava, LMF-19-76, which has a trace element pattern akin to Rock Creek samples but is too high in silica for such association, unless it is again a fractionated Rock Creek composition as suggested by the Sr trough.

4.11. Willow Creek

An area about 8 km north-northwest of the town of Brogan, along Willow Creek, was investigated and samples taken (Figure 4). Here, pre-Cenozoic schists of the accreted terranes crop out along the valley floor and younger basalt forms a prominent rimrock along the western valley side as well as along the eastern side but only south of the investigated area. CRBG aged lavas crop out in between and crosscut schists in select areas. Prominent columnar jointing with variable orientations is also evident [51] (S1 Supplemental Material). All field observations together suggest that this area represents a near-surface vent area and subaerial flows. All Willow Creek samples are phenocryst-poor (<4%), with a coarse to fine-grained groundmass. Observed compositions are more restricted, although sampling around the area with columnar jointing reveals compositions that are more fractionated, also reaching 53.3 wt.% SiO_2. Trace elemental patterns are again most revealing and suggest all samples reflect AB1&2 compositions with similar differences as noted for the last two sampling sites. Major elements (TiO_2 vs SiO_2 and Mg# vs. SiO_2) of the Willow Creek samples also point to AB1&2 (or similar) compositions (S2, S3 Supplemental Material).

4.12. Brownlee Dam and Single Basal Samples from Elsewhere

Two samples were collected along the Snake River just north of Brownlee Dam that were the closest to the terrane/CRBG contact (Figure 4). This location is also the closest to northern area sampling sites. Additional samples include one sample from a basal flow on the south flank of Big Lookout Mountain, and one sample overlying terrane rocks west of Huntington (Figure 4). One of the Brownlee Dam samples is clearly AB1&2, while the second shares characteristics with AB1&2 but also has concentrations suggesting it is transitional to AB3+ but on the lower incompatible trace elements side. Major element plots suggest both are AB1&2 (S2 Supplemental Material). Similarly, both of the other two samples are best associated with AB1&2, although they have incompatible patterns as documented for the other southern areas. Interestingly, the Brownlee Dam samples are more similar to the original pattern of AB1&2 (S3 Supplemental Material).

4.13. Summary of Unit Classification

In Figure 8, we compare our samples from all sample locations and their unit assignment with the data from [26] that were reanalyzed by [16] (see also S7 Supplemental Material). This comparison indicates the following. All lavas from the north area assigned as AB1&2 closely match AB1&2 samples reported by [16] and the average given in [26], with the exception of one Eagle Creek sample that displays lower SiO_2 wt.%. Lavas from the south area assigned as AB1&2 show a much greater compositional range but incompatible element concentrations (e.g. Nb, Th, La, Zr), and the concentrations of the characteristic major element TiO_2 are consistent with values reported for AB1&2 samples by previous workers. Our sample assignment to Imnaha subunits AB3+ and RC is consistent with published data. It is notable that both of these groups are only effectively separated when using silica on bivariate plots. This particularly applies to the published data, as our AB3+ and RC samples indicate generally narrower ranges which may simply be due to the fact that we did not systematically sample these subunits. Overall, however, our classification approach seems adequate to separate lower American Bar lavas, AB1&2, from middle and upper American Bar as well as Rock Creek samples. This fact is particularly well illustrated when we compare average incompatible trace element systematics. Figure 9 shows mantle-normalized incompatible trace element patterns that clearly reveal a striking contrast between AB1&2 averages for northern and southern sampling area with averages for AB3+ and Rock Creek samples across the entire area. This also shows the dif-

ferences in AB1&2 compositions between the northern and southern sampling area. Lastly, it also shows close compositional affinity of both AB1&2 averages with the average of PGB samples.

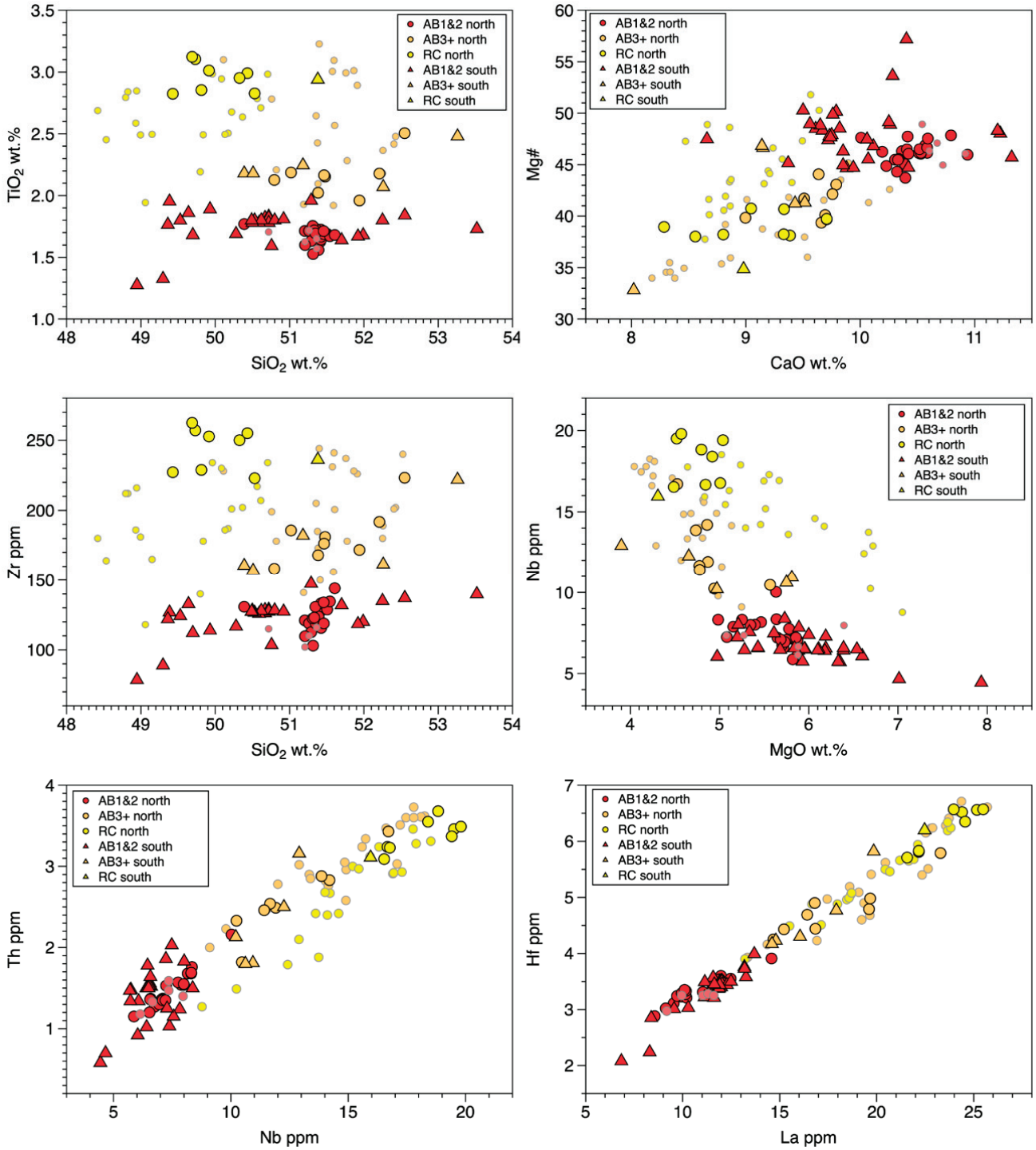

Figure 8. Comparing assigned samples of this study (large symbols) to Imnaha Basalt data of [16] (small symbols); red = American Bar 1&2 flows, orange = American Bar 3+ (#3 to 9) flows, yellow = Rock Creek flows without the two top flows, Fall Creek and Log Creek flow.

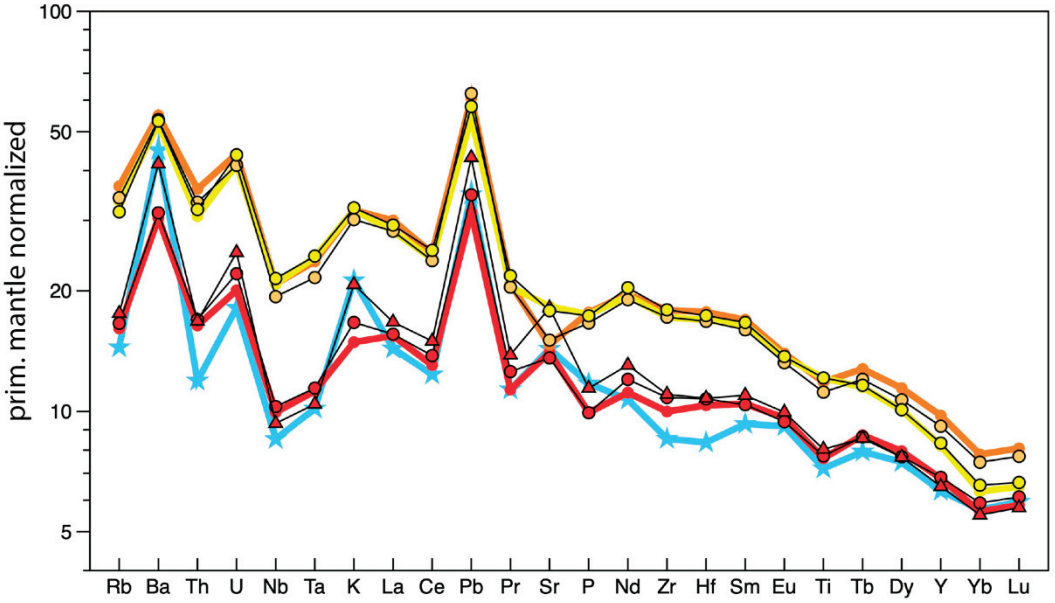

Figure 9. Primitive mantle-normalized incompatible element diagram comparing composition averages of AB1&2 (red), AB3+ (orange), and RC (yellow) flow data of [16] with averages for data of this study (black lines) and distinguishing averages for AB1&2 from the northern area (red circles) and southern area (red triangles). Average PGB composition shown in blue using data of [2,16,24].

4.14. New Age Dates

We selected three samples for dating via $^{40}Ar/^{39}Ar$ geochronology from the southern area (Table 1). Two samples were collected from the Richland section and resulting ages are supported by field relationships and their relative stratigraphic position. The stratigraphically lower sample (sample LF-21-54) was collected from a lava flow overlying terrane rocks at the base of the section and yields a mini plateau age of 17.18 ± 0.07 Ma, within error of the inverse isochron age (Figure 10; S5.1 Supplemental Material). The other dated Richland sample is from a lava flow stratigraphically higher in the section (sample MM-CRB-32) and yields a mini plateau age of 17.11 ± 0.15 Ma, also within error of the inverse isochron age (Figure 10; S5.2 Supplemental Material). Sample MM-CRB-32 was collected from a lava flow that corresponds to approximately the fourth sample of transect, LF-21-47 (S1 Supplemental Material); both samples exhibit a distinctly more primitive composition and as such could be correlated (Figure 9; S6 Supplemental Material). The third sample selected for geochronology was collected from the Willow Creek section (sample LMF-19-80). The Willow Creek sample yields a plateau age of 16.84 ± 0.07 Ma that is within error of the inverse isochron age (Figure 10; S5.3 Supplemental Material).

Our new ages are older than the upper age bracket for Imnaha Basalt and are overall consistent with published data. The younger age bracket for Imnaha is 16.57 Ma, determined by two U-Pb zircon ages from a tuffaceous sedimentary unit stratigraphically above Imnaha Basalt AB1&2 and supported by a $^{40}Ar/^{39}Ar$ age from a Imnaha Basalt lava flow immediately below the Imnaha/GRB contact and likely emplaced at the end of Imnaha volcanic activity [12,14]. Earlier Imnaha activity is further constrained by another U-Pb age of 16.601 Ma from a lapilli tuff intercalated between two Imnaha lava flows. Ref. [52] report a $^{40}Ar/^{39}Ar$ age of 16.85 ± 0.21 Ma for a Imnaha lava flow at the top of Squaw Butte in west-central Idaho, located approximately 100 km southwest from our Willow Creek location. While the upper Imnaha Basalt is well-dated, none of these existing ages are derived from samples representing the base of the Imnaha Basalt.

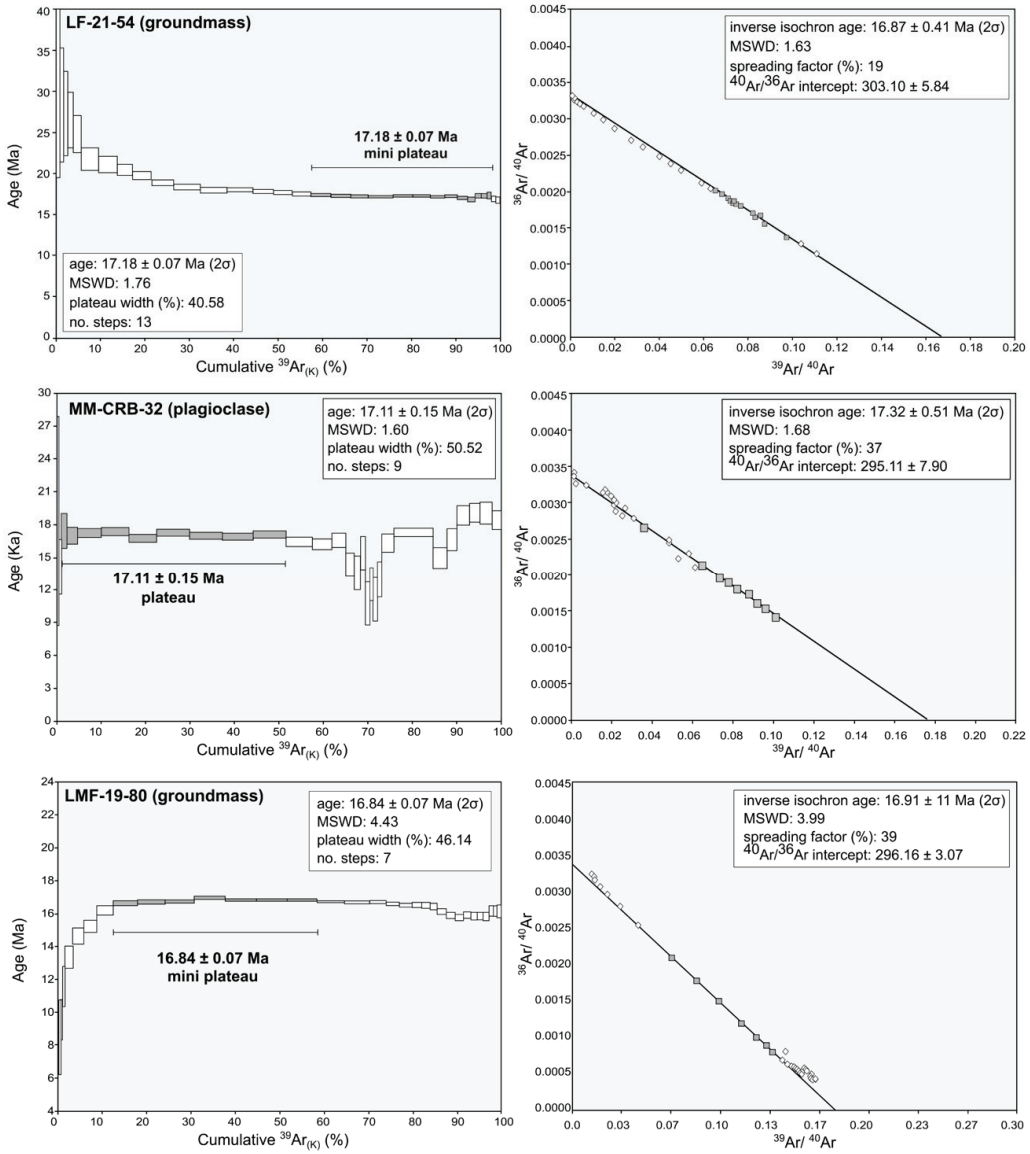

Figure 10. Weighted Ar-Ar ages for select samples of this study. See also Table 1. Full analytical data can be found in the Supplemental Material (S5).

5. Discussion

We structure our discussion by reviewing compositional similarities of lower Imnaha Basalt flows with Picture Gorge Basalt, examining regional differences in widespread onset of depleted CRBG volcanism as represented by PGB and lower American Bar lavas, evaluating the influence of this mantle component through time with the implications for magma diversity within the Imnaha Basalt. We finish the discussion by comparing samples of this study to basaltic samples of the nearby oceanic Siletzia large igneous province and to typical calc-alkaline lava compositions of the Cascade volcanic arc.

5.1. Comparison of Lower American Bar Flows (AB1&2) to the Picture Gorge Basalt

The first two American Bar flow units of the Imnaha Basalt are remarkably similar to the Picture Gorge Basalt; this was the source of early speculation about their equivalence [27,31], but was recognized in subsequent work up to the present [2,16,24,31]. In fact, [2] included samples by [49] from the Brogan area to argue for PGB lavas cropping out far southeast of where PGB was thought to occur.

On most element covariation diagrams and element ratio plots, the PGB and AB1&2 values plot with PGB or in an area of overlap (Figures 11 and 12). In mantle-normalized incompatible element diagrams, the pattern of average PGB only deviates from the one of our sample averages as calculated for the northern and southern area in a few specific features (Figure 9). More specifically, PGB samples possess a slight Zr-Hf trough that is not observed in AB1&2, while those lavas, in turn, have a negative P anomaly that is not observed in the average PGB. PGB lavas tend to have a steeper Th–U transition and are more enriched in Ba and K relative to AB1&2 lavas of our northern area, yet this is not the case for southern samples of this study (Figure 9). These differences are not only observed when average values are plotted but noted differences also show up in plots with Hf/Sm, Nd/P_2O_5, Th/U, Ba/Th, La/K_2O capturing the Zr-Hf trough, P anomaly, and Ba and K enrichment, respectively (S7 Supplemental Material).

Major element concentrations are less useful to differentiate PGB and AB1&2 lavas from other Imnaha subunits, although one consistent characteristic is that PGB and AB1&2 have lower TiO_2 values than either Rock Creek or middle to upper American Bar lavas. Although AB1&2 lavas have a similar range of SiO_2 values, they are separated from the AB3+ flows by generally higher MgO values, making them more similar to the higher-silica, lower-MgO Picture Gorge lavas (Figure 11). AB1&2 are higher in CaO than AB3+ and RC lavas, as is PGB (Figure 8).

Using concentrations of 27 trace elements obtained via ICP-MS, a principal component analysis (PCA) was conducted on AB1&2 samples, AB3+ (subdivided into flows 3 to 5, and 6 to 9), RC flows, and Picture Gorge Basalt lavas. We find that, statistically, AB1&2 flows are more similar to the Picture Gorge Basalt than they are to the rest of the American Bar and Rock Creek subunits of the Imnaha Basalt (Figure 13). The principal components displayed in Figure 13 account for 88% of the variance between variables (76% for PC1 and 12% for PC2). Imnaha AB1&2 is subdivided into "north" and "south" according to our sampling area. This spatial dependence on composition will be elaborated on in the next section.

To summarize, the many important compositional commonalities of AB1&2 and PGB lavas documented here tie these units together as the earliest lavas of the CRBG north of 43.5° N, and in turn indicates the first basalts to erupt were those derived from a relatively depleted mantle, yet these lavas indicate some regional variability. Similar signatures are also observed among lavas of the Steens Basalt that erupted in the southern portion of the CRBG. In fact, the first two lavas of the newly recognized lowest-most Steens Basalt unit (Lower Steens A, [25]) have an extremely similar incompatible normalization elemental pattern as AB1&2 and PGB (Figure 14A), yet again with subtle differences that on one hand makes them more similar to AB1&2 (e.g., lower Ba enrichment), others are more like PGB (Zr-Hf trough, overall lower Th, U enrichment) and others that appear unique to Steens (steeper REE pattern) (Figure 14A).

Previously, due to its distinctly high Ba/Nb and apparent contemporaneity with Grande Ronde Basalt (Figure 2), the PGB was considered distinctive among all the main phase CRBG formations, for example attributed to an episode of back-arc magma generation of uncertain relation to the rest of the CRBG by [16]. However, the newer $^{40}Ar/^{39}Ar$ ages of [2] indicate that the PGB, including lavas of the type locality, is significantly older and contemporaneous with the Imnaha Basalt. Recently, [13] has re-interpreted the age significance of the paleomagnetic relationships to suggest that a magnetic reversal near the top of the PGB sequence corresponds to that at the Imnaha—Grande Ronde boundary, rendering the bulk of the PGB, at the youngest, age-equivalent to the Imnaha. This now gives a more consistent overall picture for the whole main-phase CRBG of early relatively primitive basalts (PGB, Steens, Imnaha) giving way to more evolved compositions with time (Grande Ronde, Wanapum). Therefore, it is important to recognize now that the earliest CRBG lavas across the province show depleted signatures, yet with regionally distinct differences, but all indicating the tapping of a depleted source. We address the regional variability of this depleted mantle source in the next section.

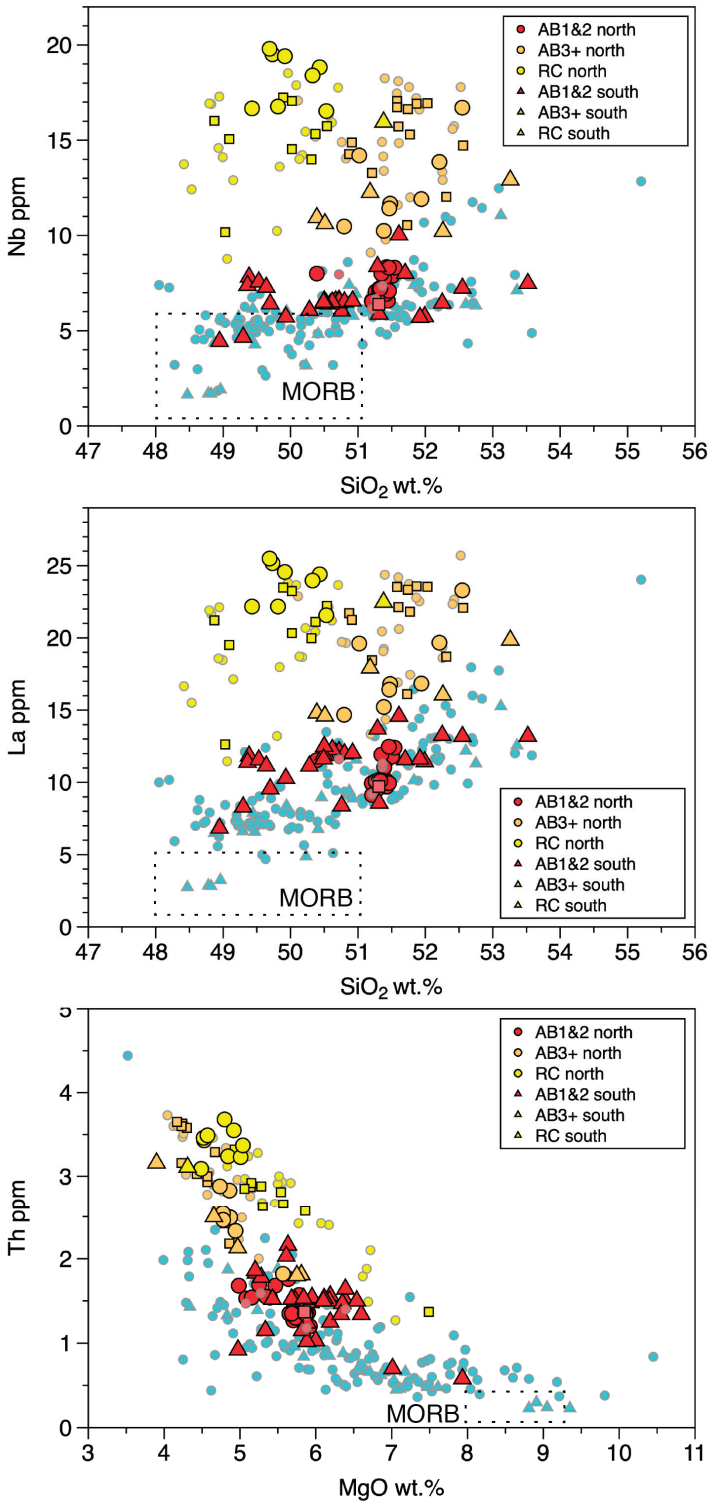

Figure 11. Comparing AB1&2 samples to PGB ([24]—blue circles, [16]—blue triangles). Large symbols are for samples of this study, small symbols are literature data; additional Imnaha data by [23] shown in small squares. MORB field after [53].

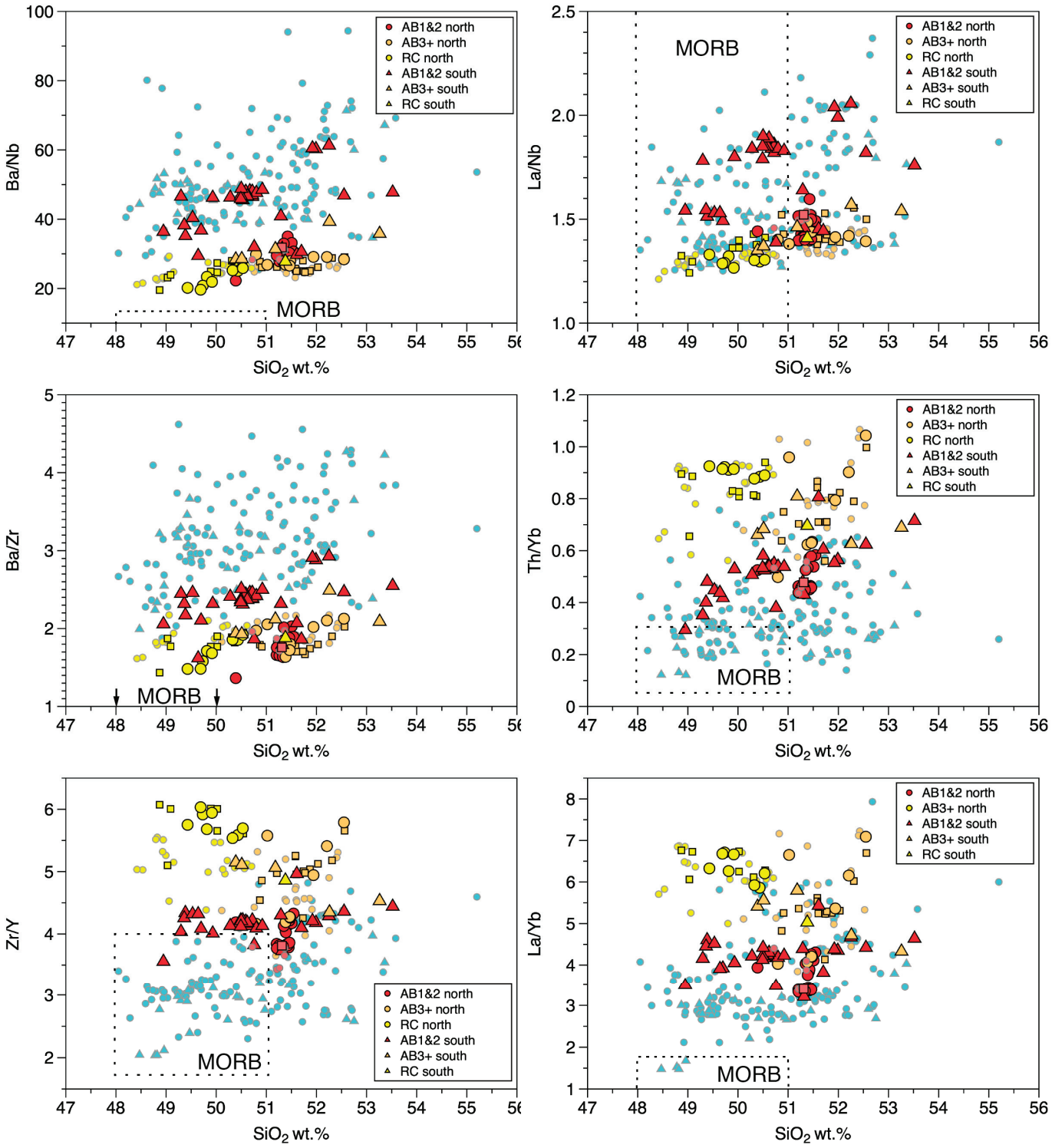

Figure 12. Comparing elemental ratios of AB1&2 samples to PGB ([24]–blue circles, [16]—blue triangles). Large symbols for samples of this study, small symbols are literature data; additional Imnaha data by [23] shown in small squares. MORB field after [53]; open rectangles or arrows indicate that values extend beyond displayed range.

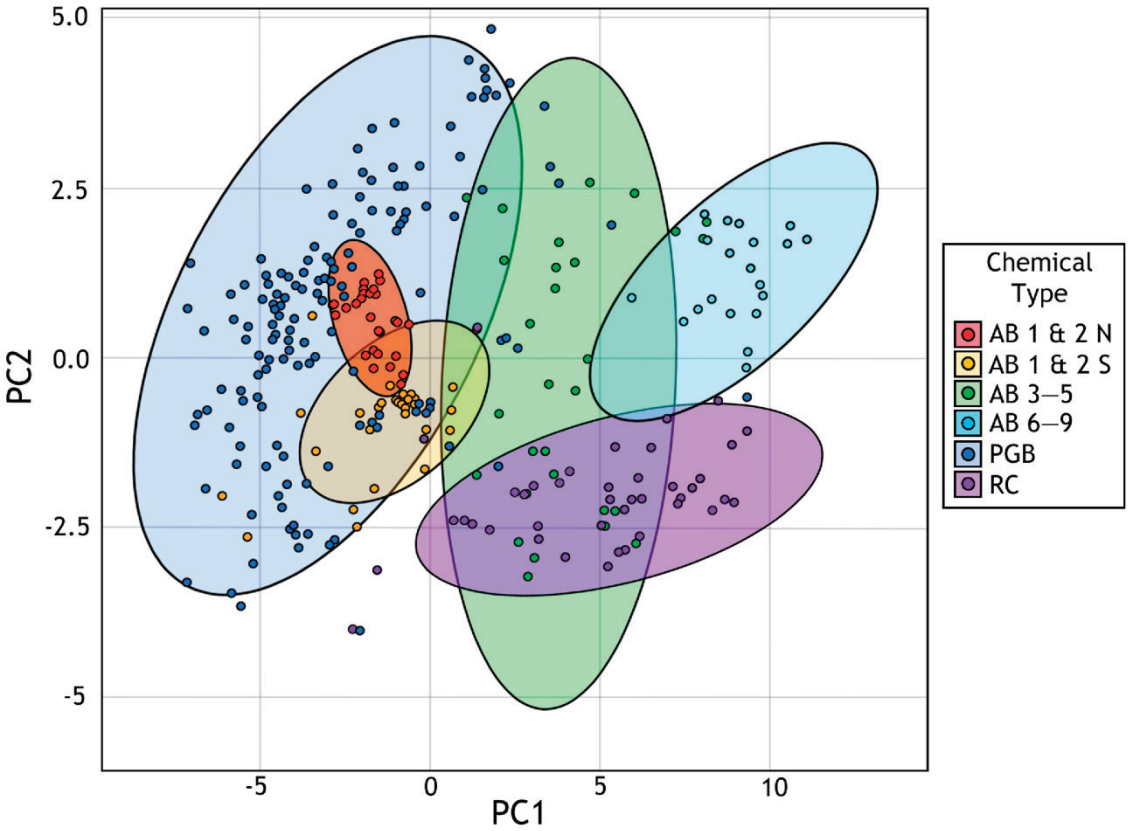

Figure 13. Scatter plot of trace element principal component scores for samples of AB1&2 north samples (N = 26), AB1&2 south (N = 32), AB3–5 (N = 27), AB6–9 (N = 21), RC (N = 37), and PGB (N = 146). Shaded areas are 89% confidence ellipses corresponding to their respective classifications. Data from [2,16,23,24] and this study.

5.2. Compositional Provinciality of Depleted and Metasomatized Mantle Signal

Both major and trace element compositions of basal Imnaha Basalt lavas of this study clearly reveal that their compositions vary regionally. Most basal Imnaha samples collected south of the 45th parallel are characterized by a greater positive Ba anomaly, possess a deeper Nb-Ta trough, and possess a slight Zr-Hf trough, characteristics of PGB (Figure 9). Additionally, they possess lower silica and higher MgO than northern AB1&2 flows (Figure 11). The few southern flows of this study that are more like the north are samples from Brownlee Dam, Big Lookout, and the basal Slaughterhouse lava. In general, however, basal Imnaha flows show a range of compositions with respect to select chemical parameters. This was also observed by [20] who collectively called these lavas "south-of-OWL basalts" (OWL = Olympic Wallowa Lineament) and noted their resemblance to PGB. Many workers [16,18–20,37] have noted that PGB lavas are incompatible element-depleted compositions and have argued they are derived from a depleted mantle that experienced reenrichment reflecting a subduction-related overprint. We posit that all basal CRBG flows record an upper depleted and reenriched lithospheric mantle, but there are regional differences in the degree of the depletion and of this subduction-related metasomatic overprint. In other words, earliest CRBG lavas tapped a variably depleted and metasomatized mantle. What is less agreed upon is whether this depleted mantle is asthenospheric mantle with a nearly contemporaneous subduction overprint [11,16] or if this mantle is lithospheric and the subduction overprint is much older [20,54] As mentioned above, the differences in the degree of metasomatic overprint, and the apparent age range, led to PGB being regarded as having an uncertain relationship to other main stage CRGB formations [11]. Here we argue the opposite, that the depleted characteristic of all basal lavas (e.g., Figures 14 and 15) suggest a rather common upper mantle source and

that the differences in degree of depletion and metasomatic overprint of this source may be related to proximity to subduction-related fluids and melts, as well as to the possible involvement of sublithospheric mantle related to the accreted terranes. Figure 16 illustrates these regional differences among AB1&2, PGB, and Steens Basalt lavas. In general, Zr/Y, La/Yb, low Nb content (as are, e.g., Rb, Th, U, LREE contents) are likely parameters that predominatly reflect the degree of the depletion of this upper mantle source (Figure 15). On the other hand, Ba/Nb (and Ba/Th, Ba/La, or Sr/P) signify metasomatic overprint, yet more evolved compositions with high ratios may also result from crustal processes during which invidual lavas could have been affected by stronger assimilation effects or other non-source changes modifying the original LILE signals (e.g., [18,22,34]. The La/Yb ratio has been used as a measure for changes in the degree of partial melting, while an increase in Tb/Yb was taken as being due to an increase in residual garnet [23]. There is clear variation in both of these parameters among main phase CRBG formations (Figure 15), suggesting lower degrees of partial melting with significant residual garnet for Steens and Imnaha Rock Creek lavas, while PGB and AB1&2 would represent higher degrees of melting with little to no garnet; other AB lavas lie in between these extremes [23]. Differences in partial melting are nonetheless unlikely to affect LILE/HFSE ratios with elements of similar incompatibility (e.g., Ba/Nb). However, partial melting degrees must still be somewhat comparable for all discussed depleted CRBG lavas in order to produce silica-saturated tholeiitic melts from rather shallow depths [55,56]. Lastly, calling upon mantle mineralogy, as demonstrated with the high- and low-Ni trend of [23], would be insufficient as sole explanation for regional compositional differences (e.g., Ba/Na, La/Yb, Zr/Y) among discussed depleted CRBG lavas, because such parameters would not be strongly affected by changes in the clinopyroxene to olivine ratio in the mantle at comparable partial melting degrees.

Lavas can clearly travel long distances, allowing a mixed record in any one section, as superposed lavas may originate from different vent locations. Incompatible element ratios nonetheless vary somewhat regionally for lavas with a generally depleted signal as discussed above (Figures 9, 11, 12 and 15–17), which is a strong suggestion that regionally variably depleted and metasomatized mantle sources are surprisingly preserved in regional lava compositions. In fact, each of the general areas (PGB, Steens, AB1&2 north, AB1&2 south) seems to record its own unique combination of chemical characteristics (Figures 16 and 17).

In addition to our location data, one other specific example of how flows likely reflect local variations as well as flows that travelled far distances comes from the eastern Malheur Gorge area (Figure 1). Malheur Gorge was previously highlighted as an area where Steens lavas from the south were interfingering with Imnaha and Grande Ronde lavas derived from the north [30,35]. Refs. [2,24] expanded on this and argued that PGB lavas were interfingering as well. Select Imnaha lavas from the eastern Malheur Gorge around Namorf [17] and around Gold Creek indicate the following. Some of these have compositions like AB1&2 flows of our southern area, while there are compositions (best correlated with AB3+) that have compositional signals like northern Imnaha flows (e.g., low Ba/Nb at high Nb) (Figure 15; S8 Supplemental Material). One outcome of this compositional provinciality is that Imnaha AB1&2 flows did NOT travel from north to south, at least not southward from Brownlee Dam. One venting area for those lava flows could be the Brogan—Lookout Mountain region (cf. Figure 4); vents for American Bar-type phreatomagmatic tuffs and lavas have been described from Lookout Mountain [57] (Figures 1 and 4). On the other hand, upper Imnaha lava flows may have travelled southward from the north into our southern area of investigation, also reaching into the eastern Malheur Gorge area.

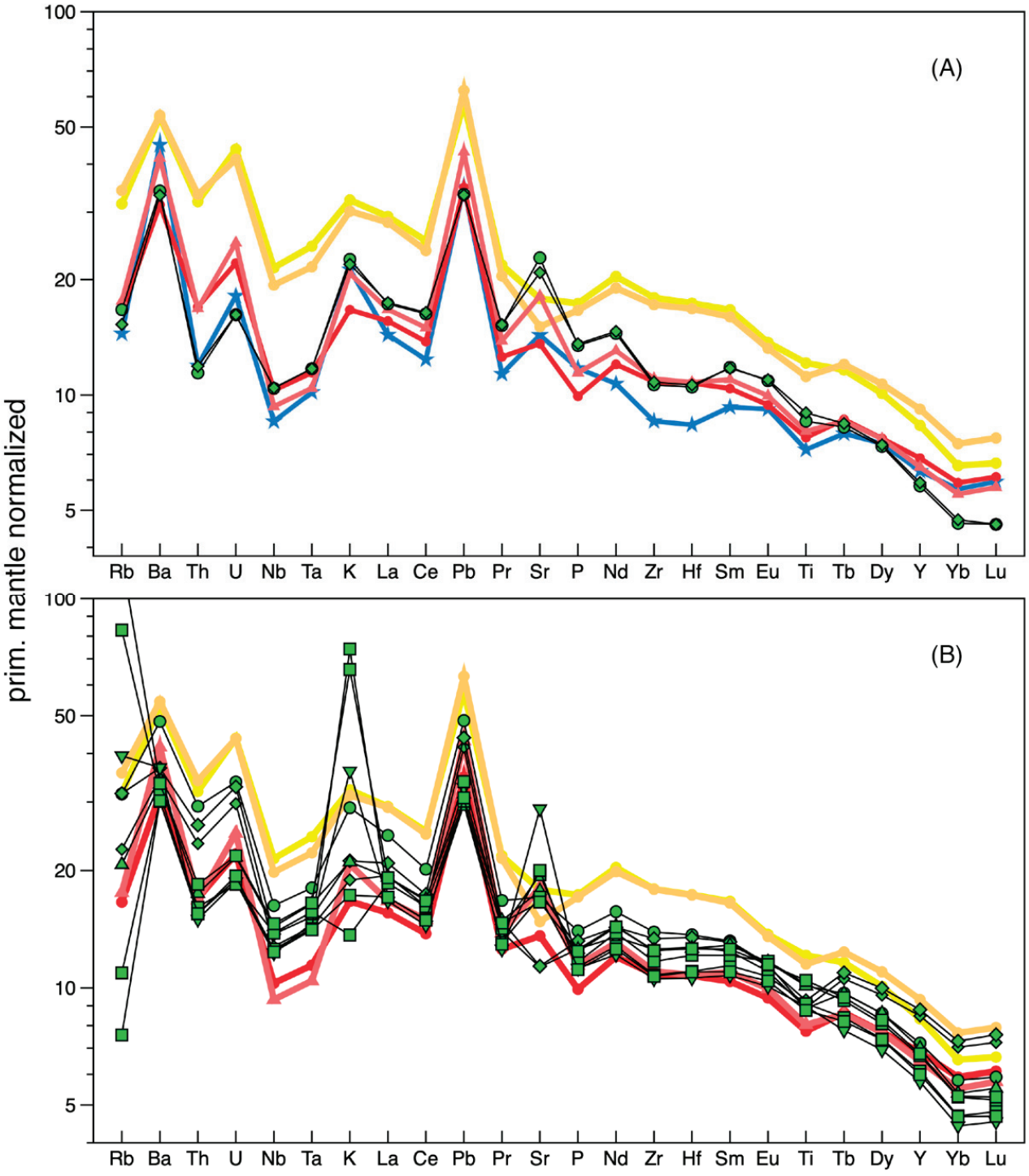

Figure 14. Primitive mantle-normalized incompatible element diagrams comparing composition averages of AB1&2 (red: northern area, light red: southern area), AB3+ (orange), RC (yellow), and average PGB (blue) to: (**A**) lowermost two flows of Steens Basalt. #NMSB-55 and NMSB-57 of Lower Steens A subunit (green) [25], (**B**) select samples of other Imnaha flows (cf. Figure 2): AB3a (green circle), AB4 (green diamond), RC2 (upright green triangle), RC2y (down triangle) and Log Creek (green squares) [16].

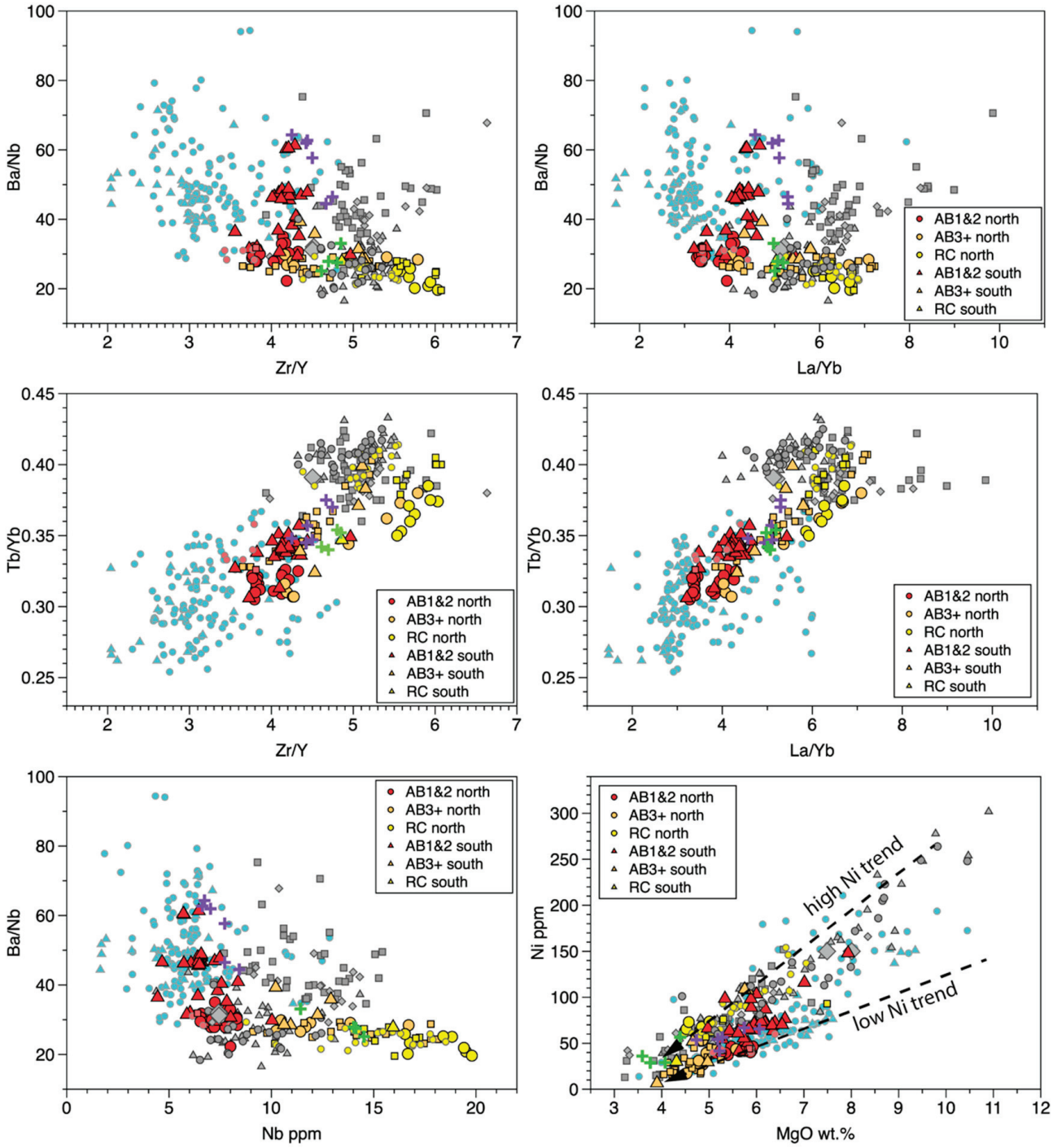

Figure 15. Comparing elemental ratios of AB1&2 of this study to PGB ([24]—blue circles; [16]—blue triangles) and to Steens Basalt (gray symbols, diamonds = Lower A (large symbols for lowest two flows), triangles = lower B [25], squares = Upper Steens of [16,25]; circles = lower Steens [16]. Large symbols are samples of this study; small symbols are literature data [16]; additional Imnaha data by [23] shown in small squares; low- and high-Ni trend from [23]. Purple and green crosses are for samples from the eastern Malheur Gorge (S8 Supplemental Material), purple for samples with AB1&2 affinities and green for samples with AB3+ affinities.

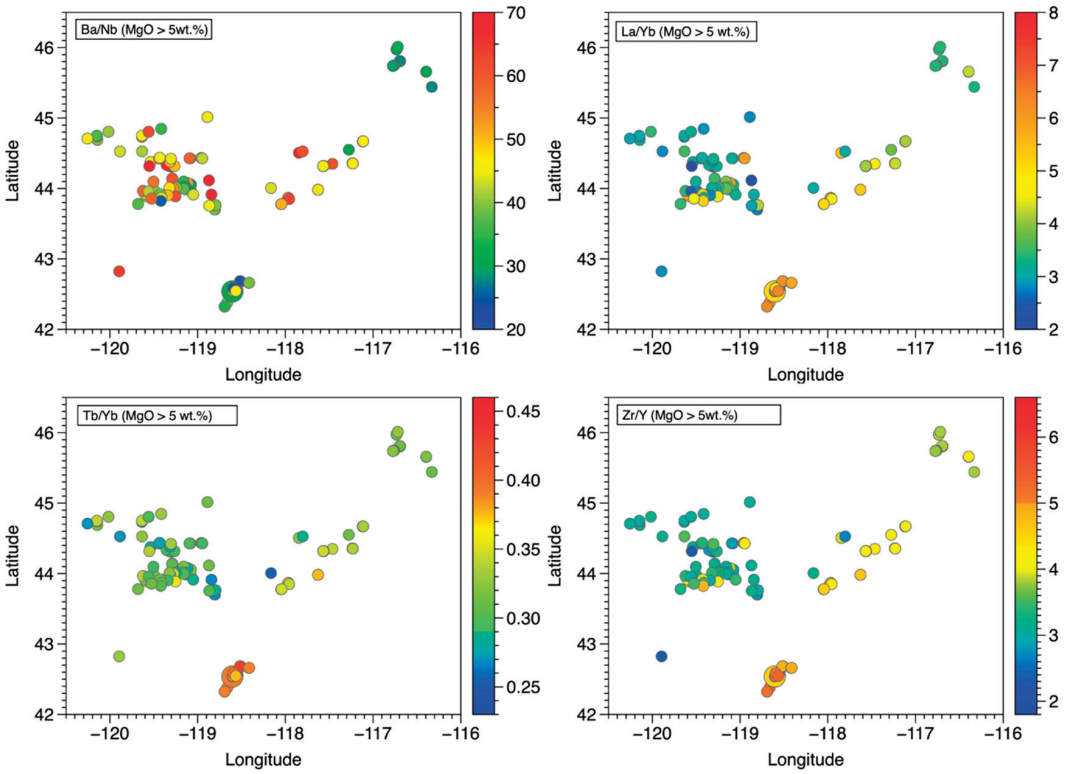

Figure 16. Regional variation in compositional parameters for AB1&2, PGB, and Steens Basalt lavas with >5 wt.% MgO. Data from this study, [23–25]). Larger circle among Steens Basalt samples for basal depleted lavas plotted in Figure 14A.

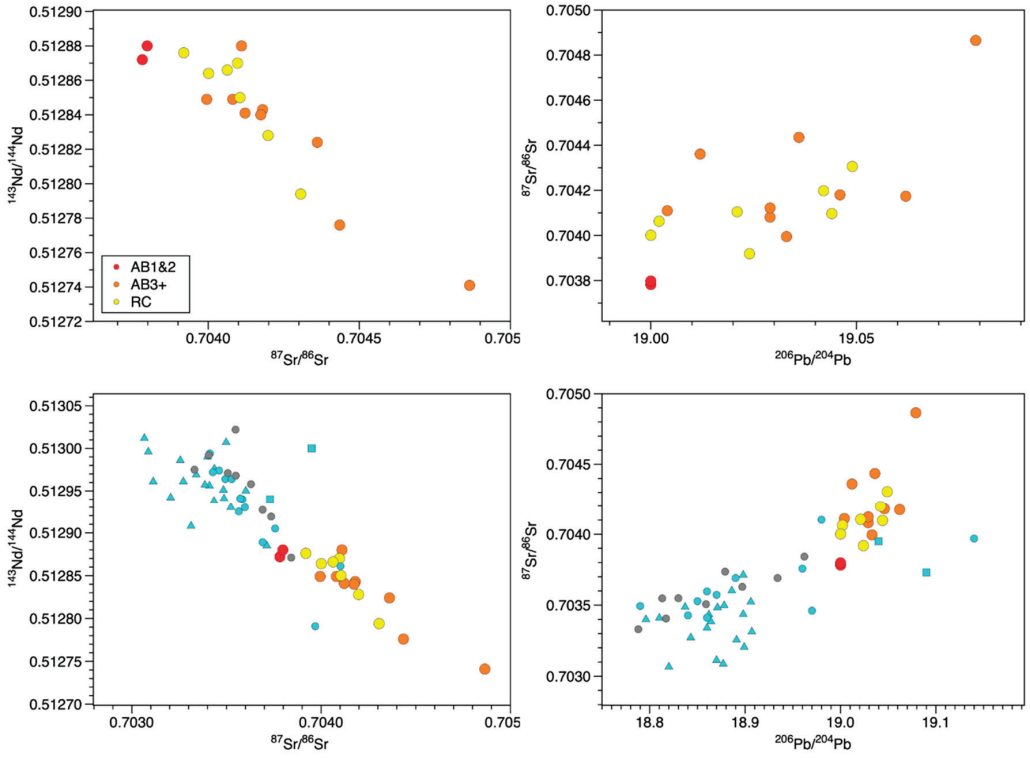

Figure 17. $^{143}Nd/^{144}$ Nd vs. $^{87}Sr/^{86}$ Sr and $^{87}Sr/^{86}$ Sr vs. $^{206}Pb/^{204}Pb$ plots of AB1&2, AB3+, and Rock Creek flows, as reported by [11]. Lower panels show plots adding data from the PGB in blue (triangles—[16]; squares—[19]; circles—[37]) and of Steens Basalt in gray circles [16].

5.3. Magma Types of Imnaha Basalt and Relationship of American Bar Flows 1 and 2 to the Overlying Imnaha Basalt Flows

As documented above, elemental concentration ranges and some element ratios clearly discriminate AB1&2 units from the other Imnaha subunits. On the other hand, overall incompatible elemental patterns are similar to other AB units and even to units of Rock Creek (Figure 14). This raises the question: what genetic relationship exists between AB flows 1 and 2 and the upper AB flows and RC flows? Ref. [58] argued that upper American Bar compositions could be largely derived by fractionation combined with recharge from lower American Bar compositions. Furthermore, ref. [20] argued for one Imnaha source but producing melts at three different degrees of partial melting, subsequently undergoing fractionation to give rise to AB1&2, AB3+, and to RC compositions. They argued that isotopic variations among Imnaha subunits were too small to call upon different mantle sources. To the contrary, ref. [11] did see evidence for source variation based on isotopic ratios (Figure 17). Radiogenic isotope ratios of AB1&2 plot between PGB and AB3+ − RC flows (Figure 17). The range of incompatible element concentrations at constant MgO is unlikely to have been produced by fractional crystallization alone (Figures 9 and 12). Some of the higher AB flows with compositions close to AB1&2 may be related by fractional crystallization to AB1&2. However, ref. [23] showed that varying mantle source mineralogy (or fractionation of primary melts at mantle depths) is responsible for some of the variation within, and overlap between, both AB and RC chemical types. This suggests that, despite similarities of AB1&2 with AB3+ and RC, AB1&2 has its unique source (or reflects a unique proportion of sources). This is consistent with all available data and argues that AB1&2 flows should not be lumped into a single source model for the Imnaha Basalt.

5.4. Recurrence of Depleted Magma Types

Our new ages of AB1&2 and the updated eruptive timeline from [2] demonstrate that PGB eruptions temporally overlaped with eruption of the Imnaha Basalt, suggesting that a relatively depleted source was tapped for the very intital Imnaha eruptions before transitioning to eruption of more typical, more enriched Imnaha basalts (AB3+) shortly thereafter. However, there are stratigraphically higher subunits of the Imnaha Basalt that are more depleted than underlying units and hence indicate a greater role of a depleted source. These are: AB4 (#BUK5 and #DB7) [16], RC2 (#W45), RC2y (#GRJ1), and RC Log Creek (several samples) from lower to higher in the stratigraphic section (Figure 14b) [16]. In summary, the Imnaha Basalt stratigraphy suggest a depleted mantle was tapped at the very beginning of Imnaha Basalt volcanism, but it also played an increased role intermittently during subsequent eruptions. An intermittent depleted mantle signal is also preserved in the geochemical signals of the stratigraphy of the Steens Basalt lava flows [25].

5.5. Compositional Context of Earliest CRBG Lavas to Siletzia LIP and Cascade Volcanic Arc Lavas

This compositional comparison provides additional evidence for tapping a shallow and variably metasomatized mantle source without clear compositional plume signal. Numerous studies have suggested that the mostly mid-Miocene flood basalt lavas of the CRBG are a result of a rising deep-sourced mantle plume impinging on the base of the North American lithosphere [59–67]. On the other hand, there are a number of non-plume models that ascribe flood basalt volcanism to regional upper plate tectonics [6,65] or processes associated with the downgoing slab of the Cascadia subduction zone, such as a growing tear in the subducted oceanic lithosphere [7]. Most recently, a model is gaining popularity in which CRBG flood basalts are not the expression of the initial impingement of a deep-seated rising mantle plume but a secondary upwelling with the original plume impingement dating back to the Eocene along the North American Pacific coastal area, producing a nearby oceanic plateau that is known as the Siletzia large igneous province [68]. In this model, the initial plume—lithosphere interactions began at ~53 Ma and continued to present day as the North American plate has migrated over the plume tail e.g., [8,68]. The Siletzia LIP is estimated to have a volume of 1.7–2.6 $\times$ 10^6 km^3, 8–12 times the lava

volume of the CRBG and hence is more on par with volumes of other flood basalt provinces than the CRBG [68]. Siletzia basalts crop out in various places from southern British Columbia/northern Washington State to southern Oregon, and the province is imaged in the subsurface by a strong aeromagnetic high along the entire length [68]. The model is attractive, as it explains two LIPs formed side-by-side that are ~36 myr apart.

In this context, it is interesting to compare lava compositions of Siletzia basalts with those of the CRBG, particularly the ones that are the focus of this study, the earliest CRBG lavas. Doing so reveals the following. Siletzia basalts range from MORB-like, low-Ti compositions to more enriched and high-Ti compositions (Figure 18) [69–72]. And this range is thought to reflect the interaction of a depleted source with isotopic and trace element characteristics expected for a MORB source of a spreading center with a plume with a HIMU signal [70]. While low-Ti Siletzia samples share some compositional similarities with samples of this study, as all record a more depleted source, they are distinctly different with regards to other important chemical characteristics as observed in mantle-normalized incompatible element diagrams and radiogenic isotopes. All low-Ti Siletzia basalts lack the Nb-Ta and Ti trough that is so characteristic for PGB, AB1&2 north and south, and Steens (Figure 18A) (cf. Figure 5 of [71]; Figure 7 in [72]. They also typically lack the Zr-Hf trough as compared to samples of our study, although this is less consistent. Higher-Ti Siletzia basalts strongly display a HFSE enrichment with a clear OIB signature, and hence the range of Siletzia basalts fall into the MORB-OIB array in a Ba/Nb versus Nb/Zr plot (Figure 18C). Such an array is not observed in CRBG lavas, although a minute shift to higher Nb/Zr signal is observed in Rock Creek, upper AB, and some PGB samples. Siletzia samples also contrast with trends of CRBG samples in isotopic plots with $^{87}Sr/^{86}Sr$ (or $^{143}Nd/^{144}Nd$) vs $^{206}Pb/^{204}Pb$, where Siletzia samples make for a horizontal array from lower-Ti, more MORB-like samples to higher-Ti samples (Figure 18D), while CRBG samples trend mostly diagonally from samples near the C1 component of [19] towards the C2 and Imnaha (IC) components of [19] and [16], respectively. The C1 component was influenced by an incompatible element-depleted source, while C2 and Imnaha components are influenced by an enriched reservoir with a debatable source of enrichment [16,19]. On the other hand, comparing samples of this study to typical calc-alkaline lavas of the Cascade volcanic range reveals great similarity in incompatible element patterns, such as LILE enrichment and HFSE depletion, and isotopic composition (Figure 18B–D).

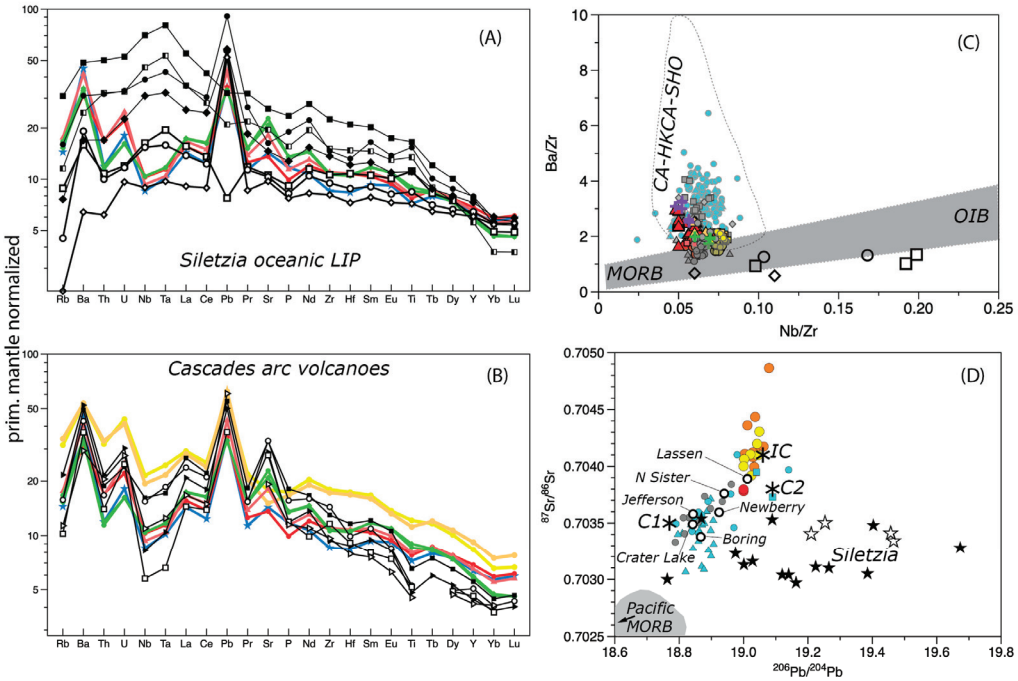

Figure 18. (**A**,**B**): primitive mantle-normalized incompatible diagrams of samples shown in Figure 14A

(red for AB1&2 north, light red for AB1&2 south, blue for PGB, and green for basal lavas of Steens Basalt) along with sample averages of Siletzia LIP basalts in (**A**) and select mafic calc-alkaline Cascade arc lavas (basalt to ~53 wt.% basaltic andesite) in (**B**). Data for Siletzia samples are: open diamond: <1.6 wt.% TiO_2, closed diamond: >2.0 TiO_2 [71]; open circle: <2.0 TiO_2, closed circle: >2.5 TiO_2 [72]; open square: <2.5 TiO_2, half-filled square: 2.5–3 wt.%, filled square: 3–4 wt.% TiO_2 ([69] with data found in Supplemental Material S8). Data for Cascade samples (also found in S8 Supplemental Material): open square: Crater Lake [73], open triangle: Lassen volcano [73], solid triangle: average of Newberry samples [56]; open circle: Mount Jefferson [74]); filled square: average of Wuksi volcanic chain samples (Streck, unpublished data); (**C**) samples of this study (cf. Figure 15) in Ba/Zr vs. Nb/Zr with MORB-OIB array (gray field) and dotted field for calc-alkaline (CA), high K calc-alkaline (HKCA), and shoshonitic (SHO) Cascade arc samples after [75]; open symbols are for average Siletzia compositions of samples shown in (**A**): diamonds: [71]; circles: [72], squares: [69], samples towards MORB are low-TiO_2 compositions, more towards OIB are high-TiO_2 compositions. (**D**) Figure 17D with Siletzia samples (solid stars: [72], open stars: [69], Cascade compositions (same data sources as before, except data of N. Sister volcano from [75], and compositions of select components: C1, C2: [19], and IC for Imnaha component of [11]; Pacific MORB field from [25] that extends beyond shown range.

The discussion above reiterates the following aspects of PGB, AB1&2 north and south, and discussed Steens lavas. Low HFSE and radiogenic isotopes trending towards MORB indicate that the lavas are variably depleted approaching those of MORB-like composition of the oceanic Siletzia LIP. The recognition of the involvement of a depleted source in these compositions is a well-accepted view that has been mentioned in papers for decades [11,16,19,20,25]. Another well appreciated point, typically made for PGB, is that the deviation from a flat incompatible element pattern with enrichment in select LIL elements and LREE is due to elemental overprint of this relatively depleted source [11,16,19,20,60]. The comparison of PGB, AB1&2 north, south, and Steens with typical calc-alkaline mafic lavas of the young Cascade volcanic arc supports this view, and now, not only for PGB but also for the other earliest lavas. The Cascade volcanic arc at 17 Ma was located near where the arc is now (Figure 1) [76]. The distance to the arc at 17 Ma is too far for this overprint to be contemporaneous with CRB magma production, and hence it must have been imparted by earlier subduction-related processes. This in turn allows us to surmise that these lavas were sourced to large degree shallowly (i.e., <90 km) within the zone where slab-derived fluids (and possibly melts) were able to cause this earlier metasomatic overprint [54,77]. Furthermore, comparison of lavas of this study with Siletzia samples indicates that isotopic composition as well as incompatible elemental patterns do not reveal a clear plume signature, contrary to the high-Ti Siletzia samples. This does not preclude some plume component, but these compositional aspects just do not reveal this. The continental flood basalts of the CRBG mostly erupted through young lithosphere of accreted terranes west of the North American craton [78]. This is relevant as this precludes an overestimation of this upper metasomatized mantle component as modeled for the Karoo flood basalts [79]. In the case of the Karoo basalts, ref. [79] could show that a highly enriched component derived from an old subcontinental thick cratonic lithospheric mantle has a significant compositional leverage to impart a subcontinental lithospheric signature by small degree mixing.

6. Conclusions

Our study focused on reevaluating the compositional relationships of the lower-most flows of the American Bar subunit, AB1&2 units, of the Imnaha Basalt to the Picture Gorge Basalt (PGB). Samples of this study were collected from sites distributed along a north—south distance of ~250 km covering most of the outcrop area of the Imnaha Basalt, including some sites in the north that were originally used to establish the flow stratigraphy of Imnaha Basalt in the 1980s. We added our new data to published data of the Imnaha Basalt and grouped samples into three flow packages: (i) lower American Bar flows (AB1&2),

(ii) middle to upper American Bar flows (AB3+), and (iii) flows of the Rock Creek chemical type of the Imnaha Basalt (RC). We used these groups for comparison to PGB lavas, and for evaluating AB1&2 flows internally, to other Imnaha flows and relative to other earliest flows of the CRBG across the province. Our findings are the following:

- AB1&2 have more major and trace elemental compositional similarities to PGB than to overlying AB3+ and RC flows. Because of their unique composition, AB1&2 flows among the Imnaha Basalt stand out and hence should be highlighted as their own Imnaha chemical type;
- AB1&2 samples of the northern sampling area have subtle but distinct compositional differences to AB1&2 samples of the southern area;
- Compositional provinciality among PGB, AB1&2 south, north, and Steens Basalt is expressed in (e.g.) Zr/Y, La/Yb, Ba/Nb, Tb/Yb, and radiogenic isotopes. Observed variations cannot be explained by simple mixtures, but rather source material and conditions are unique to give rise to earliest CRBG lava as recorded by AB1&2 south, north, PGB, and Steens Basalt, yet all record tapping a variably depleted and metasomatized mantle;
- The provinciality of the earliest CRBG lavas across the source area of the province in eastern and northeastern Oregon (i.e., the area delimited by the main dike swarms, cf. Figure 1) suggests that lavas were tapped relatively locally, and emplacement distribution was not widespread enough to disrupt the observed regional variations at this eruption stage;
- Absolute ages of all earliest lavas of the CRBG indicate ~synchronous onset of eruptions: >16.7 Ma for AB1&2 north, 17.1 Ma for AB1&2 south, 17.2 Ma for PGB, and 17.0 Ma for Steens Basalt.
- There is little compositional evidence for a plume component in the first lavas erupting across the CRBG province.

Supplementary Materials: The following supporting information can be downloaded at: https://www.mdpi.com/article/10.3390/min13121544/s1, PPT File S1: Location imgaes; PPT File S2: Assignment (majors); PPT File S3: Assignment (traces); Text S4: Ar-Ar analytical methodology [80–86]; PDF S5-1: LF-21-54_GM; PDF S5-2: MM-CRB-32_PLAG; PDF S5-3: LMF-19-80_GM; Excel File S6: Chemical data; PPT File: S7: Additional plots; Excel File S8: additional Chemical data.

Author Contributions: Conceptualization, M.J.S. and E.B.C.; methodology, M.J.S., L.J.F., L.M.F. and E.B.C.; software; validation, L.J.F., L.M.F., M.J.M., E.B.C. and M.J.S.; formal analysis, L.J.F., L.M.F., M.J.M. and E.B.C.; investigation, L.J.F., L.M.F., M.J.M. and E.B.C.; resources, M.J.S.; data curation, L.J.F., L.M.F., M.J.M., E.B.C. and M.J.S.; writing—original draft preparation, M.J.S., L.J.F. and L.M.F.; writing—review and editing, E.B.C., L.J.F. and L.M.F.; visualization, L.J.F., L.M.F. and M.J.S.; supervision, M.J.S. and E.B.C.; project administration, M.J.S.; funding acquisition, M.J.S., L.J.F., L.M.F. and E.B.C. All authors have read and agreed to the published version of the manuscript.

Funding: National Science Foundation grant EAR-1220676 to Streck; Scion Foundation Grant to Fredenberg and Portland State University Geology Grant-in-Aid support to Fredenberg and Fox.

Data Availability Statement: Data are contained within the article and supplementary materials or are published in cited papers.

Acknowledgments: This paper is based in large part on the results of two Masters theses, and MS Thesis support came from the Scion Foundation to Fredenberg and PSU Geology Grant-in-Aid support to Fredenberg and Fox. A National Science Foundation grant EAR-1220676 to Streck also partially supported this work. We greatly appreciate an early reading and editing of this paper by John Wolff. Informal review by William Leeman and the formal review of three anonymous reviewers further improved this presentation and are also appreciated. Lastly, we appreciate the work and additional comments related to this paper by the guest editor Richard Ernst.

Conflicts of Interest: The authors declare no conflict of interest.

References

1. Reidel, S.P.; Camp, V.E.; Tolan, T.L.; Martin, B.S. The Columbia River flood basalt province: Stratigraphy, areal extent, volume, and physical volcanology. In *The Columbia River Flood Basalt Province: Geological Society of America Special Paper*; Reidel, S.P., Camp, V.E., Ross, M.E., Wolff, J.A., Martin, B.S., Tolan, T.L., Wells, R.E., Eds.; Geological Society of America: Boulder, CO, USA, 2013; Volume 497, pp. 1–43. [CrossRef]
2. Cahoon, E.B.; Streck, M.J.; Koppers, A.A.P.; Miggins, D.P. Reshuffling the Columbia River Basalt chronology—Picture Gorge Basalt, the earliest and longest-erupting formation. *Geology* **2020**, *48*, 348–352. [CrossRef]
3. Swanson, D.A.; Wright, T.L.; Hooper, P.R.; Bentley, R.D. Revisions in Stratigraphic Nomenclature of the Columbia River Basalt Group. *Geol. Surv. Bull.* **1979**, *1457-G*, 59.
4. Hooper, P.R. Chemical discrimination of Columbia River basalt flows. *Geochem. Geophys. Geosyst.* **2000**, *1*. [CrossRef]
5. Camp, V.E. Mid-Miocene propagation of the Yellowstone mantle plume head beneath the Columbia River basalt source region. *Geology* **1995**, *23*, 435–438. [CrossRef]
6. Christiansen, R.L.; Foulger, G.R.; Evans, J.R. Upper-mantle origin of the Yellowstone Hotspot. *GSA Bull.* **2002**, *114*, 1245–1256. [CrossRef]
7. Liu, L.; Stegman, D.R. Origin of Columbia River flood basalt controlled by propagating rupture of the Farallon slab. *Nature* **2012**, *482*, 386–389. [CrossRef]
8. Camp, V.E.; Wells, R.E. The Case for a Long-Lived and Robust Yellowstone Hotspot. *GSA Today* **2021**, *31*, 4–10. [CrossRef]
9. Swenton, V.M.; Streck, M.J.; Miggins, D.P.; McIntosh, W.C. Filling critical gaps in the space-time record of High Lava Plains and co-Columbia River Basalt Group rhyolite volcanism. *GSA Bull.* **2022**, *135*, 1415–1428. [CrossRef]
10. Barry, T.L.; Kelley, S.P.; Camp, V.E.; Self, S.; Jarboe, N.A.; Duncan, R.A.; Renne, P.R. Eruption chronology of the Columbia River Basalt Group? In *The Columbia River Flood Basalt Province Geological Society of America Special Paper*; The Geological Society of America: Boulder, CO, USA, 2013; Volume 497, pp. 45–67.
11. Wolff, J.A.; Ramos, F.C. Source materials for the main phase of the Columbia River Basalt Group: Geochemical evidence and implications for magma storage and transport. *Geol. Soc. Am.* **2013**, *497*, 273–391.
12. Kasbohm, J.; Schone, B. Rapid eruption of the Columbia River flood basalt and correlation with the mid-Miocene climate optimum. *Sci. Adv.* **2018**, *4*, eaat8223. [CrossRef]
13. Baksi, A.K. New $^{40}Ar/^{39}Ar$ ages from the Grande Ronde and Wanapum Basalt Columbia River Basalt Group: Compilation of all ages and relationship to the geomagnetic polarity time scale for ~17–15 Ma. *J. Earth Syst. Sci.* **2022**, *131*, 158. [CrossRef]
14. Kasbohm, J.; Schoene, B.; Mark, D.F.; Murray, J.; Reidel, S.; Szymanowski, D.; Barfod, D.; Barry, T. Eruption history of the Columbia River Basalt. *Earth Planet. Sci. Lett.* **2023**, *617*, 118269. [CrossRef]
15. Hales, T.C.; Abt, D.L.; Humphreys, E.D.; Roering, J.J. A lithospheric instability origin for Columbia River flood basalts and Wallowa Mountains uplift in northeast Oregon. *Nature* **2005**, *438*, 842–845. [CrossRef]
16. Wolff, J.A.; Ramos, F.C.; Hart, G.L.; Patterson, J.D.; Brandon, A.D. Columbia River flood basalts from a centralized crustal magmatic system. *Nat. Geosci.* **2008**, *1*, 177–180. [CrossRef]
17. Webb, B.M.; Streck, M.J.; McIntosh, W.; Ferns, M.L. The Littlefield Rhyolite and associated mafic lavas: Bimodal volcanism of the Columbia River magmatic province, with constraints on age and storage sites of Grande Ronde Basalt magmas. *Geosphere* **2018**, *15*, 60–84. [CrossRef]
18. Carlson, R.W.; Lugmair, G.W.; MacDougall, J.D. Columbia River volcanism: The question of mantle heterogeneity or crustal contamination. *Geochim. Cosmochim. Acta* **1981**, *45*, 2483–2499. [CrossRef]
19. Carlson, R.W. Isotopic constraints on Columbia River flood-basalt genesis and the nature of the subcontinental mantle. *Geochim. Cosmochim. Acta* **1984**, *48*, 2357–2372. [CrossRef]
20. Hooper, P.R.; Hawkesworth, C.J. Isotopic and geochemical constraints on the origin and evolution of the Columbia River Basalts. *J. Petrol.* **1993**, *34*, 1203–1246. [CrossRef]
21. Camp, V.E.; Ross, M.E. Mantle dynamics and genesis of mafic magmatism in the intermontane Pacific Northwest. *J. Geophys. Res. Solid Earth* **2004**, *109*. [CrossRef]
22. Moore, N.E.; Grunder, A.L.; Bohrson, W.A.; Carlson, R.W.; Bindeman, I.N. Changing mantle sources and the effects of crustal passage on the Steens Basalt, SE Oregon; chemical and isotopic constraints. *Geochem. Geophys. Geosystems* **2020**, *21*, e2020GC008910. [CrossRef]
23. Soderberg, E.R.; Wolff, J.A. Mantle source lithologies for the Columbia River flood basalt province. *Contrib. Mineral. Petrol.* **2023**, *178*, 11. [CrossRef]
24. Cahoon, E.G.; Streck, M.J.; Koppers, A.A.P. Picture Gorge Basalt: Internal stratigraphy, eruptive patterns, and its importance for understanding Columbia River Basalt Group magmatism. *Geosphere* **2023**, *19*, 1–25. [CrossRef]
25. Moore, N.E.; Grunder, A.L.; Bohrson, W.A. The three-stage petrochemical evolution of the Steens Basalt (southeast Oregon, USA) compared to large igneous provinces and layered mafic intrusions. *Geosphere* **2018**, *14*, 2505–2532. [CrossRef]
26. Hooper, P.R.; Kleck, W.D.; Knowles, C.R.; Reidel, S.P.; Thiessen, R.L. Imnaha Basalt, Columbia River Basalt Group. *J. Petrol.* **1984**, *25*, 473–500. [CrossRef]
27. Waters, A.C. Stratigraphic and lithologic variations in the Columbia River basalt. *Am. J. Sci.* **1961**, *259*, 583–611. [CrossRef]
28. Wright, T.L.; Grolier, M.J.; Swanson, D.A. Chemical variation related to the stratigraphy of the Columbia River Basalt. *GSA Bull.* **1973**, *84*, 371–386. [CrossRef]

29. Hooper, P.R. Petrology and chemistry of the Rock Creek flow, Columbia River basalt, Idaho. *GSA Bull.* **1974**, *85*, 15–26. [CrossRef]
30. Camp, V.E.; Ross, M.E.; Hanson, W.E. Genesis of flood basalts and Basin and Range volcanic rocks from Steens Mountain to the Malheur River Gorge, Oregon. *GSA Bull.* **2003**, *115*, 105–128. [CrossRef]
31. Kleck, W.D. Chemistry, petrography, and stratigraphy of the Columbia River Group in the Imnaha River Valley region, eastern Oregon and western Idaho. Ph.D. Thesis, WashingtonState University, Pullman, WA, USA, 1976; 203p.
32. Watkins, N.D.; Baksi, A.K. Magnetostratigraphy and oroclinal folding of the Columbia River, Steens, and Owyhee basalts in Oregon, Washington, and Idaho. *Am. J. Sci.* **1974**, *274*, 148–189. [CrossRef]
33. Brandon, A.D.; Hooper, P.R.; Goles, G.G.; Lambert, R.S.J. Evaluating crustal contamination in continental basalts: The isotopic composition of the Picture Gorge Basalt of the Columbia River Basalt Group. *Contrib. Mineral. Petrol.* **1993**, *114*, 452–464. [CrossRef]
34. Bailey, M.M. Revisions to stratigraphic nomenclature of the Picture Gorge Basalt Subgroup, Columbia River Basalt Group. In *Volcanism and Tectonism in the Columbia River Flood-Basalt Province: Geological Society of America Special Paper*; Reidel, S.P., Hooper, P.R., Eds.; The Geological Society of America: Boulder, CO, USA, 1989; Volume 239, pp. 67–84. [CrossRef]
35. Hooper, P.R.; Binger, G.B.; Lees, K.R. Ages of the Steens and Columbia River flood basalts and their relationship to extension-related calc-alkalic volcanism in eastern Oregon. *GSA Bull.* **2002**, *114*, 43–50. [CrossRef]
36. Camp, V.E.; Hanan, B.B. A plume-triggered delamination origin for the Columbia River Basalt Group. *Geosphere* **2008**, *4*, 480–495. [CrossRef]
37. Cahoon, E.B.; Streck, M.J.; Carlson, R.W.; Bindeman, I. Mantle source and geochemical evolution of the Picture Gorge Basalt. *Minerals* 2024, *submitted*.
38. Camp, V.E.; Ross, M.E.; Duncan, R.A.; Jarboe, N.A.; Coe, R.S.; Hanan, B.B.; Johnson, J.A. The Steens Basalt: Earliest Lavas of the Columbia River Basalt Group. In *The Columbia River Flood Basalt Province: Geological Society of America Special Paper*; Geological Society of America: Boulder, CO, USA, 2013; Volume 497.
39. Nash, B.P.; Perkins, M.E. Neogene fallout tuffs from the Yellowstone hotspot in the Columbia Plateau region, Oregon, Washington and Idaho, USA. *PLoS ONE* **2012**, *7*, e44205. [CrossRef] [PubMed]
40. Ladderud, J.A.; Wolff, J.A.; Rember, W.C.; Brueseke, M.E. Volcanic ash layers in the Miocene Lake Clarkia beds: Geochemistry, regional correlation, and age of the Clarkia flora. *Northwest Sci.* **2015**, *89*, 309–323. [CrossRef]
41. Höfig, D.; Zhang, Y.G.; Giosan, L.; Leng, Q.; Liang, J.; Wu, M.; Miller, B.; Yang, H. Annually resolved sediments in the Classic Clarkia lacustrine deposits (Idaho, USA) during the middle Miocene Climate Optimum. *Geology* **2021**, *49*, 916–920. [CrossRef]
42. Streck, M.J.; Swenton, V.M.; McIntosh, W.; Ferns, M.L.; Heizler, M. Columbia River Rhyolites: Age-Distribution Patterns and Their Implications for Arrival, Location, and Dispersion of Continental Flood Basalt Magmas in the Crust. *Geosciences* **2023**, *13*, 46. [CrossRef]
43. Hart, R.; Wolff, J.A.; Steiner, A.; Ramos, F.C. A new look at the genesis of the Wanapum Basalt, Columbia River Basalt Group. *Geol. Soc. Am. Abstr. Programs* **2023**, *55*.
44. Lees, K.R. Magmatic and Tectonic Changes Through Time in the Neogene Volcanic Rock of the Vale Area, Oregon, Northwestern USA. Ph.D. Thesis, The OoebUniversity, Department of Earth Sciences, Milton Keynes, UK, 1994; 284p.
45. Johnson, D.M.; Hooper, P.R.; Conrey, R.M. XRF analysis of rocks and minerals for major and trace elements on a single low dilution Li-tetraborate fused bead. *Adv. X-ray Anal.* **1999**, *41*, 843–867.
46. Knaack, C.; Cornelius, S.; Hooper, P.R. Trace elemnt analysis of rocks and minerals by ICP-MS. In *Open File Report*; Washington State University: Pullman, WA, USA, 1994; 18p.
47. Kuiper, K.F.; Deino, A.; Hilgen, F.J.; Krijgman, W.; Renne, P.R.; Wijbrans, J.R. Synchronizing rock clocks of Earth history. *Science* **2008**, *320*, 500–504. [CrossRef]
48. Sun, S.S.; McDonough, W.F. Chemical and Isotopic Systematics of Oceanic Basalts: Implications for Mantle Composition and Processes. *Geol. Soc. Lond. Spec. Publ.* **1989**, *42*, 313–345. [CrossRef]
49. Fredenberg, L.J. Investigation of Basal Imnaha Basalt Flows and Their Relationship to the Picture Gorge Basalt of the Columbia River Basalt Group. Master's Thesis, Portland State University, Portland, OR, USA, 2022; p. 6187. [CrossRef]
50. Lewis, R.S.; Schmidt, K.L.; Gaschnig, R.M.; LaMaskin, T.A.; Lund, K.; Gray, K.D.; Tikofd, B.; Stetson-Lee, T.; Moore, N. Hells Canyon to the Bitterroot front: A transect from the accretionary margin eastward across the Idaho batholith. In *Geol Soc Am Fieldguide: Exploring the Northern Rocky Mountains*; Shaw, C.A., Tikoff, B., Eds.; Geological Society of America: Boulder, CO, USA, 2014; Volume 37. [CrossRef]
51. Fox, L.M. Stratigraphic and Geochemical Evaluation of Distal Flows of the Columbia River Flood Basalts in the Greater Vale Area, Southeastern Oregon. Master's Thesis, Portland State University, Portland, Oregon, 2022; p. 5921. [CrossRef]
52. Jarboe, N.A.; Coe, R.S.; Renne, P.R.; Glen, J.M.G. The age of the Steens reversal and the Columbia River Basalt Group. *Chem. Geol.* **2010**, *274*, 159–168. [CrossRef]
53. Salters, V.J.M.; Stracke, A. Composition of the depleted mantle. *Geochem. Geophys. Geosystems* **2004**, *5*, Q05B07. [CrossRef]
54. Leeman, W.; Streck, M.J. Late Cenozoic magmatism of the northwestern U.S.—The role of sub-continental lithospheric mantle (SCLM). Geological Society of America Abstracts with Programs. In Proceedings of the GSA Connects 2021, Portland, OR, USA, 11 October 2021. [CrossRef]

55. Till, C.B.; Grove, T.L.; Carlson, R.W.; Donnelly-Nolan, J.M.; Fouch, M.J.; Wagner, L.S.; Hart, W.K. Depths and temperatures of <10.5 Ma mantle melting and the lithosphere-asthenosphere boundary below southern Oregon and northern California. *Geochem. Geophys. Geosystems* **2013**, *14*, 864–879. [CrossRef]
56. Carlson, R.W.; Grove, T.L.; Donnelly-Nolan, J.M. Origin of primitive tholeiitic and calc-alkaline basalts at Newberry Volcano, Oregon. *Geochem. Geophys. Geosystems* **2018**, *19*, 1360–1377. [CrossRef]
57. Unruh, D.W.; Wolff, J.A.; Davis, K.N. Early phreatomagmatic tuffs in the Columbia River flood basalts. In Proceedings of the Abstracts of the 7th International Maar Conference, Olot, CL, Spain, 21–25 May 2018; pp. 88–89.
58. Hooper, P.R. Crystal fractionation and recharge (RFC) in the American Bar flows of the Imnaha Basalt, Columbia River basalt group. *J. Petrol.* **1988**, *29*, 1097–1118. [CrossRef]
59. Morgan, W.J. Hotspot tracks and the opening of the Atlantic and Indian Oceans. In *The Oceanic Lithosphere*; Emiliani, C., Ed.; John Wiley: New York, NY, USA, 1981; pp. 443–487.
60. Brandon, A.D.; Goles, G.G. A Miocene subcontinental plume in the Pacific Northwest: Geochemical evidence. *Earth Planet. Sci. Lett.* **1988**, *88*, 273–283. [CrossRef]
61. Griffiths, R.W.; Campbell, I.H. On the dynamics of long-lived plume conduits in the convecting mantle. *Earth Planet. Sci. Lett.* **1991**, *103*, 214–227. [CrossRef]
62. Pierce, K.L.; Morgan, L.A. The track of the Yellowstone hot spot: Volcanism, faulting, and uplift. In *Regional Geology of Eastern Idaho and Western Wyoming*; Link, P.K., Kuntz, M.A., Piatt, L.B., Eds.; Geological Society of America Memoir: Boulder, CO, USA, 1992; Volume 179, pp. 1–53.
63. White, R.S.; McKenzie, D. Mantle plumes and flood basalts. *J. Geophys. Res.* **1995**, *100*, 1754317585. [CrossRef]
64. Hooper, P.R. The Columbia River flood basalt province: Current status, in large igneous provinces: Continental, oceanic, and planetary flood volcanism. *Geophys. Monogr. Ser.* **1997**, *100*, 1–27. [CrossRef]
65. Hooper, P.R.; Camp, V.E.; Reidel, S.P.; Ross, M.E. The origin of the Columbia River Flood Basalt province: Plume versus nonplume models. *GSA Spec. Pap.* **2007**, *430*, 635–668.
66. Coble, M.A.; Mahood, G.A. Initial impingement of the Yellowstone plume located by widespread silicic volcanism contemporaneous with Columbia River flood basalts. *Geology* **2012**, *40*, 655–658. [CrossRef]
67. Camp, V.E. Origin of Columbia River Basalt: Passive Rise of Shallow Mantle, or Active Up-welling of a Deep Mantle Plume. In *The Columbia River Flood Basalt Province Geological Society of America Special Paper*; Reidel, S.P., Camp, V.E., Ross, M.E., Wolff, J.A., Martin, B.S., Tolan, T.L., Wells, R.E., Eds.; The Geological Society of America: Boulder, CO, USA, 2013; Volume 497, pp. 181–199. [CrossRef]
68. Wells, R.; Bukry, D.; Friedman, R.; Pyle, D.; Duncan, R.; Haeussler, P.; Wooden, J. Geologic history of Siletzia, a large igneous province in the Oregon and Washington Coast Range: Correlation to the geomagnetic polarity time scale and implications for a long-lived Yellowstone hotspot. *Geosphere* **2014**, *10*, 692–719. [CrossRef]
69. Smith, R.S. The Making of Fore-Arc Andesite of the Portland Basin: Implications for the Fate of Diverse Primitive Mantle Inputs. Master's Thesis, Portland State University, Portland, OR, USA, 2008; pp. 1–235.
70. Pyle, D.G.; Duncan, R.A.; Wells, R.E.; Graham, D.W.; Hanan, B.B.; Harrison, B.K.; Haileab, B. Longevity of Yellowstone hotspot volcanism: Isotopic evidence linking the Siletzia LIP (56 Ma) and early Columbia River Basalt Group (17 Ma) mantle sources American Geophysical Union. In Proceedings of the Fall Meeting 2015, San Francisco, CA, USA, 14–18 December 2015.
71. Phillips, B.A.; Kerr, A.C.; Mullen, E.K.; Weiss, D. Oceanic mafic magmatism in the Siletz terrane, NWNorth America: Fragments of an Eocene oceanic plateau? *Lithos* **2017**, *274–275*, 291–303. [CrossRef]
72. Ciborowski, T.J.; Phillips, B.A.; Kerr, A.C.; Barfod, D.N.; Mark, D.F. Petrogenesis of Siletzia: The world's youngest oceanic plateau. *Results Geochem.* **2020**, *1*, 100004. [CrossRef]
73. Bacon, C.R.; Bruggman, P.E.; Christiansen, R.L.; Clynne, M.A.; Donnelly-Nolan, J.M.; Hildreth, W. Primitive magmas at five Cascade volcanic fields: Melts from hot, heterogenous sub-arc mantle. *Can. Miner.* **1997**, *35*, 397–423.
74. Conrey, R.M.; Hooper, P.R.; Larson, P.B.; Chesley, J.; Ruiz, J. Trace element and isotopic evidence for two types of crustal melting beneath a High Cascade volcanic center, Mt Jefferson, Oregon. *Contr. Mineral. Petrol.* **2001**, *141*, 710–731. [CrossRef]
75. Schmidt, M.E.; Grunder, A.L.; Rowe, M.C. Segmentation of the Cascade Arc as indicated by Sr and Nd isotopic variation among diverse primitive basalts. *Earth Planet Sci. Ltr.* **2008**, *266*, 166–181. [CrossRef]
76. DuBray, E.A.; John, D.A. Petrologic, tectonic, and metallogenic evolution of the Ancestral Cascades magmatic arc, Washington, Oregon, and northern California. *Geosphere* **2011**, *7*, 1102–1133. [CrossRef]
77. Leeman, W.P.; Lewis, J.F.; Evarts, R.C.; Conrey, R.M.; Streck, M.J. Petrologic constraints on the thermal structure of the Cascades arc. *J. Volcanol. Geotherm. Res.* **2005**, *140*, 67–105. [CrossRef]
78. LaMaskin, T.A.; Vervoort, J.D.; Dorsey, R.J.; Wright, J.E. Early Mesozoic Paleogeography, and Tectonic Evolution of the Western United States: Insights from Detrital Zircon U-Pb Geochronology, Blue Mountains Province, Northeastern Oregon. *GSA Bull.* **2011**, *123*, 1939–1965. [CrossRef]
79. Heinonen, J.S.; Luttinen, A.V.; Bohrson, W.A. Enriched continental flood basalts from depleted mantle melts: Modeling the lithospheric contamination of Karoo lavas from Antarctica. *Contrib. Miner. Petrol.* **2016**, *171*, 9. [CrossRef]
80. Steiger, R.; Jäger, E. Subcommission on Geochronology: Convention on the Use of Decay Constants in Geo-and Cosmochronology. *Earth Planet. Sci. Lett.* **1997**, *36*, 359–362. [CrossRef]

81. Min, K.; Mundil, R.; Renne, P.R.; Ludwig, K.R. A test for systematic errors in 40Ar/39Ar geochronology through comparison with U/Pb analysis of a 1.1-Ga rhyolite. *Geochim. Cosmochim. Acta* **2000**, *64*, 73–98. [CrossRef]
82. Koppers, A.A.; Staudigel, H.; Pringle, M.S.; Wijbrans, J.R. Short-lived and discontinuous intraplate volcanism in the South Pacific: Hot spots or extensional volcanism? *Geochem. Geophys. Geosystems* **2003**, *4*. [CrossRef]
83. Taylor, J.R. *An Introduction to Error Analysis: The Study of Uncertainties in Physical Measurements*; Univ. Science Books: Mill Valley, CA, USA, 1997; 327p.
84. York, D. Least squares fitting of a straight line with correlated errors. *Earth Planet. Sci. Lett.* **1968**, *5*, 320–324. [CrossRef]
85. Koppers, A.A. ArArCALC—Software for 40Ar/39Ar age calculations. *Comput. Geosci.* **2002**, *28*, 605–619. [CrossRef]
86. Duncan, R.A.; Keller, R.A. Radiometric ages for basement rocks from the Emperor Seamounts, ODP Leg 197. *Geochem. Geophys. Geosystems* **2004**, *5*. [CrossRef]

minerals

MDPI

Article

Mantle Sources and Geochemical Evolution of the Picture Gorge Basalt, Columbia River Basalt Group

Emily B. Cahoon [1,*], Martin J. Streck [2], Richard W. Carlson [3] and Ilya N. Bindeman [4]

[1] College of Earth, Ocean, and Atmospheric Sciences, Oregon State University, Corvallis, OR 97331, USA
[2] Department of Geology, Portland State University, P.O. Box 751, Portland, OR 97207, USA; streckm@pdx.edu
[3] Earth and Planets Laboratory, Carnegie Institution for Science, 5241 Broad Branch Road NW, Washington, DC 20015, USA; rcarlson@carnegiescience.edu
[4] Department of Geological Sciences, University of Oregon, Eugene, OR 97403, USA; bindeman@uoregon.edu
* Correspondence: emily.cahoon@oregonstate.edu

Abstract: The Columbia River Basalt Group (CRBG) is the youngest continental flood basalt province, proposed to be sourced from the deep-seated plume that currently resides underneath Yellowstone National Park. If so, the earliest erupted basalts from this province, such as those in the Picture Gorge Basalt (PGB), aid in understanding and modeling plume impingement and the subsequent evolution of basaltic volcanism. Using geochemical and isotopic data, this study explores potential mantle sources and magma evolution of the PGB. Long known geochemical signatures of the PGB include overall large ion lithophile element (LILE) enrichment and relative depletion of high field strength elements (HFSE) typical of other CRBG main-phase units. Basaltic samples of the PGB have $^{87}Sr/^{86}Sr$ ratios on the low end of the range displayed by other CRBG lavas and mantle-like $\delta^{18}O$ values. The relatively strong enrichment of LILE and depletion of HFSE coupled with depleted isotopic signatures suggest a metasomatized upper mantle as the most likely magmatic source for the PGB. Previous geochemical modeling of the PGB utilized the composition of two high-MgO primitive dikes exposed in the northern portion of the Monument Dike swarm as parental melt. However, fractionation of these dike compositions cannot generate the compositional variability illustrated by basaltic lavas and dikes of the PGB. This study identifies a second potential parental PGB composition best represented by basaltic flows in the extended spatial distribution of the PGB. This composition also better reflects the lowest stratigraphic flows identified in the previously mapped extent of the PGB. Age data reveal that PGB lavas erupted first and throughout eruptions of main-phase CRBG units (Steens, Imnaha, Grande Ronde Basalt). Combining geochemical signals with these age data indicates cyclical patterns in the amounts of contributing mantle components. Eruption of PGB material occurred in two pulses, demonstrated by a ~0.4 Ma temporal gap in reported ages, 16.62 to 16.23 Ma. Coupling ages with observed geochemical signals, including relative elemental abundances of LILE, indicates increased influence of a more primitive, potentially plume-like source with time.

Keywords: Picture Gorge Basalt; Columbia River Basalt; Oregon; Yellowstone; mantle sources; crustal contamination; continental flood basalt; eruptive pulses

1. Introduction

The Columbia River Basalt Group (CRBG) of the Pacific Northwest, USA, is the world's youngest and least volumetric flood basalt (Figure 1). The CRBG can be subdivided into four main-phase formations, which include the Steens, Imnaha, Grande Ronde, and Picture Gorge Basalts (PGB) [1,2]. Of these formations, the PGB is the least volumetrically extensive and exhibits geochemical signatures that suggest that it represents a separate magmatic system potentially resulting from lithospheric thinning in a back-arc tectonic setting [3–6]. The PGB is the earliest main-phase unit of the CRBG [7], followed by the Steens Basalt [8]. Thus, a detailed reexamination of PGB geochemistry and magma petrogenesis provides

insight into mantle source components and their temporal and/or spatial boundaries. Examining the spatial, temporal, and geochemical similarities between PGB and other CRBG main-phase units like the Steens Basalt, this study assesses the mantle sources and their respective contributions to the petrogenesis of the PGB.

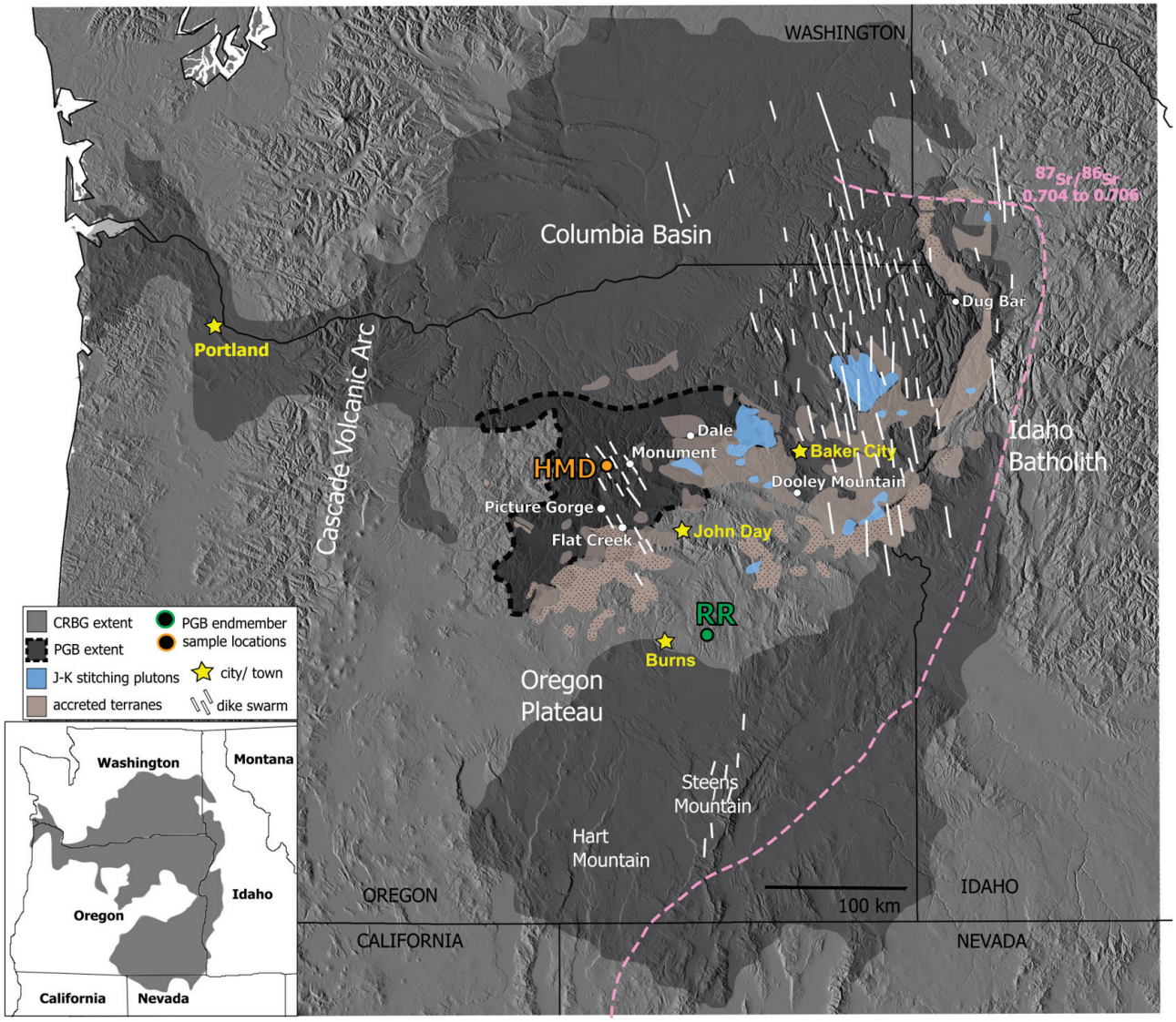

Figure 1. Regional map illustrating distribution of the CRBG and extended spatial distribution of PGB lavas. Locations of dikes shown for the Chief Joseph, Steens, and Monument Dike swarms. High MgO (HMD) and Rattlesnake Road (RR) highlight sample locations for compositions used in MELTS modeling and definition of PGB compositional endmembers. Spatial extent of accreted terranes (Baker, Wallowa, Olds Ferry, and Izee terranes) throughout the Blue Mountains Province in eastern Oregon, with the extent of the Izee terrane shown with a mottled pattern (modified from Schwartz et al., 2011 [9]). Blue polygons represent spatial extent of Jurassic to Cretaceous (J-K) plutonic rocks that constrain timing of terrane accretion. Dashed 0.704/0.706 line represents the $^{87}Sr/^{86}Sr$ contact between accreted terranes and the western margin of the North American craton. Inset map showing distribution of Columbia River Basalt Group (CRBG) in northwestern U.S. with state lines for reference.

Through the decades of research on the CRBG flood lavas, numerous origins and source materials have been proposed by many workers to contribute to the geochemical diversity exhibited by the basalts [3–5,10–15]. These source components include a mantle plume, a subcontinental lithospheric mantle that is variably metasomatized by prior subduction zone processes, and various crustal lithologies within the North American plate. Many workers agree that a mantle plume is ultimately responsible for the CRBG [16] and the Snake River Plain–Yellowstone hotspot track [17] to the east, although different non-plume models have been proposed. Examples of some of these models invoke a rapid increase in back-arc extension caused by steepening of the subducting oceanic plate to the west [18,19], a northward opening tear in the descending slab [20], peeling off of the Farallon plate [13], and a similar model of peeling off of the Farallon plate with the added component of lithospheric foundering at the root of the Wallowa Mountains in northeastern Oregon [12].

1.1. Geochemical Relationships between Main-Phase CRBG Formations

Endmember compositions within main-phase formations of the CRBG reflect the contribution of multiple mantle source components, as interpreted by trace element and isotopic data [3–5,10,13,21]. In isotopic space, the Grande Ronde Basalts and Imnaha Basalts define their own trend, while the PGB and the Steens Basalt share other distinct geochemical and isotopic traits [3,5,6,21]. Partial melting processes within the various source regions likely also contribute to some of the observed similarities and differences in trace element contents [21]. The Grande Ronde Basalts form a trend emanating from the Imnaha Basalts in isotopic space and could represent crustally contaminated Imnaha Basalts [3,5,10]. The "endmember" identified within the Imnaha Basalts was originally interpreted as re-enriched mantle, possibly the result of added sediment to a depleted mantle component [3]. This mantle source was defined as "C2" by Carlson (1984) [3] and later named the "Imnaha Component" by Wolff et al. (2008) [5], who suggested it to best represent the plume source, although there are no identified OIB with Pb isotopic compositions like C2.

The Steens Basalt is modeled as the result of a depleted mantle component (C1 of Carlson, 1984 [3]) mixing with the Imnaha component [18] or plume source [5]. Within lavas of the Steens Basalt, the proportion of depleted mantle decreases with time, moving stratigraphically upwards through the lower to the upper Steens Basalt [15]. Lower Steens lavas reflect a higher contribution of a depleted mantle component than do upper Steens lavas, suggesting that the proportion of the Imnaha component in the Steens Basalt increases with time. This is evidenced in isotopic space by $^{87}Sr/^{86}Sr$ versus $^{206}Pb/^{204}Pb$, where the upper Steens Basalt plots closer to the defined Imnaha Component than the lower Steens Basalt [5,6]. This observation also applies to the lower Imnaha Basalts; the depleted mantle component is most prevalent in the earliest erupted Imnaha lavas [2,6,15].

The PGB shares the most geochemical characteristics with the Steens Basalt and the American Bar subtype of the Imnaha Basalts (Figure 2). Similar to the Steens Basalt, PGB magmas are interpreted as being derived from a depleted mantle source, but one that was significantly influenced by prior subduction [4,21]. The observed enrichment of LILE relative to HFSE is one of the more characteristic geochemical signatures in PGB lavas and dikes. This feature has been interpreted as evidence for a fluid-fluxed mantle component (Figure 3) [3–6,10,21–23]. In the context of the entire flood basalt province, it has been suggested that the PGB reflects a subduction overprinted back-arc mantle less influenced by plume magmatism compared to the rest of the CRBG [5].

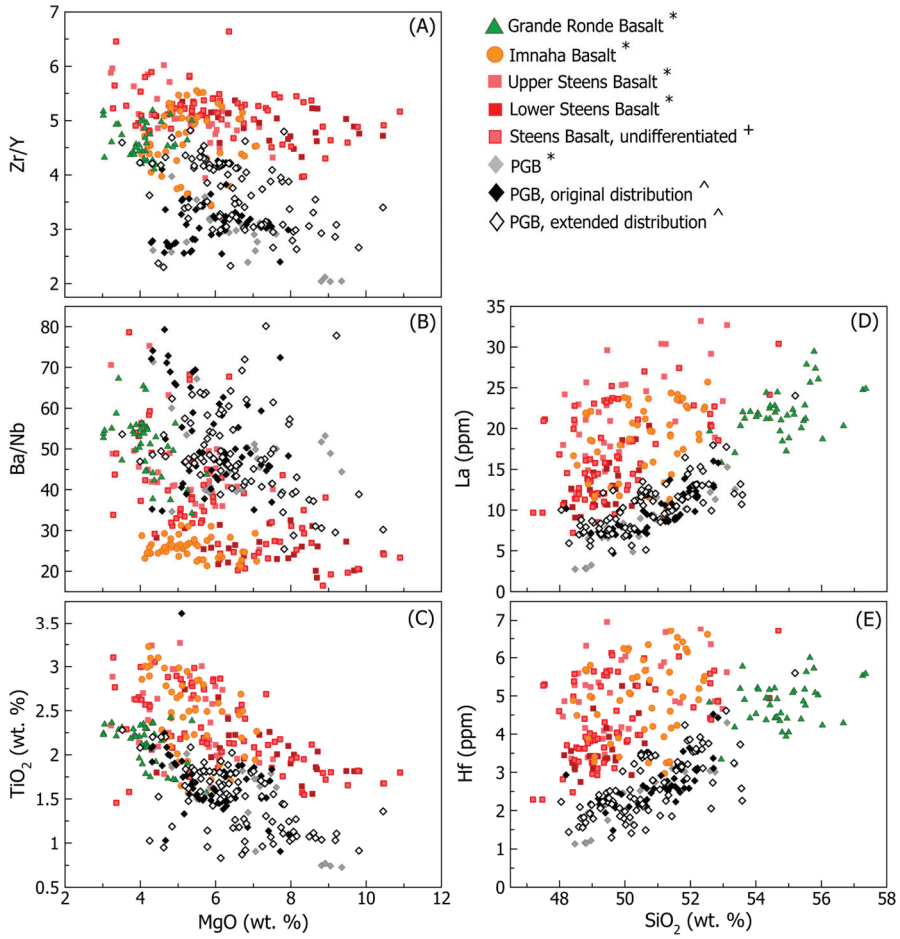

Figure 2. Geochemical major and trace elements for PGB relative to all main-phase CRBG. (**A**) Zr/Y, (**B**) Ba/Nb, and (**C**) TiO_2 (wt. %) versus MgO (wt. %), (**D**) La (ppm), and (**E**) Hf (ppm) versus SiO_2 (wt. %). Samples of PGB are subdivided based on their location; the previously mapped extent of PGB (original distribution) shown with open diamonds or additional locations (extended distribution) shown with solid diamonds. Geochemistry compiled from * Wolff et al. (2008) [5], $^+$ Moore (2018) [8], and ^ this study.

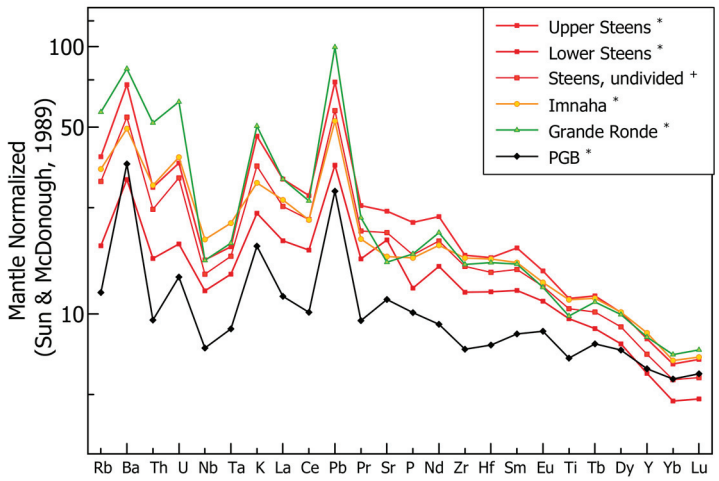

Figure 3. Mantle normalized incompatible element diagram (Sun and McDonough, 1989 [24]) with average compositions for main-phase formations of the CRBG. Geochemistry compiled from * Wolff et al. (2008) [5] and $^+$ Moore (2018) [8].

1.2. Petrogenetic Significance of Picture Gorge Basalt Stratigraphy

The PGB is best exemplified by the type locality at Picture Gorge, where 18 basaltic lava flows are exposed in a continuous stratigraphic section. These lavas erupted from north-northwest trending dikes of the Monument Dike swarm [2,4,23] and can be subdivided based on plagioclase modal abundance; major element concentrations, specifically TiO_2 and MgO; and magnetic orientation (Figure 4) [2,22,23,25–28]. The previous stratigraphic terminology used to describe these PGB subdivisions is inconsistent and resulted in application of stratigraphic nomenclature that does not abide by the Stratigraphic Code of North America (North American Commission on Stratigraphic Nomenclature, 2005) [29]. Here, we use the term "subunit" to reference these three previously mentioned subdivisions. the Twickenham, Monument Mountain, and Dayville Basalts, and "chemical type" to reference the further subdivisions of these subunits into 17 groupings of lava flows in addition to a distinct composition classified as high-MgO dikes (referred to as "members" by Bailey, 1989) [23].

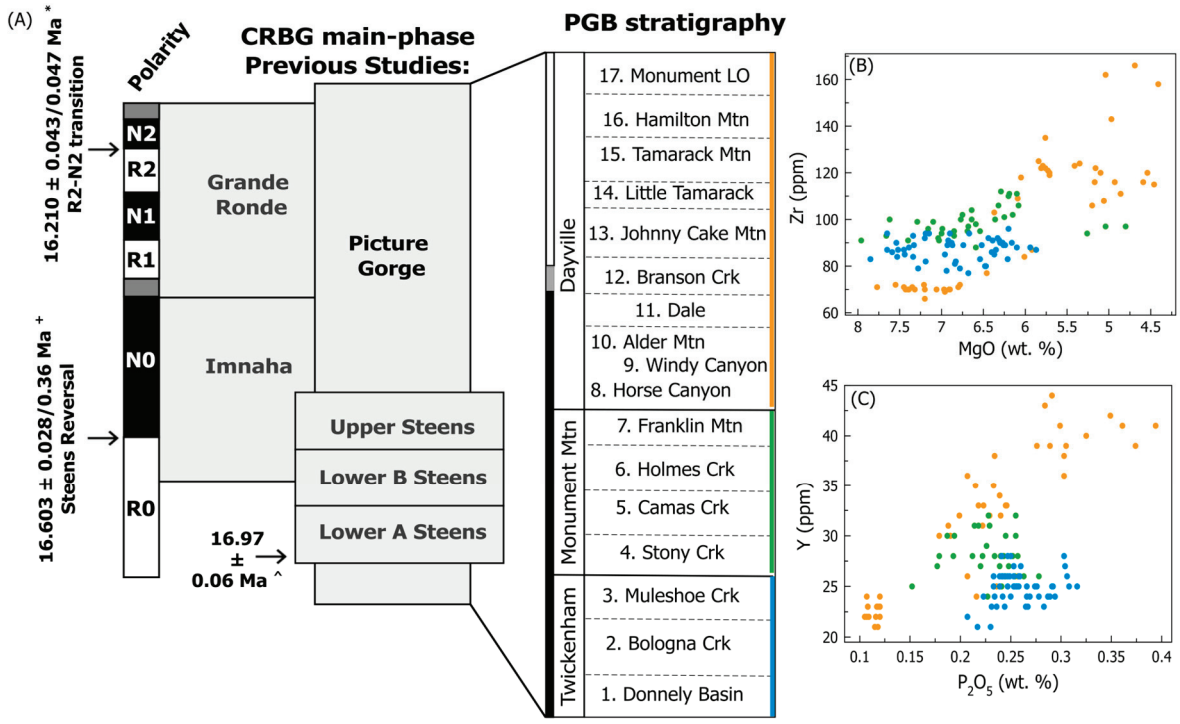

Figure 4. (**A**) Stratigraphic section with magnetic polarity of CRBG main-phase units that include six major polarity chrons R0-N2 ('R' represents 'reverse polarity' and 'N' represents 'normal polarity'), highlighting PGB internal stratigraphy (including subunits and chemical types). Geochemical plots of identified subunits of the PGB, noting their internal subdivisions, the Twickenham, Monument Mountain, and Dayville Basalts, including (**B**) Zr (ppm) versus MgO (wt. %) and (**C**) Y (ppm) versus P_2O_5 (wt. %) compositions for PGB subunits from Bailey (1989) [23]. Additional ages: * Kasbohm and Schoene (2018) [30]; $^+$ Mahood and Benson (2017) [31]; ^ Moore, et al. (2018) [8]. All $^{40}Ar/^{39}Ar$ dates were calculated using the Fish Canyon Tuff sanidine age of 28.201 ± 0.023 Ma, after Kuiper et al. (2008) [32], and the U-Pb errors for the Kasbohm and Schoene (2018) [30] age are reported as 95% confidence intervals given for internal uncertainty and decay constant uncertainty. Note on (**C**): The pixelation of data points on this plot is a result of older Y data that lack precision to concentrations below 1.0 ppm.

The high-MgO dikes, identified as potential parental material [23], are enriched in Ba, K, and Rb relative to elements of similar incompatibility, suggesting some crustal contamination or slab-derived fluids fluxing the source. This enrichment in large ion lithophile elements (LILE) is also observed in the Twickenham Basalt subunit and in the

Monument Mountain Basalt subunit but to a lesser degree [23]. A decrease in eruptive activity followed extrusion of Monument Mountain lavas, as the subsequent Dayville Basalt is characterized by lava flows that are both spatially limited and compositionally diverse. Overall, the Twickenham and Monument Mountain Basalts exhibit minor compositional variation, which cannot be the result of closed-system fractionation [23], and the younger Dayville Basalt forms its own evolutionary trend characterized by lava flows that are grouped into ten chemical types that are highly variable in their geochemical signatures (Figure 4).

2. Methods

2.1. Major and Trace Element Concentrations

Major and trace element data were acquired at the Peter Hooper GeoAnalytical Lab at Washington State University (WSU) using a Thermo-ARL Advant'XP automated X-ray fluorescence spectrometer (XRF) (Waltham, MA, USA) and an Agilent 7700 inductively coupled plasma mass spectrometer (ICP-MS) (Santa Clara, CA, USA). For sample preparation, basaltic samples were crushed into chips using the Braun Chipmunk at WSU and following sample preparation as outlined in Johnson et al. (1999) [33]. Then, chips exhibiting weathered surfaces were removed to reduce the influence of alteration on the resulting data. Rock chips were further crushed into a powder in a tungsten carbide swing mill. The sample powder was then combined with dilithium tetraborate ($Li_2B_4O_7$) in a ratio of 2:1, dilithium tetraborate to sample. The sample was fused into a bead in an oven at a temperature of 1000 °C. The beads were reground into powder, and one gram of powder was separated in order to make the ICP-MS bead. Two beads per sample were then made, again at 1000 °C, one for XRF and one for ICP-MS analysis. The XRF bead was analyzed in the XRF instrument, and the ICP-MS bead was dissolved for final analysis. All major and trace element geochemical data for our PGB samples are compiled in Table S2. and Mg# is plotted against a variety of these geochemical parameter for visualization through geochemical evolution in Figure S4.

2.2. Radiogenic Isotope Analyses

Sample preparation and analysis for Sr, Nd, Pb, and Hf were performed at the Carnegie Institution for Science, Earth and Planets Laboratory (EPL) in Washington D.C. Sample preparation and analyses were conducted in 2017 and 2018 during two separate laboratory visits. During both visits, over 10 g of fresh rock chips from each sample were powdered in an agate ceramic bowl to avoid contamination of metals (i.e., Ta from WC grinding bowls). Once the sample was powdered, approximately 50 mg was weighed and dissolved in ~2 mL of concentrated HNO_3 and 4 mL concentrated HF. The mixture in a Savillex Teflon vial was capped and heated on a 90 °C hotplate for ~12–18 h. Samples were heated longer (i.e., 18 h) during the 2017 sample preparation as the result of a laboratory closure. Each sample solution was then evaporated, redissolved twice in 1 mL of concentrated HNO_3, and dissolved again in 4 mL of 4M HCl. Finally, samples were evaporated, dried two more times with 0.5 mL 0.5 N HBr, and redissolved in 3 mL of 0.5 N HBr. Following these acid digestions, elements of interest (Sr, Nd, Hf, and Pb) were separated and purified via column chromatography following the procedures described below.

Lead was separated first by loading the samples (in 3 mL 0.5 N HBr) on 0.04 mL Teflon columns with AG1-X8 100–200 mesh anion exchange resin following the methodology of Carlson et al. (2006) [34]. Following elution of the majority of the elements using 0.5 N HBr, the Pb fraction was collected in 1.5 mL HNO_3, dried on a hotplate, and, after adding 1 mL 0.5 N HBr, loaded onto the columns a second time for purification. The final Pb fraction was collected in 1.5 mL 0.5 N HNO_3. The remaining sample in 0.5 N HBr was then dried, oxidized with 0.5 mL of concentrated HNO_3, evaporated again, redissolved in 5 mL of 0.1 N HF-1 N HCl, and heated for approximately one hour at 80 °C. Next, samples were centrifuged to remove any precipitates and loaded on AG 50 W × 8 resin (200–400 mesh), 20 cm height × 6 mm ID.

The high field strength elements, including hafnium, were separated next by collecting the initial solution and an additional 5 mL of 0.1 N HF-1 N HCl following a procedure modified from Patchett and Tatsumoto (1980) [35]. The eluant was then switched to 2.5 N HCl with 30 mL eluted until the Sr cut was collected in an additional 14 mL of 2.5 N HCl. Switching to 4 N HCl, the light REE was collected in 16 mL after eluting and discarding 12 mL.

Hafnium was purified on 0.6 × 10 cm columns using Eichrom LN 100–150 μm resin. The sample was loaded in 5 mL of 2.5 N HCl and rinsed with 10 mL 2.5 N HCl, 10 mL 6 N HCl, 4 mL of Milli-Q (MQ) water, 60 mL of 0.09 N citric acid-0.45 N HNO_3-1 wt. % H_2O_2, 5 mL of 0.09 N citric acid-0.45 N HNO_3, and 20 mL of 6 N HCL-0.06 N HF. The final Hf sample was collected in 8 mL of 6 N HCl-0.4N HF. Strontium was purified on 0.25 mL Teflon columns with Eichrom Sr resin. The purified Sr sample was collected in 2 mL of 0.05M HNO_3. Neodymium was separated from the other REE following the procedure of Garcon et al. (2018) [36] on columns with 10–50 μm LN spec resin and collected in 9 mL of 0.173N HCl.

Isotopic compositions for Sr and Nd were measured via thermal ionization mass spectrometry (TIMS) on the Thermo-Fisher Triton. Sr was run on single Re filaments loaded in a Ta_2O_5 powder in dilute H_3PO_4-HF. Each $^{87}Sr/^{86}Sr$ ratio reported in Table 2 is the average of 279–290 ratios obtained using 8 s integrations with a signal size from 5 to 20 × 10^{-11} A of ^{88}Sr. Mass fractionation was corrected to $^{86}Sr/^{88}Sr = 0.1194$ using exponential mass dependency and reported relative to a value of 0.71025 for the NBS987 Sr standard. The Sr standard NBS987 was measured multiple times during the 2017 and 2018 analytical sessions and averaged 0.710240 ± 0.0000027 (n = 3) in 2017 and 0.710249 ± 0.000003 (n = 3) in 2018, where uncertainty is 2σ. For all but one sample, the individual run uncertainty on $^{87}Sr/^{86}Sr$ was 0.000003. Uncertainties for all samples are reported in Figure S5.

Each $^{143}Nd/^{144}Nd$ ratio reported in Table 2 is the average of 199–203 ratios (in 2017) or 233–279 (in 2018) statically obtained using 8 s integrations with a signal size from 1–3 × 10^{-11} A of ^{144}Nd. Mass fractionation was corrected using exponential mass dependency and $^{146}Nd/^{144}Nd = 0.7219$. The Nd standard JNdi was measured multiple times during the 2017 analytical sessions and averaged 0.5121117 ± 0.0000023 (n = 3), where uncertainty is 2σ. During the 2018 analytical sessions, the data for JNdi averaged 0.5120940 ± 0.0000017 (n = 3), where uncertainty is 2σ. The difference in values measured for the standard reflects the aging of the Faraday cups, with the lower value obtained on fresher cups. Data for the samples are adjusted to a JNdi value of 0.512115 [37] based on the average value determined for JNdi during the separate analytical sessions.

Isotopic compositions for Pb and Hf were measured on the Nu HR multicollector ICP-MS and Nu Plasma II multicollector ICP-MS. Each Pb ratio reported in Table 2 is the average of 41–50 ratios. Samples that yielded ^{208}Pb signals below 100 mv were not reported. Mass fractionation during the 2017 analyses was corrected to $^{205}Tl/^{203}Tl = 2.417$ and then adjusted for the difference between the NBS981 Pb standards measured every 4 samples and the reported value for the standard [38]. Mass fractionation during the 2018 analyses was corrected to $^{205}Tl/^{203}Tl = 2.410$ and then adjusted for the difference between the NBS981 Pb standards measured every 4 samples and the reported value for the standard [38]. Average values for NBS981 obtained during 2017 analytical sessions for n = 7 measurements were $^{208}Pb/^{204}Pb = 36.714 \pm 0.006$, $^{207}Pb/^{204}Pb = 15.497 \pm 0.003$, and $^{206}Pb/^{204}Pb = 16.941 \pm 0.003$, where uncertainty is 2σ. Average values for NBS981 obtained during 2018 analytical sessions for n = 6 measurements were $^{208}Pb/^{204}Pb = 36.703 \pm 0.028$, $^{207}Pb/^{204}Pb = 15.495 \pm 0.011$, and $^{206}Pb/^{204}Pb = 16.938 \pm 0.012$, where uncertainty is 2σ. Uncertainties for all samples are provided in Figure S5.

Hafnium isotopic compositions were measured by introducing samples into the plasma in 0.08N HNO_3-0.06 N HF via a Teflon nebulizer. Each ratio reported in Table 2 is the average of 52–80 ratios, and the signal size of ^{178}Hf ranged from 3 to 8 × 10^{-11} A. Mass fractionation was corrected to $^{179}Hf/^{177}Hf = 0.7325$. The average of JMC475 obtained during the 2017 analytical sessions for n = 3 measurements was $^{176}Hf/^{177}Hf = 0.282148 \pm 0.000002$

(2σ). The average of JMC475 obtained during the 2018 analytical sessions for n = 13 measurements was $^{176}Hf/^{177}Hf = 0.282144 \pm 0.000002$ (2σ). Reported $^{176}Hf/^{177}Hf$ ratios were adjusted based on the average value determined for JNdi during the separate analytical sessions corrected to a JMC475 value of 0.282160. Values for ε_{Hf} and ε_{Nd} are calculated using the average chondrite parameters from Bouvier et al. (2008) [39] of $^{176}Hf/^{177}Hf = 0.282785$ and $^{143}Nd/^{144}Nd = 0.512630$. All Sr, Nd, Hf, Pb isotope uncertainty and isobaric interferences for our PGB samples are compiled in Table S3.

2.3. Oxygen Isotope Analyses

In order to better quantify crustal contamination, $\delta^{18}O$ values are revisited with modern techniques applied to both plagioclase mineral separates and basaltic groundmass that was exposed to multiple acid leachings to remove excess alteration. Basaltic groundmass and plagioclase separates were analyzed from 16 basaltic flows. The samples were crushed, sieved to grain sizes between 180 and 150 or 250 μm, magnetically separated via Franz, and leached in acid. Samples were prepared at Oregon State University following procedures for $^{40}Ar/^{39}Ar$ dating, and the remaining groundmass and mineral separates were used for oxygen isotope analysis. Oxygen isotopic compositions were then measured at the University of Oregon via an integrated CO_2 laser fluorination MAT 253 isotope ratio mass spectrometer (IRMS) system [40,41]. The range of material analyzed from each sample was 1.2 to 1.6 mg. During the analytical session, the Gore Mountain Garnet standard (UOG, accepted $\delta^{18}O = 6.52‰$) was measured multiple times (n = 7) to correct for instrumental drift [41]. Analytical precision of UOG analyses from the session was 0.06% (2σ) and is reported in Table S4.

2.4. MELTS Calculations

MELTS calculations were conducted using version rhyoliteMELTS v1.2x with two distinct primitive compositions identified as PGB [5,7,23]. This version of MELTS is intended for modeling crystallization over 0–20 kb using bulk compositions that correspond to natural magmas; the melt is interpreted to contain dissolved H_2O, but the magma is not quartz saturated [42,43]. Compositions were modeled at 6 different pressures (2, 3, 4, 7, 8, and 9 kb) with 0.1 and 0.5 wt. % water. For each experiment, the pressure stayed constant, and the temperature decreased to 100 degrees C below the wet liquidus temperature, as calculated by MELTS. Utilized partition coefficients are compiled in Table S1, and the results of each individual model are summarized in Table S5.

3. Results

3.1. PGB Composition

3.1.1. Major and Trace Element Compositions

Newly identified basaltic lavas and dikes of PGB composition extend across a wide swath of eastern Oregon. Along with PGB samples from the type locality and the original distribution area described by Bailey (1989) [23], PGB samples from these newly identified areas have relatively primitive to evolved (MgO ~4–9 wt. %) compositions with flat to slightly negatively sloping patterns on mantle-normalized incompatible trace element diagrams, but with troughs (HFSE) and spikes (Ba, K, Pb) typically associated with volcanic arc-related lavas of the Pacific Northwest (Figure 3). Samples of PGB composition exhibit relative depletions in many incompatible elements (i.e., La, Nb, Rb, Hf, Th), overall elevated large ion lithophile element (LILE) to high field strength element (HFSE) ratios, and less LREE enrichment on a mantle-normalized trace element diagram (Figures 2 and 3) relative to other CRBG units.

To gauge fractionation and assess the geochemical variation of the PGB, major and trace elements are plotted against Mg# (molar Mg# = (Mg/(Mg + Fe) × 100)) (Figures S1–S3). Observed trends in both major and trace element space define broad bands on most such geochemical plots. Major element concentrations exhibit larger variability between Mg#

65–45 (i.e., Al_2O_3, MnO, P_2O_5, and FeO*), and both FeO* and MgO exhibit a slight inflection at Mg# of 45, which could be due to crystallization of ilmenite and magnetite.

At the high Mg# end of the compositional arrays, several elements (e.g., Si, Al, Fe, Ca, Ni, Cu, LREE, Pb), and Sr in particular, show a wide range in concentration, suggesting that the primary magmas for the PGB are compositionally variable (Figures S1–S3). Some basalts are characterized by Mg# > 60 and could represent potential parental magmas. The high Mg# PGB samples are best represented by samples of the high-MgO dikes and lava flows exposed along Rattlesnake Road in the southeastern region of the PGB extended distribution (Figure 1, Table 1). Although other samples could have been chosen, samples of Rattlesnake Road were selected as representatives of the parental magma because there are four analyses from this location and their classification as PGB has been further confirmed by the Oregon Department of Geology and Mineral Industries (DOGAMI) (R. A. Houston et al., 2017) [44]. Overall, these high Mg# samples reflect two groups of primitive compositions observed within the PGB, referred to as the high-MgO dike (HMD) and the Rattlesnake Road (RR) groups (Table 1).

Table 1. Summary Table of Picture Gorge Basalt Primitive Endmember Samples.

Sample Name	Mg#	$^{87}Sr/^{86}Sr$	$^{143}Nd/^{144}Nd$	Age (Ma)
high-MgO dike (HMD) Endmember				
MMB D69A	65.4	0.703400	0.512980	no age data
MMB D69B	64.5	0.703066	0.513012	
MMB D70A *	66.1	0.703400	0.512990	
MMB D70B	64.1	-	-	
Rattlesnake Road (RR) Endmember				
DM255B	57.4	0.703757	0.512905	15.76
CAH15-007	64.4	0.703691	0.512889	16.22
CAH17-241A *^	59.6	-	-	15.5–16.16
CAH17-241B ^	59.5	-	-	
CAH17-242A ^	57.8	0.703565	0.512925	
MS-15-18ba ^	58.8	-	-	

^ Samples collected along Rattlesnake Road (see Figure 1 for location). * Samples used for MELTS modeling.

3.1.2. Radiogenic and Oxygen Isotope Compositions

Isotopically, PBG lavas have the lowest $^{87}Sr/^{86}Sr$ ratios of all main-phase CRBG units, and the most primitive PGB dikes contain the lowest $^{87}Sr/^{86}Sr$ ratios observed within PGB [45]. New radiogenic isotope data are reported for 16 sampled basaltic lavas and dikes of the PGB. Samples from within and outside of the previously mapped extent have $^{87}Sr/^{86}Sr$ ratios from 0.70341 to 0.70376 and $^{143}Nd/^{144}Nd$ ratios from 0.51299 to 0.51289 (Figure 5). The only exceptions are samples of PGB lavas from Pole Creek in the Malheur Gorge. These samples have higher $^{87}Sr/^{86}Sr$ ratios > 0.7039 and lower $^{143}Nd/^{144}Nd$ ratios < 0.5129 than the rest of the PGB but resemble the PGB in major and trace element concentrations.

Combining isotopic data with trace element data, samples of the identified primitive groups (HMD and RR) are evaluated to see if they share isotopic similarities. The HMD group is best characterized by three samples in trace element and isotopic space (sample ID: MMB-D69A, MMB-D69B, and MMB-D70A). The RR group is characterized by three samples (CAH16-241A, DM255B, and CAH15-007). Because RR group sample CAH16-241A does not have isotopic data, it is substituted with a similar basaltic lava along Rattlesnake Road (CAH16-242A) that does (Figure 6D–F). Considering trace element and radiogenic isotope data together, samples of the RR group exhibit lower Y/P_2O_5 and higher LREE concentrations at lower $^{143}Nd/^{144}Nd$ values (Figure 6B). Samples of each group show variable $^{87}Sr/^{86}Sr$ ratios relative to other isotope ratios (i.e., $^{143}Nd/^{144}Nd$ or $^{206}Pb/^{204}Pb$, Figure 7C,D). Within the RR group, $^{87}Sr/^{86}Sr$ values are >0.7035, and $^{143}Nd/^{144}Nd$ values

are <0.51293. In the HMD group, $^{87}Sr/^{86}Sr$ values are <0.7034, and $^{143}Nd/^{144}Nd$ values are >0.51298 (Figure 7).

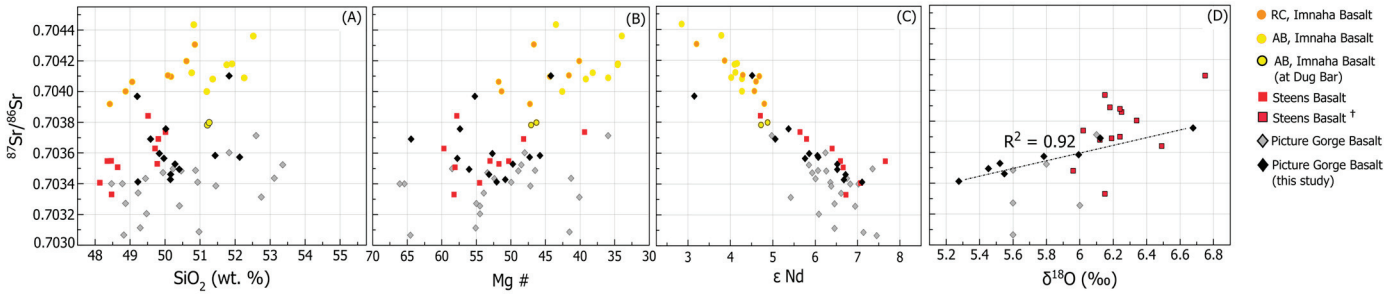

Figure 5. Comparison of $^{87}Sr/^{86}Sr$ isotopic ratios versus (**A**) SiO_2 (wt. %), (**B**) Mg#, (**C**) Epsilon Nd, and (**D**) $\delta^{18}O$ (‰) data for main-phase units of the CRBG: PGB, Steens Basalt (upper and lower), and Imnaha Basalts (Grande Ronde Basalt not depicted). Both subtypes of the Imnaha Basalts are distinguished, American Bar and Rock Creek, in addition to the American Bar lavas located at Dug Bar, which reflect some PGB characteristics. Geochemical data from † Moore et al. (2020) [15]; this study and all other isotopic and geochemical data from Wolff et al. (2008) [5].

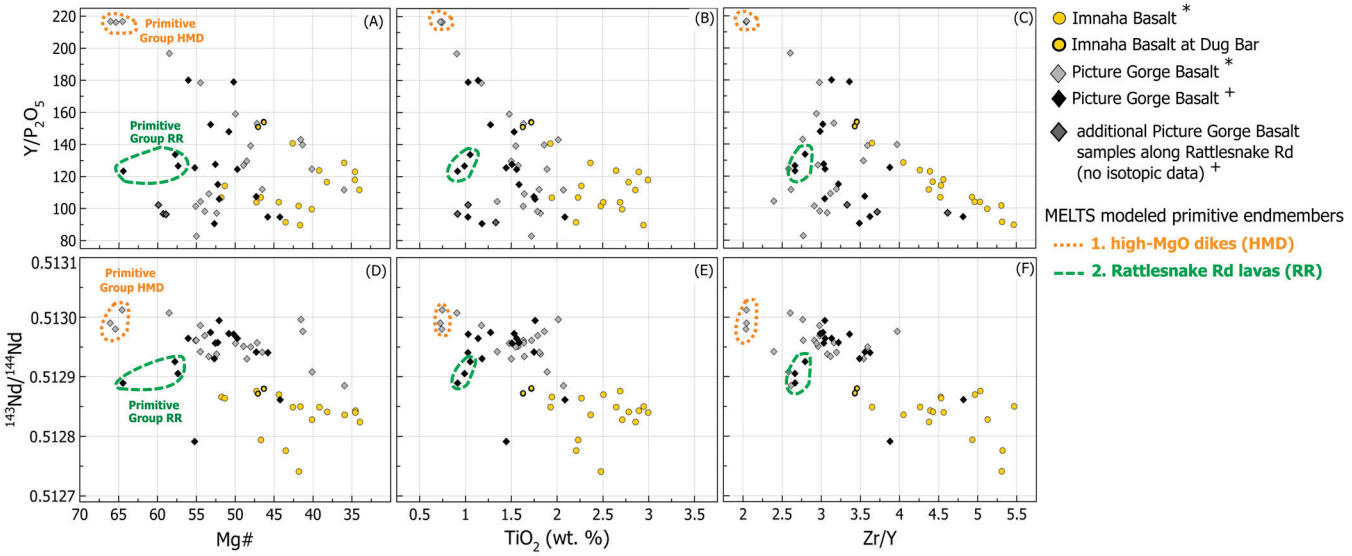

Figure 6. Elemental ratio plots to distinguish identified PGB endmembers. Y/P_2O_5 versus (**A**) Mg#, (**B**) TiO_2 (wt. %), (**C**) Zr/Y, and $^{143}Nd/^{144}Nd$ isotopic ratios versus (**D**) Mg#, (**E**) TiO_2 (wt. %), (**F**) Zr/Y for the Imnaha Basalt and PGB main-phase units of the CRBG. Both identified PGB endmember compositions; HMD (orange) and RR (green) are noted along with additional PGB lavas located along Rattlesnake Road. These samples are included in the trace element plots for comparison but do not have isotopic data. Trace element and isotopic data from * Wolff et al. (2008) [5] and + this study.

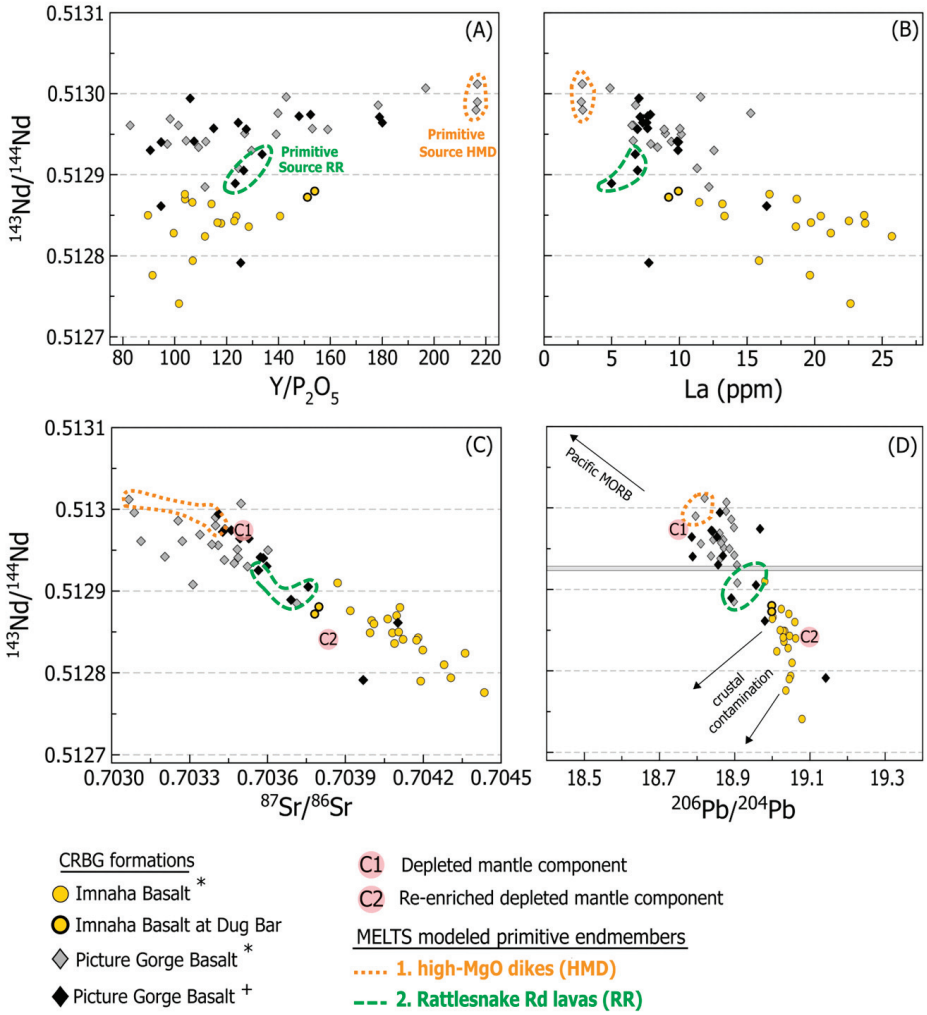

Figure 7. Geochemical plots of major elements, trace elements, and isotope ratios to distinguish identified PGB endmember samples (RR, three representative samples; HMD, three representative samples). Isotopic ratios of $^{143}Nd/^{144}Nd$ versus (**A**) Y/P_2O_5, (**B**) La (ppm), (**C**) $^{87}Sr/^{86}Sr$, and (**D**) $^{206}Pb/^{204}Pb$ for the Imnaha Basalt and PGB main-phase units of the CRBG. The C1 enriched mantle and C2 depleted mantle components of Carlson (1984) [3] are noted on plots (**C**,**D**) along with both identified PGB endmember compositions, HMD (orange) and RR (green). The gray horizontal band on plot (**D**) represents the $^{143}Nd/^{144}Nd$ value of one RR endmember sample where the $^{206}Pb/^{204}Pb$ value was not reported. Geochemical data from * Wolff et al. (2008) [5] and $^{+}$ this study.

Oxygen isotope data for the PGB yield $\delta^{18}O$ values ranging from 5.28 to 6.68 ‰ in groundmass and 5.32 to 5.92‰ in plagioclase (Table 2). At 49–53 wt. % SiO_2, plagioclase $\delta^{18}O$ values straddle the boundary of the $\delta^{18}O$ melt; such that$\delta^{18}O$ plagioclase = $\delta^{18}O$ melt at ~53 wt. % SiO_2, which is 0.13‰ lighter at 49 wt. % SiO_2 and 0.1‰ heavier at 56 wt. % SiO_2 [40]. When compared with previous work, these data demonstrate a larger range of values from groundmass and a similar overall trend of increasing $\delta^{18}O$ values for younger samples (Figure 13). This trend is observed with the earlier $^{87}Sr/^{86}Sr$ isotopic data, where PGB flows lower in the stratigraphy had lower ratios and higher stratigraphic flows had slightly higher ratios. Comparing $^{87}Sr/^{86}Sr$ data with $\delta^{18}O$ values collected as part of this study, there is a clear linear correlation (R^2 = 0.92) (Figure 5D).

Table 2. Sr, Nd, Hf, Pb, and $\delta^{18}O$ Isotopic Compositions for the PGB.

Sample Name	Dike or Lava	$^{87}Sr/^{86}Sr$	$^{143}Nd/^{144}Nd$	ε Nd	$^{176}Hf/^{177}Hf$	ε Hf	$^{208}Pb/^{204}Pb$	$^{207}Pb/^{204}Pb$	$^{206}Pb/^{204}Pb$	$^{208}Pb/^{206}Pb$	$^{207}Pb/^{206}Pb$	$^{204}Pb/^{206}Pb$	$\delta^{18}O$ GM (‰)	$\delta^{18}O$ PL (‰)	Mg#	Age (Ma)	Error ($\pm 2\sigma$)
DM255B	Lava	0.703757	0.512905	5.4	0.283093	10.9	38.62	15.64	18.96	2.04	0.83	0.05	6.68	-	57.4	15.76	0.11
CAH16-179B	Lava	-	-	-	-	-	-	-	-	-	-	-	-	5.92	53.5	16.02	0.08
MS-11-6	Dike	0.703461	0.512974	6.7	-	-	38.70	15.68	18.97	2.04	0.83	0.05	5.55	5.79	53.2	16.06	0.14
CAH16-163	Lava	0.703584	0.512940	6.1	0.283093	10.9	-	-	-	-	-	-	5.99	5.83	45.8	16.18	0.05
CAH15-007	Lava	0.703691	0.512889	5.1	-	-	38.52	15.60	18.89	2.04	0.83	0.05	6.12	-	64.4	16.22	0.06
MC-76-16	Lava	-	0.512957	6.4	0.283128	12.1	-	-	-	-	-	-	-	5.76	52.2	16.23	0.09
CAH16-148	Lava	-	-	-	-	-	-	-	-	-	-	-	-	5.54	49.8	16.62	0.07
CAH16-138	Dike	-	0.512971	6.7	0.283109	11.4	38.43	15.58	18.84	2.04	0.83	0.05	5.75	5.81	50.2	16.70	0.09
CAH16-065	Lava	0.704102	0.512861	4.5	0.283039	9.0	38.59	15.60	18.98	2.03	0.82	0.05	-	-	44.2	16.72	0.03
CAH15-023	Dike	0.703494	0.512964	6.5	0.283100	11.1	38.40	15.57	18.79	2.04	0.83	0.05	5.45	-	56.1	16.88	0.06
CAH16-174A	Lava	0.703528	0.512964	6.5	0.283111	11.5	38.52	15.60	18.85	2.04	0.83	0.05	5.52	-	49.7	16.96	0.07
CAH17-200	Lava	-	0.512956	6.4	0.283126	12.1	-	-	-	-	-	-	5.75	5.72	52.6	17.02	0.03
CAH17-245	Lava	0.703573	0.512941	6.1	0.283097	11.0	38.49	15.58	18.87	2.04	0.83	0.05	5.78	-	47.3	17.14	0.04
CAH17-222A	Lava	0.703412	0.512994	7.1	0.283126	12.1	38.52	15.61	18.86	2.04	0.83	0.05	5.28	5.32	52.1	17.23	0.04
CAH16-073A	Lava	0.703969	0.512791	3.1	-	-	38.93	15.73	19.14	2.03	0.82	0.05	-	-	55.2	-	-
CAH16-171A	Lava	0.703597	0.512930	5.9	0.283071	10.1	38.51	15.60	18.86	2.04	0.83	0.05	-	-	52.7	-	-
CAH16-195	Dike	0.703428	0.512972	6.7	0.283109	11.4	38.44	15.57	18.84	2.04	0.83	0.05	-	-	50.8	-	-
CAH17-242A	Lava	0.703565	0.512925	5.8	0.283084	10.6	-	-	-	-	-	-	-	-	57.8	-	-
CAH16-140	Dike	-	-	-	-	-	-	-	-	-	-	-	-	5.9	55.6	-	-

GM: groundmass. PL: plagioclase.

3.2. Distinguishing Basaltic Lavas and Dikes of the PGB

Samples of PGB are distinguished from other main-phase CRBG formations (Grande Ronde, Imnaha, and Steens Basalts) by specific geochemical parameters. Relative to the Grande Ronde Basalt, the PGB is easy to differentiate, as it contains higher MgO (mostly > 4 wt. %) and lower concentrations of SiO_2 (mostly < 53 wt. %) and generally lower incompatible trace element contents, for example, La, Y, and Hf (Figure 2). Compared to the Imnaha Basalts, which can be subdivided into two subtypes, Rock Creek (<51% wt. % SiO_2) and American Bar (>51% wt. % SiO_2, cf. Hooper, 1974 [46]), the PGB exhibits a comparable SiO_2 range (48.5 to 53 wt. %) but with lower concentrations of various incompatible elements (i.e., Th, Hf, La) at a similar SiO_2 content (Figure 2).

A more complicated goal is distinguishing the PGB near the northern extent of the Steens Basalt, as both the PGB and the Steens Basalt are coarsely plagioclase-phyric and contain similar SiO_2 ranges. However, they are easily differentiated using Zr/Y ratios—at low SiO_2, the PGB samples have Zr/Y < 4, and at high SiO_2, the PGB samples have Zr/Y < 4.5, while samples of the Steens Basalt have ratios > 4 and > 4.5, respectively (Figure 2). Additionally, PGB samples have lower concentrations of LREE, TiO_2, and Hf at a given SiO_2 value (Figure 2).

3.3. Parental Magmas and Implications for Mantle Sources

Samples of each endmember (i.e., RR and HMD) represent some of the most primitive basalts identified within the PGB (Mg# > 57). The samples defining the HMD endmember plot closer to the C1 depleted mantle component of Carlson (1984) [3], while the samples defining the RR endmember exhibit a more enriched composition (Figure 7C,D). Magmatically evolved PGB samples are also consistent with a petrogenetic model involving two different mantle sources, as compositional variability at a given Mg# cannot be explained by fractionation or contamination alone, as documented in the following discussion.

The two defined primitive groups (HMD and RR) represent PGB endmember compositions and are distinct in both trace element and isotopic spaces with minimal overlapping attributes (Figure 7). Isotopic data suggest that the PGB samples define two populations of $^{87}Sr/^{86}Sr$ values, demonstrated by samples representative of both the RR and HMD endmembers. Plots of major and trace element data similarly suggest that samples of both endmember groups show distinct compositional differences. However, sample CAH15-007

plots closer to the HMD endmember array in most major and trace element spaces, and in isotopic geochemical space, this sample clusters with the RR endmember array (Figure 7). These relatively small enrichments in $^{87}Sr/^{86}Sr$ could be the result of crustal contamination or reflect larger contributions over time from a less-depleted magmatic source (i.e., with less conspicuous HFSE depletions and LILE enrichments).

Distinct geochemical and isotopic traits distinguish the RR endmember group from the HMD endmember group, suggesting that they were sourced from two different primitive compositions. Compared with other isotopic ratios such as $^{143}Nd/^{144}Nd$ or $^{206}Pb/^{204}Pb$ (Figure 7C,D), samples of each exhibit a wider range of $^{87}Sr/^{86}Sr$ ratios. For example, $^{87}Sr/^{86}Sr$ ratios range between 0.7030 and 0.7034 in the HMD endmember and 0.7035–7038 in the RR endmember. This variability is not observed in $^{143}Nd/^{144}Nd$ ratios, as the ratio is comparable between endmembers (HMD ~0.5130, RR 0.5129). This could be because Sr is a more fluid mobile element compared to Nd, so minor subduction metasomatism of a mantle source would be likely to result in more variability in Sr isotopic composition (compared to Nd). Higher LREE concentrations and Zr/Y values at higher $^{87}Sr/^{86}Sr$ ratios (i.e., >0.7035) in RR endmember samples suggest that some PGB parental magmas already contained slightly elevated ratios (Figure 7).

3.4. Fractionation Models to Account for PGB Geochemical Variability

Given the observed range of compositions even at the high MgO end of the PGB data, we take two endmembers from this dispersion as starting points for modeling the fractionation processes that resulted in the trends towards lower MgO contents. The data array from the RR endmember contains geochemical signatures similar to the earliest PGB subunit, the Twickenham Basalt (Figure 8B), while the data array from the HMD endmember is from high-MgO dikes that are independent of the three previously defined PGB subunits [23,47]. Comparing the three PGB subunits, there is one evolutionary trend for the Twickenham and Monument Mountain Basalts and another for the Dayville Basalts, which are anchored by the high-MgO dikes (Figures 4 and 8). Select trace and major elements distinguish the geochemical evolution of each, such as P_2O_5 (wt. %) for similar Y (ppm) concentrations. This is useful to consider as a ratio (i.e., Y/P_2O_5), as Y has a close correlation with magmatic evolution (Figures 6, 8 and 9). Although Ti and P contents are effective at distinguishing various CRB units, the specific petrogenetic processes responsible for their relative differences remain unclear.

Identified primitive endmembers (HMD and RR) are used as parent compositions for fractionation models in MELTS. These compositions include a sample from the high-MgO dikes (HMD sample ID: MMB D70A, [5]) and a sample from a lava flow located along Rattlesnake Road (RR sample ID: CAH16-241A, this study) (Figure 1, Table 1). Using these two PGB compositions, a total of 24 MELTS models were conducted under variable crustal pressures (2–4 kb and 7–9 kb) and water contents (0.1 and 0.5 wt. % H_2O). During each model, pressure is held constant, and temperature is lowered to 100 degrees below the calculated liquidus in increments of 2–5 degrees C. Model outputs include crystallizing mineral phases and their modal abundance, major element concentrations, and select trace element concentrations calculated using bulk partition coefficients (Di). Select trace elements include Y, La, Ba, Th, Sc, and Cr, where the behavior of each element in the magma is dictated by a bulk partition (or distribution) coefficient (Di). Utilized partition coefficients are summarized in Table S1, and MELTS modeling results are summarized in Table S5.

Model fractionation trends for the HMD endmember composition yielded results between ~75%–82% crystallization at all pressures with 0.1 wt. % H_2O and varied between ~54%–67% when the starting composition contained 0.5 wt. % H_2O. For models conducted under low pressures (2–4 kb), plagioclase and spinel are the first crystallizing phases, followed by olivine and clinopyroxene. At higher pressures (7–9 kb), clinopyroxene and spinel crystallize first, followed by plagioclase. Olivine is only a crystallizing phase under low pressure conditions (i.e., 2–4 kb), and spinel is a minor phase (<1%) under low

pressure conditions and ranges from 1%–2.3% with higher pressure. High- and low-Ca clinopyroxene crystallize during each model, except at 2 and 9 kb at 0.5 wt. % H_2O. The high-Ca clinopyroxene (~17 wt. %) crystallizes just a bit earlier than the low-Ca clinopyroxene (~4–7 wt. %). Considering both clinopyroxene populations, the modal abundance of clinopyroxene is similar (~ 48–49) for models run at higher pressures (7–9 kb). Model results also indicate increases in the modal abundance of the earlier formed high-Ca clinopyroxene with increasing pressure, where the later formed and lower-Ca clinopyroxene decreases with increasing pressure. At low pressures (2–4 kb), the modal abundance of both clinopyroxene populations is much more variable and increases with pressure (i.e., 2–3 kb and 3–4 kb).

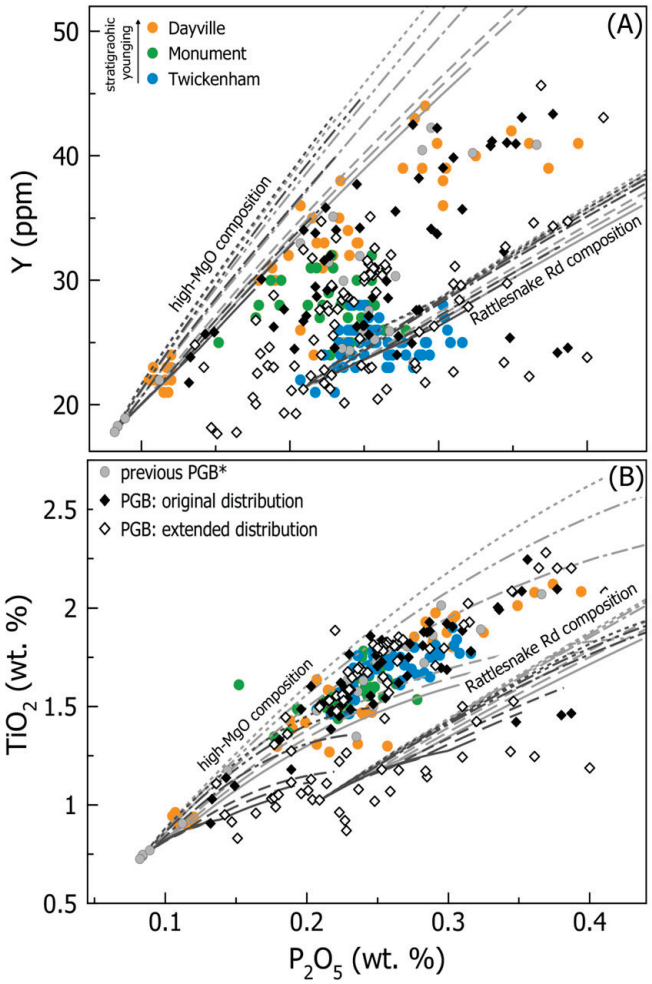

Figure 8. Geochemical comparison of PGB samples collected in this study relative to the three PGB subunits distinguished by Bailey (1989) [23]. (**A**) Y (ppm) and (**B**) TiO_2 (wt. %) versus P_2O_5 (wt. %) for PGB samples collected as part of this study compared to all previously analyzed PGB samples. Composition evolution of both identified PGB endmembers (HMD and RR) shown with predicted evolution from MELTS modeling results. Dark gray lines represent modeling at 0.5 wt. % H_2O, and light gray lines represent modeling at 0.1 wt. % H_2O. Solid lines are 9 kb progressively more from dashed to dotted lines, representing 2 kb. PGB subunit geochemistry from Bailey (1989) [23] and * previous PGB geochemistry from Wolff et al. (2008) [5].

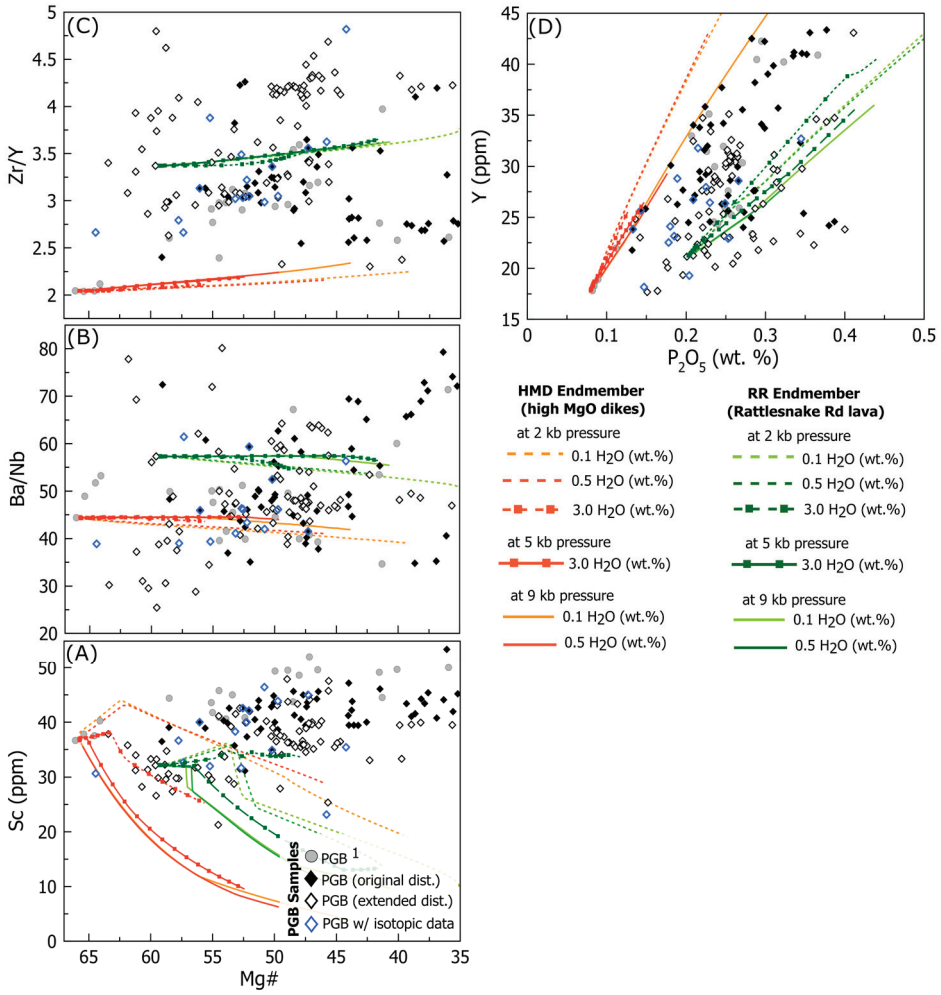

Figure 9. MELTS modeling results for parental RR and HMD endmember compositions. Scatterplots include (**A**) Sc (ppm), (**B**) Ba/Nb, and (**C**) Zr/Y versus Mg# and (**D**) Y (ppm) versus P_2O_5 (wt. %). All plots include models conducted at low pressure (2 kb) and high pressure (9 kb), at both 0.1 and 0.5 wt. % H_2O, and include two model runs with 3.0 wt. % H_2O (2 kb and 5 kb). Blue diamonds illustrate which samples also have Sr, Nd, Hf, and Pb isotopic analyses.

Modeling results of the 100 °C decrease in temperature using the RR endmember composition indicate maximum fractionation degrees between 74% and 80% at lower pressures (2–4 kb) and 52%–62% at higher pressures (7–9 kb) with 0.1 wt. % H_2O. When the melt contained 0.5 wt. % H_2O, maximum fractionation degrees varied between 58% and 63% at lower pressures (2–4 kb) and 35–45% at higher pressures (7–9 kb) (Table S5). Mineral phases typically crystallized in the following sequence: orthopyroxene, followed by spinel, plagioclase, and clinopyroxene. Similar to the results using the HMD endmember, fractionation of the RR endmember composition predicts two populations of clinopyroxene, a high (>15 wt. %) and a low (<10 wt. %) Ca clinopyroxene. Both the high- and low-Ca populations of clinopyroxene crystallize with every model. For all modeled conditions, the modal abundance of clinopyroxene (both high and low Ca) remains similar, and plagioclase decreases with increasing pressure, and only under low pressure (2 kb) and wet (0.5 wt. % H_2O) conditions will model results predict olivine as a crystallizing phase (Table S5).

Orthopyroxene is an early crystallizing phase predicted in each model using the RR endmember composition (likely due to the elevated SiO_2 content) but never crystallizes during models conducted with the HMD composition (Table S5). Using the predicted modal abundance of crystallizing phases in MELTS with calculated bulk partition coefficients, concentrations for select trace elements were calculated from each model output. Trace element

concentrations calculated from each model border the observed concentrations of Th, Ba, and La and could result from mixing of the magmas along the two differentiation trends. Predicted concentrations of Sc and Cr do not reflect the majority of observed PGB compositions (Figures 9 and S2). Finally, the most conspicuous differences between these two primitive PGB endmembers is the enrichment of light rare earth elements (LREE) in the RR endmember composition relative to the HMD endmember composition (Figure S2). These endmembers may reflect differences in source compositions (e.g., amount of subduction metasomatism) or simply the relative depth and degree of melting.

3.5. Evaluating Crustal Contamination

To determine if assimilation of crustal material is playing a role in the petrogenesis of PGB lavas and dikes across its distribution area, K/P and K/Ti are plotted against Mg# (Figure 10). Typically, crustal contamination is evaluated via isotopic compositions, but here, the potential crustal endmembers from the young, accreted terranes are not isotopically distinct enough to have much effect on Sr and Nd isotopic compositions if assimilated. Regardless of age, felsic rocks have much higher K/P and K/Ti than mantle melts (even after crustal fractionation), so felsic crustal additions would show up in these elements no matter how old the crust is that was assimilated. Both ratios K/P and K/Ti will be modified if felsic material is assimilated, as K is concentrated in felsic material, while P and Ti are progressively depleted because of apatite and ilmenite fractionation, respectively. Additionally, if felsic crustal melts were assimilated, this should also be visible in other geochemical parameters such as SiO_2, numerous incompatible elements (i.e., Rb, Nb, La, etc.), and radiogenic and oxygen isotopic data. Incompatible elements and isotopic data exhibit no clear evidence of assimilated granitic material.

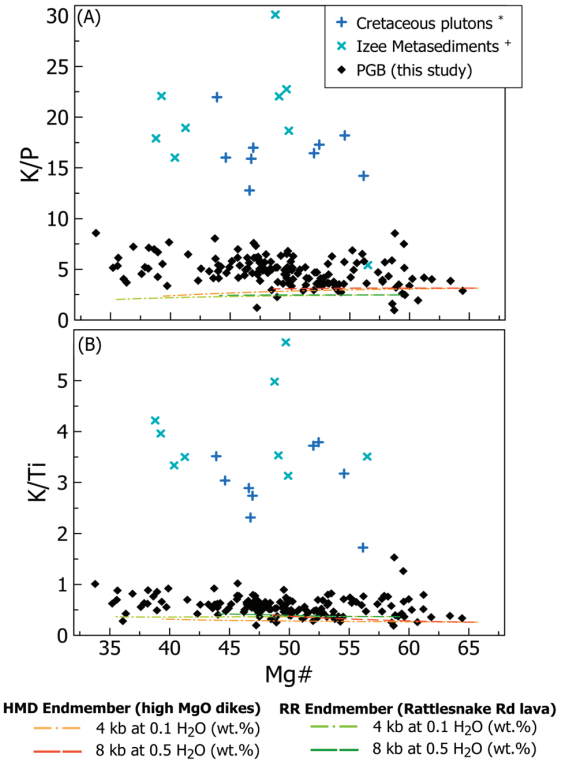

Figure 10. Trace element ratios (**A**) K/P and (**B**) K/Ti versus Mg# for PGB samples (this study). Both ratios are sensitive to assimilation when the crustal contaminant is felsic and may indicate if crustal contamination influences geochemical signatures of the PGB. * Cretaceous plutons include the Lookout Mountain, Turemen Ranch, Amelia, and Pedro Mountain plutons (data from Gaschnig et al., 2017 [48]; Standhaft, 2018 [49]). + Samples of Izee metasediments, predominantly argillite and shale lithologies (data from Streck, unpub.).

The crustal section through which PGB magmas erupted consists of a series of accreted Paleozoic-Mesozoic oceanic volcanic arcs [50]. Although there is a range of compositions present in this crustal basement, we use the composition of the Izee metasediments as a representative of the potential crustal contaminant in the area of the PGB eruptions. Compositions of Izee metasediments relative to all PGB samples are plotted on Ba/Th versus La/Sm (normalized), which is often used to help unravel influences of oceanic crust compared with added sediment (Figure 11) [51]. The addition of such sediment into a magma is important to evaluate, as a volumetrically minor amount of sediment (~2%–3%) can dramatically alter the abundances of the most incompatible elements of an erupting basalt [51]. To investigate whether metasediments sourced from the Izee formation could yield the observed PGB geochemical signatures, we utilize a simple mixing model.

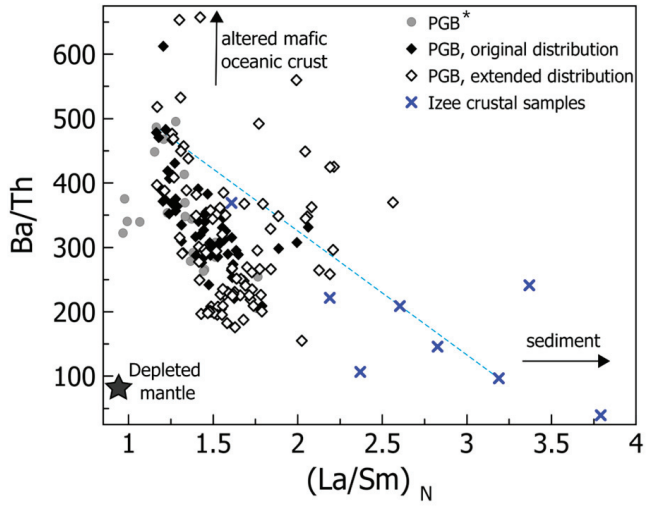

Figure 11. Ba/Th versus La/Sm (normalized) of PGB and Izee metasediments. Trace element data from * Wolff et al. (2008) [5] and Izee crustal samples from Streck, unpublished data.

Models were done with the following mixing calculation:

$$m = xA + B(1 - x) \quad (1)$$

Different mixing compositions were investigated at 2, 5, 10, 15, and 20% (x), where (A) is a primitive PGB composition (i.e., HMD or RR), (B) is the average bulk composition for Izee metasediments, and (m) is the resulting contaminated PGB composition. The objective was to determine if assimilation of Izee metasediments (B) could yield observed PGB compositions (Figure 12). Results of this modeling indicate that contamination of PGB by Izee argillitic material would not sufficiently modify concentrations of many HREE, such as Tb, Dy, Yb, and Lu. Elevated HREE of average PGB is more likely to reflect their extensive amount of fractionation. Patterns for all PGB compositions do not reflect as large a depletion (i.e., deep trough) in Nb and Ta concentrations on a mantle normalized trace element diagram compared to the metasediments (Figure 12). One of the most prominent compositional changes of metasediment contribution is in K concentrations, but observed concentrations show no significant evidence that sediment assimilation is a dominant process over magmatic evolution (Figure 10). Concentrations of HREE and HFSE in PGB samples could not be produced from assimilation of Izee metasedimentary material; thus, additional processes need to be invoked to produce the observed compositional array in PGB rocks.

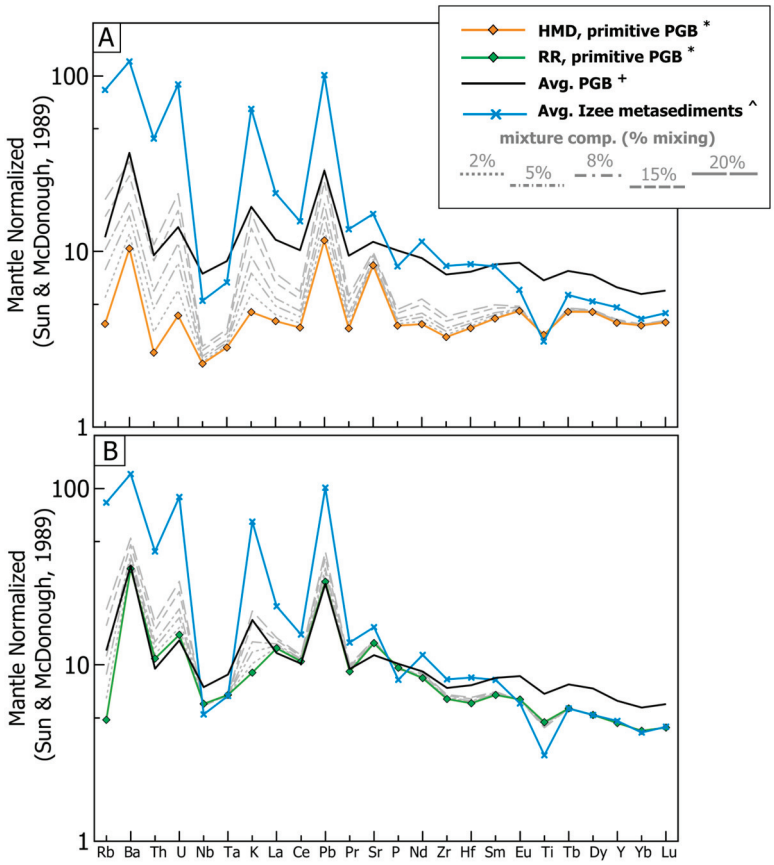

Figure 12. Mixing models illustrating initial compositions of (**A**) the primitive HMD endmember and (**B**) the primitive RR endmember and mixture compositions (m) resulting from 2, 5, 8, 15, and 20% contamination with average Izee metasediments on mantle normalized trace element diagrams (Sun and McDonough, 1989 [24]). Geochemical compositions for average PGB and Izee metasedimentary material shown for reference; data compiled from * this study; $^{+}$ Wolff et al., 2008 [5]; and $^{\wedge}$ Streck, unpublished data.

4. Discussion

4.1. Evidence of a Contaminated Mantle?

Lava flows and dikes of the PGB contain the lowest $^{87}Sr/^{86}Sr$ ratios of any main-phase formations of the CRBG (Figures 6 and 7), and oxygen isotopes are near the mantle range at ~5.8 ± 0.2‰. When combined with elevated concentrations of Ba and overall high LILE/HFSE ratios, these characteristics have been used to argue sourcing from a back-arc-type mantle [3,6]. Previous petrogenetic modeling suggests that low $^{87}Sr/^{86}Sr$ ratios (<0.7030–0.7034) are characteristic of early and less-modified PGB lavas, and any relative increase in $^{87}Sr/^{86}Sr$ ratios was attributed to crustal contamination [3–6]. Relative to the existing PGB stratigraphy, low $^{87}Sr/^{86}Sr$ ratios (<0.7032) are observed in only three PGB samples: a Twickenham Basalt flow, a Dayville Basalt flow, and a high-MgO dike [5,23,45]. Higher $^{87}Sr/^{86}Sr$ ratios are observed in some of the lavas of the youngest PGB subunit, the Dayville Basalt; however, $^{87}Sr/^{86}Sr$ ratios in the Dayville Basalt range from 0.703087 to 0.703713, almost the full range of the entire PGB [5,23]. By contrast, a sample with relatively elevated $^{87}Sr/^{86}Sr$ (0.703691) of this study (CAH15-007, RR endmember) is among the most primitive PGB samples in terms of elemental composition (Figure 6). Another relatively primitive PGB sample (DM255B, Mg# 57.4) also has a relatively elevated $^{87}Sr/^{86}Sr$ ratio of 0.703757. This sample location at Dooley Mountain represents the northeastern extent of the added PGB distribution and clusters with other samples of the RR endmember in isotopic space (Figure 6).

The previous reported $\delta^{18}O$ values from groundmass for the PGB ranged from 5.6 to 6.1‰, where stratigraphically lower basalts of the PGB have the lowest $\delta^{18}O$ values, identical to the canonical mantle range of 5.7–5.8‰, and stratigraphically higher lavas have slightly elevated $\delta^{18}O$, up to 6.1 ‰ [4] (Figure 13). This study notes higher $\delta^{18}O$ values in samples with younger ages, in agreement with observed increases with stratigraphy from earlier studies (i.e., Brandon et al., 1993 [4]) (Figure 13). Increases in $\delta^{18}O$ values through time could be generated by prolonged volcanism through the same area gradually increasing the amount of crustal assimilation that was occurring—supported by the observed correlation between $\delta^{18}O$ and $^{87}Sr/^{86}Sr$ (Figure 5D). Fractionation of mafic phases (i.e., olivine, clinopyroxene, and plagioclase) from a basaltic magma should minimally (~0.2‰) increase $\delta^{18}O$, assuming a starting composition of 5.7–5.8‰ in the basalt [40]. During magmatic evolution, $\delta^{18}O$ increases and becomes isotopically heavier in minerals with more covalent bonds, yielding lower $\delta^{18}O$ in more mafic phases and higher $\delta^{18}O$ in the remaining melt [40]. However, $\delta^{18}O$ ratios also increase as a result of crustal contamination, as most continental rocks have $\delta^{18}O$ ratios > 6‰. Observed increases in $\delta^{18}O$ values in more primitive PGB lavas are, then, more likely a result of contamination rather than fractional crystallization (Figure 13).

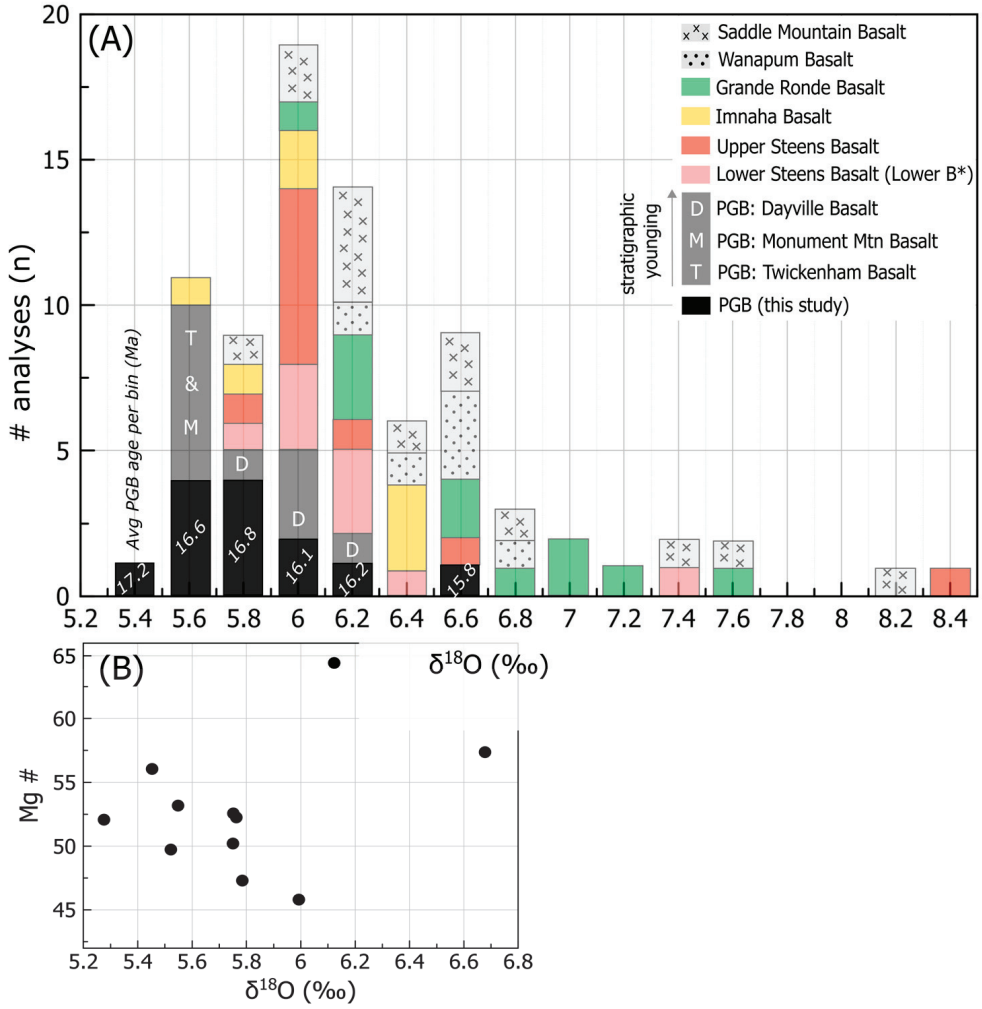

Figure 13. (**A**) Histogram of $\delta^{18}O$ compositions for PGB and other CRBG units. $\delta^{18}O$ data compiled from Nelson, 1983 [52]; Carlson, 1984 [3]; Hooper and Swanson, 1990 [53]; Brandon et al., 1993 [4], and Moore, 2018 [8]. Steens analyses are from plagioclase separates, and all other CRBG analyses are from whole-rock samples. (**B**) Scatterplot of Mg# versus the $\delta^{18}O$ value for PGB samples analyzed as part of this study; x-axis scaled similarly to panel.

Assuming that these higher PGB groundmass $\delta^{18}O$ values (6.12 and 6.68‰) are representative of both RR endmember samples (i.e., CAH15-007, DM255B in Table 2), the question becomes if this contamination occurred in the source or later as the magma traversed the crust. The most elevated $\delta^{18}O$ signatures are from two primitive samples of the RR group (CAH15-007 and DM255B, respectively). Both samples are groundmass separates but have undergone acid leaching following $^{40}Ar/^{39}Ar$ procedures to remove excess alteration, which could lead to misleading (i.e., elevated) values. This observation is unique relative to other CRBG units, which often have elevated $\delta^{18}O$ with lower MgO content (i.e., Grande Ronde Basalt). The range in $\delta^{18}O$ in Grande Ronde is too big for magmatic fractionation, so this correlation between $\delta^{18}O$ and MgO is likely reflective of combined fractionation-assimilation [54].

Addition of sediment to magma during crustal contamination affects the Sr isotope ratio of the contaminated magma less than addition of "sediment" to the mantle through subduction zone processes because of the much higher Sr content of a basaltic magma compared to its peridotitic source in the mantle [55]. There are no $^{87}Sr/^{86}Sr$ data for Izee material, but Nd isotopic data yield ε_{Nd} values between −4 and 0, suggesting arc material that is compositionally evolved [56,57] with $^{87}Sr/^{86}Sr$ between 0.7045–0.707 based on the mantle correlation of Sr and Nd isotopic composition. $\delta^{18}O$ values for Izee samples are also approximated to be > 9, as is common for most clays and clastic material [40].

To help determine if crustal contamination originated from melting a contaminated mantle source or during fractionation of primary magmas in the crust, $\delta^{18}O$ and $^{87}Sr/^{86}Sr$ are plotted against one another, following James (1981) [55] (Figure 14). It is difficult to draw a definitive conclusion, as the crustal composition is not precisely known, but this does suggest that crustal contamination plays a role in petrogenesis of PGB magmas. Observations of PGB isotopic data suggest that source contamination with metasediment primarily increases $^{87}Sr/^{86}Sr$ prior to influencing $\delta^{18}O$ values. By contrast, crustal contamination of the magma increases both $^{87}Sr/^{86}Sr$ and $\delta^{18}O$. PGB data are offset from mantle values in $^{87}Sr/^{86}Sr$ at mantle $\delta^{18}O$ (source contamination) but show a trend of steeply increasing $\delta^{18}O$, with minor changes in $^{87}Sr/^{86}Sr$ (crustal contamination) likely reflecting assimilation of a high-$\delta^{18}O$ mafic source. Samples of the HMD endmember may represent source contamination of a depleted mantle, whereas the RR endmember may represent a more enriched composition that experienced subsequent contamination.

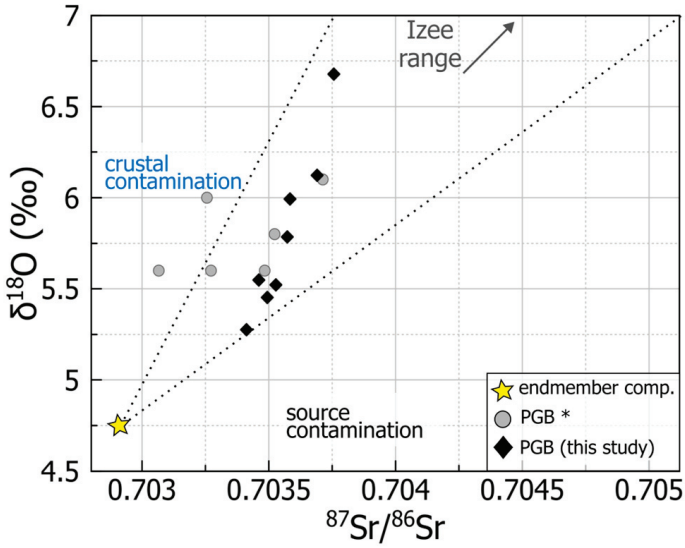

Figure 14. Plot of $\delta^{18}O$ versus $^{87}Sr/^{86}Sr$ ratios for PGB samples and approximated Izee crustal material as a potential contaminant. Mixing lines are not included, as there is not a well-defined isotopic composition for this potential contaminant. PGB * data from Wolff et al. (2008) [5].

4.2. PGB Magmas: Source Lithologies and Modification

Source lithologies for PGB lavas and dikes are interpreted to vary between pyroxenite to peridotite based on variable degrees of trace element enrichment and depletion, compared to Ni concentration within olivine phenocrysts [58]. The Ni content in the bulk rock can be skewed as a result of olivine accumulation. However, geochemical data combined with petrographic observations suggest that Ni content in PGB lavas is not driven by olivine accumulation, as our PGB samples that fall along the high-Ni trend are olivine poor (e.g., Soderberg and Wolff, 2023 [58], their Figure 7).

Distinguishing processes that result in incompatible element enrichment can be difficult, especially when the processes of interest have comparable geochemical consequences. Melting a sediment metasomatized mantle or adding sediment to a melt can yield comparable geochemical and isotopic characteristics in the resulting basaltic magma (Figure 9B). Both LILE and LREE can be enriched as a result of slab fluxing in the mantle or addition of sediment in the crust, and both modification scenarios have to be considered. Samples of both primitive PGB endmembers (HMD and RR) contain elevated Ba/Nb ratios (i.e., ~60) compared to MORB and OIB (Figure 9B). With respect to the RR endmember, all four sampled basaltic lavas from along Rattlesnake Road were candidates to represent a parental PGB composition (Mg# 58–59) for modeling in MELTS. However, these four lavas contain highly variable Ba/Nb ratios, ranging from 39 to 100, almost the full range observed in all PGB samples and providing evidence that PGB primary magmas must have been derived from compositionally distinct sources. The variability in Ba/Nb values within the same inferred mantle source (RR endmember) suggests that this source itself varied spatially and that it is more likely a source characteristic than the result of crustal contamination of the magmas while in the crust.

The data require a range in compositions of the primary magmas for the PGB, as shown in a variety of trace element plots (e.g., Ce/P, Ba/Nb). Simply put, magmatic differentiation alone cannot explain the huge range in the data for these ratios, and we demonstrate the minimal consequences of crustal contamination. Taken together, this suggests there must have been a wide range in primary PGB magmas derived from compositionally distinct sources.

The limited degree of crustal contamination could result from the rapid ascent rate of PGB magmas [4]. Earlier modeling tried to calculate the amount of contamination using an isotopic component that represents the crust in the Blue Mountains Province (Paleozoic accreted terranes) and a redefined C1-depleted mantle [3,4,23]. To achieve observed radiogenic Sr and $\delta^{18}O$ values, Brandon et al. (1993) [4] estimated 8%–21% crustal contamination, which was consistent with the estimate of Carlson (1984) [3]. Although the bulk of these rocks provide little isotopic leverage in composition when compared to the CRBG, if the LILE enrichment in PGB lavas is a result of sediment input, metasedimentary Izee rocks are the most representative composition.

Trace element modeling suggests that crustal contamination with Izee metasedimentary material could not yield the observed compositional patterns in some incompatible elements in samples of the PGB, such as Nb, Ta, and some HREEs (Figure 13). Observed Zr/Y ratios in PGB lavas and dikes are highly variable, ranging from ~2 to 4.5 (Figure 9C). Both Zr and Y are similarly incompatible with partition coefficients that make them difficult to decouple during magmatic evolution. Variable Zr/Y values at high MgO suggests more than one contributing mantle source, as these ratios distinguish both primitive PGB endmembers (Zr/Y > 2.5 in RR, Zr/Y < 2.5 in HMD) (Figure 9C). If changes in Zr/Y primarily reflect compositional variability in the mantle source, the RR endmember is more heterogeneous. This is because samples defining the RR group exhibit a larger range in Zr/Y ratios than samples of the HMD group, similar to the variability of Ba/Nb ratios mentioned above (Figure 9B). Alternatively, these Izee sediments may not serve as the most compositionally representative material assimilated by PGB magmas.

High Mg basalts of the PGB contain Sc concentrations between 30 and 40 ppm; meanwhile, more evolved PGB samples contain Sc concentrations between 40 and 50 ppm

(Figure 9A). The results of every MELTS model do not predict an increase in Sc but rather a decrease with magmatic evolution, suggesting that the modeling input parameters were not representative of the magmatic conditions at which differentiation occurred. Even under initial conditions that were highly saturated in H_2O (3.0 wt. %), MELTS modeling still did not account for the observed increase in Sc concentrations (Figure 9A). This, combined with higher-than-predicted Cr concentrations, suggests that fractionation of clinopyroxene was not a dominating process in the formation of PGB basalts. Instead, the elevated concentrations of both Sc and Cr trace elements indicate that crystallization of clinopyroxene and potentially orthopyroxene was delayed or suppressed—and MELTS may be overestimating the importance of pyroxene crystallization (Figure 9). The arrival of clinopyroxene on the liquidus can be delayed when fractionation occurs at lower pressures [59]. In order for Sc content to steadily rise, it needs to remain incompatible, and that could possibly be achieved by either significant crystallization of olivine and plagioclase over pyroxene or episodic magmatic recharge at low pressures (< 3 kb) that may buffer basalt magmas at conditions prior to pyroxene crystallization (and may also explain highly variable Cr/Ni ratios among PGB magmas).

4.3. Petrogenetic Relationships to Other CRBG Formations

Of the CRGB formations, PGB shares the most geochemical and isotopic characteristics with the Steens Basalt, with comparable $^{87}Sr/^{86}Sr$ ratios (0.7035–0.7038). While observed $\delta^{18}O$ values in PGB samples are not anomalously low, they are slightly lower than in the Steens Basalt. Reported $\delta^{18}O$ values for the Steens Basalt range between 5.91 and 6.75‰ (n = 17), excluding one outlier at 8.5‰ [8]. The majority of reported $\delta^{18}O$ values for PGB range between 5.28 and 5.99‰ (n = 17 of 19, Table 2) with two values > 6‰, which is generally representative of the mantle. Within basaltic lavas and dikes of the CRBG, $\delta^{18}O$ values below ~5.9‰ are proposed to result from hydrothermal alteration by heated groundwater [54]. Since a portion of $\delta^{18}O$ values in PGB are consistently below the average mantle, which differs from other CRBG formations, an alternative consideration could be exposure to hydrothermal processes. However, this interpretation seems unlikely given the correlation of $\delta^{18}O$ values to $^{87}Sr/^{86}Sr$, the minor depletion of $\delta^{18}O$ values, and the large spatial extent and age range of analyzed PGB samples. We also note that Sr could be very sensitive to hydrothermal alteration, which may explain the range of $^{87}Sr/^{86}Sr$ at more or less constant $^{143}Nd/^{144}Nd$.

4.4. Two Temporal Pulses of Magmatism

Eruptive activity for the PGB spans ~1.4 Ma, as evidenced by numerous high-precision ArAr dates from samples dispersed across a wide region in eastern Oregon. These ages demonstrate that lavas and dikes of the PGB were emplaced during two discrete intervals, a temporal pattern that this research has also identified in main-phase CRBG (Figure 15). Within the PGB, it is inconclusive whether there are clear geochemical trends with time. However, younger ages are often correlated with lower Sc (ppm) concentrations, which may suggest increasing pressure during crystallization and more pyroxene fractionation relative to olivine (Figure 15).

Two of the youngest reported PGB ages represent primitive samples used to characterize the RR group within radiogenic isotope space (samples CAH15-007 and DM255B) (Table 1, Figure 7). These samples erupted during the second and later pulse of PGB activity with $^{40}Ar/^{39}Ar$ ages between 16.22 and 15.76 Ma and contain the lowest TiO_2 values of any of the dated samples (0.91 and 0.99 wt. %, respectively). While these two samples are the only dated samples within either identified endmember (RR or HMD), the other primitive samples that comprise the RR endmember have stratigraphic age control. Multiple basaltic lava flows along Rattlesnake Road both underlie and overlie the rhyolitic Dinner Creek Tuff unit 2, dated at ~15.5 Ma [61]. The exposures here are faulted, but the section overlies the Dinner Creek Tuff unit 1 and underlies unit 3, dated at 16.16 and 15.5, respectively [61]. This stratigraphic relationship constrains eruptive age and suggests

that these lavas were emplaced between 15.5 and 16.16 Ma. These basaltic lavas along Rattlesnake Road erupted during the later pulse of PGB volcanism and contain low TiO_2 concentrations (~0.92–1.11 wt. %). In addition to samples of the RR endmember, HMD endmember samples contain the lowest TiO_2 concentrations of any analyzed PGB lava or dike, between 0.72 and 0.77 (wt. %). If these basaltic lavas and dikes do represent two parental components for the PGB, they were not emplaced until the second pulse of PGB eruptive activity (Figure 15).

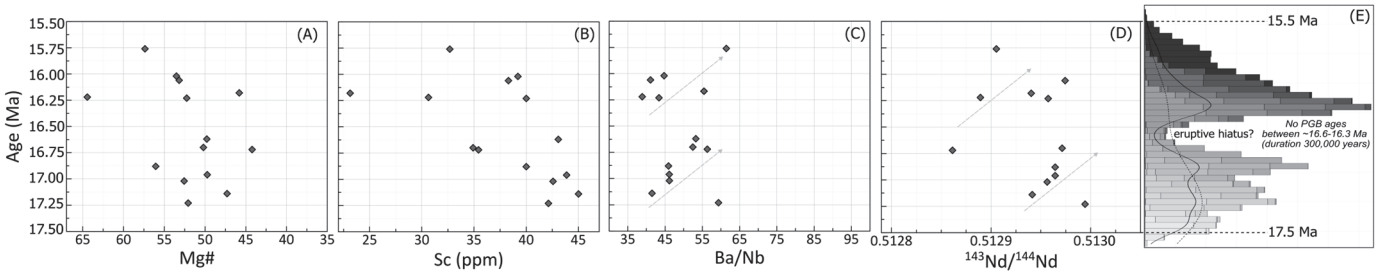

Figure 15. Geochemical signatures through time for dated PGB samples in this study. Age (Ma) versus (**A**) Mg#, (**B**) Sc (ppm), (**C**) Ba/Nb, and (**D**) $^{143}Nd/^{144}Nd$ isotopic ratios (arrows illustrate potential trends through each eruptive pulse/time). (**E**) Histogram of PGB ages (15 total) at 2-sigma using 1000 uniformly distributed points from Cahoon et al., 2023 [60]; ages along the y-axis are scaled to align with panels and greyscale color indicates samples where dark to light grey represents PGB temporal endmembers (**A**–**D**). A bimodal distribution of PGB ages suggests two temporal pulses of volcanism that are comparable in their geochemical variability, although $^{143}Nd/^{144}Nd$ appears to increase within each age population.

4.5. PGB Endmember Compositions: Trust but Verify

The modeled HMD endmember composition is sourced from two dikes mapped in the Monument Dike swarm, originally interpreted as compositionally dissimilar to any CRBG geochemical subunit (samples D-16 and D-17 [47]). Although there are no published data, earlier studies also reported basaltic lavas of a similar high-MgO (and low TiO_2) composition in Flat Creek, approximately 20 km southeast of the type locality at Picture Gorge [2,62] (D. Swanson, 201—personal comm.) (Figure 1). Both sample locations (D-16/-17 and Flat Creek) were targeted as part of this study to gain a context of sample exposures, field relationships, and textures. Multiple dikes were sampled at the mapped location of D-16/-17, along with basaltic outcrops exposed at the Flat Creek section. However, none of the basaltic samples collected from either site (D-16/-17 dikes, Flat Creek exposures) contained elevated MgO and depleted TiO_2 (the geochemical composition that characterizes the high-MgO dikes). Thus, our field reconnaissance could not confirm the presence of any basaltic exposure with HMD composition as suggested by earlier workers [2,47,62] (D. Swanson, 201—personal comm.) While these high-MgO dikes are similar in their location and orientation to known PGB dikes of the Monument swarm, they are spatially and geochemically localized—with few samples existing between them and the rest of the PGB in geochemical parameter space (Figures 6–8). Thus, although additional samples have been identified with similar compositions, we question whether these high MgO dikes represent a significant and volumetrically dominant parental magma of the PGB.

5. Conclusions

Geochemical compositions of the PGB and Steens Basalt were influenced by mantle contributions from a subduction-related component, likely from prior slab-sourced fluid fluxing [3–5,18]. In context to the PGB, this mantle source must be spatially widespread and variable in its relative contribution, as lavas and dikes with PGB composition identified as far east as Lake Owyhee and as far south as Hart Mountain, Oregon.

Samples of PGB composition exposed in both the original and extended distributions exhibit petrochemical diversity that trends toward two primitive endmembers in geo-

chemical and isotopic spaces. MELTS modeling of both endmember compositions (HMD and RR) demonstrates that PGB geochemical variability cannot be attributed to fractionation processes alone. Evolution of the RR composition can account for a larger portion of the observed PGB trace element concentrations compared to the HMD composition, supporting the observation that samples of the HMD endmember are spatially localized and limited—and may represent a different basaltic suite.

Each group displays distinct trends with magmatic evolution, as seen in major and trace element compositional arrays. The HMD group is more sensitive to pressure fluctuations during fractionation, as exhibited by larger compositional changes between MELTS models conducted at different pressures. Predicted crystallizing phases are also dissimilar; olivine crystallizes from the HMD endmember composition but not from the RR endmember composition, while orthopyroxene crystallizes from the RR endmember composition but not from the HMD endmember composition. Results of trace element modeling is inconsistent with increasing concentrations of Sc and Cr (ppm) with magmatic evolution of natural samples. This could suggest suppression of clinopyroxene (or possibly orthopyroxene) fractionation and the continuous recharging of a Sc-enriched melt.

Differences in partial melting, compositionally distinct sources, fractional crystallization, and crustal contamination all play into creating compositional diversity in basalts. The geochemical diversity of PGB magmas cannot be solely attributed to magmatic fractionation, requiring some modification via crustal contamination. Modeling potential crustal contamination to produce the average composition for the PGB or the HMD endmember group, bulk assimilation of compositions like Izee metasedimentary rocks does not result in compositions similar to the PGB. More specifically, Izee rocks exhibit large relative depletions in trace elements such as Nb, Ta, and some HREEs. Mixing models indicate that the assimilating material could not have such significant depletions in these elements to produce average PGB compositional patterns on a mantle-normalized trace element diagram if the contamination occurred in the crust. Crustally derived material, however, does play a role in the generation of PGB, clearly indicated by the observed positive correlation of $\delta^{18}O$ versus $^{87}Sr/^{86}Sr$ and enrichment of various LILEs. Considering additional mantle, magmatic, and surficial processes that influence these geochemical traits, the degree of contamination is likely < 10%, given that the majority of the PGB contains $\delta^{18}O$ values below 6‰.

Combining geochemical traits, MELTS modeling results, and reported ages for the PGB, which range from 15.76 to 17.23 Ma, indicates that the most primitive PGB samples erupted during the later episode of PGB volcanic activity. A trend in composition over this time scale more likely reflects changing source compositions or conditions/degree of partial melting—also supported by decreases in TiO_2 (wt. %) with time, the opposite of what would be expected with magmatic evolution. On the other hand, a fluid-fluxed mantle component is present in both temporal periods of PGB volcanic activity and may become more significant over time within each eruptive pulse of volcanism.

Supplementary Materials: The following supporting information can be downloaded at https://www.mdpi.com/article/10.3390/min14050440/s1: Table S1. Partition Coefficients Used in Trace Element Calculations [63–67]. Table S2. XRF and ICP-MS Data: Geochemical table with sample locations. Table S3. Sr, Nd, Hf, Pb Isotope Uncertainty and Isobaric Interferences. Table S4. Oxygen Isotope Summary Table. Table S5. Summary Table of MELTS Modeling Results Trace Element Calculations. Figure S1. MELTS modeling results for major elements versus Mg# for both RR and HMD endmember compositions. Figure S2. MELTS modeling results for selected trace elements versus Mg# for both RR and HMD endmember compositions. Figure S3. MELTS modeling results for major and trace element ratios versus Mg# for both RR and HMD endmember compositions. Figure S4. Major and Trace Elements versus Mg# Plots. Figure S5. Onuma Diagrams [68].

Author Contributions: Conceptualization, E.B.C. and M.J.S.; methodology, E.B.C., M.J.S., R.W.C. and I.N.B.; software, E.B.C.; validation, E.B.C., M.J.S., R.W.C. and I.N.B.; formal analysis, E.B.C., M.J.S. and R.W.C.; investigation, E.B.C. and M.J.S.; resources, E.B.C., M.J.S., R.W.C. and I.N.B.; data curation, E.B.C., M.J.S., R.W.C. and I.N.B.; writing—original draft preparation, E.B.C., M.J.S. and R.W.C.;

writing—review and editing, E.B.C., M.J.S., R.W.C. and I.N.B.; visualization, E.B.C.; supervision, M.J.S. and R.W.C.; project administration, E.B.C.; funding acquisition, E.B.C., M.J.S. All authors have read and agreed to the published version of the manuscript.

Funding: This work was nominally supported through NSF-EAR grant #1220676 to Streck and Geological Society of America, Evolving Earth Foundation, and internal Portland State University graduate student research grants to Cahoon.

Data Availability Statement: Data are contained within the article and Supplementary Materials.

Acknowledgments: We acknowledge and appreciate the reviewers who helped improve the content and quality of this manuscript.

Conflicts of Interest: The authors declare no conflicts of interest.

References

1. Camp, V.E.; Ross, M.E.; Duncan, R.A.; Jarboe, N.A.; Coe, R.S.; Hanan, B.B.; Johnson, J.A. The Steens Basalt: Earliest Lavas of the Columbia River Basalt Group. *Spec. Pap. Geol. Soc. Am.* **2013**, *497*, 87–116. [CrossRef]
2. Swanson, D.A.; Wright, T.L.; Hooper, P.R.; Bentley, R.D. *Revisions in Stratigraphic Nomenclature of the Columbia River Basalt Group*; US Government Printing Office: Washington, DC, USA, 1979.
3. Carlson, R.W. Isotopic Constraints on Columbia River Flood Basalt Genesis and the Nature of the Subcontinental Mantle. *Geochim. Cosmochim. Acta* **1984**, *48*, 2357–2372. [CrossRef]
4. Brandon, A.D.; Hooper, P.R.; Goles, G.G.; St, R.; Lamberp, J. Contributions to Mineralogy and Petrology Evaluating Crustal Contamination in Continental Basalts: The Isotopic Composition of the Picture Gorge Basalt of the Columbia River Basalt Group. *Contrib. Mineral. Petrol.* **1993**, *114*, 452–464. [CrossRef]
5. Wolff, J.A.; Ramos, F.C.; Hart, G.L.; Patterson, J.D.; Brandon, A.D. Columbia River Flood Basalts from a Centralized Crustal Magmatic System. *Nat. Geosci.* **2008**, *1*, 177–180. [CrossRef]
6. Wolff, J.A.; Ramos, F.C. Source Materials for the Main Phase of the Columbia River Basalt Group: Geochemical Evidence and Implications for Magma Storage and Transport. *Spec. Pap. Geol. Soc. Am.* **2013**, *497*, 273–291. [CrossRef]
7. Cahoon, E.B.; Streck, M.J.; Koppers, A.A.P.; Miggins, D.P. Reshuffling the Columbia River Basalt Chronology-Picture Gorge Basalt, the Earliest-and Longest-Erupting Formation. *Geology* **2020**, *48*, 348–352. [CrossRef]
8. Moore, N.; Grunder, A.; Bohrson, W. The Three-Stage Petrochemical Evolution of the Steens Basalt (Southeast Oregon, USA) Compared to Large Igneous Provinces and Layered Mafic Intrusions. *Geosphere* **2018**, *14*, 2505–2532. [CrossRef]
9. Schwartz, J.J.; Snoke, A.W.; Cordey, F.; Johnson, K.; Frost, C.D.; Barnes, C.G.; LaMaskin, T.A.; Wooden, J.L. Late Jurassic magmatism, metamorphism, and deformation in the Blue Mountains Province, northeast Oregon. *Bulletin* **2011**, *123*, 2083–2111. [CrossRef]
10. Carlson, R.W.; Lu, G.W.; Macdock, J.D. Columbia River Volcanism: The Question of Mantle Heterogeneity or Crustal Contamination. *Geochim. Cosmochim. Acta* **1981**, *45*, 2483–2499. [CrossRef]
11. Geist, D.; Richards, M. Origin of the Columbia Plateau and Snake River Plain: Deflection of the Yellowstone Plume. *Geology* **1993**, *21*, 789–792. [CrossRef]
12. Hales, T.C.; Abt, D.L.; Humphreys, E.D.; Roering, J.J. A Lithospheric Instability Origin for Columbia River Flood Basalts and Wallowa Mountains Uplift in Northeast Oregon. *Nature* **2005**, *438*, 842–845. [CrossRef] [PubMed]
13. Camp, V.E.; Hanan, B.B. A Plume-Triggered Delamination Origin for the Columbia River Basalt Group. *Geosphere* **2008**, *4*, 480–495. [CrossRef]
14. Camp, V.E. Plume-Modified Mantle Flow in the Northern Basin and Range and Southern Cascadia Back-Arc Region since ca. 12 Ma. *Geology* **2019**, *47*, 695–699. [CrossRef]
15. Moore, N.E.; Grunder, A.L.; Bohrson, W.A.; Carlson, R.W.; Bindeman, I.N. Changing Mantle Sources and the Effects of Crustal Passage on the Steens Basalt, SE Oregon: Chemical and Isotopic Constraints. *Geochem. Geophys. Geosystems* **2020**, *21*, e2020GC008910. [CrossRef]
16. Richards, M.A.; Duncan, R.A.; Courtillot, V.E. Flood Basalts and Hot-Spot Tracks: Plume Heads and Tails. *Science* **1989**, *246*, 103–107. [CrossRef] [PubMed]
17. Pierce, K.L.; Morgan, L.A.; Morgan, A. *The Track of the Yellowstone Hot Spot: Volcanism, Faulting, and Uplift*; Geological Society of America Memoir: Boulder, CO, USA, 1992; Volume 179.
18. Carlson, R.W.; Hart, W.K. Crustal Genesis on the Oregon Plateau (Pacific). *J. Geophys. Res.* **1987**, *92*, 6191–6206. [CrossRef]
19. Long, M.D.; Till, C.B.; Druken, K.A.; Carlson, R.W.; Wagner, L.S.; Fouch, M.J.; James, D.E.; Grove, T.L.; Schmerr, N.; Kincaid, C. Mantle Dynamics beneath the Pacific Northwest and the Generation of Voluminous Back-Arc Volcanism. *Geochem. Geophys. Geosystems* **2012**, *13*, 2012GC004189. [CrossRef]
20. Liu, L.; Stegman, D.R. Origin of Columbia River Flood Basalt Controlled by Propagating Rupture of the Farallon Slab. *Nature* **2012**, *482*, 386–389. [CrossRef] [PubMed]
21. Hoopers, P.R.; Hawkesworth, C.J.; Hooper, P.R.; Hawkesworth, C.J. Isotopic and Geochemical Constraints on the Origin and Evolution of the Columbia River Basalt. *J. Petrol.* **1993**, *34*, 1203–1246. [CrossRef]

22. Mcdougall, I. Geochemistry and Origin of Basalt of the Columbia River Group, Oregon and Washington. *Geol. Soc. Am. Bull.* **1976**, *87*, 777–792. [CrossRef]
23. Bailey, M.M. Evidence for Magma Recharge and Assimilation in the Picture Gorge Basalt Subgroup, Columbia River Basalt Group. *Geol. Soc. Am. Spec. Pap.* **1989**, *239*, 343–355.
24. Sun, S.S.; McDonough, W.F. Chemical and isotopic systematics of oceanic basalts: Implications for mantle composition and processes. *Geol. Soc. Lond. Spec. Publ.* **1989**, *42*, 313–345. [CrossRef]
25. Osawa, M.; Goles, G. Trace Element Abundances in Columbia River Basalts. In Proceedings of the Columbia River Basalt Symposium, Cheney, WA, USA, 21–23 March 1969; Eastern Washington State College Press: Cheney, WA, USA, 1970; pp. 173–175.
26. Nathan, S.; Fruchter, J.S. Geochemical and Paleomagnetic Stratigraphy of the Picture Gorge and Yakima Basalts (Columbia River Group) in Central Oregon. *Geol. Soc. Am. Bull.* **1974**, *85*, 63–76. [CrossRef]
27. Watkins, N.D.; Baksi, A.K. Magnetostratigraphy and Oroclinal Folding of the Columbia River, Steens, and Owyhee Basal ts in Oregon, Washington, and Idaho. *Am. J. Sci.* **1974**, *274*, 148–189. [CrossRef]
28. Goles, G.G. Miocene Basalts of the Blue Mountains Province in Oregon. I: Compositional Types and Their Geological Settings. *J. Petrol.* **1986**, *27*, 495–520. [CrossRef]
29. NORTH AMERICAN STRATIGRAPHIC CODE. North American Commission on Stratigraphic Nomenclature. *AAPG Bull.* **2005**, *89*, 1547–1591. [CrossRef]
30. Kasbohm, J.; Schoene, B. Rapid eruption of the Columbia River flood basalt and correlation with the mid-Miocene climate optimum. *Sci. Adv.* **2018**, *4*, eaat8223. [CrossRef]
31. Mahood, G.A.; Benson, T.R. Using 40Ar/39Ar ages of intercalated silicic tuffs to date flood basalts: Precise ages for Steens Basalt Member of the Columbia River Basalt Group. *Earth Planet. Sci. Lett.* **2017**, *459*, 340–351. [CrossRef]
32. Kuiper, K.F.; Deino, A.; Hilgen, F.J.; Krijgsman, W.; Renne, P.R.; Wijbrans, J.R. Synchronizing rock clocks of Earth history. *Science* **2008**, *320*, 500–504. [CrossRef]
33. Johnson, D.; Hooper, P.; Conrey, R. XRF Method XRF Analysis of Rocks and Minerals for Major and Trace Elements on a Single Low Dilution Li-Tetraborate Fused Bead. *Adv. X-ray Anal.* **1999**, *41*, 843–867.
34. Carlson, R.W.; Czamanske, G.; Fedorenko, V.; Ilupin, I. A Comparison of Siberian Meimechites and Kimberlites: Implications for the Source of High-Mg Alkalic Magmas and Flood Basalts. *Geochem. Geophys. Geosyst.* **2006**, *7*, 2006GC001342. [CrossRef]
35. Patchett, P.J.; Tatsumoto, M. Hafnium Isotope Variations in Oceanic Basalts. *Geophys. Res. Lett.* **1980**, *7*, 1077–1080. [CrossRef]
36. Garçon, M.; Boyet, M.; Carlson, R.W.; Horan, M.F.; Auclair, D.; Mock, T.D. Factors Influencing the Precision and Accuracy of Nd Isotope Measurements by Thermal Ionization Mass Spectrometry. *Chem. Geol.* **2018**, *476*, 493–514. [CrossRef]
37. Tanaka, T.; Togashi, S.; Kamioka, H.; Amakawa, H.; Kagami, H.; Hamamoto, T.; Yuhara, M.; Orihashi, Y.; Yoneda, S.; Shimizu, H.; et al. JNdi-1: A Neodymium Isotopic Reference in Consistency with LaJolla Neodymium. *Chem. Geol.* **2000**, *168*, 279–281. [CrossRef]
38. Todt, W.; Cliff, R.A.; Hanser, A.; Hofmann, A.W. Evaluation of a 202Pb–205Pb Double Spike for High—Precision Lead Isotope Analysis. In *Geophysical Monograph Series*; Blackwell Publishing Ltd.: Oxford, UK, 1996; Volume 95, pp. 429–437; ISBN 9781118664230.
39. Bouvier, A.; Vervoort, J.D.; Patchett, P.J. The Lu-Hf and Sm-Nd Isotopic Composition of CHUR: Constraints from Unequilibrated Chondrites and Implications for the Bulk Composition of Terrestrial Planets. *Earth Planet Sci. Lett.* **2008**, *273*, 48–57. [CrossRef]
40. Bindeman, I. Oxygen Isotopes in Mantle and Crustal Magmas as Revealed by Single Crystal Analysis. *Rev. Miner. Geochem.* **2008**, *69*, 445–478. [CrossRef]
41. Loewen, M.W.; Bindeman, I.N. Oxygen Isotope and Trace Element Evidence for Three-Stage Petrogenesis of the Youngest Episode (260–279 Ka) of Yellowstone Rhyolitic Volcanism. *Contrib. Mineral. Petrol.* **2015**, *170*, 39. [CrossRef]
42. Gualda, G.A.R.; Ghiorso, M.S.; Lemons, R.V.; Carley, T.L. Rhyolite-MELTS: A Modified Calibration of MELTS Optimized for Silica-Rich, Fluid-Bearing Magmatic Systems. *J. Petrol.* **2012**, *53*, 875–890. [CrossRef]
43. Gualda, G.A.R.; Ghiorso, M.S. MELTS-Excel: A Microsoft Excel-Based MELTS Interface for Research and Teaching of Magma Properties and Evolution. *Geochem. Geophys. Geosyst.* **2015**, *16*, 315–324. [CrossRef]
44. Houston, R.A.; McClaughry, J.D.; Duda, C.J.M.; Ferns, M.L. Geologic Map of the Harney 7.5′ Quadrangle, Harney County, Oregon. 2017.
45. Brandon, A.D.; Gordon, G.G. Assessing Subcontinental Lithospheric Mantle Sources for Basalts: Neogene Volcanism in the Pacific Northwest, USA as a Test Case. *Contrib. Miner. Pet.* **1995**, *121*, 364–379. [CrossRef]
46. Hooper, P.R. Petrology and chemistry of the Rock Creek flow, Columbia River basalt, Idaho. *Geological Society of America Bulletin* **1974**, *85*, 15–26. [CrossRef]
47. Fruchter, J.S.; Baldwin, S.F. Correlations between Dikes of the Monument Swarm, Central Oregon, and Picture Gorge Basalt Flows. *Geol. Soc. Am. Bull.* **1975**, *86*, 514–516. [CrossRef]
48. Gaschnig, R.M.; Macho, A.S.; Fayon, A.; Schmitz, M.; Ware, B.D.; Vervoort, J.D.; Kelso, P.; LaMaskin, T.A.; Kahn, M.J.; Tikoff, B. Intrusive and depositional constraints on the Cretaceous tectonic history of the southern Blue Mountains, eastern Oregon. *Lithosphere* **2017**, *9*, 265–282. [CrossRef]
49. Standhaft, D. Textural and Compositional Analysis of Early Miocene Dacite Lavas in Malheur National Forest, Eastern Oregon: Testing Models of Granodiorite Remobilization to Yield Dacite Magmas. Masters Thesis, Portland State University, Portland, OR, USA, University of Greifswald, Greifswald, Germany, 2018.

50. Dickinson, W.R. Mesozoic Forearc Basin in Central Oregon. *Geology* **1979**, *7*, 166–170. [CrossRef]
51. Elliot, T. Tracers of the Slab. In *Inside the Subduction Factory*; Geophysical Monograph-American Geophysical Union: Washington, DC, USA, 2004. [CrossRef]
52. Nelson, D.O. Implications of oxygen-isotope data and trace-element modeling for a large-scale mixing model for the Columbia River Basalt. *Geology* **1983**, *11*, 248–251. [CrossRef]
53. Hooper, P.R.; Swanson, D.A. *The Columbia River Basalt Group and Associated Volcanic Rocks of the Blue Mountains Province*; US Geological Survey Professional Paper; US Geological Survey: Reston, VA, USA, 1990; Volume 1437, pp. 63–99.
54. Bindeman, I.N.; Greber, N.D.; Melnik, O.E.; Artyomova, A.S.; Utkin, I.S.; Karlstrom, L.; Colón, D.P. Pervasive Hydrothermal Events Associated with Large Igneous Provinces Documented by the Columbia River Basaltic Province. *Sci. Rep.* **2020**, *10*, 10206. [CrossRef] [PubMed]
55. James, D.E. The Combined Use of Oxygen and Radiogenic Isotopes as Indicators of Crustal Contamination. *Annu Rev Earth Planet Sci.* **1981**, *9*, 311–344. [CrossRef]
56. Lamaskin, T.A.; Dorsey, R.J.; Vervoort, J.D. Tectonic Controls on Mudrock Geochemistry, Mesozoic Rocks of Eastern Oregon and Western Idaho, U.S.A.: Implications for Cordilleran Tectonics. *J. Sediment. Res.* **2008**, *78*, 765–783. [CrossRef]
57. LaMaskin, T.; Vervoort, J.; Dorsey, R. Crustal Growth by Tectonic Accretion of Island Arc Terranes: Radioisotopic Provenance of Late Paleozoic–Mesozoic Rocks of the Blue Mountains, Western United States. *Geol. Soc. Am. Abstr. Programs* **2013**, *45*, 441.
58. Soderberg, E.R.; Wolff, J.A. Mantle Source Lithologies for the Columbia River Flood Basalt Province. *Contrib. Mineral. Petrol.* **2023**, *178*, 11. [CrossRef]
59. Takahashi, E.; Kushiro, I. Melting of a Dry Peridotite at High Pressures and Basalt Magma Genesis. *Am. Mineral.* **1983**, *68*, 859–879.
60. Cahoon, E.B.; Streck, M.J.; Koppers, A.A. Picture Gorge Basalt: Internal stratigraphy, eruptive patterns, and its importance for understanding Columbia River Basalt Group magmatism. *Geosphere* **2023**, *19*, 406–430. [CrossRef]
61. Streck, M.J.; Ferns, M.L.; McIntosh, W. Large, Persistent Rhyolitic Magma Reservoirs above Columbia River Basalt Storage Sites: The Dinner Creek Tuff Eruptive Center, Eastern Oregon. *Geosphere* **2015**, *11*, 226–235. [CrossRef]
62. Thayer, T.P.; Brown, E. *Local Thickening of Basalts and Late Tertiary Silicic Volcanism in the Canyon City Quadrangle, Northeastern Oregon*; U.S. Geological Survey: Reston, VA, USA, 1966; pp. C73–C78.
63. McKenzie, D.A.N.; O'nions, R.K. Partial melt distributions from inversion of rare earth element concentrations. *J. Petrol.* **1991**, *32*, 1021–1091. [CrossRef]
64. Hart, S.R.; Dunn, T. Experimental cpx/melt partitioning of 24 trace elements. *Contrib. Mineral. Petrol.* **1993**, *113*, 1–8. [CrossRef]
65. Green, T.H. Experimental studies of trace-element partitioning applicable to igneous petrogenesis—Sedona 16 years later. *Chem. Geol.* **1994**, *117*, 1–36. [CrossRef]
66. Hauri, E.H.; Wagner, T.P.; Grove, T.L. Experimental and natural partitioning of Th, U, Pb and other trace elements between garnet, clinopyroxene and basaltic melts. *Chem. Geol.* **1994**, *117*, 149–166. [CrossRef]
67. Dunn, T.; Senn, C. Mineral/matrix partition coefficients for orthopyroxene, plagioclase, and olivine in basaltic to andesitic systems: A combined analytical and experimental study. *Geochim. Cosmochim. Acta* **1994**, *58*, 717–733. [CrossRef]
68. Onuma, N.; Higuchi, H.; Wakita, H.; Nagasawa, H. Trace element partition between two pyroxenes and the host lava. *Earth Planet. Sci. Lett.* **1968**, *5*, 47–51. [CrossRef]

minerals

MDPI

Article

Thermobarometry of the Rajmahal Continental Flood Basalts and Their Primary Magmas: Implications for the Magmatic Plumbing System

Nilanjan Chatterjee [1,*] and Naresh C. Ghose [2,†]

[1] Department of Earth, Atmospheric and Planetary Sciences, Massachusetts Institute of Technology, Cambridge, MA 02139, USA
[2] Department of Geology, Patna University, Patna 800005, India
* Correspondence: nchat@mit.edu; Tel.: +1-617-253-1995
† Current address: G/608, Raheja Residency, Koramangala, Bangalore 560034, India.

Abstract: The Late Aptian Rajmahal Traps originated through Kerguelen-Plume-related volcanism at the eastern margin of the Indian Shield. Clinopyroxene and whole-rock thermobarometry reveals that the Rajmahal magmas crystallized at P-T conditions of ≤~5 kbar/~1100–1200 °C. These pressures correspond to upper crustal depths (≤~19 km). Modeling shows that the Rajmahal primary magmas were last in equilibrium with mantle at P-T conditions of ~9 kbar/~1280 °C. The corresponding depths (~33 km) are consistent with gravity data that indicate a high-density layer at lower crustal depths below an upwarped Moho. Thus, the high-density layer probably represents anomalous mantle. It is likely that the mantle-derived magmas accumulated below the upwarped Moho and were subsequently transported via trans-crustal faults/fractures to the upper crust where they evolved by fractional crystallization in small staging chambers before eruption. In the lower part of the Rajmahal plumbing system, buoyant melts from the Kerguelen Plume may have moved laterally and upward along the base of the lithosphere to accumulate and erode the eastern Indian lithospheric root. The Rajmahal plumbing system was probably shaped by tectonic forces related to the breakup of Gondwana.

Keywords: flood basalt; Rajmahal Traps; thermobarometry; primary magma; magma plumbing system

1. Introduction

Flood basalt eruptions have important environmental effects, and magma volumes and eruption rates of flood basalts are directly related to the structure of the plumbing system through which mantle-derived magmas reach the Earth's surface [1–3]. The structure of the plumbing system in continental flood basalt provinces may depend on the regional tectonics and proximity to a mantle plume [4,5]. Exposures of dikes, sills and other magma bodies, and geophysical surveys shed light on the structure of the plumbing system [6–9]. The plumbing system of plume-related continental large igneous provinces (LIP) can be divided into four parts corresponding to four depth levels [3]. These are the asthenospheric mantle level where melt is generated (level 1), the lithospheric mantle level through which magmas ascend and accumulate below the Moho (level 2), the crustal level where magma is transported via dikes and sills into and out of small staging chambers where magma differentiation occurs (level 3), and the surface level where volcanoes develop (level 4).

An LIP related to the activity of the Kerguelen Plume has been recognized in eastern India, southwestern Australia (Bunbury), the eastern Antarctic margin, the Kerguelen Plateau, the Ninetyeast Ridge, the Broken Ridge, and the Naturaliste Plateau [10–15] (Figure 1). The oldest basalts (~132 Ma) erupted in southwestern Australia. However, there are some reports of even older Kerguelen-Plume-related volcanic activity at ~145–130 Ma in the eastern Himalayas [16]. The eastern Indian basalts and most of the basalts of the Kerguelen Plateau erupted during

the peak of Kerguelen Plume activity at ~120–95 Ma [15]. In eastern India, the Late Aptian (~118–114 Ma) Rajmahal–Bengal Basin–Sylhet Traps (RBST) and the associated dolerite dikes and alkalic-carbonatitic-ultramafic intrusives comprise a large flood basalt province with an area of ~1 million km^2 [17–26]. The Rajmahal and Sylhet Traps are located in the western and eastern parts of the province (Figure 2), and drill-core data indicate that the two are continuous under the Gangetic alluvium of the Bengal Basin [27]. Dolerite dikes with NW to NNW-trend and similar age (118–109 Ma) intrude the Precambrian basement to the southwest and west of the Rajmahal outcrop [28] (Figure 2). Geochemical, isotopic, and textural studies of the RBST basalts have provided clues to the processes of fractional crystallization and crustal contamination in their origin [10,19,21,23,25,26,29–32]. However, the crystallization and mantle melting conditions of the basalts are yet to be established, and the structure of the pathways through which the basalts erupted is poorly understood. Although geophysical surveys have helped to clarify subsurface structures [33,34], and two- and three-dimensional modeling of gravity data have identified possible magmatic underplating below the lower crust [35,36], the structure of the magma plumbing system in the upper mantle and crust remains unclear. Thermobarometry based on the chemical composition of minerals and whole rock provides the temperatures and depths of magma equilibration, which may be used to complement geophysical studies to understand the structure of the magma plumbing system. This study aims to understand the structure of the Rajmahal plumbing system through thermobarometry based on clinopyroxene compositions analyzed here and whole-rock compositions available from the literature. The P-T conditions of crystallization obtained from thermobarometry are then used to backtrack along the fractionation paths of the basalts and calculate compositions of primary magmas and their equilibration depths.

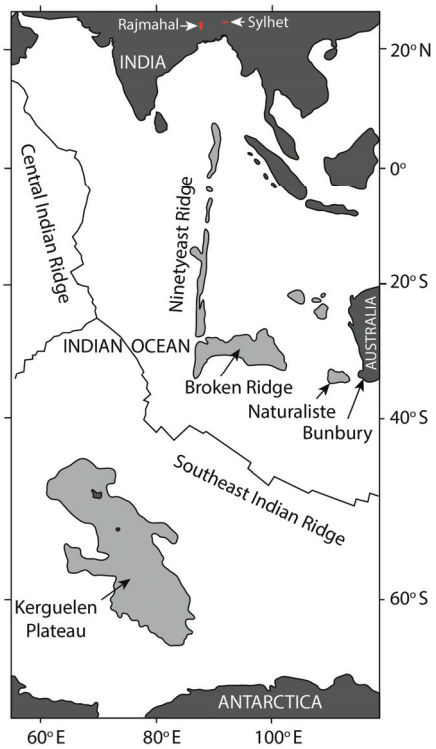

Figure 1. Location of the different parts of Kerguelen LIP. The continental landmasses are shown in black and the submarine plateaus and ridges are shown in grey.

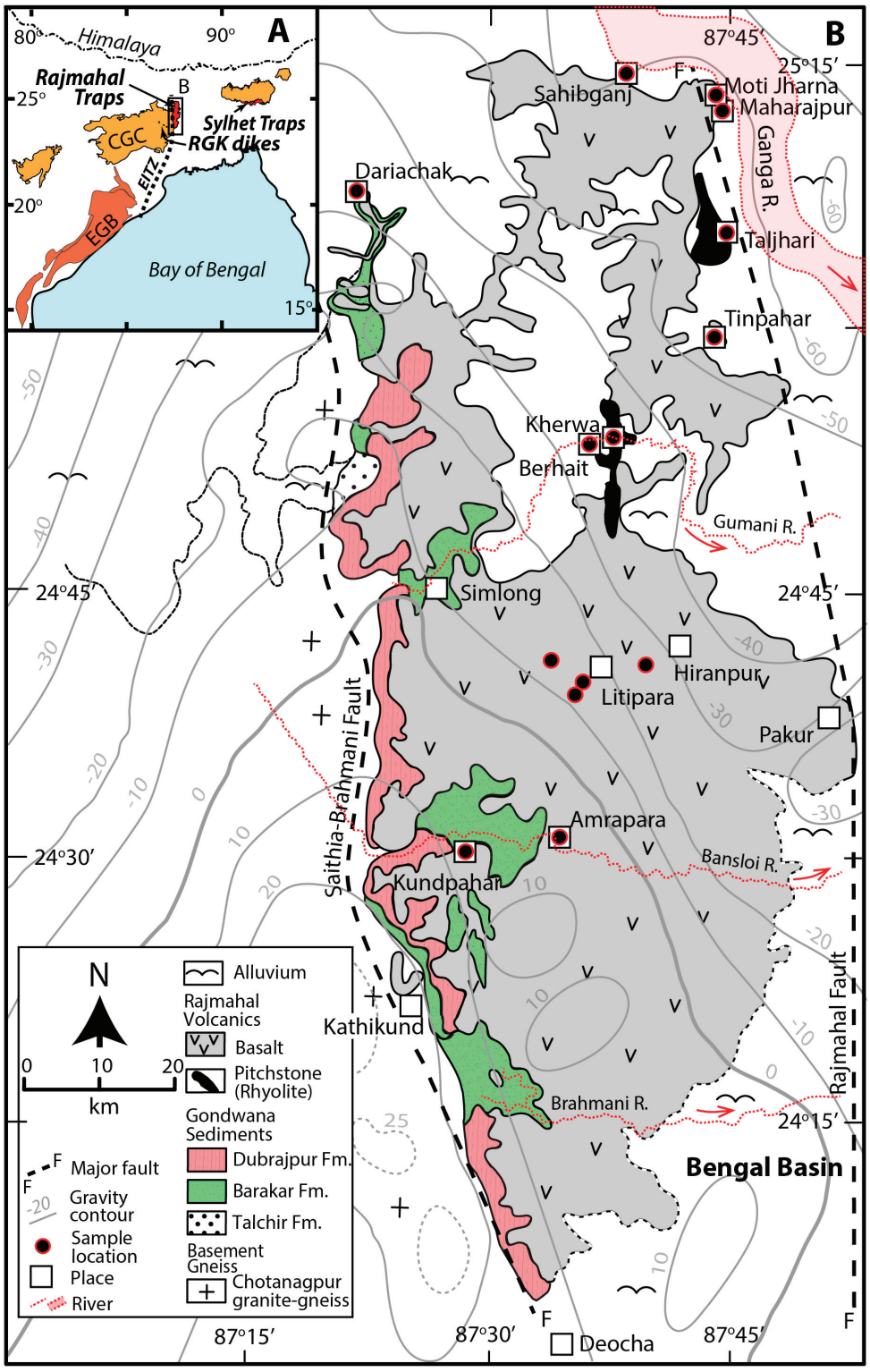

Figure 2. (**A**) Location of the Rajmahal Traps, Sylhet Traps, and Raniganj-Giridih-Koderma (RGK) dikes on the Indian Shield. CGC—Chotanagpur Gneiss Complex, EGB—Eastern Ghats belt, EITZ—Eastern Indian Tectonic Zone. (**B**) Detailed geological map of the Rajmahal Traps (after [32]). The Bouguer gravity contours (−60 to +25 mGal) are after [36].

2. Geological and Geochemical Background

The Rajmahal Traps (area: ~4300 km^2) are exposed along the north-south-oriented Rajmahal Hills in the northern part of the eastern margin of the Proterozoic Chotanagpur

Gneissic Complex (CGC) (Figure 2). The CGC forms the basement of the Gondwana Supergroup, the uppermost part of which contains the Rajmahal basalts [37,38]. The Rajmahal flows are sub-horizontal with the dip increasing to ~5° eastward at the eastern flank of the hills, and the total thickness of the flows increases from ~230 m in surface exposure to >332 m subsurface in the Bengal Basin [27,35]. The thickness of individual flows varies from <1 m to 85 m [39–41]. Thin beds of shale, black shale, mudstone, siltstone, cross-bedded sandstone, and oolite associated with bentonite lenses and volcaniclastic rocks occur between lava flows in the lower one-third of the volcanic sequence, indicating sub-aqueous eruptions during the early phase of volcanism [32,41–43]. The upper part of the sequence is devoid of sedimentary and volcaniclastic rocks, and consists of subaerially erupted lava flows [23,32]. The volcanics are dominated by tholeiitic basalt and basaltic andesite with minor trachyandesite, andesite, dacite and rhyolite, and rare orthopyroxene-bearing basalt and andesite [21,23,32]. The tholeiites have been classified into two geochemical groups [10] (Figure 3). The Group I samples have higher Ti/Zr ratios and lower Zr/Y ratios than the Group II samples. According to the total alkali-silica classification (TAS diagram, [44]), the Group I samples are basalt and basaltic andesite, whereas the Group II samples are all basaltic andesite. Isotopic and trace element data suggest that the Group I samples are uncontaminated, whereas the Group II samples with incompatible element patterns showing large-ion-lithophile element (LILE) enrichment and negative Nb-Ta anomalies are variably contaminated with the continental crust (Figure 3c) [10,18,21,23,26,31,32]. The chemical distinctions between the two groups of basalt also correlate with their textures, the early erupting Group I basalts in the lower part of the sequence being phyric with plagioclase and/or clinopyroxene phenocrysts, and the late erupting Group II basalts in the upper part of the sequence being mostly aphyric [23].

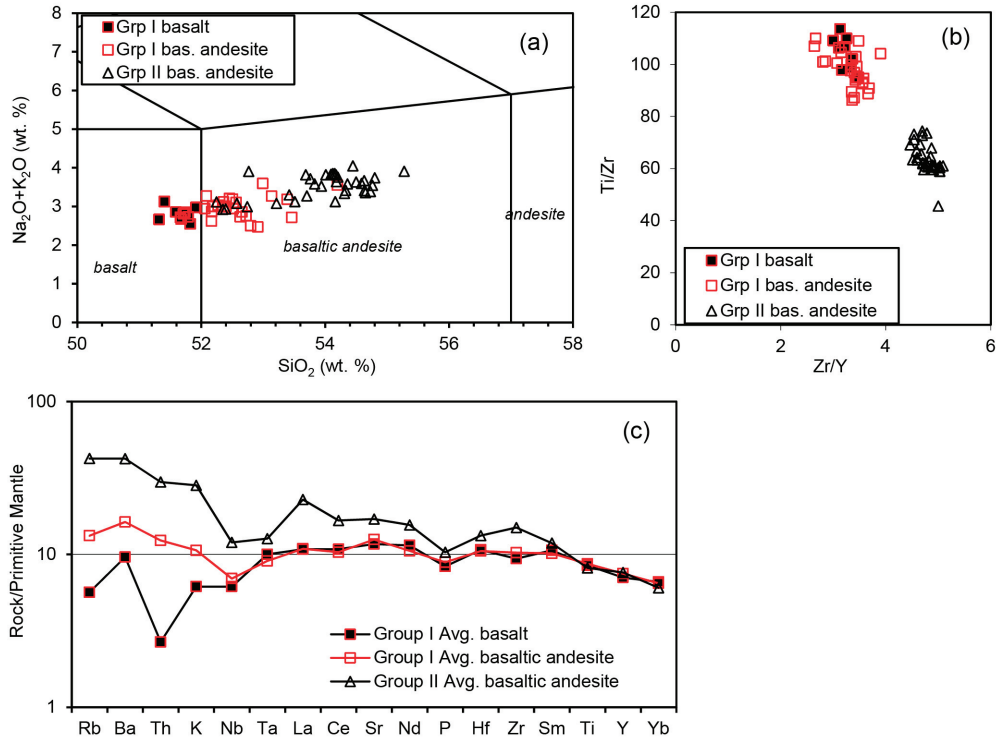

Figure 3. Bulk chemical compositions of the Rajmahal basalts and basaltic andesites (data from [10,21]). (**a**) Total alkali versus SiO_2 after [44]. (**b**) Ti/Zr versus Zr/Y. (**c**) Primitive mantle-normalized [45] incompatible elements.

The eastern margin of the CGC is characterized by north-trending, east-dipping asymmetric folds that formed during high-grade metamorphism and deformation along the north–south-oriented, mid-Neoproterozoic Eastern Indian Tectonic Zone, a major linear

orogen that extends from eastern India through Kerguelen Plateau to eastern Antarctica [46–48]. The eastern and western margins of the Rajmahal outcrop are bounded by two major N–S-oriented faults, the Rajmahal and Saithia–Brahmani faults (Figure 2), and the basement near the western margin of the Bengal Basin, adjacent to the Rajmahal Traps, also contains N–S-oriented, E-dipping step-faults that presumably formed during the pre-Rajmahal break-up of Gondwana [27,35,49]. Furthermore, there is a broad and elongated positive gravity anomaly with its axis along the western boundary, and several +10 mGal to +25 mGal gravity highs along either side of the southwestern boundary (Kathikund to Deocha) of the Rajmahal outcrop [35,36] (Figure 2). Multichannel reflection data and elastic thickness structure of the lithosphere also indicate the presence of a north–south-oriented pseudofault under the Rajmahal Traps whose formation is attributed to the activity of the Kerguelen plume [50,51]. Thus, the Rajmahal eruptions may have been guided by faults generated through reactivation of a major, pre-existing N–S-oriented mid-Neoproterozoic lineament during the break-up of Gondwana.

3. Sample Locations and Bulk Compositions

For the purpose of mineral thermobarometry, 40 basalt samples containing phenocrysts were analyzed from the northeastern (Sahibganj, Moti Jharna, Maharajpur, Taljhari, Tinpahar, Kherwa, Berhait), northwestern (Dariachak), and central (Litipara, Amrapara, Kundpahar) sectors of the Rajmahal outcrop (Figure 2, Table 1). The bulk compositions of four of the samples are available from [10]. According to the TAS diagram [44], samples TT3 and LH1 from near Litipara are basalts, and samples LA2 (near Litipara) and RB88-35 (Tinpahar) are basaltic andesites (Figure 3a). According to the Ti/Zr vs. Zr/Y plot [10], samples LA2, TT3, and LH1 belong to the uncontaminated Group I, and sample RB88-35 belongs to the contaminated Group II Rajmahal basalts (Figure 3b). The bulk analyses of these samples show totals higher than ~99 wt% [10], and LOI values determined by [21] for the Rajmahal basalts are <1 wt.%. This indicates that the Rajmahal magmas were essentially anhydrous.

Table 1. Mineral assemblages in the Rajmahal basalts.

Region	Location		Aug	Pgt	Pl	Hem	Ilm	Other
Northeast								
	Sahebganj	RB88-12	mph	mph	phen		gm	
	Moti Jharna	RB88-19	phen		phen		gm	
	Maharajpur	RB88-16	phen	mph	phen	gm	gm	
		RB88-17	phen		phen	gm	gm	
		RB88-18	phen		phen	gm	gm	
	Taljhari	EB89-154	phen		phen			
		RB88-24	phen		phen	gm	gm	
	Tinpahar	RB88-31	phen		phen		gm	Mgh
		RB88-32	phen		phen	gm	gm	
		RB88-39	mph		phen			Ol
		RB88-35	mph		phen	gm	gm	Cumm
	Kherwa	EB89-112	mph	mph	phen	gm		Zeol
		EB89-117	mph	mph	phen	gm	gm	Zeol
		EB89-118	mph	mph	phen	gm		
	Berhait	EB89-121	phen	mph	phen	gm	gm	
		EB89-123	mph		phen		gm	
		EB89-127	mph		mph	gm		
		EB89-128	mph	mph	phen	gm	gm	
Northwest								
	Dariyachak	DAR-2GB	phen		phen		gm	Mgh
		DAR-5YL	phen	mph	phen	gm	gm	
		DAR10-90	phen		phen	gm	gm	

Table 1. *Cont.*

Region	Location		Aug	Pgt	Pl	Hem	Ilm	Other
Central								
	Litipara-Amrapara Rd.	LA1	phen		phen	gm	gm	
		LA2	phen		phen	gm	gm	
		LA4	phen		phen	gm	gm	
		LA5	phen		phen	gm	gm	
		LA6	phen		phen	gm	gm	
	Litipara-Simlong Rd.	TT1	phen		phen	gm	gm	
		TT2	phen		phen	gm		
		TT3	phen	mph	phen	gm	gm	
		TT4	phen		phen	gm	gm	
	Litipara-Hiranpur Rd.	LH1	phen		phen	gm	gm	
	Amrapara	BL1	phen		phen	gm	gm	Kfs, Zeol
		BL3	phen		phen	gm	gm	Kfs, Zeol
	Kundpahar	KP1	phen		phen	gm	gm	
		KP2	mph		phen	gm	gm	Kfs, Zeol
		KP3	mph		phen	gm	gm	
		KP4	mph		phen			
		KP5	phen		phen	gm	gm	
		KP6	phen		phen	gm	gm	
		KP7	phen		phen	gm	gm	

Aug—augite, Pgt—pigeonite, Pl—plagioclase, Hem—hematite, Ilm—ilmenite, Mgh—maghemite, Ol—olivine, Cumm—cummingtonite, Kfs—K-feldspar, Zeol—zeolite, phen—phenocryst, mph—microphenocryst, gm—groundmass.

4. Analytical Methods

Textural studies and mineral analyses were performed on a JEOL JXA-8200 Superprobe electron probe microanalyzer (EPMA) at Massachusetts Institute of Technology, Cambridge, MA, USA operating with a 15 kV accelerating voltage, a 10 nA beam current, and 1 μm beam diameter. Typical counting times were 40 s per element that yielded accumulated counts with 1σ standard deviations of 0.3%–1.0% for major elements and 1%–5% for minor elements from counting statistics. The EPMA was calibrated using a set of synthetic and natural standards (DJ35 diopside-jadeite, ALP7 aluminous orthopyroxene, Synthetic anorthite, Amelia albite, Marjalahti olivine, rutile, hematite). The raw data were corrected for matrix effects with the CITZAF package [52].

5. Petrography and Mineral Chemistry

The samples are all of porphyritic basalt with phenocrysts (~2–4 mm) and microphenocrysts (~100–500 μm) surrounded by a fine-grained groundmass (Figure 4). The mineral assemblage in each sample is provided in Table 1. The phenocrysts are dominated by tabular clinopyroxene (augite) and lath-shaped plagioclase. Pigeonite occurs in some samples, notably from Berhait and Kherwa. Olivine is present in only one sample from Tinpahar. Rare K-feldspar occurs in one sample from Kundpahar and two samples from Amrapara. The average phenocryst content is ~5 vol.% with subequal amounts of augite and plagioclase. The groundmass consists of clinopyroxene and plagioclase. Ilmenite and hematite are ubiquitous in the groundmass and two samples contain maghemite. Some of the samples contain small spherules filled with zeolites.

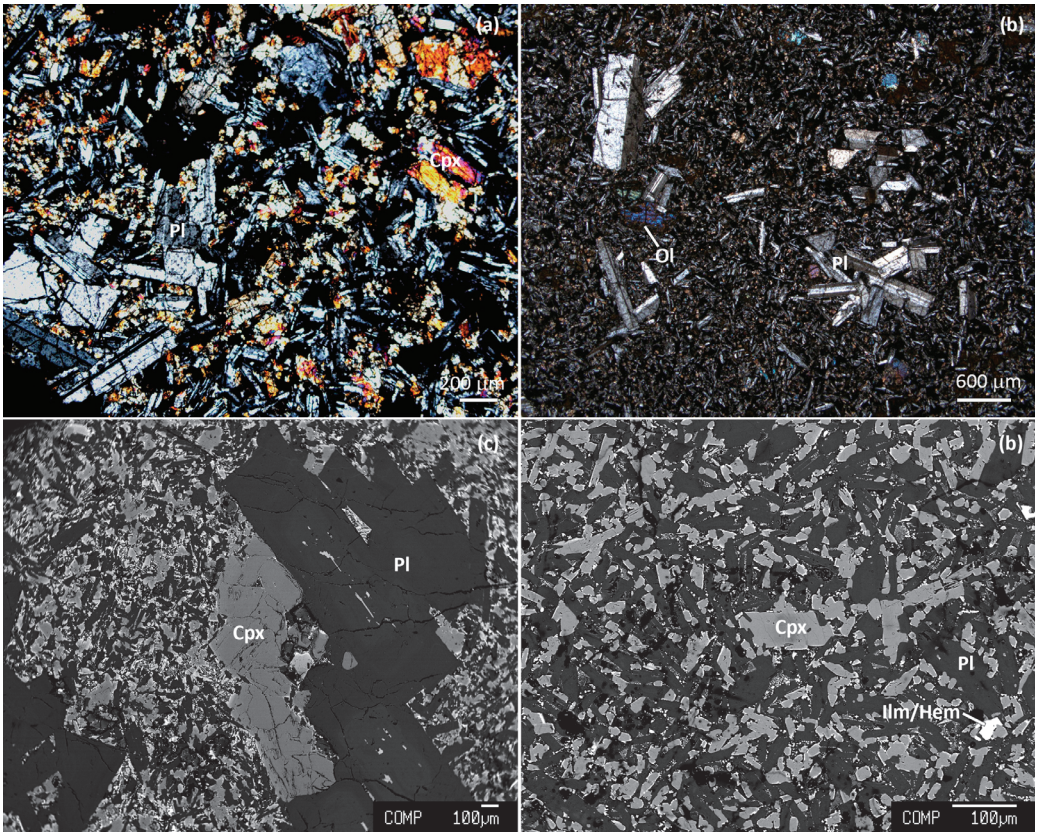

Figure 4. Cross-polarized light images of (**a**) Maharajpur basalt showing plagioclase (Pl) and clinopyroxene (Cpx) phenocrysts, and (**b**) Tinpahar basalt showing Pl and olivine (Ol) phenocrysts, and backscattered electron images of (**c**) Taljhari basalt showing Pl and Cpx phenocrysts, and (**d**) Kherwa basalt showing Pl and Cpx microphenocrysts surrounded by a fine-grained groundmass comprising Cpx, Pl, ilmenite (Ilm), and hematite (Hem).

The composition of the phenocrysts and microphenocrysts are summarized in Table 2 and presented in detail in Table S1. Clinopyroxene does not show compositional zoning with the exception of two samples from Dariachak in the northwest. It is dominantly augite, and its composition range in samples from the northeast, northwest and central sectors are $En_{45–56}Fs_{8–21}Wo_{29–39}$, $En_{48–54}Fs_{9–15}Wo_{36–40}$, and $En_{47–54}Fs_{7–19}Wo3_{1–41}$, respectively (Table 2). Augite from the central sector are slightly higher in the wollastonite component compared to the northeastern sector (Figure 5a). The latter is also slightly higher in jadeite, though the jadeite and aegirine contents are low ($\leq$2 mole%, Figure 5b). The composition range of pigeonite is $En_{42–74}Fs_{18–46}Wo_{4–12}$ considering all samples.

Plagioclase is mildly zoned with higher albite contents near the rim, especially in samples from the northwest and central sectors (Figure 5c). Its composition ranges from labradorite to bytownite, and rarely andesine (Table 2, $An_{57–82}Ab_{18–42}Or_{0–4}$, $An_{45–71}Ab_{28–54}Or_{0–1}$, and $An_{51–81}Ab_{19–48}Or_{0–1}$, in the northeast, northwest, and central sectors).

The olivine in a Tinpahar (northeast) sample has a composition of $Fo_{71–76}Fa_{24–30}$. The composition ranges of ilmenite and hematite are $Hem_{0–7}Ilm_{85–97}Pph_1Gk_{1–9}$, and $Hem_{43–92}Ilm_{6–53}Pph_{0–12}Gk_{0–6}$, respectively (Table 2, Figure 5d), considering all samples.

Table 2. Composition range of minerals in the Rajmahal basalts.

A. Augite and Plagioclase						
Sector	**Northeast**		**Northwest**		**Central**	
	core	rim	core	rim	core	rim
Augite						
En	45–56	49–52	48–54	49–50	47–54	49–54
Fs	8–21	10–15	9–12	11–15	7–15	7–19
Wo	29–39	34–39	36–40	37–40	36–41	31–41
Mg#	68–87	76–83	80–85	77–82	76–89	73–88
Plagioclase						
An	57–82	58–75	61–71	45–66	60–81	51–77
Ab	18–42	25–41	28–38	34–54	19–39	22–48
Or	0–4	0–3	0–1	0–1	0–1	0–1

B. Other minerals						
All sectors						
	Ilmenite	Hematite		Pigeonite		Olivine
Hem	0–7	43–92	En	42–74	Fo	71–76
Ilm	85–97	6–53	Fs	18–46	Fa	24–30
Pph	1–1	0–12	Wo	4–12		
Gk	1–9	0–6	Mg#	48–81		

En—enstatite, Fs—ferrosilite, Wo—wollastonite, Mg# = 100.molar Mg/(Mg + Fe), An—anorthite, Ab—albite, Or—orthoclase, Hem—hematite, Ilm—ilmenite, Pph—pyrophanite, Gk—geikelite, Fo—forsterite, Fa—fayalite.

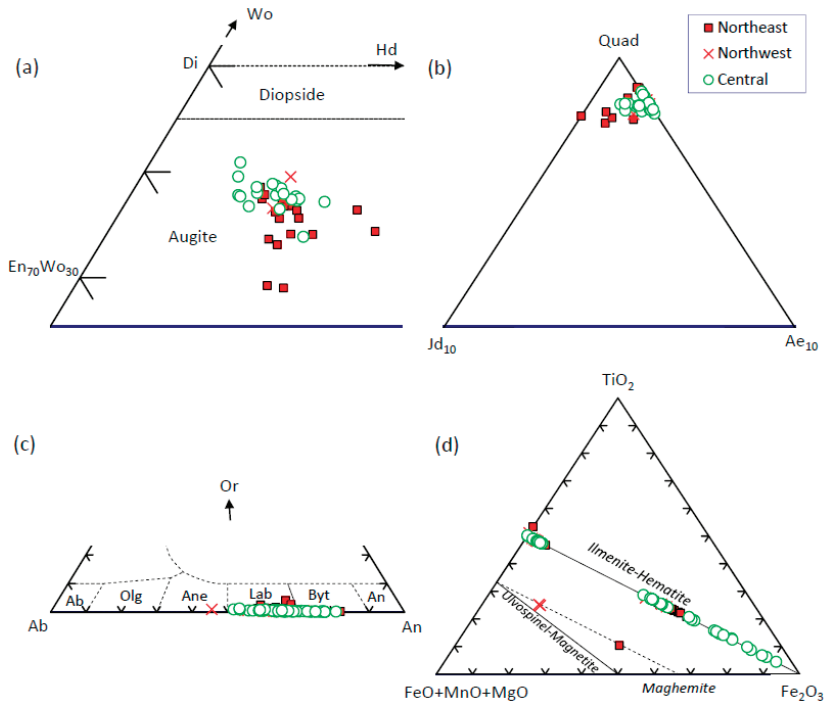

Figure 5. Chemical composition of minerals in the Rajmahal basalts from the northeast, northwest, and central sectors (see Figures S1–S3 for further details). (**a**,**b**) Average augite (En—enstatite, Di—diopside, Hd—hedenbergite, Wo—wollastonite, Quad—quadrilateral components, Jd—jadeite, and Ae—aegirine) plotted according to [53]. (**c**) Plagioclase (Ab—albite, Olg—oligoclase, Ane—andesine, Lab—labradorite, Byt—bytownite, An—anorthite, Or—orthoclase). (**d**) Oxides.

6. Thermobarometry

The pressure-temperature (P-T) of crystallization of the Rajmahal basalts were calculated using clinopyroxene compositions, clinopyroxene-bulk equilibria, and whole-rock (bulk) compositions.

6.1. Clinopyroxene Thermobarometry

This method uses only clinopyroxene composition to determine the P-T of crystallization. The T-dependent barometric expression (Equation (32a)) and P-dependent thermometric expression (Equation (32d)) of [54] were solved simultaneously to obtain P-T. These equations are based on multiple regression of clinopyroxene compositions (854 analyses for (32a), 910 analyses for (32d)) obtained from anhydrous partial melting experiments on basalts in the P-T range of 1 bar–75 kbar/800–2200 °C. The equations use the enstatite-ferrosilite and diopside-hedenbergite components and cation proportions of clinopyroxene calculated on the basis of six oxygen atoms. The quoted uncertainties are ±3.1 kbar and ±58 °C for clinopyroxene crystallizing from anhydrous melts [54]. In addition, the P-T conditions were also calculated with the random forest machine learning-based algorithms of [55,56] that provided independent estimates of the uncertainties. The two studies [55,56] use the same methodology, but [56] uses an expanded dataset that includes alkalic liquids. These thermobarometers are also based on clinopyroxene compositions obtained from partial melting experiments on basalts that cover a P-T range of 0.002–30 kbar/750–1250 °C.

Using the augite compositions in Table S1 and Equations (32a) and (32d) of [54], the P-T of clinopyroxene crystallization are 1 bar–5.4 kbar (±3.1 kbar) and 1134–1195 °C (±58 °C) (Table 3, negative pressure values >−2 kbar are considered as 1 bar). Samples from Tinpahar and Moti Jharna in the northeastern sector show the highest average pressures of 5.4 kbar and 3.2 kbar, respectively. All other samples show pressures of <2 kbar. The method of [55] also yields low pressures (2.0–4.6 kbar, highest pressures at Tinpahar and Moti Jharna) but with lower uncertainties (±0.6–2.6 kbar) compared to [54] (Table 3). With the method of [56], the pressures are 0.0–1.8 kbar with uncertainties of less than ±4.5 kbar. The temperature estimates are similar with the methods of [55] (1093–1151 °C, ±19–62 °C) and [56] (1119–1157 °C, ±21–48 °C) compared to [54] (Table 3).

6.2. Clinopyroxene-Bulk Thermobarometry

The P-T conditions of crystallization were determined with the clinopyroxene-anhydrous liquid thermobarometer (Equations (P1) and (T1)) of [57] with quoted uncertainties of ±1.4 kbar and ±27 °C. The Cpx-bulk equilibrium was assessed in terms of the Fe^{2+}-Mg distribution, the equilibrium value of the Cpx-bulk $K_D(Fe^{2+}\text{-Mg})$ being 0.28 ± 0.08 [54]. A knowledge of the bulk FeO content is necessary to apply this thermobarometer. The oxidation state of the bulk can be determined from the olivine-liquid [58] and magnetite-ilmenite [59] equilibria. Equation (8) of [58] provides a method to calculate the bulk $Fe^{3+}/\Sigma Fe$ ratio from the olivine-melt Fe^{T}-Mg distribution (where Fe^{T} is total Fe) in samples containing equilibrium olivine. The bulk $Fe^{3+}/\Sigma Fe$ ratio can also be calculated from the magnetite-ilmenite equilibrium that yields oxygen fugacity [59], which can be converted to $Fe^{3+}/\Sigma Fe$ using Equation (6b) of [60]. Unfortunately, bulk composition of the olivine-bearing sample RB88-39 is not available, and magnetite is absent in all of the samples analyzed. So, the bulk $Fe^{3+}/\Sigma Fe$ ratio could not be determined, and assumed values were used to assess Cpx-bulk equilibrium.

Table 3. Clinopyroxene thermobarometry of the Rajmahal basalts.

Location	Sample	P kbar	T °C	P kbar Avg	T °C Avg	P kbar	T °C	P kbar	T °C
		Equations (32a) and (32d) [54]				[55]		[56]	
Northeast sector									
Sahibganj	RB88-12	0.3	1156	0.3	1156	2.0 ± 1.0	1138 ± 44	0.0 ± 0.0	1139 ± 21
Moti Jharna	RB88-19	3.2	1180	3.2	1180	4.6 ± 2.0	1151 ± 19	0.0 ± 2.3	1157 ± 25
Maharajpur	RB88-16	0.001	1119	1.6	1145	2.0 ± 0.7	1133 ± 46	0.0 ± 0.1	1125 ± 23
	RB88-18	3.2	1172						
Taljhari	EB89-154	0.001	1147	0.001	1147	2.0 ± 0.5	1137 ± 52	0.0 ± 0.2	1141 ± 23
	RB88-24	0.001	1147						
Tinpahar	RB88-31	4.6	1209	5.4	1195	4.5 ± 2.2	1127 ± 43	1.8 ± 4.5	1147 ± 33
	RB88-32	4.4	1196						
	RB88-39	7.5	1218						
	RB88-35	5.0	1156						
Kherwa	EB89-112	0.001	1111	1.3	1136	3.7 ± 2.1	1099 ± 62	0.0 ± 0.7	1119 ± 43
	EB89-117	2.7	1160						
Berhait	EB89-121	6.6	1213	1.8	1160	3.3 ± 2.6	1148 ± 32	0.4 ± 1.0	1134 ± 34
	EB89-123	0.001	1127						
	EB89-127	0.1	1147						
	EB89-128	0.5	1152						
Northwest sector									
Dariachak	DAR-2GB	2.0	1170	0.7	1134	2.0 ± 0.8	1093 ± 42	0.1 ± 0.3	1137 ± 28
	DAR-5YL	0.001	1100						
	DAR10-90	0.001	1131						
Central sector									
Litipara-Amrapara	LA1	2.2	1160	1.5	1160	2.0 ± 0.6	1137 ± 50	0.0 ± 0.6	1139 ± 29
	LA2	3.0	1177						
	LA4	0.8	1155						
	LA5	0.6	1156						
	LA6	0.8	1154						
Litipara-Simlong	TT1	2.8	1185	1.1	1163	3.1 ± 1.9	1141 ± 32	0.0 ± 0.5	1149 ± 25
	TT2	0.04	1162						
	TT3	1.7	1166						
	TT4	0.001	1138						
Litipara-Hiranpur	LH1	0.1	1155	0.1	1155	4.1 ± 2.6	1150 ± 27	0.0 ± 1.0	1149 ± 28
Amrapara	BL1	2.3	1188	1.9	1182	3.8 ± 2.4	1096 ± 51	0.0 ± 1.2	1152 ± 48
	BL3	1.6	1175						
Kundpahar	KP1	3.6	1192	1.9	1162	2.3 ± 1.1	1123 ± 52	0.0 ± 0.5	1136 ± 27
	KP2	3.3	1190						
	KP3	2.0	1157						
	KP4	0.7	1156						
	KP5	2.5	1161						
	KP6	0.001	1125						
	KP7	1.3	1153						

Assuming a bulk $Fe^{3+}/\Sigma Fe$ ratio of 0.1, augite in samples LA2, TT3 and LH1 shows equilibrium Cpx-bulk Fe^{2+}-Mg distribution ($K_D(Fe^{2+}$-Mg) values between 0.29 and 0.32, Table 4). Assuming bulk $Fe^{3+}/\Sigma Fe$ ratios of zero and 0.2 change the Cpx-bulk $K_D(Fe^{2+}$-Mg) to 0.26–0.29 and 0.32–0.35, respectively, which are also within the variability of the equilibrium value [54]. Hence, P-T of the abovementioned samples were calculated using the clinopyroxene-liquid equilibrium with the formulations of [57]. Using the augite compositions in Table S1 and bulk compositions in [10], Equations (P1) and (T1) of [57] yielded P-T of 1 bar–4.6 kbar (±1.4 kbar) and 1137–1185 °C (±27 °C) for samples LA2, TT3, and LH1. These P-T results are similar to the P-T obtained from augite composition for the same samples (0.1–3.0 kbar, 1155–1177 °C) with the formulations of [54] (Table 4).

Table 4. Clinopyroxene-bulk and whole rock thermobarometry of the Rajmahal basalts.

Location	Sample	P (kbar)	T (°C)	K_D [a]	Pl (%) [b]
Equations (P1) and (T1) [57]**:**					
Central sector					
Litipara-Amrapara	LA2	4.6	1185	0.29	
Litipara-Simlong	TT3	1.6	1166	0.32	
Litipara-Hiranpur	LH1	0.001	1137	0.31	
[61]**, and Equation (16)** [54]**:**					
Northeast sector					
Moti Jharna	88-21	4	1188		4
Tinpahar	88-30	2	1168		7
	88-42	3.5	1183		4
Northwest sector					
S of Dariachak [c]	RJ1-25-1	1	1168		6
S of Dariachak [d]	RJ1-26-7	0.001	1147		4
Central sector					
Litipara-Simlong	TT3	2	1169		5
Litipara-Hiranpur	LH1	0.001	1158		10.5
W of Pakur [e]	RJ1-30-3	0.001	1158		3.5
	RJ1-30-4	0.001	1156		3.5
Kundpahar	KP6	0.001	1157		10

[a] Fe^{2+}-Mg exchange coefficient for Cpx-bulk, [b] amount of plagioclase subtracted from bulk to determine melt composition, [c] Lalmatia, [d] Bejam Pahar, [e] Dhanbad village.

6.3. Whole Rock Thermobarometry

This method uses the predicted pressure-dependent fractionation path of a basalt to determine its pressure of crystallization. During fractionation, the basaltic melt is in equilibrium with one or several different mineral phases. At a multiple saturation point (MSP), the melt is in equilibrium with multiple phases. Parameterized expressions of experimental data [61] predict the composition of a basaltic liquid at its plagioclase lherzolite (Ol + Pl + Cpx + Opx) multiple saturation point (PL-MSP) as a function of pressure and bulk composition. The PL-MSP provides an anchor point for the fractional crystallization path that is defined by the olivine control line, and the Ol-Pl and Ol-Pl-Cpx cotectic boundaries whose intersection is determined by the method of [62]. The bulk composition of the sample and its PL-MSPs at different pressures are plotted in the Ol-Pl-Cpx (from Qz) and Ol-Cpx-Qz (from Pl) pseudoternary projections of the basalt tetrahedron according to the methods of [63,64]. If the sample shows displacement from its fractionation path, it contains excess crystal accumulation. Subtracting the excess crystals from the bulk results in a corrected bulk composition, and the sample plots on its fractionation path at a specific pressure. The corrected bulk composition represents the composition of the melt derived directly from its primitive parental magma by fractional crystallization at the specific pressure. The estimated pressure is accurate within ±2.5 kbar [61]. Using the corrected composition of the melt, its temperature is then calculated with Equation (16) of [54], which has a quoted uncertainty of ±27 °C.

The bulk compositions of the uncontaminated Rajmahal Group I basalts (excluding basaltic andesites) [10,21] and their PL-MSPs at different pressures were plotted in the Ol-Pl-Cpx (from Qz) and Ol-Cpx-Qz (from Pl) pseudoternary projections of the basalt tetrahedron (Figure 6). The basalts show displacement from their projected PL-MSPs toward the plagioclase apex in the Ol-Pl-Cpx diagram (Figure 6a), indicating cumulus enrichment of plagioclase. Subtracting 4%–10% equilibrium plagioclase from the bulk results in corrected bulk compositions of the samples that plot on their PL-MSPs between 1 bar and 4 kbar pressures in Figure 6a. Note that the Ol + Pl + Cpx cotectic boundaries shown in the Ol-Cpx-Qz diagram (Figure 6b) approximately project to the same point as the PL-MSP in Figure 6a, and it is not possible to determine whether a sample plots on its Ol + Pl + Cpx cotectic or on its PL-MSP only from Figure 6a. However, Figure 6b clearly shows that the samples plot on their Ol + Pl + Cpx cotectics at 1 bar–4 kbar (±2.5 kbar)

pressures. Note that because Figure 6b is projected from plagioclase, subtracting plagioclase from the bulk has no effect on the sample's position. The corrected bulk compositions are the compositions of the Ol-Pl-Cpx saturated melts that are derived directly from their primitive parental magmas through fractional crystallization. The temperatures of these melts calculated with Equation (16) of [54] are 1147–1188 °C (±27 °C). Notably, the calculated P-T of samples TT3, LH1, and KP6 (1 bar–2 kbar, 1157–1169 °C) are similar to the P-T determined from augite composition (1 bar–1.7 kbar, 1125–1166 °C) with the formulations of [54] (Table 4).

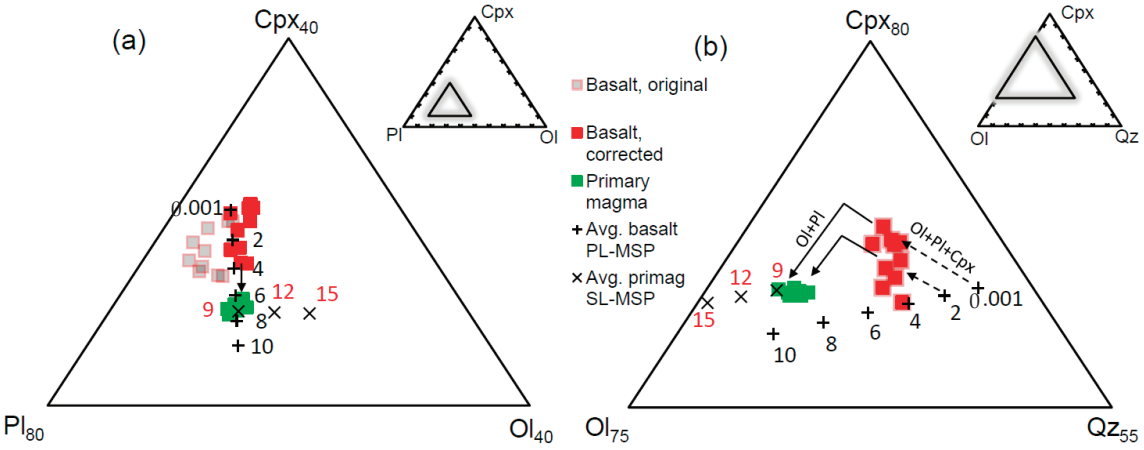

Figure 6. Portions of the pseudoternary projections of the basalt tetrahedron: (**a**) Ol-Pl-Cpx from Qz, and (**b**) Ol-Cpx-Qz from Pl (after [63,64]) showing the compositions of the Rajmahal Group I basalts and their corresponding melts (determined by subtracting plagioclase). For clarity, only the multiple saturation points for plagioclase lherzolite (PL-MSP at 1 bar and 2–10 kbar with 2 kbar intervals, after [59]) of the average basalt and spinel lherzolite (SL-MSP at 9–15 kbar with 3 kbar intervals, after [63]) of the average primary magma are shown. The solid lines with arrowheads represent examples of model reverse fractionation paths along the Ol + Pl + Cpx and Ol + Pl cotectic boundaries, and the dashed lines with arrowheads in (**b**) represent part of the inferred Ol + Pl + Cpx cotectic boundary at 1 bar and 2 kbar.

7. Primary Magma Modeling

Modeling was performed only on the Rajmahal Group I basalts [10,21], whose isotopic compositions indicate that they are uncontaminated by continental crust [10,18,21,26,31]. Because these basalts crystallized at pressures of ≤5 kbar, they evolved by fractional crystallization of olivine, followed by Ol + Pl and Ol + Pl + Cpx from their primitive parental magmas [61,65]. Hence, their primary magmas were modeled through low-pressure reverse fractional crystallization involving addition of Ol + Pl + Cpx (stage 1) and Ol + Pl (stage 2, the olivine-only stage was not necessary) to the bulk [66–69] (Figure 6). The phase assemblages were added in small steps (step size < 0.5%) with phase proportions and compositions shown in Table 5 and Table S2. Equilibrium Fe^{2+}-Mg distribution between olivine-liquid ($K_D(Fe^{2+}$-Mg) = 0.3, [70]) and Cpx-liquid ($K_D(Fe^{2+}$-Mg) = 0.25), and equilibrium Ca-Na distribution between plagioclase-liquid [65] were maintained at each step of the calculation. In the Ol-Cpx-Qz projection (Figure 6b), the melt moved toward the Ol-Cpx sidebar in stage 1, and toward the olivine apex in stage 2. In the Ol-Pl-Cpx projection (Figure 6a), the melt remained approximately stationary in stage 1, and moved toward the Ol-Pl sidebar in stage 2. The phase proportions and the switching point between stage 1 and stage 2 with constraints from [62] were adjusted so that the melt moved toward its spinel lherzolite MSP (SL-MSP) at high pressures predicted by parameterized expressions of experimental data [66] (uncertainties in P-T at the SL-MSP: ±1.5 kbar, ±11 °C). At the end of the calculation, the melt was in equilibrium with mantle olivine ($Fo_{90–91.5}$, for different samples), and it plotted exactly on its SL-MSP at a specific high pressure (Figure 6). The result was unique, as any deviation from the

phase proportions and switching point between stages 1–2 would result in a melt not on its lherzolite MSP at any pressure, though it may show equilibrium with mantle olivine. In stage 1, MgO, Ni, CaO, and Al_2O_3 increased, and SiO_2, FeO^T (total FeO), and Na_2O decreased (Figure 7). In stage 2, the oxides and Ni variations followed the same trends except for CaO, which decreased slightly (Figure 7).

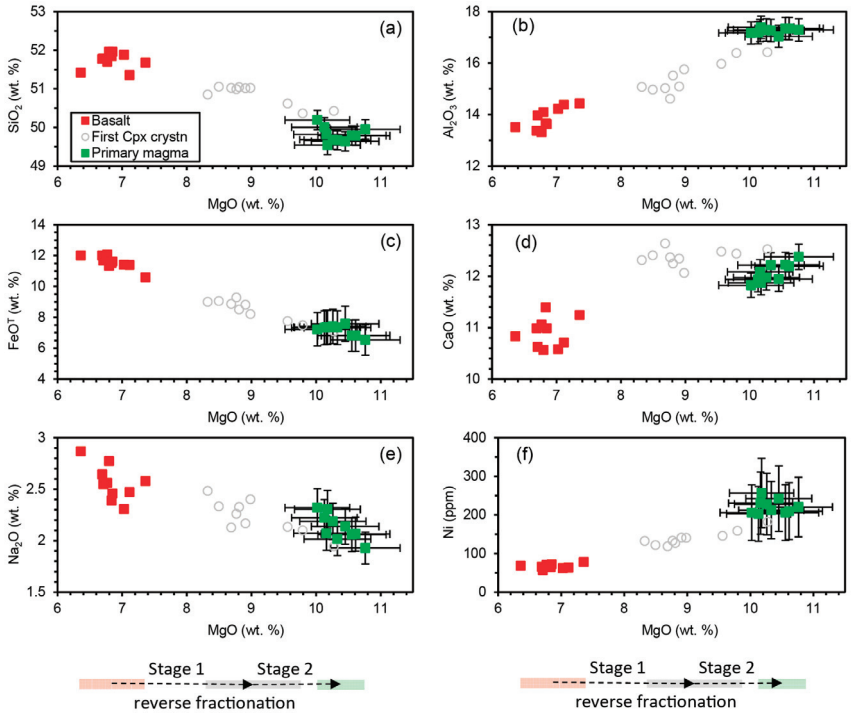

Figure 7. Bivariate plots showing the variation of the major oxides (**a**–**e**) and Ni with MgO (**f**) for the Rajmahal Group I basalts (corrected melt compositions) and their primary magmas. The compositions of melt in which clinopyroxene first crystallizes (end of stage 1) are also plotted. The direction of reverse fractionation with increasing MgO is shown by arrows at the bottom.

Table 5. P-T of crystallization and last equilibration of primary magma with mantle for the Rajmahal Group I basalts.

	Crystallization		Stage 1 [a]				Stage 2 [a]			Primary Magma [b]	
	P (kbar)	T (°C)	F%	Ol	Pl	Cpx	F%	Ol	Pl	P (kbar)	T (°C)
Northeast sector											
88-21	4	1188	60.7	13.7	52.4	33.9	12.2	28.6	71.4	9	1286
88-30	2	1168	60.3	13.0	52.6	34.4	19.8	30.2	69.8	9	1284
88-42	3.5	1183	57.8	13.0	53.4	33.6	14.8	30.2	69.8	9	1284
Northwest sector											
RJ1-25-1	1	1168	46.8	12.2	53.1	34.7	22.9	30.2	69.8	9	1280
RJ1-26-7	0.001	1147	57.8	10.9	52.6	36.4	30.3	30.2	69.8	9	1280
Central sector											
TT3	2	1169	53.8	12.5	53.6	33.9	19.8	29.4	70.6	8	1268
LH1	0.001	1158	54.2	13.0	51.9	35.2	26.0	28.6	71.4	8.5	1275
RJ1-30-3	0.001	1158	55.6	12.1	50.2	37.7	29.6	30.2	69.8	9	1281
RJ1-30-4	0.001	1156	56.5	10.9	52.6	36.4	29.6	30.2	69.8	9	1281
KP6	0.001	1157	54.2	11.8	51.6	36.6	28.1	30.2	69.8	9	1282

[a] Percent fractionation and proportions of phases added. [b] Primary magmas (Mg# 73–76) are equilibrated with olivine $Fo_{90–91.5}$, Cpx Mg# 91.5–93, and Opx Mg# 91–92.

The calculations show that the basalts are the products of 47%–61% fractionation of their primary magmas, and the primary magmas were last equilibrated with mantle at a pressure of ~9 kbar and temperatures of 1275–1286 °C (excluding one sample, Table 5 and Table S2). The uncertainties in these results arise from the uncertainties in mineral-melt $K_D(Fe^{2+}$-Mg) and the mantle olivine composition that may vary between Fo_{88} and Fo_{92}. Assuming a ±10% uncertainty in the Ol-melt and Cpx-melt $K_D(Fe^{2+}$-Mg), and $Fo_{88–92}$ mantle olivine compositions, the uncertainties in the MgO and FeO contents of the model primary magma are about ±6%, and the uncertainties in P-T are ±15% and ±3% (e.g., 9.0 ± 1.4 kbar, 1280 ± 40 °C). The compositional uncertainties are depicted as error bars in Figure 7.

8. Discussion

The lowermost level (level 1, [3]) of the Rajmahal plumbing system is poorly constrained. It has been suggested on the basis of isotopic data that the Rajmahal basalts originated by melting of a MORB-type mantle source with only heat supplied by the Kerguelen Plume [21,31]. According to [21], viscous drag in a steady-state Kerguelen Plume conduit at the rifted eastern Indian margin may have helped in asthenospheric upwelling and melting of the MORB-type mantle. From inversion of rare-earth element data, [21] calculated a mantle potential temperature of ~1350 °C for the origin of the Rajmahal and Sylhet magmas, indicating a moderately hot mantle at the northern edge of the Kerguelen Plume. The P-T of last equilibration of the Rajmahal primary magmas with the mantle (~9 kbar and ~1280 °C, potential temperatures up to ~130 °C higher [69]) calculated in this study are consistent with the results of [21] and melting in the spinel lherzolite field concluded by [26]. However, [25,26] presented trace element and isotopic evidence to show that the source of the least contaminated Rajmahal and Sylhet basalts was the primitive Kerguelen Plume, as previously suggested by [10], and a MORB-type source was not involved. Using Nd-Sr isotopic data ($\varepsilon_{Nd(I)}$ between −8.6 and +3.2, $^{87}Sr/^{86}Sr_{(I)}$ between 0.70347 and 0.70965), [25,26] also modeled the origin of the contaminated Rajmahal–Sylhet basalts by mixing between lherzolite-derived melts and the Eastern Ghats granulites, and speculated that the basalts were contaminated through interaction and erosion of the Indian lithospheric root by the Kerguelen Plume. Considering that the axis of the Kerguelen Plume was south of the Rajmahal–Sylhet eruption site [21], the buoyant plume material may have moved laterally and upward through sublithospheric corridors [71–73] to accumulate and interact with the eastern Indian lithosphere.

Geophysical studies and primary magma modeling provide clues to the structure of levels 2 and 3 [3] of the Rajmahal plumbing system. Bouguer gravity data indicate the presence of a broad and elongated positive gravity anomaly with its axis along the western boundary of the Rajmahal Traps [35,36] (Figure 2). Three-dimensional gravity modeling and integration with seismic data delineated a high-density (3 g/cm^3) layer, 16–18 km thick under the Rajmahal Traps and ~12 km thick in the region to the south, above the 36–38 km deep regional Moho [36]. This indicates that the high-density layer under Rajmahal Traps is at lower crustal depths below an upwarped Moho that may be at a depth of ~20 km. The Rajmahal primary magmas were last in equilibrium with the mantle at a pressure of ~9 kbar that corresponds with a depth of ~33 km considering an average crustal density of 2.8 g/cm^3. Thus, the Rajmahal primary magmas were last in equilibrium with the mantle within the high-density layer, which probably represents anomalous mantle within the lower crust.

The level 3 [3] of the Rajmahal plumbing system is characterized by the anomalous mantle at lower crustal depths, dikes and trans-crustal fractures/faults, and upper crustal magma staging chambers. Dikes are rare in the main Rajmahal outcrop [23,40], though NW to NNW-trending basaltic andesite dikes of similar age (118–109 Ma) to the Rajmahal basalts are common in the Raniganj–Giridih–Koderma region to the southwest and west of the Rajmahal outcrop [28]. The north–south oriented Eastern Indian Tectonic Zone (EITZ) is a trans-crustal orogen, as indicated by the high metamorphic pressures (~10 kbar)

of the granulites at the western contact of the Rajmahal Traps [46,48]. The subvertical faults associated with the EITZ, the Rajmahal and Saithia–Brahmani boundary faults along the eastern and western margins of the Rajmahal outcrop (Figure 2), and the faults in the basement of the Bengal Basin adjacent to the outcrop [27,35,49] may have acted as pathways for upward ascent of the Rajmahal primary magmas [74,75]. Thermobarometry in this study shows that the Rajmahal magmas crystallized in the upper crust. Robust estimates of the P-T conditions for magma crystallization by three different methods are between 1 bar and ~5 kbar, and 1093–1195 °C (Tables 3 and 4), indicating a maximum depth of ~19 km considering an upper crustal density of 2.7 g/cm^3. Crystallization probably occurred in small, upper crustal magma chambers distributed throughout the Rajmahal province [8,9]. The Rajmahal magmas differentiated through fractional crystallization and upper crustal assimilation [32] in the small, near-surface magma staging chambers before erupting on the surface.

Based on plate tectonic reconstructions [76], and analogy with basin evolution at the southwest Australian rifted margin [21,77] concluded that rifting associated with the breakup of Gondwana at the eastern Indian margin preceded or occurred synchronously with the eruption of the Rajmahal–Sylhet basalts. The recently dated 118–109 Ma old dikes of the Raniganj–Giridih–Koderma area [28] indicate that dike intrusion was synchronous with the emplacement of the Rajmahal Traps, and possibly occurred by exploiting fractures created by Gondwana breakup. Thus, plate tectonics may have played an important role in shaping the structure of the Rajmahal plumbing system [4,5].

9. Conclusions

Thermobarometry shows that the Rajmahal basalts crystallized in the upper crust (P-T of $\leq$5 kbar and 1093–1195 °C), and the Rajmahal primary magmas last equilibrated with the mantle near the Moho (P-T of ~9 kbar and ~1280 °C). A high-density layer below an upwarped Moho previously discovered through modeling of gravity data is probably anomalous mantle at shallow, lower crustal depths. The P-T results of this study complements the results of gravity modeling and provides a clearer picture of the upper levels of the Rajmahal plumbing system. It is likely that the mantle-derived primary magmas accumulated below the Moho and were subsequently transported via trans-crustal faults/fractures to the upper crust where the magma evolved by fractional crystallization in small staging chambers before erupting on the surface.

Supplementary Materials: The following supporting information can be downloaded at: https://www.mdpi.com/article/10.3390/min13030426/s1, Table S1. Chemical composition of minerals in the Rajmahal basalts; Table S2. Bulk composition of the Rajmahal Group I basalts, their primary magmas, and P-T of equilibration. Figure S1. (a) Core and (b) rim compositions of augite in the Rajmahal basalts (En—enstatite, Di—diopside, Hd—hedenbergite, Wo—wollastonite, Quad—quadrilateral components, Jd—jadeite, and Ae—aegirine) plotted according to [53]. Figure S2. (a) Core and (b) rim compositions of plagioclase in the Rajmahal basalts (Ab—albite, An—anorthite, Or—orthoclase). Figure S3. Chemical composition of Fe-Ti oxides in the Rajmahal basalts.

Author Contributions: Conceptualization, N.C.; methodology, N.C.; validation, N.C. and N.C.G.; formal analysis, N.C.; investigation, N.C. and N.C.G.; resources, N.C. and N.C.G.; data curation, N.C.; writing—original draft preparation, N.C.; writing—review and editing, N.C. and N.C.G.; visualization, N.C.; supervision, N.C. and N.C.G. All authors have read and agreed to the published version of the manuscript.

Funding: This research received no external funding.

Data Availability Statement: All data are included in the main text and online Supplementary Materials.

Acknowledgments: We are grateful for the constructive comments of two anonymous reviewers during the peer review process that substantially improved the presentation of the manuscript.

Conflicts of Interest: The authors declare no conflict of interest.

References

1. Bryan, S.E.; Ukstins Peate, I.; Peate, D.W.; Self, S.; Jerram, D.A.; Mawby, M.R.; Marsh, J.S.; Miller, J.A. The largest volcanic eruptions on Earth. *Earth Sci. Rev.* **2010**, *102*, 207–229. [CrossRef]
2. Burchardt, S. (Ed.) Introduction to volcanic and igneous plumbing systems—Developing a discipline and common concepts. In *Volcanic and Igneous Plumbing Systems: Understanding Magma Transport, Storage, and Evolution in the Earth's Crust*; Elsevier: Amsterdam, The Netherlands, 2018; pp. 1–12.
3. Ernst, R.E.; Liikane, D.A.; Jowitt, S.M.; Buchan, K.L.; Blanchard, J.A. A new plumbing system framework for mantle plume-related continental Large Igneous Provinces and their mafic-ultramafic intrusions. *J. Volcanol. Geotherm. Res.* **2019**, *384*, 75–84. [CrossRef]
4. Tibaldi, A. Structure of volcano plumbing systems: A review of multi-parametric effects. *J. Volcanol. Geotherm. Res.* **2015**, *298*, 85–135. [CrossRef]
5. Van Wyk de Vries, B.; van Wyk de Vries, M. Tectonics and volcanic and igneous plumbing systems. In *Volcanic and Igneous Plumbing Systems: Understanding Magma Transport, Storage, and Evolution in the Earth's Crust*; Burchardt, S., Ed.; Elsevier: Amsterdam, The Netherlands, 2018; pp. 167–189.
6. Burchardt, S.; Walter, T.R.; Tuffen, H. Growth of a volcanic edifice through plumbing system processes—Volcanic rift zones, magmatic sheet-intrusion swarms and long lived conduits. In *Volcanic and Igneous Plumbing Systems: Understanding Magma Transport, Storage, and Evolution in the Earth's Crust*; Burchardt, S., Ed.; Elsevier: Amsterdam, The Netherlands, 2018; pp. 89–112.
7. Galland, O.; Bertelsen, H.S.; Eide, C.H.; Guldstrand, F.; Haug, Ø.T.; Leanza, H.A.; Mair, K.; Palma, O.; Planke, S.; Rabbel, O.; et al. Storage and transport of magma in the layered crust—Formation of sills and related flat-lying intrusions. In *Volcanic and Igneous Plumbing Systems: Understanding Magma Transport, Storage, and Evolution in the Earth's Crust*; Burchardt, S., Ed.; Elsevier: Amsterdam, The Netherlands, 2018; pp. 113–138.
8. Mittal, T.; Richards, M.A. The magmatic architecture of continental flood basalts: 2. A new conceptual model. *J. Geophys. Res. Solid Earth* **2021**, *126*, e2021JB021807. [CrossRef]
9. Mittal, T.; Richards, M.A.; Fendley, I.M. The magmatic architecture of continental flood basalts 1: Observations from the Deccan Traps. *J. Geophys. Res. Solid Earth* **2021**, *126*, e2021JB021808. [CrossRef]
10. Storey, M.; Kent, R.W.; Saunders, A.D.; Hergt, J.; Salters, V.J.M.; Whitechurch, H.; Sevigny, J.H.; Thirlwall, N.F.; Leat, P.; Ghose, N.C.; et al. Lower Cretaceous rocks on continental margins and their relationship to the Kerguelen plateau. *Proc. Ocean Drill. Prog. Sci. Res.* **1992**, *120*, 33–53.
11. Mahoney, J.J.; Jones, W.B.; Frey, F.A.; Salters, V.J.M.; Pyle, D.G.; Davies, H.L. Geochemical characteristics of lavas from Broken Ridge, the Naturaliste Plateau and southernmost Kerguelen Plateau: Cretaceous plateau volcanism in the southeast Indian Ocean. *Chem. Geol.* **1995**, *120*, 315–345. [CrossRef]
12. Frey, F.A.; Coffin, M.F.; Wallace, P.J.; Weis, D.; Zhao, X.; Wise, S.W. Origin and evolution of a submarine large igneous province: The Kerguelen Plateau and Broken Ridge, southern Indian Ocean. *Earth Planet. Sci. Lett.* **2000**, *176*, 73–89. [CrossRef]
13. Frey, F.A.; McNaughton, N.J.; Nelson, D.R.; Delaeter, J.R.; Duncan, R.A. Petrogenesis of the Bunbury basalt, western Australia: Interaction between the Kerguelen plume and Gondwana lithosphere? *Earth Planet. Sci. Lett.* **1996**, *144*, 163–183. [CrossRef]
14. Weis, D.; Frey, F.A. Isotope geochemistry of Ninetyeast Ridge basement basalts: Sr, Nd and Pb evidence for the involvement of the Kerguelen hotspot. *Proc. Ocean Drill. Prog. Sci. Res.* **1991**, *121*, 591–610.
15. Coffin, M.F.; Pringle, M.S.; Duncan, R.A.; Gladczenko, T.P.; Storey, R.D.; Müller, R.D.; Gahagan, L.A. Kerguelen hotspot magma output since 130 Ma. *J. Petrol.* **2002**, *43*, 1121–1140. [CrossRef]
16. Srivastava, R.K. Early Cretaceous Greater Kerguelen large igneous province and its plumbing systems: A contemplation on concurrent magmatic records of the eastern Indian Shield and adjoining regions. *Geol. J.* **2022**, *57*, 681–693. [CrossRef]
17. Talukdar, S.C.; Murthy, M.V.N. The Sylhet traps, their tectonic history and their bearing on problems of Indian flood basalt provinces. *Bull. Volcanol.* **1970**, *35*, 602–618. [CrossRef]
18. Baksi, A.K. Petrogenesis and timing of volcanism in the Rajmahal flood basalt province, Northern India. *Chem. Geol.* **1995**, *121*, 73–90. [CrossRef]
19. Baksi, A.K.; Barman, T.R.; Paul, D.K.; Ferar, E. Widespread early Cretaceous flood basal volcanism in eastern India: Geochemical data from the Rajmahal-Bengal-Sylhet traps. *Chem. Geol.* **1987**, *63*, 133–141. [CrossRef]
20. Kent, R.W.; Saunders, A.D.; Storey, M.; Ghose, N.C. Petrology of the Early Cretaceous flood basalts and dykes along the rifted volcanic margin of eastern India. *J. Southeast Asian Earth Sci.* **1996**, *13*, 95–111. [CrossRef]
21. Kent, R.W.; Saunders, A.D.; Kempton, P.D.; Ghose, N.C. Rajmahal basalts, Eastern India: Mantle sources and melt distribution at a volcanic rifted margin. In *Large Igneous Provinces: Continental, Oceanic, and Planetary Flood Volcanism*; Mahoney, J.J., Coffin, M.F., Eds.; American Geophysical Union: Washington, DC, USA, 1997; Volume 100, pp. 145–182.
22. Kent, R.W.; Pringle, M.S.; Muller, R.D.; Saunders, A.D.; Ghose, N.C. $^{40}Ar/^{39}Ar$ geochronology of the Rajmahal basalts, India and their relationship to the Kerguelen Plateau. *J. Petrol.* **2002**, *43*, 1141–1153. [CrossRef]
23. Ghose, N.C.; Kent, R.W. The Rajmahal basalts: A review of their geology, composition and petrogenesis. *Geol. Soc. India Mem.* **2003**, *53*, 167–196.
24. Ray, J.S.; Pattanayak, S.K.; Pande, K. Rapid emplacement of the Kerguelen plume-related Sylhet Traps, eastern India: Evidence from 40Ar-39Ar geochronology. *Geophys. Res. Lett.* **2005**, *32*, 1–4. [CrossRef]
25. Ghatak, A.; Basu, A.R. The Sylhet Traps: Vestiges of the Kerguelen plume in northeastern India. Earth Planet. *Sci. Lett.* **2011**, *308*, 52–64.

26. Ghatak, A.; Basu, A.R. Isotopic and trace element geochemistry of alkalic–mafic–ultramafic–carbonatitic complexes and flood basalts in NE India: Origin in a heterogeneous Kerguelen plume. *Geochim. Cosmochim. Acta* **2013**, *115*, 46–72. [CrossRef]
27. Sengupta, S. Geological and geophysical studies in western part of Bengal basin, India. *Amer. Assoc. Petrol. Geol. Bull.* **1966**, *50*, 1001–1017.
28. Srivastava, R.K.; Wang, F.; Shi, W.; Ernst, R.E. Early Cretaceous mafic dykes from the Chhota Nagpur Gneissic Terrane, eastern India: Evidence of multiple magma pulses for the main stage of the Greater Kerguelen mantle plume. *J. Asian Earth Sci.* **2023**, *241*, 105464. [CrossRef]
29. Agrawal, J.K.; Rama, F.A. Chronology of Mesozoic volcanic of India. *Proc. Indian Acad. Sci.* **1976**, *84A*, 157–179. [CrossRef]
30. Acharya, S.K. Chemical Behavior of the Volcanic Rocks of South Rajmahal, Bihar. Ph.D. Thesis, Patna University, Patna, India, 1988.
31. Mahoney, J.J.; Macdougall, J.D.; Lugmair, G.W.; Gopalan, K. Kerguelen hotspot source for Rajmahal and Ninetyeast Ridge? *Nature* **1983**, *303*, 385–389. [CrossRef]
32. Ghose, N.C.; Chatterjee, N.; Windley, B.F. Subaqueous early eruptive phase of the late Aptian Rajmahal volcanism, India: Evidence from volcaniclastic rocks, bentonite, black shales, and oolite. *Geosci. Front.* **2017**, *8*, 809–822. [CrossRef]
33. NGRI. *Gravity Maps of India Scale 1:5,000,000. NGRI/GPH-1 to 5*; National Geophysical Research Institute (NGRI): Hyderabad, India, 1978.
34. Kaila, K.L.; Reddy, P.R.; Mall, D.M.; Venkateswarlu, N.; Krishna, V.G.; Prasad, A.S.S.S.R.S. Crustal structure of the West Bengal basin, India, from deep seismic sounding investigations. *Geophys. J. Int.* **1992**, *111*, 45–66. [CrossRef]
35. Mukhopadhyay, M.; Verma, R.K.; Ashraf, M.H. Gravity field and structures of the Rajmahal Hills: Examples of the Paleo-Mesozoic continental margin in eastern India. *Tectonophysics* **1986**, *131*, 353–367. [CrossRef]
36. Singh, A.P.; Kumar, N.; Singh, B. Magmatic underplating beneath the Rajmahal Trap: Gravity signature and derived 3D configuration. *Proc. Indian Acad. Sci.* **2004**, *113*, 759–769. [CrossRef]
37. Ghose, N.C. Geology, tectonics and evolution of the Chhotanagpur granite gneiss complex, eastern India. In *Recent Research in Geology 10*; Hindustan Publish. Co.: Delhi, India, 1983; pp. 211–247.
38. Chatterjee, N.; Ghose, N.C. Extensive Early Neoproterozoic high-grade metamorphism in north Chotanagpur Gneissic Complex of the Central Indian Tectonic Zone. *Gond. Res.* **2011**, *20*, 362–379. [CrossRef]
39. Raja Rao, R.C.S.; Purushottam, A. Pitchstone flows in the Rajmahal Hills, Santhal Paraganas, Bihar. *Geol. Surv. India Rec.* **1963**, *91*, 341–348.
40. Sarbadhikari, T.K. Petrology of the northeastern portion of the Rajmahal Traps. *Quar. J. Geol. Min. Met. Soc. India* **1968**, *60*, 151–171.
41. Ghose, N.C.; Singh, S.P.; Singh, R.N.; Mukherjee, D. Flow stratigraphy of a selected sections of Rajmahal basalts, eastern India. *J. Southeast Asian Earth Sci.* **1996**, *13*, 83–93. [CrossRef]
42. Deshmukh, S.S. Geology of the area around Taljhari and Berhait, Rajmahal hills, Santhal Paraganas, Bihar. *Rep. 22nd Intern. Geol. Cong.* **1964**, *7*, 61–84.
43. Ghose, N.C. Pyroclastic rocks of India in space and time. In *Proceedings of the Indian Geological Congress (IGC)*; Indian Geological Congress: Roorkee, India, 2000.
44. Le Bas, M.J.; Le Maitre, R.W.; Streckeisen, A.; Zanettin, B. A chemical classification of volcanic rocks based on the total alkali-silica diagram. *J. Petrol.* **1986**, *27*, 745–750. [CrossRef]
45. McDonough, W.F.; Sun, S.-S. The composition of the Earth. *Chem. Geol.* **1995**, *120*, 223–253. [CrossRef]
46. Chatterjee, N. An assembly of the Indian Shield at c. 1.0 Ga and shearing at c. 876-784 Ma in Eastern India: Insights from contrasting P-T paths, and burial and exhumation rates of metapelitic granulites. *Precamb. Res.* **2018**, *317*, 117–136. [CrossRef]
47. Chatterjee, N.; Nicolaysen, K. An intercontinental correlation of the mid-Neoproterozoic Eastern Indian Tectonic Zone: Evidence from the gneissic clasts in Elan Bank conglomerate, Kerguelen Plateau. *Contrib. Mineral. Petrol.* **2012**, *163*, 789–806. [CrossRef]
48. Chatterjee, N.; Banerjee, M.; Bhattacharya, A.; Maji, A.K. Monazite chronology, metamorphism–anatexis and tectonic relevance of the mid-Neoproterozoic Eastern Indian Tectonic Zone. *Precamb. Res.* **2010**, *179*, 99–120. [CrossRef]
49. Biswas, S.K. Mesozoic volcanism in the east coast basins of India. *Ind. J. Geol.* **1996**, *68*, 237–254.
50. Desa, M.A.; Ramana, M.V.; Ramprasad, T.; Anuradha, M.; Lall, M.V.; Kumar, B.J.P. Geophysical signatures over and around the northern segment of the 85oE Ridge, Mahanadi offshore, eastern continental margin of India and their tectonic implications. *J. Asian Earth Sci.* **2013**, *73*, 460–472. [CrossRef]
51. Ratheesh-Kumar, R.T.; Windley, B.F.; Sajeev, K. Tectonic inheritance of the Indian Shield: New insights from its elastic thickness structure. *Tectonophysics* **2014**, *615–616*, 40–52. [CrossRef]
52. Armstrong, J.T. CITZAF—A package for correction programs for the quantitative electron microbeam X-ray analysis of thick polished materials, thin-films and particles. *Microbeam Anal.* **1995**, *4*, 177–200.
53. Morimoto, N.; Fabries, J.; Ferguson, A.K.; Ginzburg, I.V.; Ross, M.; Seifert, F.A.; Zussman, L.; Aoki, K.; Gottardi, G. Nomenclature of pyroxenes. *Mineral. Mag.* **1988**, *52*, 535–550. [CrossRef]
54. Putirka, K.D. Thermometers and barometers for volcanic systems. *Rev. Mineral. Geochem. Mineral. Soc. Amer.* **2008**, *69*, 61–120. [CrossRef]
55. Higgins, O.; Sheldrake, T.; Caricchi, L. Machine learning thermobarometry and chemometry using amphibole and clinopyroxene: A window into the roots of an arc volcano (Mount Liamuiga, Saint Kitts). *Contrib. Mineral. Petrol.* **2022**, *177*, 10. [CrossRef]

56. Jorgenson, C.; Higgins, O.; Petrelli, M.; Bégué, F.; Caricchi, L. A machine learning-based approach to clinopyroxene thermobarometry: Model optimization and distribution for use in Earth sciences. *J. Geophys. Res. Solid Earth* **2022**, *127*, e2021JB022904. [CrossRef] [PubMed]
57. Putirka, K.D.; Johnson, M.; Kinzler, R.; Walker, D. Thermobarometry of mafic igneous rocks based on clinopyroxene-liquid equilibria, 0–30 kbar. *Contrib. Mineral. Petrol.* **1996**, *123*, 92–108. [CrossRef]
58. Blundy, J.; Melekhova, E.; Ziberna, L.; Humphreys, M.C.S.; Cerantola, V.; Brooker, R.A.; McCammon, C.A.; Pichavant, M.; Ulmer, P. Effect of redox on Fe-Mg-Mn exchange between olivine and melt and an oxybarometer for basalts. *Contrib. Mineral. Petrol.* **2020**, *175*, 103. [CrossRef]
59. Andersen, D.J.; Lindsley, D.H. Internally consistent solution models for Fe-Mg-Mn-Ti spinels: Fe-Ti oxides. *Amer. Mineral.* **1988**, *73*, 714–726.
60. Putirka, K.D. Rates and styles of planetary cooling on Earth, Moon, Mars, and Vesta, using new models for oxygen fugacity, ferric-ferrous ratios, olivine-liquid Fe-Mg exchange, and mantle potential temperature. *Amer. Mineral.* **2016**, *101*, 819–840. [CrossRef]
61. Kinzler, R.J.; Grove, T.L. Primary magmas of mid-ocean ridge basalts.1. Experiments and methods. *J. Geophys. Res.* **1992**, *97*, 6885–6906. [CrossRef]
62. Yang, H.J.; Kinzler, R.J.; Grove, T.L. Experiments and models of anhydrous, basaltic olivine-plagioclase-augite saturated melts from 0.001 to 10 kbar. *Contrib. Mineral. Petrol.* **1996**, *124*, 1–18. [CrossRef]
63. Tormey, D.R.; Grove, T.L.; Bryan, W.B. Experimental petrology of normal MORB near the Kane Fracture Zone: 22–25° N, mid-Atlantic Ridge. *Contrib. Mineral. Petrol.* **1987**, *96*, 121–139. [CrossRef]
64. Grove, T.L. Corrections to expressions for calculating mineral components in "Origin of calc-alkaline series lavas at Medicine Lake volcano by fractionation, assimilation and mixing" and "Experimental petrology of normal MORB near the Kane Fracture Zone: 22°–25° N, mid-Atlantic ridge". *Contrib. Mineral. Petrol.* **1993**, *114*, 422–424.
65. Grove, T.L.; Kinzler, R.; Bryan, W. Fractionation of mid-ocean ridge basalt (MORB). In *Mantle Flow and Melt Generation at Mid-Ocean Ridges*; Phipps Morgan, J., Blackman, D., Sinton, J., Eds.; Geophysical Monograph 71; American Geophysical Union: Washington, DC, USA, 1992; pp. 281–310.
66. Till, C.B.; Grove, T.L.; Krawczynski, M.J. A melting model for variably metasomatized plagioclase and spinel lherzolite. *J. Geophys. Res.* **2012**, *117*, B06206. [CrossRef]
67. Chatterjee, N.; Sheth, H. Origin of the Powai ankaramite, and the composition, P-T conditions of equilibration and evolution of the primary magmas of the Deccan tholeiites. *Contrib. Mineral. Petrol.* **2015**, *169*, 32. [CrossRef]
68. Till, C.B. A review and update of mantle thermobarometry for primitive arc magmas. *Amer. Mineral.* **2017**, *102*, 931–947.
69. Krein, S.B.; Molitor, Z.J.; Grove, T.L. ReversePetrogen: A Multiphase dry reverse fractional crystallization-mantle melting thermobarometer applied to 13,589 mid-ocean ridge basalt glasses. *J. Geophys. Res. Solid Earth* **2021**, *126*, e2020JB021292.
70. Roeder, P.L.; Emslie, R.F. Olivine liquid equilibrium. Contrib. *Mineral. Petrol.* **1970**, *29*, 275–289. [CrossRef]
71. Thompson, R.N.; Gibson, S.A. Subcontinental mantle plumes, hotspots and preexisting thinspots. *J. Geol. Soc. Lond.* **1991**, *148*, 973–977. [CrossRef]
72. Ebinger, C.J.; Sleep, N.H. Cenozoic magmatism throughout East Africa resulting from impact of a single plume. *Nature* **1998**, *395*, 788–791. [CrossRef]
73. Duggen, S.; Hoernle, K.A.; Hauff, F.; Kluegel, A.; Bouabdellah, M.; Thirlwall, M.F. Flow of Canary mantle plume material through a subcontinental lithospheric corridor beneath Africa to the Mediterranean. *Geology* **2009**, *37*, 283–286. [CrossRef]
74. Begg, G.C.; Hronsky, J.A.M.; Arndt, N.T.; Griffin, W.L.; O'Reilly, S.Y.; Hayward, N. Lithospheric, cratonic, and geodynamic setting of Ni–Cu–PGE sulfide deposits. *Econ. Geol.* **2010**, *105*, 1057–1070. [CrossRef]
75. Begg, G.C.; Hronsky, J.M.A.; Griffin, W.L.; O'Reilly, S.Y. Global- to deposit-scale controls on orthomagmatic Ni-Cu(-PGE) and PGE reef ore formation. In *Processes and Ore Deposits of Ultramafic-Mafic Magmas through Space and Time*; Mondal, S., Griffin, W., Eds.; Elsevier: Amsterdam, The Netherlands, 2017.
76. Royer, J.-Y.; Coffin, M.F. Jurassic to Eocene plate tectonic reconstructions in the Kerguelen Plateau region. *Proc. Ocean Drill. Prog. Sci. Res.* **1992**, *120*, 917–928.
77. Marshall, J.F.; Lee, C.S. Basin framework and resource potential of the Abrolhos sub-basin. In *Geophysical Yearbook 1988–1989*; Wolf, K.H., Paine, A.G.L., Eds.; Australian Bureau of Mineral Resources: Canberra, Australia, 1989; pp. 63–67.

minerals

MDPI

Article

Continental Rift Driven by Asthenosphere Flow and Lithosphere Weakening by Flood Basalts: South America and Africa Cenozoic Rifting

Ingo L. Stotz *, Berta Vilacís, Jorge N. Hayek and Hans-Peter Bunge

Department of Earth and Environmental Science, Ludwig-Maximilians-Universität (LMU) München, 80333 Munich, Germany; b.vilacis@lmu.de (B.V.); j.hayek@lmu.de (J.N.H.); bunge@lmu.de (H.-P.B.)
* Correspondence: ingo.stotz@lmu.de

Abstract: Continental rifting is the process by which land masses separate and create new ocean basins. The emplacement of large igneous provinces (LIPs) is thought to have played a key role in (super) continental rifting; however, this relationship remains controversial due to the lack of a clearly established mechanism linking LIP emplacement to continental fragmentation. Here, we show that plume flow links LIP magmatism to continental rifting quantitatively. Our findings are further supported by the sedimentary record, as well as by the mineralogy and petrology of the rocks. This study analyzes the early Cretaceous separation of West Gondwana into South America and Africa. Prior to rifting, Jurassic hiatuses in the stratigraphic record of continental sediments from both continents indicate plume ascent and the resulting dynamic topography. Cretaceous mafic dyke swarms and sill intrusions are products of major magmatic events that coincided with continental rifting, leading to the formation of large igneous provinces in South America and Africa, including the Central Atlantic Magmatic Province, Equatorial Magmatic Province, Paraná–Etendeka, and Karoo. It has been suggested that dyke intrusions may weaken the lithosphere by reducing its mechanical strength, creating structural weaknesses that localize extensional deformation and facilitate rift initiation. The sedimentary analysis and petrological evidence from flood basalt magmas indicate that plumes may have migrated from the depths toward the surface during the Jurassic and erupted during the Cretaceous. It is thought that the resulting fast plume flow, induced by one or more mantle plumes, generated a dynamic force that, in combination with lithospheric weakening from dyke intrusion, eventually rifted the lithosphere of West Gondwana.

Keywords: Poiseuille flow; large igneous provinces; continental rifting; mantle flow; Pangea break-up; mafic dykes

1. Introduction

Early ideas about continental drift that eventually led to the theory of plate tectonics were based on observational evidence. A key observation was the geometric similarity of the east coast of South America and the west coast of Africa e.g., [1–3], suggesting that they were once together as a supercontinent before rifting apart. Later on, several other observations pointed toward the same idea. These were advances in seismology e.g., [4,5], paleomagnetism e.g., [6–8], and sedimentology e.g., [9,10], which led to the theory of plate tectonics [11]. It is now widely accepted that convection in the Earth's mantle provides the forces that drive plate motions see [12]. However, the precise mechanisms governing the

assembly and dispersal of supercontinents remain a fundamental but not well-understood aspect of plate tectonics.

Over the past decade, the asthenosphere has been shown to play a crucial role in linking mantle convection to the surface e.g., [13–15]. Its channelized nature allows it to be modeled analytically within the framework of Poiseuille flow e.g., [14,16–21], which is driven by lateral pressure gradients. Importantly, the Poiseuille flow type explicitly relates vertical plate motion changes to pressure flow variations in the asthenosphere [15,19]. Thus, it relates changes in plate motion (horizontal) to variations in dynamic topography (vertical) in a testable manner, as shown early on for the South Atlantic region i.e., [22]). Poiseuille flow in the asthenosphere can be triggered by subducting slabs, previously called slab suction i.e., [23], or by flow generated by mantle plumes—as previously argued by Morgan [24].

The hypothesis that plumes originating from the deep mantle could drive plate tectonics was first introduced by Morgan [25], who argued that plumes act as a driving force. Further, Morgan and Smith [26] and Morgan et al. [27] argued that plumes can induce sufficient pressure-driven upper-mantle flow to drive the motion of tectonic plates. The validity of this concept is supported by numerical simulations of Pacific plate dynamics e.g., [14] and by analytical models for the Atlantic and Australian regions e.g., [19,20,28]. In addition to affecting horizontal plate motion, plumes also generate prominent topographic signals, referred to as dynamically sustained topography e.g., [12,29]. In continents, the uplift signals from plumes typically manifest as domal uplift and are reflected in the sedimentary record e.g., [30–34]. This allows continents to preserve past dynamic topography information, and thus past plume activity, in the stratigraphic record.

Gondwanaland, named after [35], was a large landmass that began to break apart in the Jurassic. Its rifting began in the early to middle Jurassic, when North America and Africa rifted apart to form the North Atlantic basin [36]. Rifting of the West Gondwana plate began in the early Cretaceous (Figure 1A) when it started to separate into multiple continents, i.e., South America and Africa. At that time, the South Indian Ocean was also formed as a result of the separation of Madagascar and India from Africa. These events coincided with the widespread emplacement of igneous volcanic rocks, both extrusive and intrusive, derived from mantle plume processes [37]. During this period, the African continent underwent several phases of uplift and burial [38].

Here, we test the hypothesis that the dispersal of the West Gondwana plate was driven by the action of mantle plumes. In particular, we argue for the Cape Verde, Fernando, Ascension, Santa Elena, and Tristan plumes, which lie on the continental boundary between South America and Africa. We base this hypothesis on observations from sedimentary records, plate motions, and the dyke emplacement of large igneous provinces.

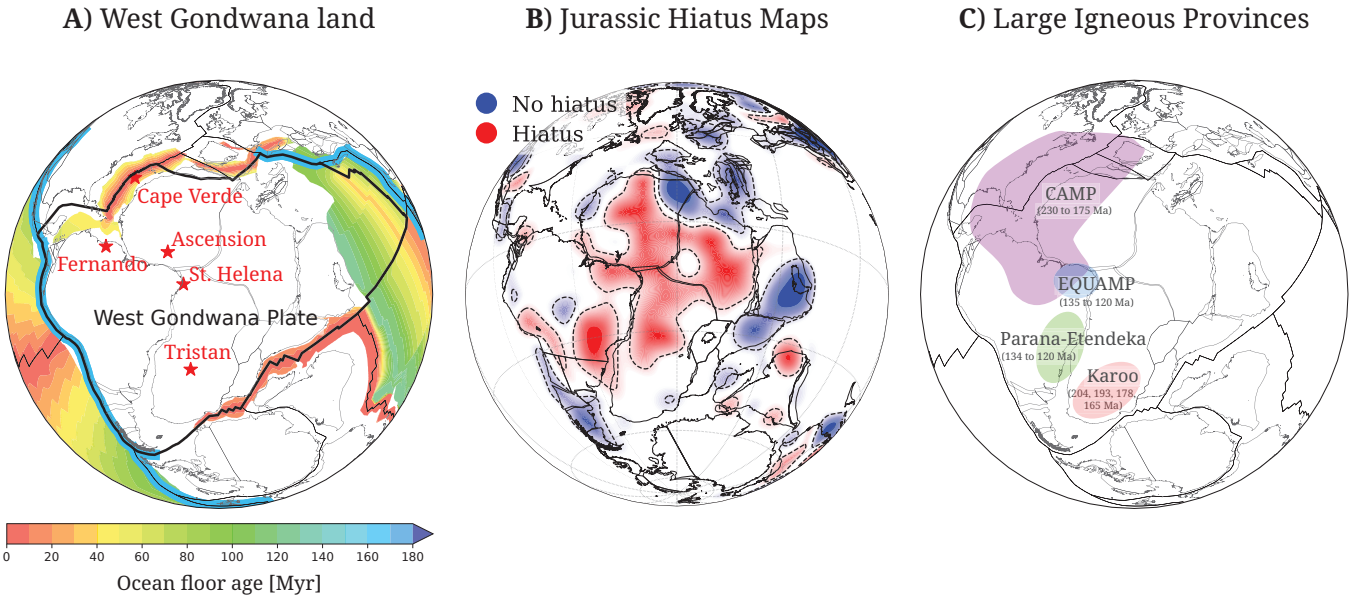

Figure 1. The West Gondwana plate during the early Cretaceous. (**A**) Tectonic setting of the West Gondwana plate in the late Cretaceous. Red dots mark hotspot locations, and blue lines indicate subducting margins. Seafloor age is color-coded from red (young) to blue (old). Continents and continental shelves are shown in white, and paleo-coastlines are shown in gray, following Mueller et al. [39]. (**B**) Hiatus surface for the early Cretaceous, obtained by expanding geological contact information between chronostratigraphic series (unconformable or conformable) using fully normalized spherical harmonics up to degree 15. The view is centered on West Gondwana for details, see [40]. Blue and red indicate areas with no hiatus and significant hiatus, corresponding to low and high topography in the target series. Blank regions indicate the absence of the series and its immediately preceding unit, suggesting a prolonged hiatus. (**C**) Spatial distribution and emplacement timing of large igneous provinces in West Gondwana.

2. Plume Signal in the Stratigraphic Record

Plumes produce a dynamic uplift signal on the Earth's lithosphere. This is seen in the stratigraphic record via hiatuses. In the pioneering work of Friedrich et al. [34], the authors developed a stratigraphic framework for analyzing continent-scale geological maps to map the surface expressions of plumes. The concept works as follows: as plumes rise from the core–mantle boundary toward the surface, they generate dynamic uplift of the surface. This, in turn, generates no deposition or erosion and leaves a gap in the sedimentary record. If the plume is deep in the mantle, its upwelling signal will be of low amplitude and large areal extent. However, closer to the surface, the uplift signal increases in amplitude but decreases in areal extent. Colli et al. [41] provide a detailed quantitative framework for this process through the use of geodynamic uplift kernels. This sequence of events leaves a characteristic sedimentary signature that can be mapped on continental regions, as described by Friedrich et al. [34] and Friedrich [42]. Recent examples of continent-scale mapping for Europe and Africa are given in [43] and Carena et al. [44]. The stratigraphic record in the continents of South America and Africa describes the path and timing of plume events.

Our analysis draws on a newly compiled inventory of hiatus surfaces documented in a series of studies by Hayek et al. [40], Vilacís et al. [15], and Vilacís et al. [45]. Their mapping efforts covered unconformable and conformable contacts globally at the time level of geological series [46]. The hiatus surfaces are modeled using spherical harmonics based on scattered contacts classified as no-hiatus or hiatus and are subsequently convolved with a Gaussian filter with a cutoff at degree 15. They serve as a proxy to map the uplift periods of the lithosphere. Figure 1B shows the hiatus surfaces for the West Gondwana

continent in the late Jurassic. Red and blue indicate high and low topography on the series in question. Blank regions indicate the absence of the series in question and its immediately preceding unit. We interpret these regions as having undergone long-lasting erosion or non-deposition. This indicates intense and/or prolonged exhumation and uplift.

Figure 1B shows the wide distribution of hiatus surfaces for the late Jurassic. Much of the African continent has hiatus surfaces. Half of the South American continent shows blank regions, reflecting the absence of Jurassic to late-Cretaceous series. There is a clear correlation between the plume locations in Figure 1A and the spatial distribution of hiatus surfaces across South America and Africa in Figure 1B. In particular, the hiatus surface extends all along the coast that connects these two continents. This wide distribution of hiatus surfaces in the late Jurassic indicates that plume pulses occurred during the early Cretaceous, accompanied by widespread volcanic activity.

3. Large Igneous Provinces at the Time of Rifting

Plume-driven eruptions produce vast, voluminous regions of mafic igneous extrusive and intrusive rocks on the Earth's surface, now recognized as large igneous provinces (LIPs) e.g., [37,47–49]. Unlike mid-ocean ridge volcanism, LIPs are not associated with seafloor spreading. In addition, these provinces are fundamentally different from any currently active volcanic systems or individual volcanoes. LIPs are fed by a vast and often complicated plumbing system that can include dyke swarms and sill complexes, as well as mid- to upper-crustal intrusive complexes. These swarms are often radiating in pattern—extending outward for more than 2500 km from a central plume center—and are commonly associated with domal uplift during the early stages of plume emplacement [50]. Dyke swarms also exhibit a circumferential pattern, ranging from 450 to 2500 km in diameter, and are mostly associated with giant radiating dyke swarms (for details, see Buchan and Ernst [51]). The coexistence of both radiating and circumferential geometries in some provinces can be exploited to link stress and magmatic processes associated with plume–lithosphere interaction e.g., [52,53]. We analyze in detail the dispersal of West Gondwana in the context of LIPs and dyke swarms to test the prediction of a causal relationship between the proposed plumes and continental rifting.

The opening of the South Atlantic Ocean may have followed the Pan-African sutures and started in the early Cretaceous (∼134–126 Ma) e.g., [54,55]. The opening followed the emplacement of vast amounts of mafic igneous extrusive and intrusive rocks associated with the central Atlantic magmatic province (CAMP) in the late Triassic to Jurassic e.g., [56,57]. This triggered the formation of multiple dyke swarms across northern South America and northwestern Africa e.g., [58,59]. Similarly, the Karoo igneous province consists of Jurassic basaltic rocks preserved in southern Africa e.g., [60], and its counterpart, the Ferrar province, extends from Antarctica to Australia and New Zealand e.g., [61]. Southern Africa has several dykes dating to this period of time e.g., [58,62]. These two vast magmatic events left the northern and southern portions of Africa and South America filled with intrusive dykes. The early Cretaceous Paraná–Etendeka flood basalts suggest that the primary magmatic phase occurred between approximately ∼138 and ∼121 Ma [63,64], with subsequent volcanic activity recorded up to 90 and 83 Ma [61]. This event was nearly simultaneous with the emplacement of the equatorial magmatic province (EQUAMP). Its main phase of eruptions occurred between ∼138 Ma and ∼81 Ma, with some younger periods of eruptions dated at ∼75–70 Ma and ∼68–49 Ma [61,65]. The extent and long duration of these large igneous provinces are related to the plume activity in the region (Figure 1A). The timing of these events suggests that more than one plume was active at that time. The preserved structures (dykes) in the lithosphere during the earlier periods of LIP emplacement play an important role in the overall strength of the lithosphere (for a

recent review, see [66]). Large igneous provinces allow one to further constrain the extent and timing of mantle plume events in relation to continental rifting [47,49].

4. Poiseuille Flow Model

The interaction between asthenosphere flow and tectonic plates has been the focus of numerous studies [67–69], with the velocity of the underlying flow often treated as a free parameter. This choice is motivated by the fact that tectonic plates obscure the asthenosphere flow beneath them, allowing it to be integrated over a wide area and making it non-unique. Thus, here we make a prediction of asthenosphere flow beneath the West Gondwana plate based on the Poiseuille flow model. The asthenosphere is assumed to be of uniform thickness with a constant viscosity beneath non-deforming plates.

Evidence for the composition and structure of the asthenosphere comes from a variety of scientific disciplines. Viscosity is typically estimated from rheological experiments on rock samples [70], while the thickness of the asthenosphere can be inferred from upper-mantle seismic tomography and anisotropy studies (e.g., [22,71–73])—inferred to reach about 250 km depth. The asthenosphere thickness and its viscosity are related by inferences from post-glacial rebound [74] via a relationship that scales with $\frac{\nu}{D^3}$, where ν is the viscosity contrast between the asthenosphere and the lowermost upper mantle and D is its thickness. Figure 2 shows the trade-off between the viscosity and thickness of the asthenosphere for two end-member values of the lowest upper-mantle viscosity, i.e., $1.4 \cdot 10^{21}$ and $1 \cdot 10^{22}$ Pa·s, down to a depth of 1400 km. These values come from the so-called *Haskell constraint* [75,76]. Postseismic deformation studies from continental regions at subduction zones have found asthenosphere viscosities ranging from $5 \cdot 10^{18}$ to $5 \cdot 10^{19}$ Pa·s [77–79]. In addition, geodynamic studies of the Pacific plate motion during the time of the Hawaiian–Emperor bend, along with glacial rebound models, suggest that the asthenosphere viscosity ranges from $4 \cdot 10^{19}$ to $5 \cdot 10^{20}$ Pa·s [80]. Mineralogical studies have constrained the depth of the asthenosphere beneath oceanic regions to between 100 and 400 km, based on phase equilibrium and physical properties [81,82]. This motivates the chosen ranges for the asthenosphere viscosity and thickness shown in Figure 2.

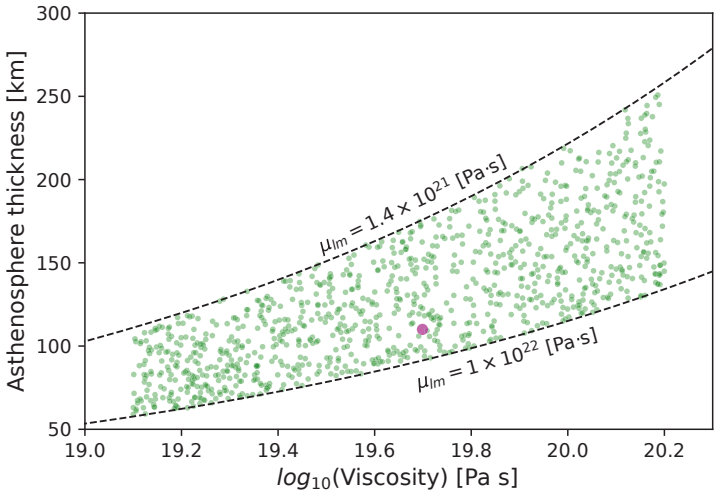

Figure 2. Diagram illustrating the relationship between asthenospheric thickness and viscosity, based on the study by Paulson and Richards [74]. Green dots sample the spatial distribution of the values used to predict asthenosphere flow. The magenta dot marks the selected values of viscosity and thickness ($5 \cdot 10^{19}$ Pa·s, 110 km) used as an example to estimate the analytical flow within the asthenosphere shown in Figure 3.

The Poiseuille flow beneath the West Gondwana plate is estimated for 10^3 possible combinations of asthenosphere viscosity and thickness. A specific combination—a thickness

of 110 km and a viscosity of $5 \cdot 10^{19}$ Pa·s—is highlighted with a magenta dot in Figure 2, as it is consistent with previous numerical (e.g., [14]) and analytical (e.g., [19]) models. This combination is used to illustrate the extent and magnitude of Poiseuille flow beneath tectonic plates. The Poiseuille flow is calculated at the plume and slab locations shown in Figure 1.

The general equation for estimating the Poiseuille flow from plumes is given by

$$V_{plumes} = \sum_j \frac{D^2}{8\mu} \frac{\Delta p_j}{\Delta x} \quad (1)$$

where j represents the number of plumes considered, D is the asthenosphere thickness, μ its viscosity, and Δx is the distance from the plume center. The expression $\frac{\Delta p_j}{\Delta x}$ represents the pressure gradient, which is estimated from the density contrast, gravity, and topographic height in the following relationship: $\Delta p_j = \rho g h_j$. Plumes are given strength based on a density contrast of 3300 kg/m^3 and a topographic height varying between 100 m and 1400 m. In Figure 3A, a height of 1400 m is assumed and taken to be equal across plumes. This assumption is in good agreement with observational and theoretical estimates of the dynamic topography (e.g., [29,41,83]). The plume Poiseuille flow beneath the West Gondwana plate spreads radially from each plume center, decreasing in intensity with distance. It occurs within an asthenospheric channel characterized by zero velocity at its upper and lower boundaries. The flow velocity is maximum near the location of the plumes, particularly where multiple plumes converge. The plume flow has regional components and is still characterized by a long wavelength (Figure 3A). The flow also shows divergence at the common coastline of the South American and African continents.

The Poiseuille flow generated by slabs can be described by the following equation:

$$V_{slabs} = \sum_i -\frac{D^2}{8\mu} \frac{\Delta p_i}{\Delta x} \quad (2)$$

where i represents the number of discretized points along the geometry of the slab, assuming a density contrast of 2300 kg/m^3 and a topographic subsidence of 200 m. The locations of the subducting margins are shown in Figure 1A. The slab Poiseuille flow is maximum near the subduction zone and decreases in intensity with distance. In particular, the minimum slab-flow velocity beneath West Gondwana is near the ridges close to Antarctica and India (Figure 3B). The slab Poiseuille flow is characterized by a smooth and long-wavelength pattern. It is also characterized by divergence near the southern ridge close to Antarctica and Madagascar.

By combining these two flow regimes (plumes and slabs), the total Poiseuille flow in the asthenosphere is constructed and shown in Figure 3C. This is by construction (i.e., $V_{poiseuille} = V_{plumes} + V_{slabs}$). The superposition of these two flow regimes can generate asthenosphere flow velocities up to ~20 cm/yr (for a thickness of 110 km and a viscosity of $5 \cdot 10^{19}$ Pa·s). The fastest asthenosphere flow velocities are near the plume centers and near the subduction zones. This fast flow is due to the combination of extensive subduction margins along the western and northeastern boundaries of the West Gondwana plate and the combined effect of the five plumes within the plate. In particular, the Poiseuille flow beneath the South American plate is predominantly westward, while beneath the African plate, the flow is predominantly northeastward. This flow has a nearly constant velocity throughout the area due to the combined action of the plumes and slabs. It is also characterized by divergence close to the coastlines that connect South America to the African continent.

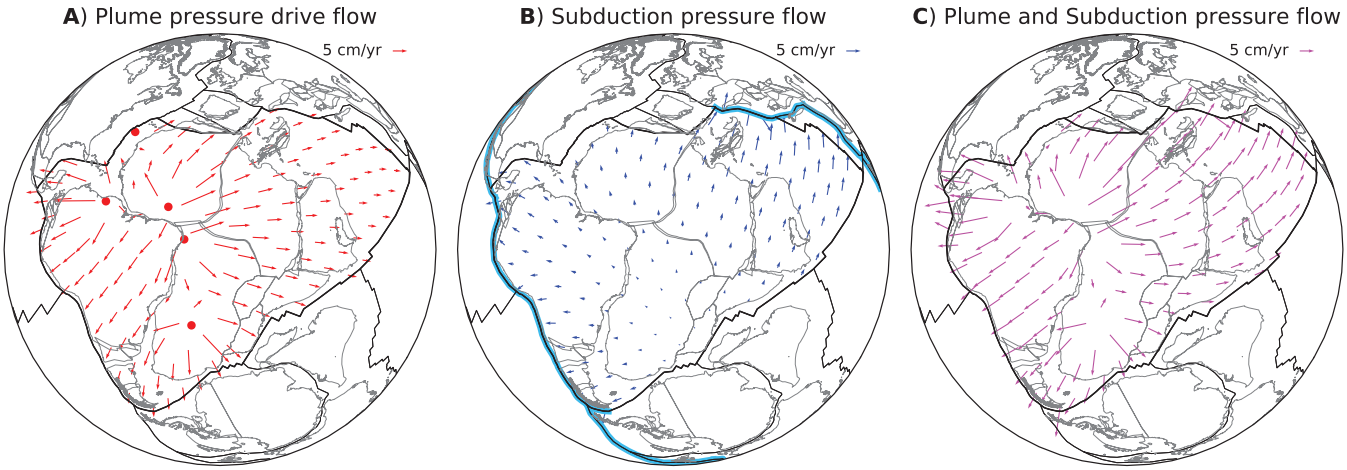

Figure 3. Example of asthenosphere flow driven by Poiseuille flow from plumes and slabs in the early Cretaceous. (**A**) Flow generated by plumes within the asthenosphere, spreading radially outward from the source. (**B**) Asthenosphere flow induced by subducting slabs, with flow directed toward the slab. (**C**) Superposition of flow generated by both a plume and a subducting slab.

5. Continental Rift and Subsequent Drift

Here we test the hypothesis that the plume, slab, or combined flow is capable of generating sufficient force to rift the lithosphere of the West Gondwana plate. This can be compared to the strength required to rift a "healthy" lithosphere and one affected by dyke intrusions [66,84]. Once the plate has fully rifted apart, the motion of the South American and African plates is driven by the asthenosphere flow generated by plumes or in combination with slab flow (Poiseuille flow). This can also be checked against observations from plate kinematic reconstructions e.g., [85,86].

The minimum tectonic force required to rift the lithosphere is shown as a solid gray line in Figure 4. This force is calculated by integrating the stress required to allow normal fault slip on optimally oriented normal faults in an Andersonian stress field, where the vertical stress is the maximum principal stress and is lithostatic (i.e., [84]). For consistency, we rewrite the tectonic force equation defined by Buck [84] in the Appendix A. The strength of the lithosphere can be weakened by the intrusion of magmatic dykes. The magmatic force is defined by the strength required to open a dyke cutting through the lithosphere and is defined in the Appendix A. Here we define magmatic rifting to describe the lithospheric extensional force supported by dyke intrusion [66,84]. Dykes may not penetrate the entire lithosphere if the supply of magma is limited or if they are predominantly emplaced laterally from their plume center. Thus, the force needed to rift the lithosphere would be intermediate between that required for tectonic and magmatic rifting. Figure 4 plots these forces as a function of brittle lithosphere thickness for two examples of magmatic rifting, assuming crustal thicknesses of H_c = 5 km and H_c = 30 km.

We calculate a first-order linear force density that the Poiseuille flow will exert on the West Gondwana plate due to the arrival of all the plumes in the asthenosphere. To do this, we estimate the shear stresses at the base of the plate using the following relationship:

$$\tau = \int_i \mu \frac{V_{flow,i}}{D} dA \tag{3}$$

where μ is the asthenosphere viscosity, $V_{flow,i}$ is the asthenosphere flow velocity below the West Gondwana plate, and D is half the asthenosphere channel thickness. Then, the magnitude of a linear force density is calculated by the following equation:

$$F_b = \tau L \tag{4}$$

which integrates the shear stress over the extent (L) of the West Gondwana plate (assumed to be 10,000 km). This gives a linear force density from the plumes alone of between $\sim 5 \cdot 10^{12}$ and $\sim 9 \cdot 10^{12}$ N/m. The variability in asthenospheric flow velocity magnitude is primarily driven by the combination of asthenosphere thickness and viscosity, with a secondary contribution from the relative strength of the plumes. A thick and highly viscous one will produce slow flow velocities, so the linear force density will be low. The opposite case, a thin and low-viscous one, will produce fast flow velocities, increasing the linear force density accordingly.

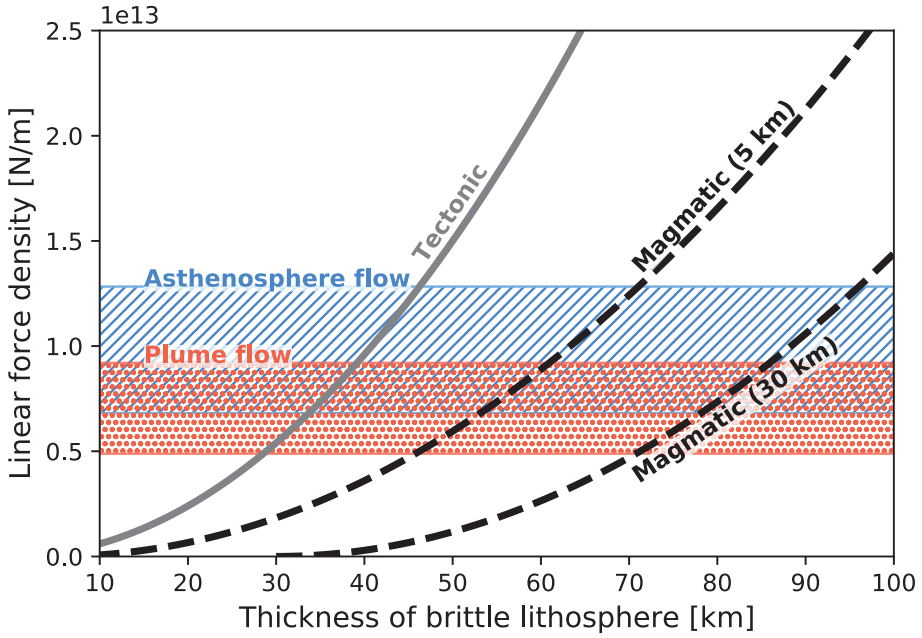

Figure 4. The analytical estimate of the linear force density required to rift the lithosphere is shown as a function of its brittle thickness, represented by the solid gray line labeled tectonic. Two end-member scenarios for magmatic intrusion are considered, corresponding to crustal thicknesses of 5 km and 30 km. When the lithosphere is intruded by dykes, the required linear force density lies between the tectonic force (gray line) and the magmatic force (black dashed line).

The results suggest that the plume flow alone should be able to rift a ∼35 km thick lithosphere, and if this has been weakened by the intrusion of dykes, it should be able to rift up to an ∼85 km thick lithosphere. These results represent two end members. This is shown in Figure 4, with a plume flow highlighted in the dashed orange area. When the crustal thickness is thinner (5 km instead of 30 km), the magmatic force increases.

The combined Poiseuille flow from plumes and slabs provides a higher linear force density of up to $\sim 1.3 \cdot 10^{13}$ N/m. This force could be capable of rifting a ∼45 km thick lithosphere. In addition, if the lithosphere were intruded by dykes, the asthenosphere flow would be capable of rifting a ∼95 km thick lithosphere (Figure 4). The Poiseuille flow in the asthenosphere is capable of rifting the West Gondwana plate into the South American and African plates.

The motion of South America and Africa can be reconstructed using the datasets from Müller et al. [85] (1999) and Doubrovine et al. [86] (2012), which are publicly available. The former dataset describes the motion of South America as it moves away from Africa, while the latter describes the absolute motion of the South American plate. We make the further assumption that Africa has remained stable over the Cretaceous time and estimate the motion of South America with respect to Africa based on the reconstruction from Müller et al. [85]. We are not interested in the magnitude of motion but rather in the direction of drifting. This can be expressed in terms of Euler poles. The advantage is that its compact

format enables the assessment of various datasets at the same time. Although the opening may have begun early, the oldest isochrons on the South Atlantic seafloor are between ∼79 and ∼83 Ma [85]. This is consistent with a geomagnetic normal-polarity superchron e.g., [87]. The reconstructed rifting direction (Euler pole) between South America and Africa is located off the east coast of Australia. This Euler pole describes a westward drift of South America and is represented by the yellow area in Figure 5. This area represents the uncertainty in the reconstruction, as described by the covariance matrix. The global plate reconstructions from Doubrovine et al. [86] are based on an optimization procedure using a moving-hotspot reference frame and relative plate motions. The motion of South America in this reconstruction model starts at 120 Ma. The oldest stage (110–120 Ma) and its uncertainty are shown in light gray in Figure 5, while the following stage (100–110 Ma) and its uncertainty are shown in orange. Interestingly, the younger (100–110 Ma) of the two stages is well within the uncertainty of the older stage (110–120 Ma). Overall, the reconstructions from Müller et al. [85] and Doubrovine et al. [86] agree on a general westward motion of South America relative to Africa or an absolute reference frame. This also implies that the assumption that Africa was stable during the Cretaceous is a good approximation.

Early rifting stages (120 to 140 Ma) in the South Atlantic were compiled by Heine et al. [55] based on an inventory of continental rifts from the conjugate margins of South America and Africa. The Euler pole location of the motion of South America relative to South and Northwest Africa is near the Arabian Peninsula (Figure 5) and describes a southwestward motion.

We estimate the direction of drift of South America away from Africa, driven by the force generated by the Poiseuille flow. This allows us to estimate geometrically, without having to make further assumptions about the magnitude of the velocity, whether the flow from plumes or in combination with slabs is capable of drifting South America, as observed from the reconstructions mentioned above. This is done by simply integrating the flow velocity from Figure 3 over the area of the South American plate. The average over its area will give the direction of South America. This is done over the various combinations of asthenosphere thickness/viscosity and plume strength. Note that the relative plume strength is the dominant controlling factor in the direction of motion due to its dependence on geometry, whereas thickness and viscosity primarily influence its magnitude. The direction of motion of South America from the plume flow alone is shown in Figure 5 with red dots. A small number of combinations drive South America in agreement with the older stages from Doubrovine et al. [86] (i.e., 110–120 Ma). In other words, the South American plate can be driven westward by plumes alone. The fit to the observations improves when the slab flow is included. The combined asthenosphere flow from plumes and slabs predicts a motion of the South American plate that fits well with the kinematic reconstructions from Doubrovine et al. [86] (100–110 Ma) and Müller et al. [85] (79.1–83.3 Ma). This is shown in Figure 5, where the direction of motion represented by the magenta dots falls well within both reconstructions.

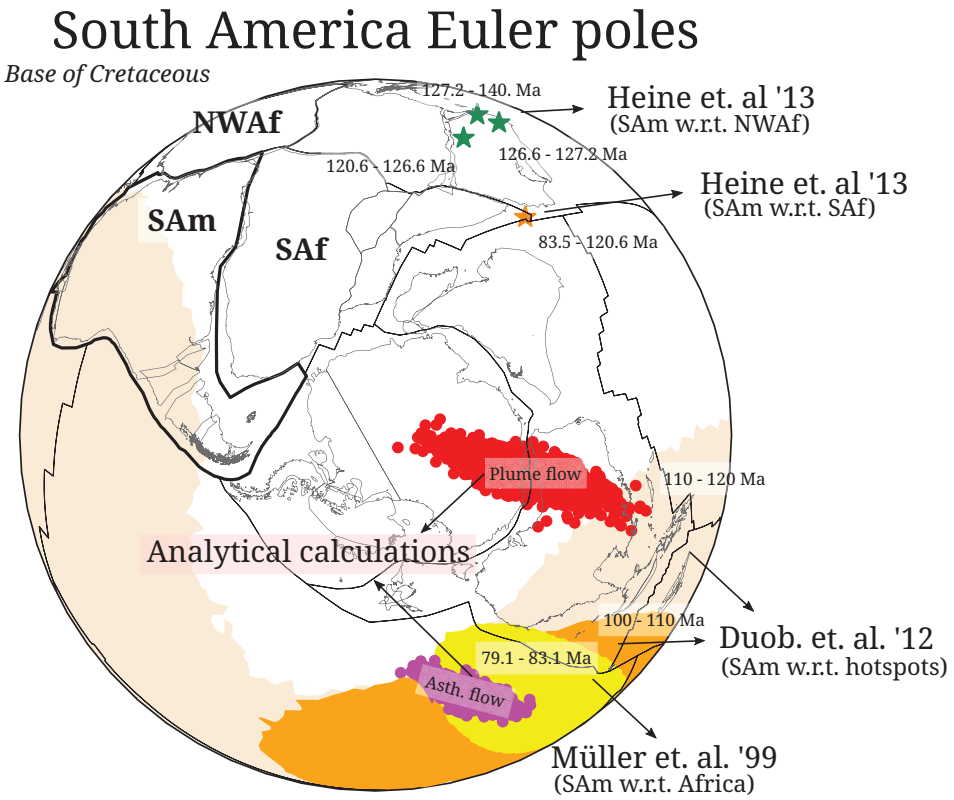

Figure 5. Movement of the South American plate in the early Cretaceous. The reconstructed Euler pole of the South American plate with respect to the African plate by Müller et al. [85] is shown in yellow, and the absolute motion of the South American plate by Doubrovine et al. [86] is shown in light gray and light brown. Both reconstructions are shown with their respective uncertainties. Reconstructions of the early stages of the South Atlantic rift by Heine et al. [55] are shown with green and yellow stars (no uncertainties provided). Red dots indicate the predicted motion of South America driven by plume-generated flow. Magenta dots indicate the predicted motion of South America driven by the flow generated by asthenosphere flow (plumes and slabs). These results show that Poiseuille flow from plumes and slabs is capable of driving South America westward, away from Africa.

6. Discussion

There is a long history of linking continental rifting, large igneous provinces (LIPs) emplacements, and mantle convection and plume events e.g., [37,58,61,66,88–92]. Much of the flow in the asthenosphere comes from the plume mode of convection (e.g., [12,93]). The channelized nature of the asthenosphere allows it to be modeled analytically within the framework of the Poiseuille flow regime (e.g., [14,16–21]). A key advantage of such fundamental models is their ability to provide clear predictions of flow behavior, identifying regions where model results agree with surface observations and where discrepancies arise. Poiseuille flow in the asthenosphere, driven by mantle plumes, provides the link between the surface observations of continental rifting and the plume mode of mantle convection.

Our results demonstrate quantitatively that mantle plumes are the primary driver of continental rifting through rapid Poiseuille flow. Divergent motions of the lithosphere will lead to its rifting. Plumes generate regional divergent flow, and the combined action of multiple plumes generates large-scale divergent flow. Figure 3A shows the divergent plume flow along the continental coastal margin of South America and Africa, with the highest flow velocity near the center of divergence. The slab flow generates a coherent, smooth, and large-scale flow that is difficult to link to rifting (Figure 3B), with the highest flow velocity far away from any possible divergence. The combined Poiseuille flow (plumes and

slabs) generates an even stronger divergence along the conjugate coast of South America and Africa (Figure 3C).

Plume activity and its temporal evolution are well constrained in the observational record. Plumes generate dynamic topography that leaves a distinct signal in the surface stratigraphy e.g., [34]. The sedimentary record, one of the most fundamental geological observations, has been studied for centuries. However, linking them to mantle convection beneath the lithosphere has required significant theoretical advances e.g., [29,41]. Beneath the West Gondwana continent, rising plumes induce lithospheric uplift (Figure 6A), a process that is supported by stratigraphic records in South America and Africa (Figure 1B). In addition, these records provide insight into the number of ascending plumes and their time of arrival in the asthenosphere. Once plumes reach the asthenosphere, they generate large amounts of igneous rock eruptions in the lithosphere at the surface. The distinct provinces of major eruptions across West Gondwana serve as a proxy for the intensity and extent of plume activity during the late Cretaceous (see Figure 1C). Plume pulses are recorded by the distribution of dykes in South America and Africa e.g., [59,60,94]. Dyke intrusions in the lithosphere also have the capacity to reduce the overall strength of the lithosphere e.g., [84]. This means that the presence of dyke intrusion reduces the necessary linear force density required to open the lithosphere via extensional forces from the divergent plume flow (see Figure 4). The maximum linear force density estimated here is $\sim 1.3 \cdot 10^{13}$ N/m, which allows rifting a "healthy" lithosphere of up to 45 km thick, but up to 90 km if it has been intruded by dykes. Buck [84] estimated that the gravitational potential force that plumes would generate from the dynamic uplift of the lithosphere is $\sim 5 \cdot 10^{12}$ N/m. This means that the combined contribution of these two forces (gravity and flow) could rift a lithosphere more than 100 km thick (see Figure 4). The channelized nature of the asthenosphere allows the development of fast plume flow and strong divergent currents below tectonic plates (Figure 6C). Plume Poiseuille flow is the most straightforward mechanism for rifting the lithosphere.

Temporal variations in the dynamic topography (non-isostatic vertical motions) of the lithosphere are often followed by changes in plate motion, as reported in several studies, including Colli et al. [22], Vibe et al. [43], and Vilacís et al. [15]. This aligns with the idea that plumes can generate substantial dynamic topography and sufficient basal shear stresses to drive changes in plate motion through a plume-push torque e.g., [95]. In fact, recent work has demonstrated that the Kerguelen plume is a dynamically viable mechanism for driving the separation of Australia from Antarctica [20]. Thus, the link between plume-induced vertical plate motions and changes in horizontal plate motions—which can be further linked to continental rifting—is made explicit. The magnitude of the linear force density is directly proportional to the magnitude of the flow velocity, which depends on the choice of the viscosity and thickness of the asthenospheric channel. We are less concerned with the magnitude of the flow because it is not well constrained. There are only indirect observations of the asthenosphere flow velocity. The best estimate was made by Hartley et al. [96], who estimated that the plume flow of the Icelandic plume at the time of high activity yielded a velocity of 35 cm/yr. This is for a single plume. Our flow calculations predict almost half ($\sim$20 cm/yr) of this value for a combination of five plumes. Thus, we are probably at the lower end of the spectrum of asthenosphere flow velocities. The direction of motion of the South American plate is well constrained because it depends on the geometry of the plates involved and their boundaries. Note that the direction of plate motion can be predicted independently of the flow magnitude. Our results hold regardless of the choice of absolute reference frame. The effect of a different reference frame on our calculations is to place the plumes in different locations relative to South America and Africa. For example, in Figure A1 in the Appendix B, the plumes are located more within the South

American continent, in contrast to Figure 3. Figure A1 in the Appendix B also shows that the plume flow predicts a South American motion that is closer to the reconstructions from Heine et al. [55] for the earlier stages of rifting between the South American and African continental blocks. The analytical flow models presented here quantitatively link plume activity, LIPs, the dynamic uplift of the lithosphere, and the evolution of continental rifting (summarized in Figure 6). Our results show that the lithosphere can be rifted by the underlying asthenosphere flow when lithospheric strength is modified by dyke intrusions.

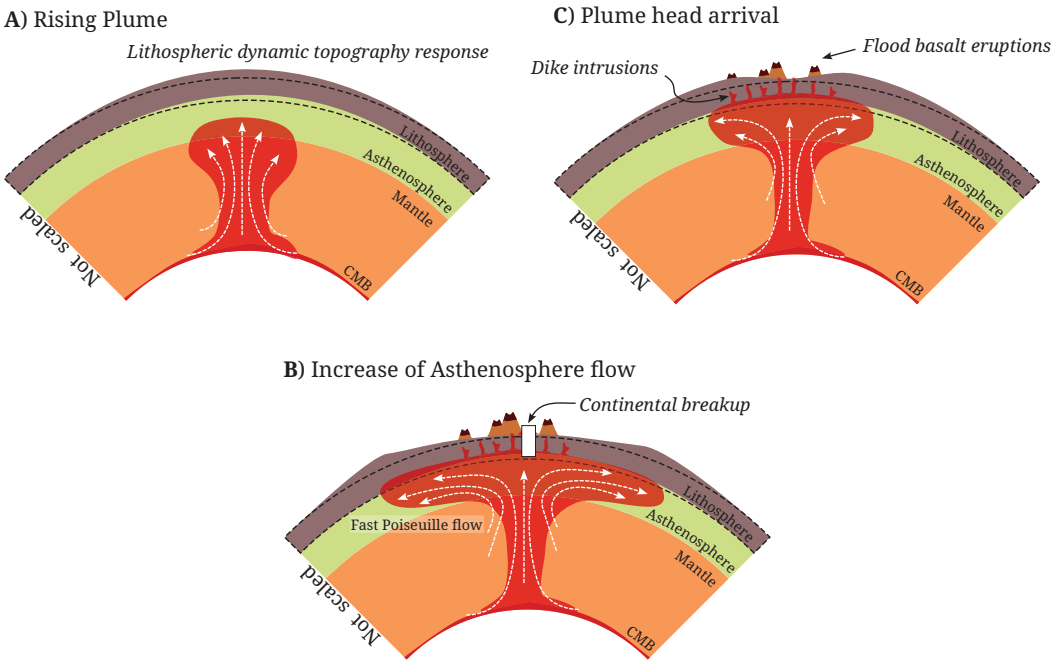

Figure 6. Conceptual evolution of rifting and drifting of continental breakup. The simple model connects observations associated with early stages of rifting and breakup. (**A**) Plumes, before arriving in the asthenosphere, generate surface uplift that is reflected in the sedimentary record. (**B**) When the plume enters the asthenosphere, it generates flood basalt eruptions and dyke intrusions. This reduces lithospheric strength. (**C**) As the plume spreads within the asthenosphere, it generates a fast Poiseuille flow that rifts the lithosphere apart. CMB stands for core–mantle boundary.

The analytical flow model has some limitations. For example, choosing a constant channel thickness might overlook the dynamic impact of continental thickness [97,98]. We highlight the influence of lithospheric thickness and address it indirectly by estimating the linear force density required to rift the lithosphere for different thicknesses (Figure 4). However, the motion of the South American plate appears to be independent of the lithospheric thickness and depends mostly on the geometry of the plate relative to the location of the plumes. So we argue that the thickness of the lithosphere plays a role in determining whether plates can rift at all; otherwise, the lithosphere would rift everywhere at all times and not allow the development of large plates. This is not the case on Earth because we have several large plates. This study does not take into account the gravitational potential energy associated with the domal uplift from the plume. Incorporating it in future analyses would strengthen the inferences regarding plume-driving forces. Furthermore, we assume a Newtonian rheology, even though there is strong evidence for a non-Newtonian rheology in the upper mantle [99], which could produce a more complex pattern of asthenosphere flow [100].

Previous studies have highlighted a spatial correlation between continental rifting and preexisting orogenic belts, often associated with the Wilson cycle [101,102]. Orogenic belts develop crustal weaknesses due to faulting that can be reactivated during periods of

extension e.g., [101,103–106]. However, the path of the Yellowstone hotspot track across western North America challenges this assumption e.g., [19]. If preexisting orogenic weakness alone dictated rifting, the North American plate should be actively rifting—but it is not. This suggests that successful continental rifting requires additional factors, i.e., dyke intrusions. In other words, the combined effects of (i) a faulted orogenic belt and (ii) the preexistence of dykes could significantly weaken the lithosphere. There are other geological processes that can also weaken the lithosphere (for an overview, see [66]). This facilitates rifting of the lithosphere. In addition, our results suggest that a single plume event may not be sufficient to initiate rifting; instead, a sequence of plume-driven events at a given location is required to sufficiently weaken the lithosphere.

Recall from the introduction that early ideas about plate tectonics came from observations of the geometry of continents that were once together e.g., [107]. Based on our results, we further argue that the global geometric distribution of hotspots could match the coastlines of continents prior to their rifting. Figure A1 in the Appendix B shows that our results remain the same if one uses an alternative reference frame and reconstruction. This will reshape the asthenosphere flow because the location of plumes relative to the plates will vary, thereby influencing how those currents drive the motion of South America. Notably, the reconstructions from Müller et al. [85] and Doubrovine et al. [86] both indicate a consistent direction of South America's motion relative to Africa and hotspots, respectively. This agreement—illustrated in Figure 5 by the alignment of Euler pole locations—suggests that the African plate remained relatively stable during the Cretaceous. Our results may therefore help guide and motivate the development of alternative absolute reference frames for plate reconstructions.

7. Conclusions

This study presents a straightforward mechanism that explains continental rifting and plate motions during this time. Our analytical calculations provide a prediction of past asthenosphere flow and its associated torque, which drove the Poiseuille flow-induced rifting of South America from Africa. In this model, Poiseuille flow in the asthenosphere arises from pressure gradients generated by mantle plumes along the common South America–Africa margin and by subduction zones surrounding the West Gondwana plate. Notably, Poiseuille flow driven by subducting slabs tends to remain relatively steady over time, except when new subduction zones form. In contrast, plume-driven Poiseuille flow can be episodic, generating transient asthenospheric flows and associated torques that influence plate motion. This has been demonstrated in previous studies that have shown that the Kerguelen Plume caused Australia and Antarctica to separate during the Eocene.

The strength of the Poiseuille flow model is its ability to quantitatively link the underlying mantle flow to surface observations. Our results successfully explain the early Cretaceous rifting of the West Gondwana plate, including the dynamic uplift of West Gondwana during the Jurassic (prior to rifting), the emplacement of large igneous provinces at the onset of rifting, and the subsequent separation and movement of the newly formed continents, South America and Africa. In addition, our findings align well with previous studies suggesting that rifting tends to occur along sutures of ancient orogenic belts. We demonstrated that mantle plume upwellings, rather than subduction, are the dominant control on continental rifting and plate tectonics. The analytical approach presented here allows for a quantitative reconstruction of past mantle flow.

Author Contributions: Conceptualization, I.L.S.; methodology, I.L.S. and B.V.; software, I.L.S., J.N.H. and B.V.; validation, I.L.S., J.N.H. and B.V.; formal analysis, I.L.S. and H.-P.B.; investigation, I.L.S. and H.-P.B.; resources, I.L.S.; data curation, I.L.S., J.N.H. and B.V.; writing—original draft preparation, I.L.S.; writing—review and editing, I.L.S., J.N.H., B.V. and H.-P.B.; visualization, I.L.S. and B.V.; project

administration, I.L.S.; funding acquisition, I.L.S. All authors have read and agreed to the published version of the manuscript.

Funding: I.L.S. received funding from the Deutsche Forschungsgemeinschaft (grant STO1271/2-1).

Institutional Review Board Statement: Not applicable.

Informed Consent Statement: Not applicable.

Data Availability Statement: The finite rotation dataset can be found in Müller et al. [85], Doubrovine et al. [86], Heine et al. [55]. The LIPS location dataset can be found in the reference list. The inventory of the Base Hiatus Surface dataset can be found in Hayek et al. [40].

Acknowledgments: I.L.S. acknowledges support from the Deutsche Forschungsgemeinschaft (DFG) under project number STO1271/2-1. We would like to thank the four anonymous reviewers and editors Richard E. Ernst and Hafida El Bilali for their valuable contributions in improving the manuscript.

Conflicts of Interest: The authors declare there are no conflicts of interest.

Appendix A

For completeness, we include here the equations from Buck [84]. The force required for tectonic rifting is calculated using the following equation:

$$F_T = \frac{C{H_L}^2}{2} \tag{A1}$$

where C is $1.2{\cdot}10^4$ Pa m^{-1} and H_L is the thickness of the brittle lithosphere. Magmatic force is defined by the strength required to open a dyke that cuts through the lithosphere and is described by the following equation:

$$F_M = g(\rho_m - \rho_f)\frac{(H_L - H_c)^2}{2} \tag{A2}$$

where g is the gravity, the density of the mantle is ρ_m = 3300 kg m^{-1}, the density of the fluid magma is ρ_f = 2700 kg m^{-1}, and H_c is the thickness of the crust.

Appendix B

The choice of an absolute reference frame to plate the locations of plumes relative to the South American and African continents does not change our results. In fact, it provides new insights into the relative motion of plumes and continents, as well as their role in rifting the lithosphere. The reference frame choices are shown in Figure A1. The reference frame labeled Ref-O05-T08 uses an Indo-Atlantic moving-hotspot reference frame from O'Neill et al. [108] for the past 100 Myrs and a True Polar Wander-corrected paleomagnetic model from Steinberger and Torsvik [109] for older times. The reference frame labeled Ref-O05-M93 applies a reference frame of Indo-Atlantic moving hotspots from O'Neill et al. [108] for the last 100 Myrs and of fixed African hotspots from Müller et al. [110] for older times.

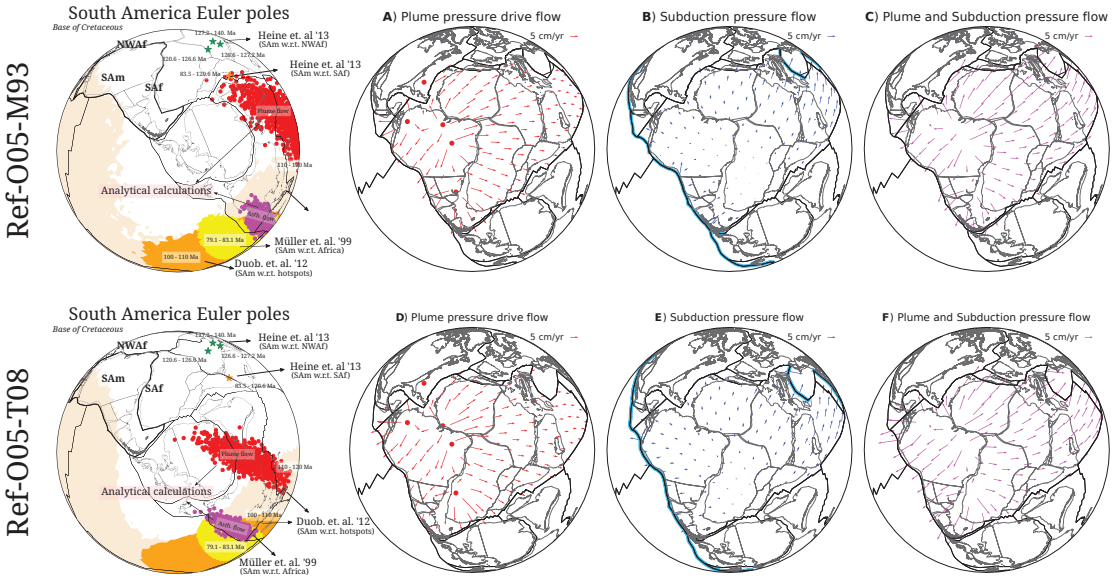

Figure A1. Movement of the South American plate in the early Cretaceous, shown for different reference frames, relative to the location of plumes and West Gondwana. The reconstructed Euler pole of the South American plate with respect to the African plate by Müller et al. [85] is shown in yellow, and the absolute motion of the South American plate by Doubrovine et al. [86] is shown in light gray and light brown. Both reconstructions include their respective uncertainties. Reconstructions of the early stages of South Atlantic rifting by Heine et al. [55] are shown with green and yellow stars (no uncertainties provided). Red dots indicate the predicted motion of South America driven by plume-generated flow. Magenta dots show the predicted motion of South America driven by flow generated by asthenosphere processes (plumes and slabs). These results show that Poiseuille flow from plumes and slabs is capable of driving South America westward, away from Africa. Example of asthenosphere flow driven by Poiseuille flow from plumes and slabs in the early Cretaceous: (**A**,**D**) Flow generated by plumes within the asthenosphere, spreading radially outward from the source. (**B**,**E**) Asthenosphere flow induced by subducting slabs, with flow directed toward the slab. (**C**,**F**) Superposition of flow generated by both a plume and a subducting slab.

References

1. Wegener, A. *Die Entstehung der Kontinente und Ozeane*, 5th ed.; Friedr. Vieweg & Sohn A.-G.: Braunschweig, Germany, 1929.
2. Carey, S.W. Wegener's South African Assembly, Fit or Misfit? *Geol. Mag.* **1955**, *92*, 196–200. [CrossRef]
3. Bullard, E.; Everett, J.; Smith, A. The fit of the continents around the Atlantic. *Philos. Trans. R. Soc. Lond.* **1965**, *258*, 41–51. [CrossRef] [PubMed]
4. Sykes, L.R. Seismicity of the South Pacific Ocean. *Geophys. Res.* **1963**, *68*, 5999–6006. [CrossRef]
5. Sykes, L.R. The seismicity of the Arctic. *Bull. Seismol. Soc. Am.* **1965**, *55*, 501–518.
6. Cox, A.; Doell, R.R.; Dalrymple, G.B. Geomagnetic polarity epochs and Pleistocene geochronometry. *Nature* **1963**, *198*, 1049–1051. [CrossRef]
7. Cox, A. Geomagnetic reversals. *Science* **1969**, *163*, 237–245. [CrossRef]
8. McDougall, I.; Tarling, D.H. Dating of polarity zones in the Hawaiian islands. *Nature* **1963**, *200*, 54–56. [CrossRef]
9. Maxwell, A.E.; Von Herzen, R.P.; Hsu, K.J.; Andrews, J.E.; Saito, T.; Percival, S.F.; Milow, E.D.; Boyce, R.E. Deep sea drilling in the South Atlantic. *Science* **1970**, *168*, 1047–1059. [CrossRef] [PubMed]
10. Ewing, M.; Ewing, J.; Talwan, M. Sediment distribution in the oceans: The Mid-Atlantic Ridge. *Bull. Seismol. Soc. Am.* **1964**, *75*, 17–36. [CrossRef]
11. Wilson, J.T. A new class of faults and their bearing on continental drift. *Nature* **1965**, *207*, 343–347. [CrossRef]
12. Davies, G.F.; Richards, M.A. Mantle convection. *J. Geol.* **1992**, *100*, 151–206. [CrossRef]
13. Richards, M.A.; Lenardic, A. The Cathles Parameter (Ct): A Geodynamic Definition of the Asthenosphere and Implications for the Nature of Plate Tectonics. *Geochem. Geophys. Geosyst.* **2018**, *19*, 4858–4875. [CrossRef]
14. Stotz, I.L.; Iaffaldano, G.; Davies, D.R. Pressure-Driven Poiseuille Flow: A Major Component of the Torque-Balance Governing Pacific Plate Motion. *Geophys. Res. Lett.* **2018**, *45*, 117–125. [CrossRef]

15. Vilacís, B.; Hayek, J.N.; Stotz, I.L.; Bunge, H.P.; Friedrich, A.M.; Carena, S.; Clark, S. Evidence for active upper mantle flow in the Atlantic and Indo-Australian realms since the Upper Jurassic from hiatus maps and spreading rate changes. *Proc. R. Soc. Math. Phys. Eng. Sci.* **2022**, *478*, 20210764. [CrossRef]
16. Hoeink, T.; Lenardic, A. Three-dimensional mantle convection simulations with a low-viscosity asthenosphere and the relationship between heat flow and the horizontal length scale of convection. *Geophys. Res. Lett.* **2008**, *35*. [CrossRef]
17. Hoeink, T.; Lenardic, A. Long wavelength convection, Poiseuille-Couette flow in the low-viscosity asthenosphere and the strength of plate margins. *Geophys. J. Int.* **2010**, *180*, 23–33. [CrossRef]
18. Hoeink, T.; Lenardic, A.; Richards, M. Depth-dependent viscosity and mantle stress amplification: Implications for the role of the asthenosphere in maintaining plate tectonics. *Geophys. J. Int.* **2012**, *191*, 30–41. [CrossRef]
19. Stotz, I.L.; Vilacís, B.; Hayek, J.N.; Bunge, H.P.; Friedrich, A.M. Yellowstone Plume Drives Neogene North American Plate Motion Change. *Geophys. Res. Lett.* **2021**, *48*, e2021GL095079. [CrossRef]
20. Stotz, I.L.; Carena, S.; Vilacís, B.; Hayek, J.N.; Bunge, H.P. Kerguelen Plume Drives the Eocene Directional Change in Australian Plate Motion. *Lithosphere* **2024**, *2024*, lithosphere_2023_289. [CrossRef]
21. Wang, Z.R.; Stotz, I.L.; Bunge, H.P.; Vilacís, B.; Hayek, J.N.; Ghelichkhan, S.; Lebedev, S. Cenozoic upper mantle flow history of the Atlantic realm based on Couette/Poiseuille models: Towards paleo-mantle-flowgraphy. *Phys. Earth Planet. Inter.* **2023**, *340*, 107045. [CrossRef]
22. Colli, L.; Stotz, I.; Bunge, H.P.; Smethurst, M.; Clark, S.; Iaffaldano, G.; Tassara, A.; Guillocheau, F.; Bianchi, M.C. Rapid South Atlantic spreading changes and coeval vertical motion in surrounding continents: Evidence for temporal changes of pressure-driven upper mantle flow. *Tectonics* **2014**, *33*, 1304–1321. [CrossRef]
23. Conrad, C.P.; Lithgow-Bertelloni, C. How Mantle Slabs Drive Plate Tectonics. *Science* **2002**, *298*. [CrossRef]
24. Morgan, W.J. Plate motions and deep mantle convection. *Mem. Geol. Soc. Am.* **1972**, *132*, 7–22.
25. Morgan, W. Convection Plumes in the Lower Mantle. *Nature* **1971**, *230*, 42–43. [CrossRef]
26. Morgan, J.P.; Smith, W.H.F. Flattening of the sea-floor depth-age curve as a response to asthenospheric flow. *Nature* **1992**, *359*, 524–527. [CrossRef]
27. Morgan, J.P.; Morgan, W.J.; Zhang, Y.S.; Smith, W.H.F. Observational hints for a plume-fed, suboceanic asthenosphere and its role in mantle convection. *J. Geophys. Res. Solid Earth* **1995**, *100*, 12753–12767. [CrossRef]
28. Stotz, I.L.; Vilacís, B.; Hayek, J.N.; Carena, S.; Bunge, H.P. Plume driven plate motion changes: New insights from the South Atlantic realm. *J. South Am. Earth Sci.* **2023**, *124*, 104257. [CrossRef]
29. Hager, B.H.; Clayton, R.W.; Clayton, R.W.; Comer, R.P.; Dziewonski, A.M. Lower mantle heterogeneity, dynamic topography and the geoid. *Nature* **1985**, *313*, 541–545. [CrossRef]
30. Şengör, A.M.C. Elevation as indicator of mantle-plume activity. *Mantle Plumes Their Identif. Through Time* **2001**, *352*, 183–245. [CrossRef]
31. Rainbird, R.H.; Ernst, R.E. The sedimentary record of mantle-plume uplift. *Spec. Pap.-Geol. Soc. Am.* **2001**, *352*, 227–246. [CrossRef]
32. Campbell, I.H. Testing the plume theory. *Chem. Geol.* **2007**, *241*, 153 – 176. [CrossRef]
33. Saunders, A.; Jones, S.; Morgan, L.; Pierce, K.; Widdowson, M.; Xu, Y. Regional uplift associated with continental large igneous provinces: The roles of mantle plumes and the lithosphere. *Chem. Geol.* **2007**, *241*, 282–318. [CrossRef]
34. Friedrich, A.M.; Bunge, H.P.; Rieger, S.M.; Colli, L.; Ghelichkhan, S.; Nerlich, R. Stratigraphic framework for the plume mode of mantle convection and the analysis of interregional unconformities on geological maps. *Gondwana Res.* **2018**, *53*, 159–188. [CrossRef]
35. Suess, E. *Das Antlitz der Erde (The Face of the Earth)*; G. Freytag: Leipzig, Germany, 1885; Volume 1.
36. Lawver, L.A.; Gahagan, L.M. Subduction Zones, Magmatism, and the Breakup of Pangea. In *Flow and Creep in the Solar System: Observations, Modeling and Theory*; Springer: Amsterdam, The Netherlands, 1993; pp. 225–247. [CrossRef]
37. Coffin, M.; Eldholm, O. Volcanism and continental break-up: A global compilation of large igneous provinces. *Geol. Soc. Lond. Spec. Publ.* **1992**, *68*, 17–30. [CrossRef]
38. Burke, K.; Gunnell, Y. The African Erosion Surface: A Continental-Scale Synthesis of Geomorphology, Tectonics, and Environmental Change over the Past 180 Million Years. *Geol. Soc. Am. Mem.* **2008**, *201*, 21–66.
39. Mueller, R.D.; Seton, M.; Zahirovic, S.; Williams, S.E.; Matthews, K.J.; Wright, N.M.; Shephard, G.E.; Maloney, K.T.; Barnett-Moore, N.; Hosseinpour, M.; et al. Ocean Basin Evolution and Global-Scale Plate Reorganization Events Since Pangea Breakup. *Annu. Rev. Earth Planet. Sci.* **2016**, *44*, 107–138. [CrossRef]
40. Hayek, J.N.; Vilacís, B.; Bunge, H.P.; Friedrich, A.M.; Carena, S.; Vibe, Y. Continent-scale Hiatus Maps for the Atlantic Realm and Australia since the Upper Jurassic and links to mantle flow induced dynamic topography. *Proc. R. Soc. Math. Phys. Eng. Sci.* **2020**, *476*, 20200390. [CrossRef]
41. Colli, L.; Ghelichkhan, S.; Bunge, H.P. On the ratio of dynamic topography and gravity anomalies in a dynamic Earth. *Geophys. Res. Lett.* **2016**, *43*, 2510–2516. [CrossRef]

42. Friedrich, A.M. Palaeogeological hiatus surface mapping: A tool to visualize vertical motion of the continents. *Geol. Mag.* **2019**, *156*, 308–319. [CrossRef]
43. Vibe, Y.; Friedrich, A.M.; Bunge, H.P.; Clark, S.R. Correlations of oceanic spreading rates and hiatus surface area in the North Atlantic realm. *Lithosphere* **2018**, *10*, 677–684. [CrossRef]
44. Carena, S.; Bunge, H.P.; Friedrich, A.M. Analysis of geological hiatus surfaces across Africa in the Cenozoic and implications for the timescales of convectively-maintained topography. *Can. J. Earth Sci.* **2019**, *56*, 1333–1346. [CrossRef]
45. Vilacís, B.; Brown, H.; Bunge, H.P.; Carena, S.; Hayek, J.N.; Stotz, I.L.; Wang, Z.R.; Friedrich, A.M. Dynamic topography and the planform of mantle convection since the Jurassic inferred from global continental hiatus maps. *Proc. R. Soc. Math. Phys. Eng. Sci.* **2024**, *480*, 20240311. [CrossRef]
46. Cohen, K.M.; Harper, D.; Gibbard, P.L. ICS International Chronostratigraphic Chart. August 2018. Available online: www.stratigraphy.org (accessed on 10 February 2025).
47. Ernst, R.E.; Buchan, K.L. Maximum size and distribution in time and space of mantle plumes: Evidence from large igneous provinces. *J. Geodyn.* **2002**, *34*, 309–342. [CrossRef]
48. Coffin, M.F.; Eldholm, O. Large Igneous Provinces. In *Encyclopedia of Ocean Sciences*, 3rd ed.; Cochran, J.K., Bokuniewicz, H.J., Yager, P.L., Eds.; Academic Press: Oxford, UK, 2019; pp. 337–345. [CrossRef]
49. Ernst, R.E.; Bond, D.P.G.; Zhang, S.H.; Buchan, K.L.; Grasby, S.E.; Youbi, N.; El Bilali, H.; Bekker, A.; Doucet, L.S. Large Igneous Province Record Through Time and Implications for Secular Environmental Changes and Geological Time-Scale Boundaries. In *Large Igneous Provinces*; American Geophysical Union (AGU): Washington, DC, USA, 2021; Chapter 1; pp. 1–26. [CrossRef]
50. Buchan, K.L.; Ernst, R.E. Plumbing systems of large igneous provinces (LIPs) on Earth and Venus: Investigating the role of giant circumferential and radiating dyke swarms, coronae and novae, and mid-crustal intrusive complexes. *Gondwana Res.* **2021**, *100*, 25–43. [CrossRef]
51. Buchan, K.; Ernst, R. Giant circumferential dykes swarms: Catalogue and characteristics. In *Dyke Swarms of the World: A Modern Perspective*; Srivastava, R., Ernst, R., Peng, P., Eds.; Springer: Singapore, 2019; pp. 1–44.
52. El Bilali, H.; Ernst, R.E. Far-travelled 3700 km lateral magma propagation just below the surface of Venus. *Nat. Commun.* **2024**, *15*, 1759. [CrossRef] [PubMed]
53. Tessier, A.D.; Ernst, R.E.; El Bilali, H. Heng-o Corona, Venus: Dyke swarms record evolution of its underlying mantle plume. *Icarus* **2024**, *417*, 116090. [CrossRef]
54. Frimmel, H.E. Configuration of Pan-African Orogenic Belts in Southwestern Africa. In *Neoproterozoic-Cambrian Tectonics, Global Change and Evolution: A Focus on Southwestern Gondwana*; Gaucher, C., Sial, A., Haverson, G., Eds.; Elsevier: Amsterdam, The Netherlands, 2010; pp. 145–151.
55. Heine, C.; Zoethout, J.; Müller, D. Kinematics of the South Atlantic Rift. *Solid Earth* **2013**, *4*, 215–253. [CrossRef]
56. Baksi, A. Critical evaluation of 40Ar/39Ar ages for the Central Atlantic Magmatic Province: Timing, duration and possible migration of magmatic centers. In *Washington DC American Geophysical Union Geophysical Monograph Series*; Wiley: Hoboken, NJ, USA, 2003; Volume 136, pp. 77–90. [CrossRef]
57. Whalen, L.; Gazel, E.; Vidito, C.; Puffer, J.; Bizimis, M.; Henika, W.; Caddick, M.J. Supercontinental inheritance and its influence on supercontinental breakup: The Central Atlantic Magmatic Province and the breakup of Pangea. *Geochem. Geophys. Geosyst.* **2015**, *16*, 3532–3554. [CrossRef]
58. Ernst, R.E.; Buchan, K.L. Giant Radiating Dyke Swarms: Their Use in Identifying Pre-Mesozoic Large Igneous Provinces and Mantle Plumes. In *Large Igneous Provinces: Continental, Oceanic, and Planetary Flood Volcanism*; American Geophysical Union (AGU): Washington, DC, USA, 1997; pp. 297–333. [CrossRef]
59. Marzoli, A.; Renne, P.R.; Piccirillo, E.M.; Ernesto, M.; Bellieni, G.; De Min, A. Extensive 200-million-year-old continental flood basalts of the central Atlantic magmatic province. *Science* **1999**, *284*, 616–618. [CrossRef]
60. Cox, K.G. The Karoo Province. In *Continental Flood Basalts*; Macdougall, J.D., Ed.; Springer: Dordrecht, The Netherlands, 1988; pp. 239–271. [CrossRef]
61. Segev, A. Flood basalts, continental breakup and the dispersal of Gondwana: Evidence for periodic migration of upwelling mantle flows (plumes). *Egu Stephan Mueller Spec. Publ. Ser.* **2002**, *2*, 171–191. [CrossRef]
62. Burke, K.; Dewey, J.F. Plume-Generated Triple Junctions: Key Indicators in Applying Plate Tectonics to Old Rocks. *J. Geol.* **1973**, *81*, 406–433. [CrossRef]
63. Piccirillo, E.M.; Melfi, A.J.; Comin-Chiaramonti, P.; Bellieni, G.; Ernesto, M.; Marques, L. S.; Nardy, A.J.R.; Pacca, I.G.; Roisenberg, A.; Stolfa, D. Continental Flood Volcanism From the Paraná Basin (Brazil). In *Continental Flood Basalts*; Macdougall, J.D., Ed.; Springer: Dordrecht, The Netherlands, 1988; pp. 195–238. [CrossRef]
64. Peate, D.W. The Paraná-Etendeka Province. In *Large Igneous Provinces: Continental, Oceanic, and Planetary Flood Volcanism*; American Geophysical Union (AGU): Washington, DC, USA, 1997; pp. 217–245. [CrossRef]

65. Hollanda, M.H.B.M.; Archanjo, C.J.; Macedo Filho, A.A.; Fossen, H.; Ernst, R.E.; de Castro, D.L.; Melo, A.C.; Oliveira, A.L., The Mesozoic Equatorial Atlantic Magmatic Province (EQUAMP). In *Dyke Swarms of the World: A Modern Perspective*; Srivastava, R.K.; Ernst, R.E.; Peng, P., Eds.; Springer: Singapore, 2019; pp. 87–110. [CrossRef]
66. Buck, R., 6.08 Dynamic Processes in Extensional and Compressional Settings: The Dynamics of Continental Breakup and Extension. *Treatise Geophys.* **2007**, *6*, 335–376. [CrossRef]
67. Bird, P. Testing hypotheses on plate-driving mechanisms with global lithosphere models including topography, thermal structure, and faults. *J. Geophys. Res.-Solid Earth* **1998**, *103*, 10115–10129. [CrossRef]
68. Brune, S. Forces within continental and oceanic rifts: Numerical modeling elucidates the impact of asthenospheric flow on surface stress. *Geology* **2018**, *46*, 191. [CrossRef]
69. Bird, P.; Liu, Z.; Rucker, W.K. Stresses that drive the plates from below: Definitions, computational path, model optimization, and error analysis. *J. Geophys. Res.* **2008**, *113*, B11406. [CrossRef]
70. Karato, S. On the origin of the asthenosphere. *Earth Planet. Sci. Lett.* **2012**, *321–322*, 95–103. [CrossRef]
71. Grand, S.P.; Helmberger, D.V. Upper mantle shear structure of North America. *Geophys. J. R. Astron. Soc.* **1984**, *76*, 399–438. [CrossRef]
72. Debayle, E.; Kennett, B.; Priestley, K. Global azimuthal seismic anisotropy and the unique plate-motion deformation of Australia. *Nature* **2005**, *433*, 509–512. [CrossRef]
73. French, S.; Lekic, V.; Romanowicz, B. Waveform Tomography Reveals Channeled Flow at the Base of the Oceanic Asthenosphere. *Science* **2013**, *342*, 227–230. [CrossRef]
74. Paulson, A.; Richards, M.A. On the resolution of radial viscosity structure in modelling long-wavelength postglacial rebound data. *Geophys. J. Int.* **2009**, *179*, 1516. [CrossRef]
75. Haskell, N.A. The viscosity of the asthenoshpere. *Am. J. Sci.* **1937**, *33*, 22–28. [CrossRef]
76. Mitrovica, J.X. Haskell [1935] revisited. *J. Geophys. Res. Solid Earth* **1996**, *101*, 555–569. [CrossRef]
77. Freed, A.M.; Bürgmann, R.; Calais, E.; Freymueller, J.; Hreinsdóttir, S. Implications of deformation following the 2002 Denali, Alaska, earthquake for postseismic relaxation processes and lithospheric rheology. *J. Geophys. Res. Solid Earth* **2006**, *111*. [CrossRef]
78. Freed, A.M.; Hashima, A.; Becker, T.W.; Okaya, D.A.; Sato, H.; Hatanaka, Y. Resolving depth-dependent subduction zone viscosity and afterslip from postseismic displacements following the 2011 Tohoku-oki, Japan earthquake. *Earth Planet. Sci. Lett.* **2017**, *459*, 279–290. [CrossRef]
79. Hu, Y.; Bürgmann, R.; Banerjee, P.; Feng, L.; Hill, E.; Ito, T.; Tabei, T.; Wang, K. Asthenosphere rheology inferred from observations of the 2012 Indian Ocean earthquake. *Nature* **2016**, *538*, 368–372. [CrossRef]
80. Iaffaldano, G.; Lambeck, K. Pacific plate–motion change at the time of the Hawaiian–Emperor bend constrains the viscosity of Earth's asthenosphere. *Geophys. Res. Lett.* **2014**, *in review*. [CrossRef]
81. Stixrude, L.; Lithgow-Bertelloni, C. Mineralogy and elasticity of the oceanic upper mantle: Origin of the low-velocity zone. *J. Geophys. Res. Solid Earth* **2005**, *110*. [CrossRef]
82. Patočka, V.; Čížková, H.; Pokorný, J. Dynamic Component of the Asthenosphere: Lateral Viscosity Variations Due to Dislocation Creep at the Base of Oceanic Plates. *Geophys. Res. Lett.* **2024**, *51*, e2024GL109116. [CrossRef]
83. Hoggard, M.J.; Winterbourne, J.; Czarnota, K.; White, N. Oceanic residual depth measurements, the plate cooling model, and global dynamic topography. *J. Geophys. Res. Solid Earth* **2017**, *122*, 2328–2372. [CrossRef]
84. Buck, W.R. The role of magma in the development of the Afro-Arabian Rift System. In *The Afar Volcanic Province within the East African Rift System*; Geological Society of London: London, UK, 2006. [CrossRef]
85. Müller, R.D.; Royer, J.Y.; Cande, S.C.; Roest, W.R.; Maschenkov, S. Chapter 2: New constraints on the late cretaceous/tertiary plate tectonic evolution of the caribbean. In *Caribbean Basins*; Mann, P., Ed.; Elsevier: Amsterdam, The Netherlands, 1999; Volume 4; pp. 33–59. [CrossRef]
86. Doubrovine, P.V.; Steinberger, B.; Torsvik, T.H. Absolute plate motions in a reference frame defined by moving hot spots in the Pacific, Atlantic, and Indian oceans. *J. Geophys. Res. Solid Earth* **2012**, *117*. [CrossRef]
87. Algeo, T.J. Geomagnetic polarity bias pattern through the Phanerozoic. *J. Geophys. Res.* **1996**, *101*, 2785–2814. [CrossRef]
88. Yuen, D.; Fleitout, L. Thinning of the lithosphere by small-scale convective destabilization. *Nature* **1985**, *313*, 125–128. [CrossRef]
89. Fleitout, L.; Froidevaux, C.; Yuen, D. Active lithospheric thinning. *Tectonophysics* **1986**, *132*, 271–278. [CrossRef]
90. Sleep, N. Lithospheric Heating by Mantle Plumes. *Geophys. J. R. Astron. Soc.* **1987**, *91*, 1–11. [CrossRef]
91. Gurnis, M. Large-scale mantle convection and the aggregation and dispersal of supercontinents. *Nature* **1988**, *332*, 695–699. [CrossRef]
92. Segev, A. Synchronous magmatic cycles during the fragmentation of Gondwana: Radiometric ages from the Levant and other provinces. *Tectonophysics* **2000**, *325*, 257–277. [CrossRef]
93. Davies, G.F. ocean bathymetry and mantle convection large-scale flow and hotspots. *J. Geophys. Res.-Solid Earth Planets* **1988**, *93*, 10467–10480. [CrossRef]

94. Marzoli, A.; Callegaro, S.; Dal Corso, J.; Davies, J.H.F.L.; Chiaradia, M.; Youbi, N.; Bertrand, H.; Reisberg, L.; Merle, R.; Jourdan, F., The Central Atlantic Magmatic Province (CAMP): A Review. In *The Late Triassic World: Earth in a Time of Transition*; Tanner, L.H., Ed.; Springer: Cham, Switzerland, 2018; pp. 91–125. [CrossRef]
95. Westaway, R. Forces associated with mantle plumes. *Earth Planet. Sci. Lett.* **1993**, *119*, 331–348. [CrossRef]
96. Hartley, R.A.; Roberts, G.G.; White, N.; Richardson, C. Transient convective uplift of an ancient buried landscape. *Nat. Geosci.* **2011**, *4*, 562–565. [CrossRef]
97. Jordan, T.H. Composition and development of the continental tectosphere. *Nature* **1978**, *274*, 544–548. [CrossRef]
98. Conrad, C.P.; Lithgow-Bertelloni, C. Influence of continental roots and asthenosphere on plate-mantle coupling. *Geophys. Res. Lett.* **2006**, *33*. [CrossRef]
99. Karato, S.i.; Wu, P. Rheology of the upper mantle: A synthesis. *Science* **1993**, *260*, 771–778. [CrossRef] [PubMed]
100. Semple, A.G.; Lenardic, A. Plug flow in the Earth's asthenosphere. *Earth Planet. Sci. Lett.* **2018**, *496*, 29–36. [CrossRef]
101. Wilson, J.T. Did the Atlantic close and then re-open? *Nature* **1966**, *211*, 676–681. [CrossRef]
102. Burke, K.; Dewey, J.F. The Wilson Cycle. In Proceedings of the Geological Society of America, Northeastern Section, 10th Annual Meeting, Abstracts with Programs, Syracuse, NY, USA, 6–8 March 1975; p. 48.
103. Dunbar, J.; Sawyer, D. How pre-existing weaknesses control the style of continental breakup. *J. Geophys. Res.* **1989**, *94*, 7278–7292. [CrossRef]
104. Vauchez, A.; Barruol, G.; Tommasi, A. Why do continents break-up parallel to ancient orogenic belts? *Terra Nova* **1997**, *9*, 62–66. [CrossRef]
105. Audet, P.; Bürgmann, R. Dominant role of tectonic inheritance in supercontinent cycles. *Nat. Geosci.* **2011**, *4*, 184–187. [CrossRef]
106. Wilson, R.; Houseman, G.; Buiter, S.; McCaffrey, K.; Dore, A. Fifty years of the Wilson Cycle Concept in Plate Tectonics: An Overview. *Geol. Soc. Lond. Spec. Publ.* **2019**, *470*, 1–17. [CrossRef]
107. Carey, S.W. The tectonic approach to continental drift. In *Continental Drift—A Symposium*; Carey, S.W., Ed.; University of Tasmania: Hobart, Australia, 1958; pp. 177–363; Expanding Earth from p. 311 to p. 349.
108. O'Neill, C.; Müller, D.; Steinberger, B. On the uncertainties in hot spot reconstructions and the significance of moving hot spot reference frames. *Geochem. Geophys. Geosyst.* **2005**, *6*, Q04003. [CrossRef]
109. Steinberger, B.; Torsvik, T.H. Absolute plate motions and true polar wander in the absence of hotspot tracks. *Nature* **2008**, *452*, 620–623. [CrossRef] [PubMed]
110. Müller, R.D.; Royer, J.Y.; Lawver, L.A. Revised plate motions relative to the hotspots from combined Atlantic and Indian Ocean hotspot tracks. *Geology* **1993**, *21*, 275–278. [CrossRef]

minerals

MDPI

Article

Reconstruction of the Magma Transport Patterns in the Permian-Triassic Siberian Traps from the Northwestern Siberian Platform on the Basis of Anisotropy of Magnetic Susceptibility Data

Anton Latyshev [1,2,*], Victor Radko [3], Roman Veselovskiy [1,2], Anna Fetisova [1,2], Nadezhda Krivolutskaya [4] and Sofia Fursova [1,2]

[1] Schmidt Institute of the Physics of the Earth, Russian Academy of Sciences, 10 Bolshaya Gruzinskaya, 123242 Moscow, Russia
[2] Faculty of Geology, Lomonosov Moscow State University, 1 Leninskie Gory, 119991 Moscow, Russia
[3] Noril'skgeologiya LLC, 11 Grazhdansky Prospect, 195220 Saint Petersburg, Russia
[4] Vernadsky Institute of Geochemistry and Analytical Chemistry, Russian Academy of Sciences, 19 Kosygina St., 119991 Moscow, Russia
* Correspondence: anton.latyshev@gmail.com

Abstract: Patterns of magma transport during the emplacement of Large Igneous Provinces (LIPs) are extremely important for the understanding of their formation. The Permian-Triassic Siberian Traps LIP is considered to be one of the largest in the Phanerozoic; however, mechanisms of magma transfer within and under the crust are still poorly studied. This problem is vital for the reconstruction of the dynamics of magmatic activity and eruption styles, ascertaining the position of magmatic centers and feeding zones, and conception of ore deposits genesis. Here, we present the detailed results of anisotropy of magnetic susceptibility measurements for lava flows and intrusions from the Noril'sk and Kulumbe regions (the northwestern Siberian platform). We reconstructed patterns of magma flow based on the magnetic fabric analysis of more than 100 sites. Distribution of the magnetic lineation in the studied intrusions and flows points out that the lateral magma flow of NW-SE directions was predominant. Our results support the idea of a magma-controlling role of Noril'sk-Kharaelakh and Imangda-Letninskiy regional fault zones. Furthermore, the reconstructed geometry of magma transport in intrusions is contrasting with that in the Angara-Taseeva depression (the southern part of the LIP) due to the presence of the long-lived mobile zones in the northwestern Siberian platform.

Keywords: Siberian Traps; Large Igneous Province; anisotropy of magnetic susceptibility; anisotropy of anhysteretic remanent magnetization; rock magnetic properties; magma flow reconstruction; Permian; Triassic; Cu-Ni-PGE deposits; Noril'sk

1. Introduction

The Siberian Traps Large Igneous Province (LIP) is one of the largest continental areas of mafic within-plate magmatic activity in the Phanerozoic. This province is considered as a reference example of LIPs and can be used for testing of various models of flood basalt volcanism. At this moment, the concept of mantle plumes is dominant [1,2], though several alternate hypotheses have been proposed as well [3–5]. However, the detailed scheme of magma transport patterns within the crust for the Siberian Traps has not been developed yet. For instance, most models suggest the position of the plume head under the Noril'sk region, in the northwestern margin of the Siberian platform [6], while other hypotheses set the center of the plume under the West Siberian basin [7], the Yenisey-Khatanga basin [8], or at the junction of these basins [9]. Furthermore, it is unclear how the huge volume of magma spread within and under the crust. The significant role of a lateral magma

transport via the sill complexes, exposed in the periphery of the Tunguska syncline, is supposed [10]. Nevertheless, structural data on the magma flow patterns and locations of regional magmatic centers are still sparse [11]. Given that the Siberian Traps LIP is subdivided into several regions with different compositions of volcanic rocks, tectonic structures of the crust, and, hence, conditions of magmatic activity (Figure 1A; [12,13]), this problem is to be resolved.

It was shown that detailed investigation of anisotropy of magnetic susceptibility (AMS) in mafic lava flows and intrusions is an effective tool for the reconstruction of magma transport patterns and modes of emplacement of intrusions within LIPs [14–18]. However, for the Siberian Traps, results of AMS measurements are sparse and represent mainly data on mafic sills from the southern and eastern periphery of the province [19,20] and only the preliminary data on lava flows [21] and intrusions [22] from the northwestern part of the platform.

Here, we present the detailed results of AMS measurements in a number of lava flows and sheet intrusions from the Noril'sk and Kulumbe regions of the northwestern Siberian platform.

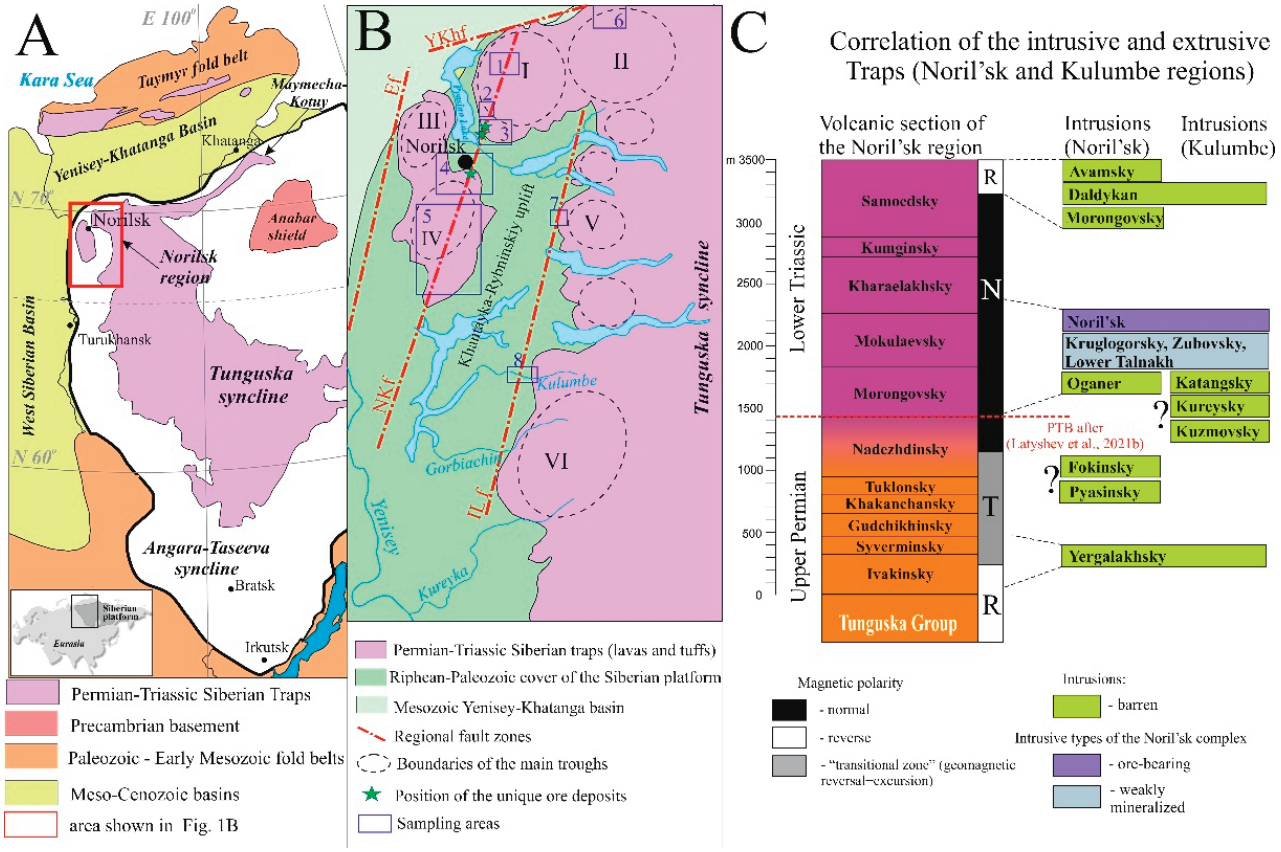

Figure 1. (**A**) Sketch map of the Siberian Traps within the Siberian platform and surrounding areas. (**B**) Position of the studied areas. Regional faults: NKf—Noril'sk-Kharaelakh fault, ILf—Imangda-Letninskiy fault, Ef—Yenisey fault, YKhf—Yenisey-Khatanga fault; main troughs: I—Kharaelakh, II—Icon, III—Vologochan, IV—Nori'lsk, V—Imangda, VI—Nirungda; sampling areas: 1—Talovaya, 2—Mokulay, 3—Kharaelakh, 4—Noril'sk, 5—South Noril'sk, 6—Icon, 7—Imangda, 8—Kulumbe. (**C**) Correlation scheme of the intrusive and extrusive Siberian Traps for the Noril'sk and Kulumbe regions. PTB—Permian-Triassic boundary; magnetic stratigraphy and correlation scheme after [23–25].

2. Geological Setting

The Noril'sk region is located in the northwestern margin of the Siberian platform and occupies the key position within the LIP due to the maximal thickness of products

of volcanic activity (up to 3.5 km [26]), highly diverse composition of volcanic rocks and intrusions, and presence of the unique Cu-Ni-PGE deposits, related to layered intrusive bodies. Main tectonic structures of the Noril'sk region are subcircular and elliptical depressions known as "troughs", filled by voluminous tuff-lava piles (Noril'sk, Kharaelakh, Imangda troughs, etc.) and rampart-like uplifts (Khantayka-Rybninskiy and Pyasino swells). Main disjunctive features are regional faults of NE strike—Noril'sk-Kharaelakh, Imangda-Letninskiy, and other faults (Figure 1B). The Permian-Triassic volcanic sequence comprises eleven formations, associated with eight intrusive complexes (Figure 1C). All world-class Cu-Ni-PGE deposits are related to the only one Noril'sk intrusive type of the same complex and located near the Noril'sk-Kharaelakh fault zone.

Petrological and geochemical features of volcanic and intrusive units were reported by many authors [26–32]. The volcanic sequence is often subdivided into the Lower Series, mainly composed of high-Ti lavas (from Ivakinsky to Gudchikchinsky formations), the Middle (or "transitional") Series (Khakanchansky-Nadezhdinsky formations), and the Upper Series, composed of low-Ti lavas (from Morongovsky to Samoedsky formations). It was also shown that ore-bearing intrusions of the Noril'sk type are close to the Morongovsky-Mokulaevsky formations in their geochemical features; however, their possible genetic links are still disputed. While some authors suppose that ore-bearing intrusions were formed in open magmatic systems as shallow conduits to volcanic flows [33–37], others suggest that intrusions were emplaced as blind bodies and do not have a direct connection with lavas [38–41].

According to a complex of geochronological, paleomagnetic, and paleontological data, it is generally accepted that formation of the main volume of Siberian Traps in the Noril'sk region took place during a short period of time (less than 1 Myr) at the Permian-Triassic boundary [23,25,42–45]. Magmatic activity was not monotonous but occurred as a series of brief intense volcanic pulses divided by more prolonged gaps [46,47].

The Kulumbe (or Kulyumber in some publications) river area is located at the junction zone of the Khantayka-Rybninskiy swell and the western slope of the Tunguska syncline. It is studied much less than the Noril'sk region, but some representative data on whole-rock chemistry for the Permian-Triassic rocks of this area have recently been published [48,49] Due to its transitional position, the Kulumbe region comprises intrusive complexes typical of the Noril'sk region (Noril'sk, Yergalakhsky, Daldykan) and the Tunguska syncline (Katangsky, Kuzmovsky). In addition, intrusions of the specific composition (the Kureysky complex) are present.

Despite the long investigation of the Noril'sk region, patterns of the magma flow during the emplacement of Traps in this area are poorly constrained. The dominant idea is that Noril'sk-Kharaelakh and Imangda-Letninskiy faults and other regional fault zones are the main magma-feeding and ore-controlling structures [50–55]. Preliminary results of AMS studies in the Noril'sk and Kulumbe regions [21,22] support this hypothesis. An alternate model suggests that magma spread along the transform fault zone transverse to Noril'sk-Kharaelakh fault [56]. Based on isopach maps for volcanic formations, some authors suppose that the center of volcanic activity migrated through time [11,32]. Within this study, we analyzed the detailed data on anisotropy of magnetic susceptibility for the intrusions and lava flows from the northwestern Siberian platform and reconstructed magma flow patterns for the Siberian Traps in these regions.

3. Sampling Areas

In total, we collected oriented samples at 195 sites, representing intrusions and lava flows from the northwestern Siberian platform. Paleomagnetic data for some of these bodies were reported before [22–25,49,57,58], and the remaining results will be published elsewhere. A brief description of sampled sites is given below.

The *Talovaya area* is located in the north of the Kharaelakh trough. The upper part of the volcanic sequence of Noril'sk (the Kumginsky and Samoedsky formations) is exposed here. We collected samples from 21 lava flows of the Samoedsky Formation and the

uppermost flow of the Kumginsky Formation in the two most complete sections in the Verkhnyaya Talovaya (sites sm1_21–sm9_21) and Nizhnyaya Talovaya (sites km10_21, sm11_21–sm22_21) river valleys. Lava flows are flat lying (dip angles are usually less than 10°), composed of basalts, and vary from 5 to 20 m in thickness (Figure 2A).

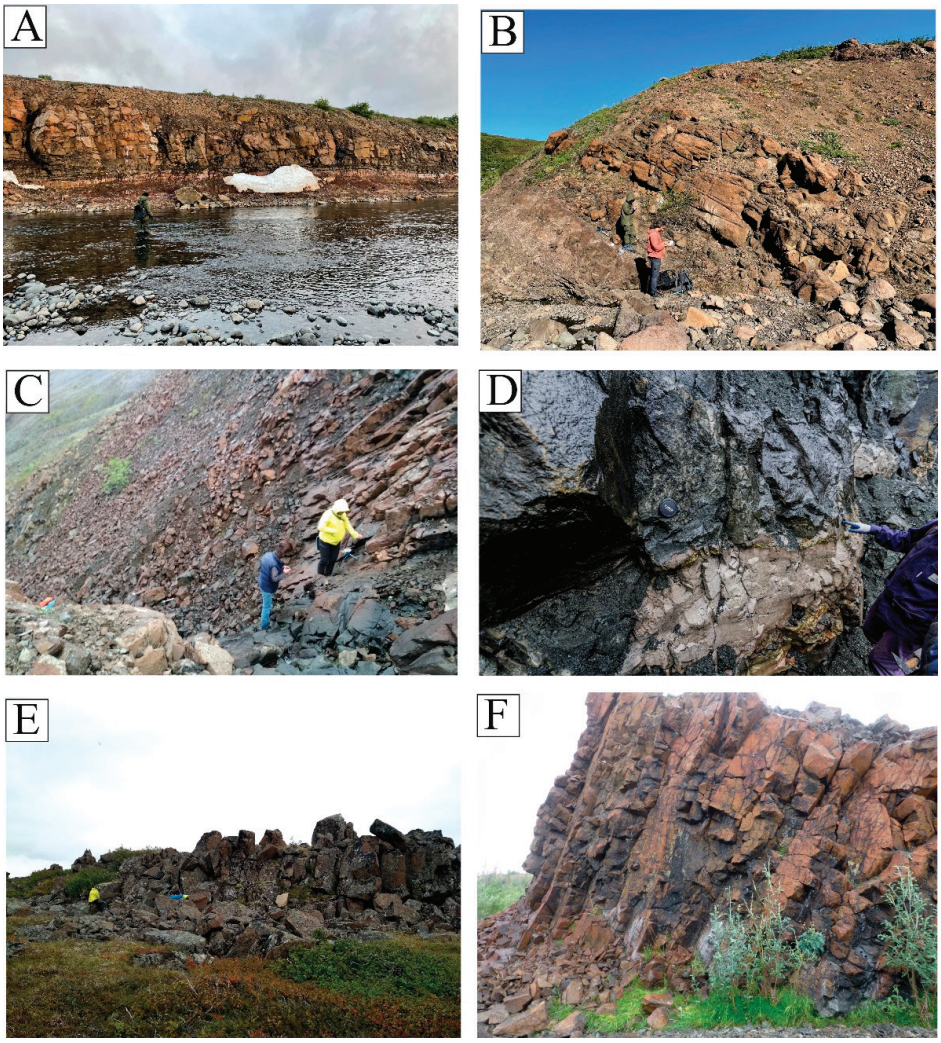

Figure 2. (**A**) Basaltic lava flow of the Samoedsky Formation, the Verkhnyaya Talovaya river; site sm22_21. (**B**) Basaltic lava flow of the Kharaelakhsky Formation, the Mokulay section; site kh24_21. (**C**) Intrusion of Zayachiy Creek, the Listvyanka gorge; site RZ1. (**D**) Hornfels from the bottom of the Noril'sk-1 intrusion, the open pit "Medvezhiy Creek"; site 14.2_17. (**E**) The Arylakh intrusion, Icon trough; site AR3. (**F**) Sill of the Yergalakhsky complex, the Imangda river; site I6.

The *Mokulay section* is composed of basaltic lava flows exposed along the Mokulay Creek (western slope of the Kharaelakh plateau). We sampled here 17 lava flows from the Mokulaevsky Formation (mk1_19–mk24_19) and 6 flows from the Kharaelakhsky Formation (kh25_19–kh26_26). Flows dip to the NE with angles of about 25–45° and are 5–80 m thick (Figure 2B).

The *Kharaelakh area* comprises ore-bearing intrusions sampled in underground mines near the town of Talnakh and sills, dikes, and lava flows in the southwestern part of the Kharaelakh trough. The ore-bearing Kharaelakh intrusion was sampled at 11 sites (16_17, 23_17–27_17, 37_17–41_17) in the Oktyabrskiy underground mine, including barren and ore-bearing gabbro-dolerites, hornfels, and massive ores. The ore-bearing Talnakh intrusion was sampled at 12 sites, representing various igneous rock types, skarns, and hornfels (sites 42_17–50_17) from the Skalisty underground mine and leucogabbro apophysis exposed near

the town of Talnakh (sites 20_17–22_17). The intrusion of Zayachiy Creek (the Kruglogorsky intrusive type), which is considered to be the apophysis of the Talnakh intrusion, was sampled at nine sites in outcrops along the creeks of Ugolniy (site 27_19ZR), Zayachiy (9_16–10_16, 12.1_17–12.2_17), Taliy (10_17), and Listvyanka (RZ1–RZ3) (Figure 2C). The description of intrusions and paleomagnetic data are given in [23].

We also collected samples from thin dikes and sills of the Daldykan (four sites: 8_16, 11.2_16, 3.2_17, 4_17) and Oganer (four sites: 1_17–3.3_17) complexes. Sills of the Yergalakhsky complex cut the coal-bearing sandstones of the Tunguska group near the foot of the Kharaelakh plateau. These sills were sampled at 13 sites (5_16–7_16, 11.1_16, 11.4_16, 5_17–9_17). The descriptions of these intrusions and paleomagnetic data are given in [25].

Finally, in the Kharaelakh area, we sampled lava flows of the Ivakinsky (site 11.3_16, the Zayachiy Creek), Syverminsky (9_16sv1–9_16sv2, the Zayachiy Creek), and Mokulaevsky formations (mk1_18–mk4_18, the Olor Creek). In total, 60 sites were sampled in the Kharaelakh area.

The Noril'sk area comprises the northern part of the Noril'sk trough, the eastern part of the Vologochan trough, and slopes of the Pyasino uplift. In the Noril'sk trough, we collected samples from the ore-bearing intrusion Noril'sk-1 at 11 sites (13.1_17–19_17) in the open pit "Medvezhiy Creek" (Figure 2D). Satellites of these bodies, Noril'sk-2 and Chernogorsky intrusions with subeconomic mineralization, were sampled at five and six sites, respectively (28_17–36_17, 12_16, 20_16). In addition, the nearby Kruglogorsky intrusion (three sites: 13_16, 15_16, 16_16) and sill of the Yergalakhsky complex (four sites: 14_16, 17_16–19_16) were sampled in the same area.

In the Vologochan trough, we sampled the sill-like intrusion in the Ambarnaya river valley (site 4_16) and four host lava flows of the Morongovsky Formation (sites 4f1_16–4f6_16). Flows have thickness up to 10 m and flatly dip to the SW.

Finally, the sill of Oganer cutting the Silurian sediments was sampled in four closely located sites (1_16, 2_16, 11.1_17, 11.2_17) near the hospital of Oganer. In total, we collected samples from 38 sites in the Noril'sk area (please see [23,25] for the detailed data).

The South Noril'sk area is located in the southern part of the Noril'sk trough. Four intrusions from different parts of the Noril'sk region were studied. The intrusion of the Ruinnaya Mountain (Morongovsky complex) cuts basalts of the Mokulaevsky Formation and is up to 70 m thick. We collected samples from this intrusion at three sites (18_19–20_19), representing layered and tholeiitic gabbro-dolerites. A possible coeval sheet intrusion of the Daldykan complex was sampled northward of the Ruinnaya Mountain (site 17_19). The sill-like sheet of the Kruglogorsky type (about 50 m thick) is located within basaltic flows of the Nadezhdinsky Formation and possibly represents the apophysis of the South Noril'sk intrusion. We sampled this intrusion at three closely located sites (14_19–16_19). Finally, we collected samples at two sites (B12, B13) from leucogabbro and gabbro-dolerites of the Burkan Mountain intrusion (the Noril'sk type). This intrusion is located within the Paleozoic sediments and is about 40 m thick in the sampling area.

The Icon area is located 150 km NE of Noril'sk, within the Icon trough. The Arylakh layered intrusion (Figure 2E) with weak mineralization (the Noril'sk type) was sampled at seven sites (AR1–AR7). This intrusion has complicated morphology, cuts basalts of Tuklonsky, Nadezhdinsky, and Morongovsky formations, and exceeds 40 m in thickness. We also collected samples from the nearby barren intrusion of the Noril'sk type (site 28_18) and two dikes of the Avamsky complex (sites 24_18 and 25_18).

The Imangda area comprises the western flank of the Imangda trough. We collected samples from the Imangda weakly mineralized intrusion (I3, I4) and Khyukta sill (I2), which are attributed to the Noril'sk type. Two sills referred to the Oganer (I5), and Yergalakhsky (I6) complexes were sampled as well (Figure 2F). All these intrusions conformably lay within the Paleozoic sediments, flatly dip to the east, and are from 15 to 40 m in thickness. In addition, basalts of the Tuklonsky Formation near the contact of the Rudnaya dike were sampled at site I1.

In the Kulumbe region, Permian-Triassic intrusions are exposed in the western slope of the Nirungda trough and conformably lay among the Paleozoic sedimentary rocks, flatly dipping to the east. Rarely, intrusions cut the lowermost flows of the Syverminsky Formation. Intrusions are composed of dolerites and gabbro-dolerites and are from 5–6 to 60 m in thickness. The tectonic structure of the region is complicated by the regional Imangda-Letninskiy fault zone, which extends northeast and limits the Khantayka-Rybninskiy uplift. We collected samples from 27 intrusions, representing the Katangsky (13 sites), Kureysky (5 sites), Daldykan (5 sites), Yergalakhsky (site K4), and Kuzmovsky (site K11) complexes and Kruglogorsky (site K8–Iltyk intrusion) and Noril'sk (site K7—Siluriyskaya intrusion) types.

4. Materials and Methods

The oriented samples were collected as drill cores or as hand blocks. The orientation of samples was performed using the magnetic and, when possible, sun compasses in natural outcrops and open pits. In the underground mines, we used mine surveying marks and a homemade system based on a laser theodolite and inclinometer for the precise orientation of samples. The local magnetic declination was calculated using the IGRF model (13th generation).

The rock-magnetic procedures were carried out using the equipment of the Shared Research Facilities Center "Petrophysics, geomechanics and paleomagnetism" Schmidt Institute of Physics of the Earth (IPE RAS, Moscow, Russia) [59]. Anisotropy of magnetic susceptibility (AMS) was measured by the kappa-bridge MFK-1FA using Safyr 7 software (AGICO, Brno, Czech Republic). The processing of the results was performed with Anisoft42 software using Jelinek statistics [60]. To analyze the AMS ellipsoid, Pj (corrected degree of anisotropy) and T (ellipsoid shape) parameters were used [61].

Thermomagnetic Ms(T) curves were measured using a vibrating magnetometer constructed by Yu.K. Vinogradov (the Borok Geophysical Observatory, Yaroslavl region, Russia) with an applied magnetic field of 0.5 T. Thermal dependence of the magnetic susceptibility was measured using a CS-3 heating add-on to the MFK-1FA kappa-bridge. The hysteresis loops, back-field demagnetization curves of saturation IRM, and first order reversal curves were recorded using the vibrating sample magnetometer PMC MicroMag 3900 (Lake Shore Cryotronics, USA) at room temperature in a 0.5 T saturating field. The domain structure of ferromagnetic grains was determined according to the Day–Dunlop plot [62,63] and FORC diagrams [64].

Anisotropy of anhysteretic remanent magnetization (AARM) measurements were carried out using an AF demagnetizer LDA5 and spinner magnetometer JR6 (AGICO). The samples were gradually demagnetized on LDA5 at AC max amplitude of 200 mT with linear decrease, then samples were magnetized at AC of 100 mT and DC max amplitude of 500 mT in C-mode (6 directions). After magnetization in each direction in the C-mode, the anisotropy was recorded on a spinner magnetometer JR6. The processing of results was performed with Anisoft42 software.

5. Results

5.1. Anisotropy of Magnetic Susceptibility

The majority of studied rocks have a low degree of anisotropy of magnetic susceptibility Pj. In about 80% of sites, Pj is less than 1.06 (Supplementary Material Table S1; Figure 3). Only 7% (12 sites) demonstrate Pj > 1.1. Low values of the Pj parameter are typical of mafic rocks with a magnetic fabric of primary magmatic origin where magnetite or titanomagnetite are the main magnetic minerals [65]. Absence of the strong metamorphic alteration and signs of deformations in most of the rocks confirm the magmatic genesis of the magnetic fabric. The highest degree of anisotropy (Pj > 1.1) is demonstrated mainly by sulfide-bearing rocks of the Noril'sk and Talnakh intrusions, massive sulfide ores, and hornfels with superimposed magnetic fabric, affected by the emplacement of nearby intrusions.

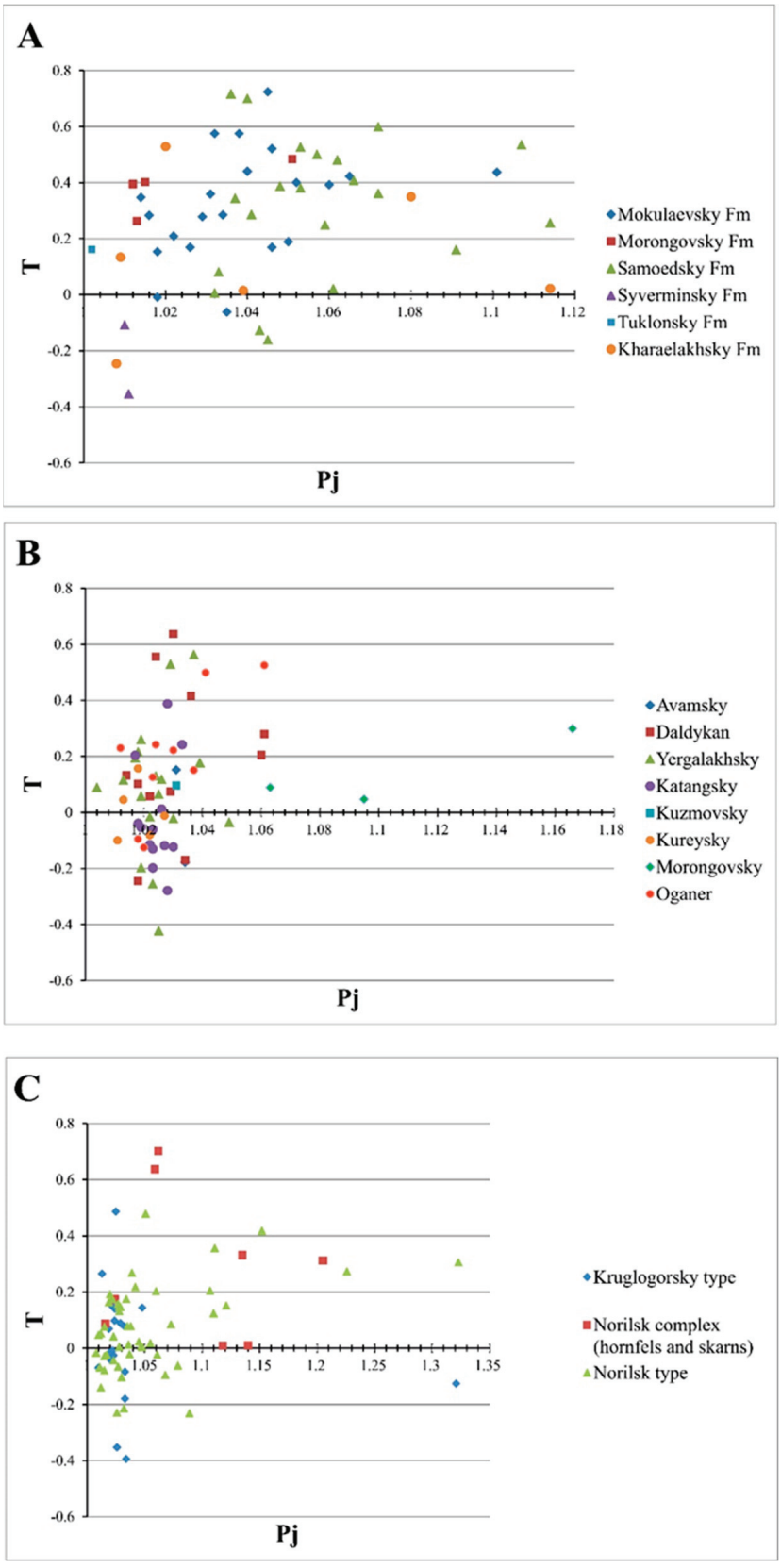

Figure 3. Jelinek plots for the studied intrusions and lava flows. Pj and T—site-mean values for the corrected degree of anisotropy and shape parameter, respectively. (**A**) volcanic formations; (**B**) intrusive complexes; (**C**) ore-bearing intrusions of the Noril'sk complex and their contact zones.

Values of the T parameter characterizing the shape of the AMS ellipsoid [61] vary from −0.4 to 0.5 for most sites. About 70% of sites demonstrate the oblate AMS ellipsoid (T > 0); herewith, the most oblate ellipsoid (T > 0) is typical of the Mokulaevsky and Samoedsky lava flows (Figure 3A,B). The prolate form of the AMS ellipsoid (T < 0) in mafic rocks is often interpreted as a result of the magma flow, while the oblate ellipsoid is considered to result from static processes such as compression during cooling, crystallization in situ, or gravitational differentiation [66,67]. As seen from Figure 3C, most of the sites with the highest degree of anisotropy demonstrate the oblate form of the ellipsoid. Thus, we suggest that sulfide mineralization leads to the highly anisotropic oblate ellipsoid of AMS.

The normal type of magnetic fabric (N-type), when the minimal axis of the AMS ellipsoid (K3) is orthogonal to the contact of lava flow or intrusion and two other axes lie in the plane of the magmatic body, was identified for 102 sites (~52%). The major part of lava flows from the Talovaya and Mokulay sections, and many sill-like intrusions from different regions, demonstrate this type of magnetic fabric (Figure 4A–C). In these sites, the K3 axis is subvertical or steep, while the two other axes have a flat orientation and lie in the plane of the sill or lava flow. In some sites, magnetic lineation (the maximal K1 axis of the AMS ellipsoid) is tightly grouped; in others, it forms a great-circle arc with the directions of the intermediate K2 axis. Imbrication of the K1 axis from the contact plane is commonly negligible, but, for some sites, it reaches 20–25°, which could have been caused by a turbulent magma flow.

In 33 sites (17%), we identified the inverse, or reverse, type of the magnetic fabric (R-type). In those sites, the K1 axis is orthogonal to the contact plane and the two other axes lie in the flow or intrusion plane. This behavior of the AMS ellipsoid was found in flat intrusions of the Yergalakhsky and Katangsky complexes and Noril'sk type, as well as in some other sites (Figure 4D–F). The possible reasons for the magnetic fabric inversion are discussed below.

An intermediate type of the magnetic fabric (I-type), when the medium axis K2 is normal to the contact, was identified in 17 sites (9%). This behavior of the AMS ellipsoid occasionally occurs in sills, dikes, and lava flows from different regions (Figure 4 G,H). In the remaining 42 sites (22%), axes of the AMS ellipsoid are either scattered (S-type) or diagonal (D-type) to the contact (Figure 4I–K). Generally, this fabric is typical of the sulfide-bearing rocks or sites with the lowest degree of anisotropy (Pj < 1.01). Sites with scattered or diagonal magnetic fabrics are not used in the further interpretation below.

Thus, studied intrusions and lava flows demonstrate variable and sometimes complicated magnetic fabric. To reconstruct the directions of magma transport, we selected the most relevant sites using the following criteria:

1. We used an F-test [68] inbuilt in the program "Safyr 7" to exclude the unreliable measurements. This test shows whether differences between measured principal susceptibilities are great enough compared with measurement errors. Usually, the critical value of the F parameter is estimated as ~3.4–4 [69,70]. We used a more conservative approach and excluded specimens with F < ~100 from further calculations. This approach led to a reduction of the within-site scatter for some intrusions.
2. Only sites with N-type magnetic fabric were analyzed. For those sites, the magnetic lineation (maximal axis K1 of the AMS ellipsoid) was interpreted as the magma flow orientation, following [14,15,71] and many others. An alternate method suggested in [72] is to use an imbrication of magnetic foliation with respect to contacts of the magmatic body. However, due to sampling conditions and the complex morphology of many intrusions, it was not possible to apply this method.
3. Samples with the essential amount of sulfides (pyrrhotite, pyrite, etc.) and a high degree of anisotropy were excluded from the analysis. Thus, the significant majority of sites representing ore-bearing intrusions and their contact zones was not used for the reconstruction.

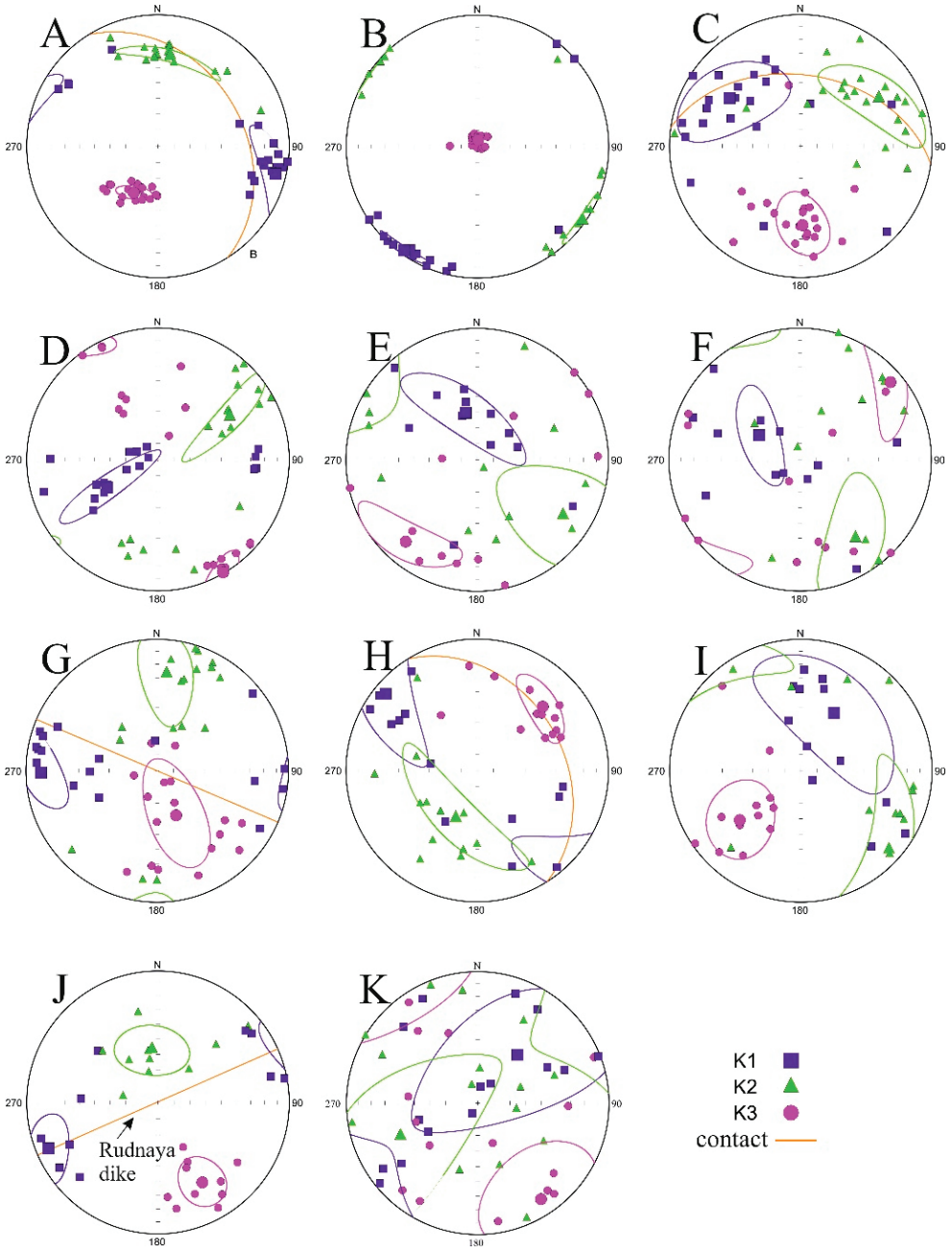

Figure 4. Examples of AMS ellipsoids for sites with various magnetic fabrics. Geographic coordinate system. (**A**) Site mk7_19, Mokulaevsky Formation, basaltic lava flow, N-type. (**B**) Site 11.2_17, Oganer sill, gabbro-dolerites, N-type. (**C**) Site 12.2_17, intrusion of Zayachiy Creek, leucogabbro, N-type. (**D**) Site 19_19, Ruinnaya intrusion (Morongovsky complex), gabbro-dolerites, R-type. (**E**) Site 49_17, Talnakh intrusion, gabbro-dolerites, R-type. (**F**) Site 7–16, sill of the Yergalakhsky complex, trachydolerites, R-type. (**G**) Site 24_18, dike of the Avamsky complex, dolerites, I-type. (**H**) Site mk10_19, Mokulaevsky Formation, basaltic lava flow, I-type. (**I**) Site 16_17, hornfels from the contact of the Kharaelakh intrusion, D-type. (**J**) Site I1, basalts of the Tuklonsky Formation nearby the Rudnaya dike, D-type. (**K**) Site AR3, Arylakh intrusion, gabbro-dolerites, S-type.

5.2. Rock-Magnetic Properties

We performed a detailed rock-magnetic investigation to determine the composition of magnetic minerals and their domain structure in the studied rocks. Based on rock-magnetic features, all samples from different intrusions can be divided into three groups. The full description of magnetic properties is presented in [23–25]; a brief summary is given below.

In the first group, magnetite or low-titanium titanomagnetite are the main magnetic minerals. Temperature dependencies of the saturation magnetization (Ms(T)) and the magnetic susceptibility (K(T)) demonstrate the predominance of the single magnetic phase with Curie temperatures of about 570–590 °C or 500–540 °C (Figure 5A–D). Occasionally, a small amount of hematite is identified at K(T) curves by the decrease of magnetic susceptibility near temperatures of about 670 °C. In a few samples, two magnetic phases are identified: magnetite and titanomagnetite or maghemite (Figure 5E). Many samples of this group are stable to heating, but, sometimes, magnetic susceptibility decreases after cooling, probably due to the decay or oxidation of magnetite or to the presence of some amount of maghemite (Figure 5F). These rock-magnetic properties are typical of the Siberian Traps and were reported before, both for lavas [43] and intrusions [23,73,74]. The majority of samples from lava flows and barren or weakly mineralized intrusions belong to this type.

The main feature of the second group is the presence of iron sulfides, which are identified by the thermomagnetic curves. Pyrrhotite occurs both as monoclinic and hexagonal forms. The former is demonstrated at Curie temperatures of about 300 °C to 350 °C (Figure 5G,H); the latter is identified by λ-peak [75] at temperatures of about 180 °C to 250 °C in the thermomagnetic curves (Figure 5I). In addition, pyrite is identified by the growth of magnetic susceptibility above 400 °C due to magnetite formation. After heating up to 700 °C, iron sulfides are strongly oxidized, causing the increase in all magnetic parameters in cooling curves. Besides sulfides, some amount of magnetite is occasionally present in the samples of this group. Sulfide-bearing samples usually demonstrate high degrees of anisotropy and widely scattered distributions of AMS axes. Many sites from ore-bearing intrusions and their contact zones represent this group.

The third group comprises weakly magnetic samples from different bodies. The Ms(T) thermomagnetic curves demonstrate a concave shape, indicating the predominance of paramagnetic material (Figure 5I). The temperature dependencies of magnetic susceptibility allow us to observe a small amount of magnetite, hematite, pyrrhotite, or pyrite. After heating up to 700 °C, the amount of magnetite and, consequently, Ms and K values increase on cooling (Figure 5J). This type is occasionally identified in different rock types, mainly leucogabbro and hornfels from contact zones of ore-bearing intrusions.

Although values of hysteresis parameters vary in wide ranges for different intrusions and lava flows, in the Day–Dunlop plot, most of samples are located in the pseudo-single domain area and concentrated along the mixing curve of single-domain and multidomain grains [63]. This behavior of hysteresis parameters is typical of the Siberian Traps intrusions [23,25]. As seen from Figure 6A, samples with different types of magnetic fabric do not reveal any differences in hysteresis parameters. For the detailed analysis of the domain structure, first order reversal curves (FORC) were recorded for the selected specimens. According to FORC diagrams, in samples from lavas and intrusions, attributed to N-type of magnetic fabric, multidomain grains of low-coercive minerals (magnetite or low-titanium titanomagnetite) interacting with each other dominate the magnetic structure (Figure 6B,C). Gabbro-dolerites of the Ruinnaya intrusion (the Morongovsky complex, R-type AMS) demonstrate the presence of interacting particles of various domain structures, mainly of low-coercive mineral (Figure 6D). Basalts from the Samoedsky Formation (R-type AMS) show the predominance of single-domain or pseudo-single-domain grains of magnetite or titanomagnetite and presence of a small amount of interacting particles of very low-coercive mineral (possibly maghemite) (Figure 6E). Finally, in sulfide-rich rocks from the contact zone of the Kharaelakh intrusion, strongly interacting multidomain grains of very low-coercive magnetic phase (pyrrhotite) are predominant (Figure 6F).

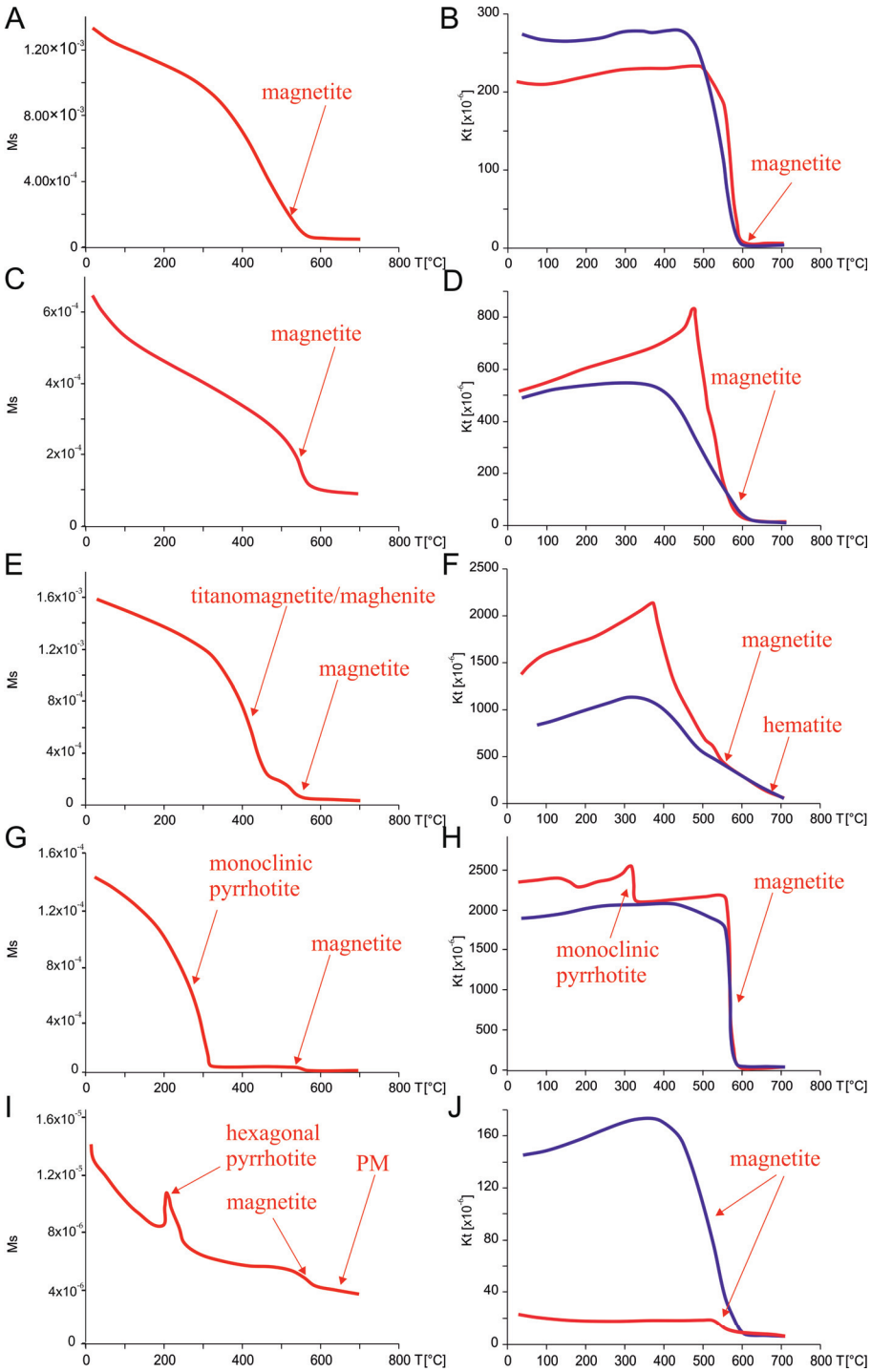

Figure 5. Representative curves of thermal dependence for the saturation magnetization (**A**,**C**,**E**,**G**,**I**) and magnetic susceptibility (**B**,**D**,**F**,**H**,**J**). Heating is shown in red, cooling in blue. (**A**) Sample 229, site mk19_19, basalts of the Mokulaevsky Formation, I-type. (**B**) Sample 160, site mk7_19, basalts of the Mokulaevsky Formation, N-type. (**C**) Sample 427, site 19_19, the Ruinnaya intrusion (Morongovsky complex), R-type. (**D**) Sample 57, site 4_17, dike of the Daldykan complex, I-type. (**E**) Sample 227, site sm12_21, basalts of the Samoedsky Formation, N-type. (**F**) Sample 18, site sm1_21, basalts of the Samoedsky Formation, R-type. (**G**) Sample ×57, site 49_17, gabbro-dolerites of the Talnakh intrusion, R-type. (**H**) Sample 696, site 26_17, Kharaelakh intrusion, R-type. (**I**) Sample ×18, site 47_17, skarns near the Talnakh intrusion, N-type. (**J**) Sample 333, site 13_16, Kruglogorsky intrusion, D-type.

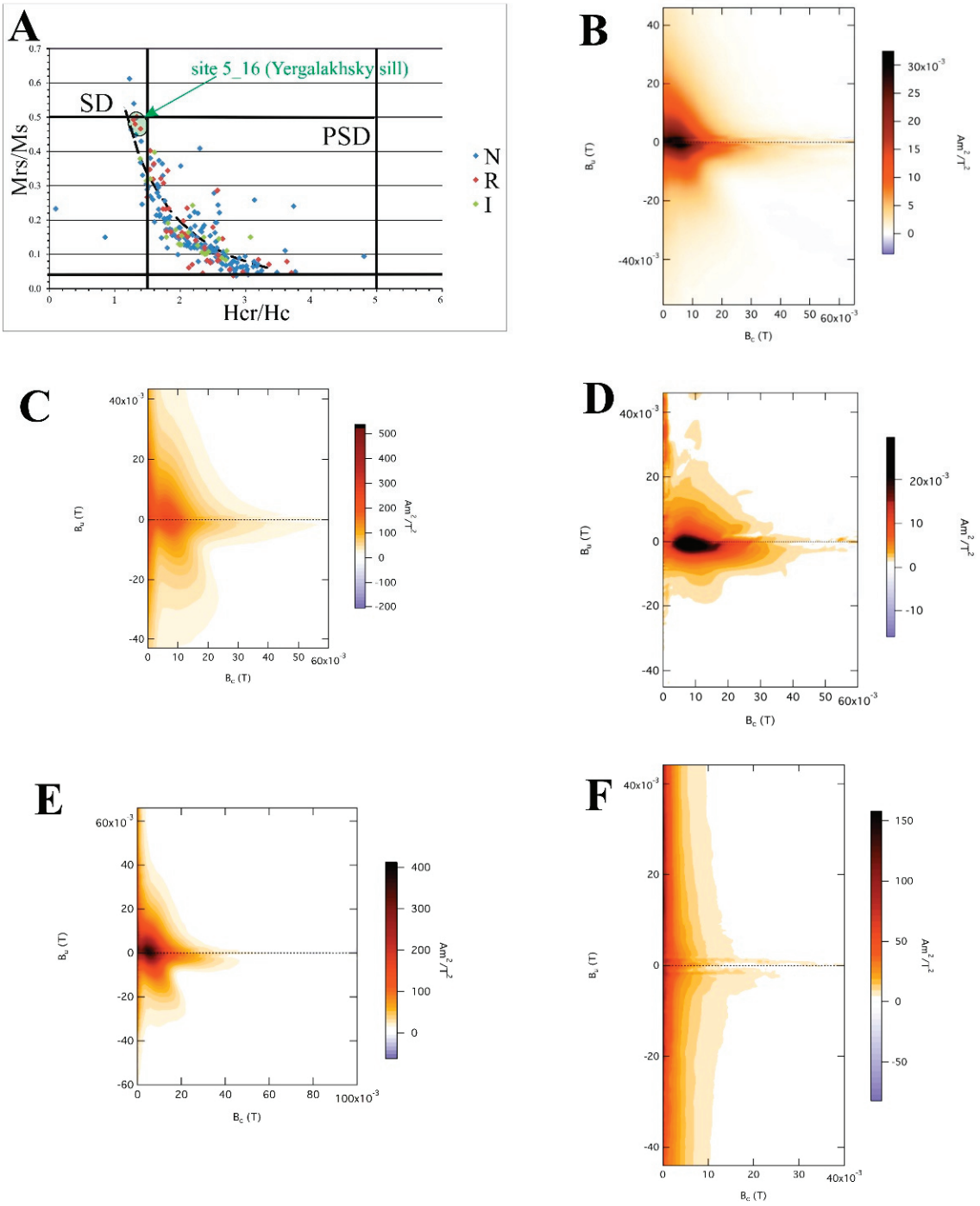

Figure 6. (**A**) Day–Dunlop plot. Sites with N-, R-, and I-types of magnetic fabric are shown in different colors. SD—single-domain; PSD—pseudo-single-domain; Ms—saturation magnetization; Mrs—remanent magnetization; Hc—coercive force; Hcr—remanent coercive force. (**B**–**F**) Representative FORC-diagrams. (**B**) Sample 295, site mk13_19, basalts of the Mokulaevsky Formation. (**C**) Sample 302, site 12.2_17, leucogabbro of the Zayachiy Creek intrusion. (**D**) Sample 427, site 19_19, the Ruinnaya intrusion (Morongovsky complex). (**E**) Sample 3, site sm1_21, basalts of the Samoedsky Formation. (**F**) Sample 622, site 16_17, hornfels near the Kharaelakh intrusion.

5.3. Anisotropy of Anhysteretic Remanent Magnetization

To isolate the contribution of ferromagnetic minerals from that of the para- and diamagnetic matrix, we measured anisotropy of anhystereric remanent magnetization (AARM) for the selected sites with various types of magnetic fabric (Table 1). Site-mean

corrected degree of AARM Pj varies from 1.1 to 1.6 and is somewhat higher than that of AMS (1.03–1.12 in the same sites), possibly due to elimination of the influence of the matrix [76]. The shape of the AARM ellipsoid differs from that for AMS and is prolate in 50% of sites (T > 0). Thus, predominance of oblate AMS fabric can partially be caused by paramagnetic minerals.

Table 1. Results of anisotropy of anhysteretic remanent magnetization measurements. N—number of samples, Pj—corrected degree of anisotropy, T—parameter of ellipsoid shape; R1, R2, R3—maximum, medium, minimum axes of AARM ellipsoid, respectively; D—declination; I—inclination. Types of AARM fabric: N—normal, I—intermediate, D—diagonal.

Site	Object	Complex/Type	N	Pj	T	R1		R2		R3		AARM Type
						D	I	D	I	D	I	
11.2_16	dike	Daldykan	5	1.152	−0.122	88.2	12.8	247.4	76.4	357.1	4.7	N
24_17	Kharaelakh intrusion	Noril'sk	6	1.200	0.089	86.8	10.8	355.7	5.6	238.9	77.8	N
26_17	Kharaelakh intrusion	Noril'sk	8	1.620	0.158	158.4	24	274.5	44.7	49.7	35.7	D
48_17	Talnakh intrusion	Noril'sk	8	1.217	−0.199	68.8	21.5	244.3	68.4	338.2	1.5	I
5_16	sill	Yergalakhsky	7	1.145	0.166	153.1	1.7	62.5	18.8	248	71.1	N
Kul32	sill	Katangsky	7	1.100	0.264	116.4	22.7	5.8	40	228.1	41.4	N
Sm12_21	Lava flow	Samoedsky	9	1.149	0.208	267.4	17.6	4.5	21.2	141	61.8	N
Sm1_21	Lava flow	Samoedsky	8	1.103	−0.121	145.2	6.5	136.7	13.4	29.7	75.1	N

Gabbro of the Kharaelakh intrusion (site 24_17) and basalts of the Samoedsky Formation (site sm12_21) demonstrate coaxial AARM and AMS fabric. For both sites, minimal site-mean axes of AARM and AMS are steep or subvertical, and other axes are flat, corresponding to the N-type of anisotropy in layered intrusions and lava flows (Figure 7A,B). Thus, magnetic fabric in these sites is dominated by remanence-bearing minerals, mostly magnetite.

Near-contact gabbro-dolerites of the Talnakh intrusion (site 48_17) also show similar orientations of AMS and AARM axes. Both ellipsoids demonstrate subvertical magnetic foliation of W-E strike and horizontal magnetic lineation (Figure 7C). Since samples were collected near the bottom of the intrusion, we suggest that observed magnetic fabric reflects the local orientation of the contact surface.

Samples from the sill of the Yergalakhsky complex (site 5_16) and basaltic flow of the Samoedsky Formation (site sm1_21) demonstrate the inversion of magnetic fabric: R-type of AMS changes to N-type of AARM (Figure 7D,E). This phenomenon is well known and usually explained as a result of single-domain magnetite behavior [77]. Supporting this, samples from site 5_16 are close to the single-domain field in the Day–Dunlop plot (Figure 6A). Furthermore, the FORC diagram for a sample from site sm1_21 points out the presence of single-domain magnetite (Figure 6E). Thus, origin of the inverse magnetic fabric in the studied intrusions and lava flows can partly be explained by features of the domain composition. However, the majority of samples with R-type of AMS are rather far from the single-domain area in the Day–Dunlop plot (Figure 6A), hence, this hypothesis cannot be applied to all sites with inverse fabric.

The dike of the Daldykan complex (site 11.2_16) demonstrates another type of inversion of magnetic fabric. Unlike previous site, AMS fabric belongs to I-type with subvertical magnetic foliation, normal to dike walls. AARM measurement shows the N-type with horizontal magnetic lineation (Figure 7F). According to [78] or [79], this kind of magnetic

fabric can result from superposition of two different fabrics. These fabrics can be formed by two generations of magnetite or ferromagnetic and paramagnetic minerals.

In site kul32 (sill of the Katangsky complex), medium and minimal axes of the AARM ellipsoid form a girdle and change over compared with AMS fabric (Figure 7G). However, the maximal axis is similar for AARM and AMS ellipsoids and lies in the plane of intrusion. Since the magnetic lineation has the same orientation both in AARM and AMS fabrics, we suggest that it can be used for the magma flow reconstruction.

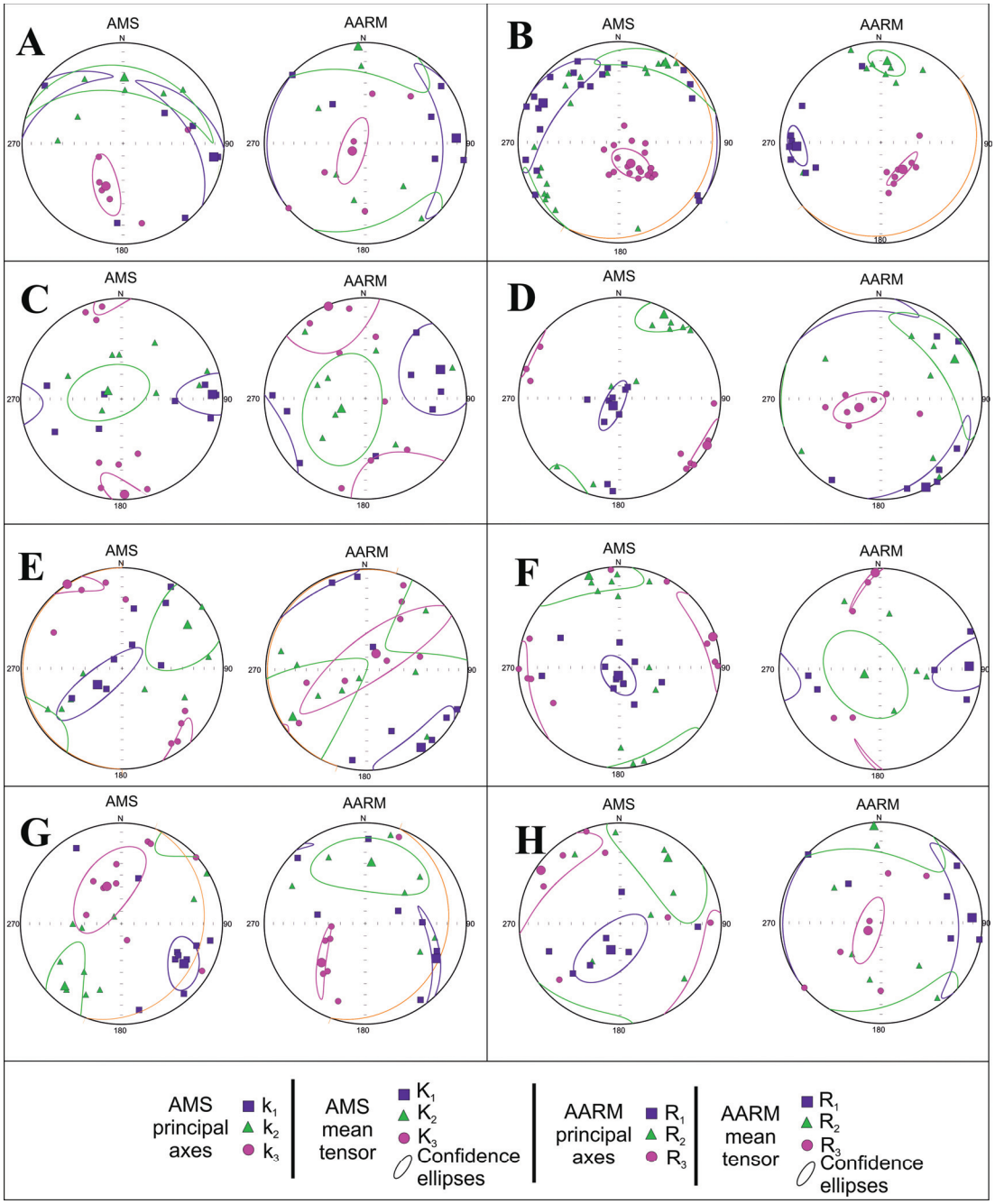

Figure 7. Comparison of AMS and AARM data for the selected sites. (**A**) Site 24_17, Kharaelakh intrusion, N-type of AMS. (**B**) Site sm12_21, lava flow of the Samoedsky Formation, N-type of AMS. (**C**) Site 48_17, Talnakh intrusion, I-type of AMS. (**D**) Site 5_16, Yergalakhsky sill, R-type of AMS and N-type of AARM. (**E**) Site 1_21, lava flow of the Samoedsky Formation, R-type of AMS and N-type of AARM. (**F**) Site 11.2_16, dike of the Daldykan complex, I-type of AMS and N-type of AARM. (**G**) Site kul32, Katangsky sill, N-type of AMS. (**H**) Site 26_17, Kharaelakh intrusion, R-type of AMS.

For site 26_17 (taxitic gabbro-dolerites of the Kharaelakh intrusion), the orientation of the AARM axes does not correspond to that of AMS and is oblique to the presumably horizontal contact of massif (Figure 7H). We suggest that monoclinic pyrrhotite, identified in magnetic susceptibility thermal curves (Figure 5H), is responsible for the imbrication of the AARM ellipsoid.

Thus, measurement of AARM showed that, for sites with N-type, magnetic fabric is controlled by ferromagnetic minerals (mainly magnetite or titanomagnetite of pseudo-single-domain or multidomain composition) and can be used for the reconstruction of magma transport patterns. An inverse magnetic fabric, in some cases, can be explained by the significant contribution of single-domain grains of magnetite or titanomagnetite. Finally, presence of iron sulfides disturbs and obscures the primary magmatic magnetic fabric and complicates the interpretation of AMS and AARM measurements.

6. Discussion

In the Mokulay section, the majority of sampled lava flows of the Mokulaevsky and Kharaelakhsky formations demonstrate normal magnetic fabric (20 from 23). For most of them, the magnetic lineation is gentle and has NW–SE strike in the geographic coordinate system (Figure 8A). Given that the entire lava sequence dips to the NE, the sense of lava motion cannot be determined. After the tilt correction, the mean value of the K1 axis for all sites gently dips to the NW (Figure 8B). Therefore, we suggest that lava flows moved from SE to NW. It should be noted that, in sites MK1_19 and MK10_19, which show intermediate magnetic fabric, magnetic lineation is close to the main group (Supplementary Material Table S1) and, possibly, reflects the motion of flows as well.

The mean magnetic lineation calculated for the Mokulay section is virtually orthogonal to the Noril'sk-Kharaelakh fault (Figure 8A), which is located eastward of the sampling area (Figure 9A). Hence, results from the Mokulay section show that the Mokulaevsky and Kharaelakhsky lava flows moved from the Noril'sk-Kharaelakh fault, where the eruptive center was located. This interpretation is consistent with previous results reported by Callot et al. [21] for the upper part of the Noril'sk volcanic section from the Icon trough.

In the Talovaya area, the majority of lava flows demonstrate N-type magnetic fabric as well (18 flows from 22). Since flows are flat lying (dip < 10°), we analyzed the orientation of the maximal AMS axis in the geographic coordinate system. In the contour plot for the K1 axis, several local centers can be distinguished (Figure 8C). They correspond to distinct groups of lava flows with different directions of motion. Mean values of major clusters gently dip to the NW or SW. The group with northwestern dip of the magnetic lineation is close to the main cluster for the Mokulay section and nearly orthogonal to the Noril'sk-Kharaelakh fault (Figure 9B). We also note that site sm1_21 (R-type of AMS) demonstrates normal fabric of AARM with a similar NW orientation of the maximal axis and can be attributed to the same group. Thus, eruptions of the Samoedsky lava flows were controlled by the Noril'sk-Kharaelakh fault as well, though several local stages with different eruptive centers can be distinguished.

Intrusions of the Imangda area demonstrate normal magnetic fabric with a predominant SE dip of the magnetic lineation (Figure 8D). Within the main cluster, two local centers are distinguished, corresponding to two different stages of emplacement. Sites I2 and I4 represent the Khyukta and Imangda intrusions, respectively, both referred to as the Noril'sk type. Sites I5 and I6 represent the Oganer and Yergalakhsky complex, respectively, and possibly mark the earlier magmatic events. In general, magnetic lineation in all these sites is orthogonal to the Imangda-Letninskiy fault (Figure 9C), pointing out the transport of magma from this magma-feeding fault zone. The only exception is site I3 (the Imangda intrusion), where the K1 axis of AMS is horizontal and has meridional strike (Supplementary material Table S1). This kind of magnetic fabric can be caused by magma flow along the Imangda-Letninskiy fault, which is located nearby. Finally, basalts of the Tuklonsky Formation (site I1) demonstrate magnetic foliation parallel to the wall of the proximate

Rudnaya dike. We suggest that the primary fabric of this site was overprinted during the dike emplacement and mineral alterations near the contact.

In the Kulumbe region, 15 sites out of 27 showed normal magnetic fabric. As seen from Figure 8E, in most sites, magnetic lineation gently plunges to the E–SE. This cluster is formed mainly by intrusions of the Katangsky and Daldykan complexes. The dip of magnetic lineation for this group is virtually orthogonal to the Imangda-Letninskiy fault, indicating the direction of emplacement of intrusions and magma-controlling role of this fault (Figure 9D). However, Siluriyskaya (site K7) and Iltyk (K8) intrusions (the Noril'sk complex) and the Kuzmovsky sill (K11) demonstrate flat meridional orientation of K1 axes, close to the strike of the Imangda-Letninskiy fault zone. These intrusions may correspond to a distinct magmatic event.

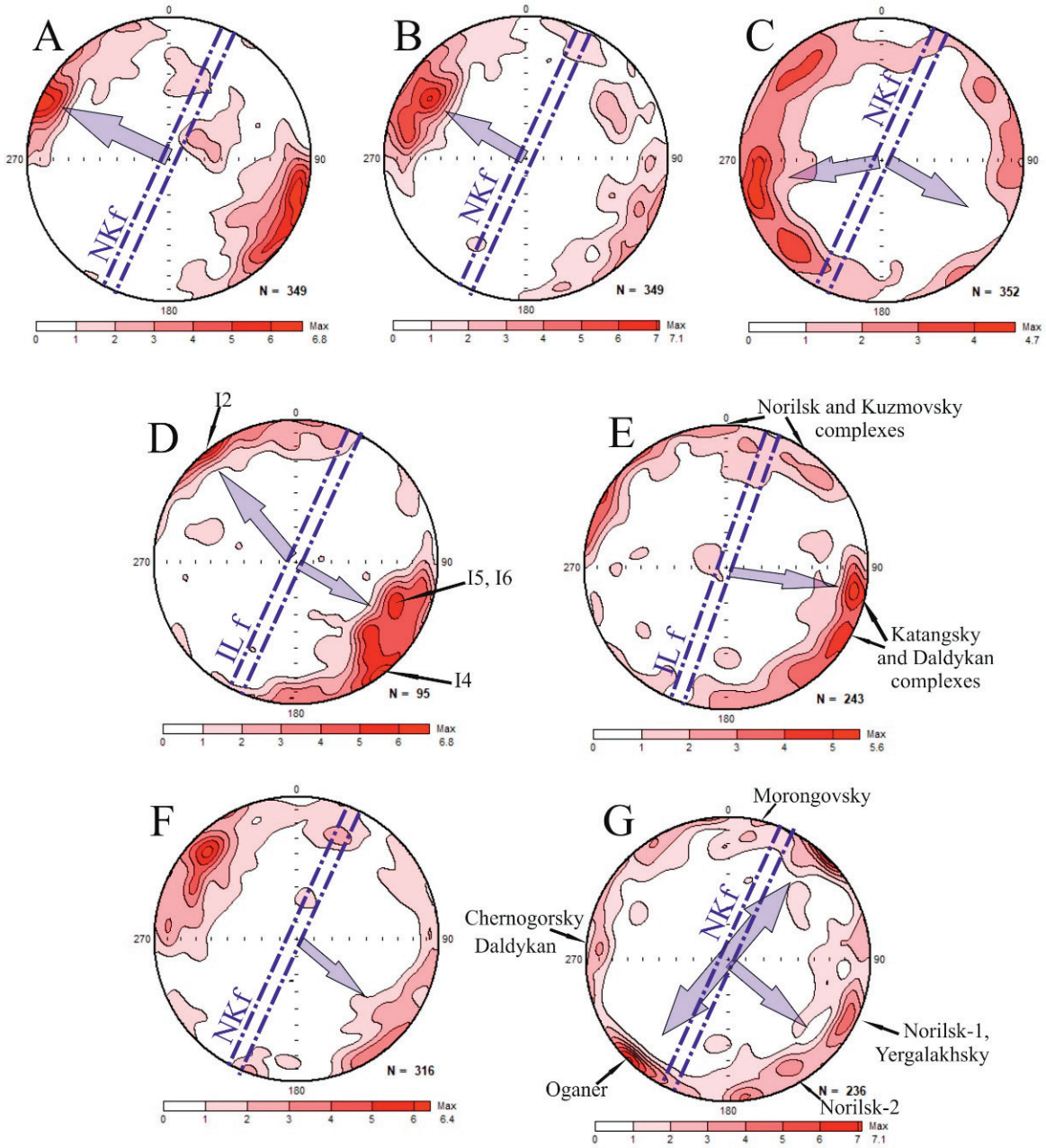

Figure 8. Contour plots of the maximal axis K1 of AMS for the studied regions. Lower hemisphere, equal area projection. (**A**,**B**) Mokulay: (**A**) "in situ", (**B**) tilt-corrected; (**C**) Talovaya; (**D**) Imangda; (**E**) Kulumbe; (**F**) Kharaelakh; (**G**) Noril'sk. Arrows show directions of the magma transport. NKf—Noril'sk-Kharaelakh fault; ILf—Imangda-Letninskiy fault.

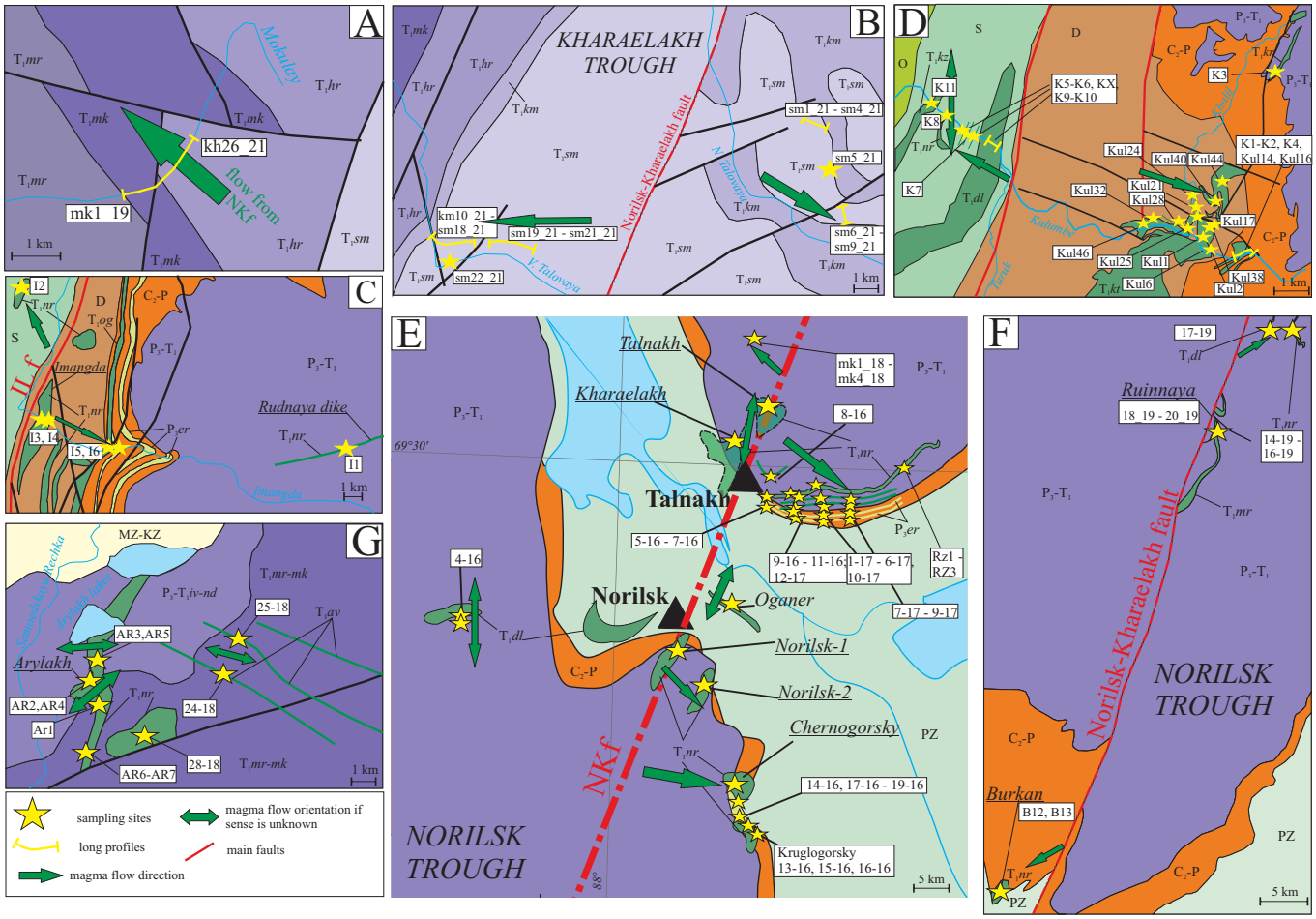

Figure 9. Main directions of magma transport for the studied regions. (**A**) Mokulay; (**B**) Talovaya; (**C**) Imangda; (**D**) Kulumbe; (**E**) Kharaelakh and Noril'sk; (**F**) South Noril'sk; (**G**) Icon. NKf—Noril'sk-Kharaelakh fault; ILf—Imangda-Letninskiy fault; T_1mr—Morongovsky Formation; T_1mk-Mokulaevsky Formation; T_1kh–Kharaelakhsky Formation; T_1km—Kumginsky Formation; T_1er—Yergalakhsky complex; T_1nr—Noril'sk complex; T_1og—Oganer complex; T_1dl—Daldykan complex; T_1kr—Kureysky complex; T_1kz—Kuzmovsky complex; T_1kt—Katangsky complex; T_1av—Avamsky complex; P_3-T_1iv-nd—undivided volcanic formations: from Ivakinsky to Nadezhdinsky.

The Kharaelakh area is more complicated for the interpretation of AMS data. Only 21 sites out of 70 yielded normal magnetic fabric. Partly, those were hornfels and skarns from the contact zones of ore-bearing intrusions, which are not applicable for the magma flow reconstruction. Among the rest, most sites demonstrate NW-dipping magnetic lineation (Figure 8F). The main center of mass in the contour plot is formed by the intrusion of Zayachiy Creek (three sites), the Kharaelakh intrusion (three sites), the Mokulaevsky Formation (four lava flows), and a single lava flow from the Ivakinsky Formation. For this group, magnetic lineation is oriented across the Noril'sk-Kharaelakh fault zone and is consistent with the idea of the lateral magma transport from the magma-conducting fault in both sides (Figure 9E). Other sites, representing sills and dikes of the Yergalakhsky and Daldykan complexes and parts of the Kharaelakh intrusion, demonstrate variable orientations of the K1 axis of AMS, different from the main group.

AARM fabric, measured for the Yergalakhsky sill 5_16 (R-type of AMS), demonstrates the normal type, where the maximal axis is flat and close to the main cluster of the Kharaelakh area (Figure 7D). For the Daldykan dike 11.2_16 (I-type of AMS), the maximal axis of AARM is horizontal, pointing out the lateral magma flow (Figure 7E). In both sites,

AARM fabric supports our interpretation of the dominant magma transport from the Noril'sk-Kharaelakh fault to the NW and SE.

For the Talnakh intrusion, we were not able to reconstruct the directions of magma emplacement because the inverse magnetic fabric is predominant (Supplementary Material Table S1). Taken together with various directions of K1 obtained for the Kharaelakh intrusion, these results show that thick, ore-bearing intrusions are challenging for the analysis of magnetic fabric. Possible reasons for that are the complex internal structure of layered multiphase intrusions and presence of iron sulfides. In addition, many sites representing dikes of Oganer and the Daldykan complex, sills of the Yergalakhsky complex, and leucogabbro of the Kruglogorsky-type intrusions have abnormal types of magnetic fabric, and reconstruction of magma flow was not performed for them.

In the Noril'sk area, only 18 sites out of 38 showed the normal type of AMS. As seen from Figure 8G, several mass centers and corresponding directions of magma flow can be distinguished in the contour plot of the magnetic lineation. For the sill of Oganer, four sampled sites demonstrate SW-NE subhorizontal magnetic lineation. Furthermore, NW-SE lineation, orthogonal to the Noril'sk-Kharaelakh fault and typical of other studied areas, has been identified in two sites of Noril'sk-1 intrusion and sills of the Yergalakhsky complex and in a single site of Noril'sk-2 intrusion. The Ambarnaya intrusion (site 4_16, Daldykan complex) and two sites of the Chernogorsky intrusion (Noril'sk type) demonstrate flat N-E magnetic lineation. Finally, for two lava flows of the Morongovsky Formation, the maximal axes of AMS gently dip to the north. Other sites from all ore-bearing layered intrusions (Noril'sk-1, Noril'sk-2, Chernogorsky) demonstrate abnormal magnetic fabric (mainly R-type) or, in a few sites, normal fabric with outlying magnetic lineation.

In the South Noril'sk area, we identified the N-type of AMS only for two sites: B12 (gabbro-dolerites of the Burkan intrusion, Noril'sk type) and 17_19 (dolerites of the Daldykan complex). Both of them demonstrate flat SW dips of magnetic lineation (Figure 9F), unlike other regions. Sampled intrusions of the Morongovsky complex and Kruglogorsky type demonstrate variable magnetic fabric, probably due to the complex morphology of bodies and rock composition.

Finally, in the Icon area, most sampled sites represent the Arylakh intrusion. Magnetic fabric varies from site to site; in general, all mean AMS axes demonstrate wide confidence ellipses. Two sites with N-type fabric (AR2 and AR5) show different orientations of the maximal K1 axis. Such magnetic fabric can be interpreted as a result of the slow cooling of the intrusion within the stationary magmatic chamber. The low degree of anisotropy in all sites ($Pj < 1.025$) favors this hypothesis. One out of two Avamsky dikes (site 24_18) demonstrates the I-type of magnetic fabric with a steep orientation of the minimal axis of AMS and a subhorizontal maximal axis. This type of fabric in mafic dikes was reported by Park et al. [80] and is interpreted as a result of vertical compaction of the static magma column during the cooling of magma after the lateral emplacement in a tectonic setting of subhorizontal extension. In this case, the orientation of K1 axes corresponds to the magma flow, and, hence, this dike was emplaced during the lateral transport of magma (Figure 9G).

Thus, in six studied areas, we distinguished predominant directions of magma transport from the Noril'sk-Kharaelakh and Imangda-Letninskiy fault zones. For the Mokulaevsky, Kharaelakhsky, and Samoedsky formations, we suggest the motion of lava flows to the NW and SE from the Noril'sk-Kharaelakh fault during the fissure eruptions. For the major parts of intrusions in the Noril'sk, Kharaelakh, and Imangda troughs and the Kulumbe area, the reconstructed pattern of magma transport supports the idea of the magma-controlling and magma-feeding role of regional fault zones of NE strike. This is important for the understanding of Cu-Ni-PGE ore genesis because in all studied regions, layered intrusions with mineral deposits are located at fault zones: Talnakh and Kharaelakh intrusions in the Kharaelakh trough, Noril'sk-1 and its satellites in the Noril'sk trough, the Imangda intrusion in the same-titled trough, and the Siluriyskaya intrusion in the Kulumbe area.

Minor directions of the magma transport correspond to the emplacement of individual intrusions during distinct magmatic events, e.g., formation of the Oganer sill. In addition, in some regions, the lateral transport along the fault zones was identified based on the NE orientation of magnetic lineation.

The patterns of magma transport in the Noril'sk and Kulumbe regions differ sharply from that in the Angara-Taseeva depression [20], where lateral transport of magma via the system of sills led to the emplacement of thick and extended intrusions (the Tolstomysovsky, Padunsky sills, etc.). The possible reason is the different crust structure and tectonic evolution of these regions. The Noril'sk and Kulumbe regions are superimposed to the Noril'sk-Igarka paleorift zone, identified on the basis of geophysical data [81]. The Noril'sk-Kharaelakh and Imangda-Letninskiy faults extend along this structure and represent long-lived mobile zones of high permeability. All economically important Cu-Ni-PGE deposits in the northwestern Siberian platform are located within these zones and are linked with the magma conduits. Proximity of the Noril'sk and Kulumbe regions to the supposed center of the Siberian plume can lead to the activation of fault zones, ascent of large volumes of magma, and fissure eruptions. In contrast, the Angara-Taseeva depression is a Paleozoic sedimentary basin within the Siberian platform, and the magma-feeding zone was located in the central, most subsided part of the syncline. The reconstructed magma transport pattern for the Angara-Taseeva depression was typical for such basins [17,82]. The peripheral position of the Angara-Taseeva depression and absence of regional extension zones led to the reduced thickness of the volcanic sequence compared with the Noril'sk region.

7. Conclusions

1. Based on the detailed AMS measurements, we reconstructed the magma transport patterns for the Siberian Traps in the Noril'sk and Kulumbe regions (northwestern Siberian platform). The lateral flow of NW-SE directions is predominant in most areas, supporting the model of a magma-feeding and ore-controlling role of the Noril'sk-Kharaelakh and Imangda-Letninskiy faults, as well as fissure type of lava eruptions.
2. Minor directions of SW-NE strike are identified in several areas, indicating the transport of magma along regional faults.
3. Lava flows and thin sills usually demonstrate N-type of magnetic fabric and are suitable for the determination of magma flow. Layered ore-bearing intrusions often show complicated magnetic fabric due to the complex morphology and presence of iron sulfides.
4. The detailed measurements of AARM and rock-magnetic investigation show that abnormal magnetic fabric in some intrusions and lava flows can be explained by features of domain composition of magnetite or titanomagnetite.
5. Patterns of magma transport for the Noril'sk-Kulumbe region and Angara-Taseeva depression are contrasting due to the different tectonic structure of the crust.

Supplementary Materials: The following supporting information can be downloaded at: https://www.mdpi.com/article/10.3390/min13030446/s1, Table S1: Results of anisotropy of magnetic susceptibility measurements. AMS types: N—normal, R—reverse, I—intermediate, S—scattered, D—diagonal. Pj—corrected degree of anisotropy, T—shape parameter; K1, K2, K3—maximal, medium and minimum axes of AMS ellipsoid, respec-tively; D—declination, I—inclination.

Author Contributions: Conceptualization, A.L.; methodology, A.L.; field work and sampling, A.L., V.R., R.V., N.K., A.F. and S.F.; measurements, A.L., R.V., A.F. and S.F.; data processing, A.L.; resources, V.R.; interpretation, A.L.; writing—original draft preparation, A.L.; writing—review and editing, R.V., A.F. and S.F.; visualization, A.L., R.V., A.F. and S.F.; funding acquisition, A.L., V.R. and N.K. All authors have read and agreed to the published version of the manuscript.

Funding: This study was funded by Limited Liability Company "Noril'skgeologiya" (projects No. NG-172/17, NG-130/18, NG-140/19), by the Russian Foundation for Basic Research (projects 18-35-20058, 17-05-01121, 18-05-70094 and 20-05-00573) and by state assignment of IPE RAS.

Institutional Review Board Statement: Not applicable.

Informed Consent Statement: Not applicable.

Data Availability Statement: Data are available on request.

Acknowledgments: Authors gratefully thank A.A. Lapkovsky and A.A. Ketrov (Noril'skgeologiya) for the help during field work and V.E. Pavlov, A.M. Pasenko, P.S. Ulyakhina, D.V. Rud'ko, P.A. Minaev, and E.A. Latanova (IPE RAS) for the participation in sampling, measurements, and processing of the results. We also thank anonymous reviewers for their valuable comments and suggestions.

Conflicts of Interest: The authors declare no conflict of interest.

References

1. Campbell, I.H. Large igneous provinces and the mantle plume hypothesis. *Elements* **2005**, *1*, 265–269. [CrossRef]
2. Dobretsov, N.L.; Borisenko, A.S.; Izokh, A.E.; Zhmodik, S.M. A termochemical model of Eurasian Permo-Triassic mantle plumes as a basis for prediction and exploration for Cu–Ni–PGE rare metals ore deposits. *Rus. Geol. Geophys.* **2010**, *51*, 1159–1187. [CrossRef]
3. Czamanske, G.K.; Gurevich, A.B.; Fedorenko, V.; Simonov, O. Demise of the Siberian plume: Paleogeographic and paleotectonic reconstruction from the prevolcanic and volcanic records, North-Central Siberia. *Int. Geol. Rev.* **1998**, *40*, 95–115. [CrossRef]
4. Elkins-Tanton, L.T. Continental magmatism caused by lithospheric delamination. *Spec. Pap.-Geol. Soc. Am.* **2005**, *388*, 449–462.
5. Ivanov, A.V. Evaluation of different models for the origin of the Siberian Traps. *Spec. Pap.-Geol. Soc. Am.* **2007**, *430*, 669–691.
6. Sobolev, S.V.; Sobolev, A.V.; Kuzmin, D.V.; Krivolutskaya, N.A.; Petrunin, A.G.; Arndt, N.T.; Radko, V.A.; Vasil'yev, Y.R. Linking mantle plumes, large igneous provinces, and environmental catastrophes. *Nature* **2011**, *477*, 312–316. [CrossRef]
7. Saunders, A.D.; England, R.W.; Reichow, M.K.; White, R.V. A mantle plume origin for the Siberian traps: Uplift and extension in the West Siberian Basin, Russia. *Lithos* **2005**, *79*, 407–424. [CrossRef]
8. Ernst, R.E.; Buchan, K.L. Large mafic magmatic events through time and links to mantle-plume heads. *Geol. Soc. Am. Spec. Pap.* **2001**, *352*, 483–575.
9. Schissel, D.; Smail, R. Deep-mantle plumes and ore deposits. *Geol. Soc. Am. Spec. Pap.* **2001**, *352*, 291–322.
10. Burgess, S.D.; Muirhead, J.D.; Bowring, S.A. Initial pulse of Siberian Traps sills as the trigger of the end-Permian mass extinction. *Nat. Commun.* **2017**, *8*, 164. [CrossRef]
11. Fedorenko, V.A. Evolution of magmatism as reflected in the volcanic sequence of the Noril'sk region. In Proceedings of the Sudbury-Noril'sk Symposium; Lightfoot, P.C., Naldrett, A.J., Eds.; Ontario Geological Survey: Toronto, ON, Canada, 1994; Volume 5, pp. 171–183.
12. Zolotukhin, V.V.; Vilensky, A.M.; Dyuzhikov, O.A. *Basalts of the Siberian Platform*; Nauka: Novosibirsk, Russia, 1986; p. 289. (In Russian)
13. Fedorenko, V.; Czamanske, G. Results of new field and geochemical studies of the volcanic and intrusive rocks of the Maymecha-Kotuy area, Siberian Flood-Basalt Province, Russia. *Int. Geol. Rev.* **1997**, *39*, 479–531. [CrossRef]
14. Ernst, R.E.; Baragar, W.R.A. Evidence from magnetic fabric for the flow pattern of magma in the Mackenzie giant radiating dyke swarm. *Nature* **1992**, *356*, 511–513. [CrossRef]
15. Raposo, M.I.B.; Ernesto, M. Anisotropy of magnetic susceptibility in the Ponta Grossa dike swarm (Brazil) and its relationship with magma flow directions. *Phys. Earth Planet. Inter.* **1995**, *102*, 183–196. [CrossRef]
16. Glen, J.M.G.; Renne, P.M.; Milner, S.C.; Coe, R.S. Magma flow in ferred from anisotropy of magnetic susceptibility in the Parana-Etendeka igneous province: Evidence for rifting before flood volcanism. *Geology* **1997**, *25*, 1131–1134. [CrossRef]
17. Polteau, S.; Mazzini, A.; Galland, O.; Planke, S.; Malthe-Sørenssen, A. Saucer-shaped intrusions: Occurrences, emplacement and implications. *Earth Planet. Sci. Lett.* **2008**, *266*, 195–204. [CrossRef]
18. Magee, C.; Muirhead, J.D.; Karvelas, A.; Holford, S.P.; Jackson, C.A.L.; Bastow, J.D.; Schofield, N.; Stevenson, C.T.E.; McLean, C.; McCarthy, W.; et al. Lateral magma flow in mafic sill complexes. *Geosphere* **2016**, *12*, 809–841. [CrossRef]
19. Konstantinov, K.M.; Mishenin, S.G.; Tomshin, M.D.; Kornilova, V.P.; Kovalchuk, O.E. Petromagnetic heterogeneities of the Permo-Triassic traps of the Daldyn-Alakit diamond province (Western Yakutia). *Lithosphere* **2014**, *2*, 77–98. (In Russian)
20. Latyshev, A.V.; Ulyakhina, P.S.; Veselovskiy, R.V. Reconstruction of magma flow in Permo–Triassic intrusions of the Angara–Taseeva syneclise (Siberian platform) based on magnetic susceptibility anisotropy data. *Russ. Geol. Geophys.* **2019**, *60*, 400–413. [CrossRef]
21. Callot, J.-P.; Gurevitch, E.; Westphal, M.; Pozzi, J.-P. Flow patterns in the Siberian traps deduced from magnetic fabric studies. *Geophys. J. Int.* **2004**, *156*, 426–430. [CrossRef]
22. Latyshev, A.V.; Krivolutskaya, N.A.; Ulyakhina, P.S.; Bychkova, Y.V.; Gongalsky, B.I. Intrusions of the Kulumbe river valley, NW Siberian traps province: Paleomagnetism, magnetic fabric and geochemistry. In *Recent Advances in Rock Magnetism, Environmental Magnetism and Paleomagnetism*; Nurgaliev, D.K., Shcherbakov, V.P., Kosterov, A.A., Spassov, S., Eds.; Springer Geophysics: Berlin/Heidelberg, Germany, 2019; pp. 67–82. [CrossRef]

23. Latyshev, A.V.; Radko, V.A.; Veselovskiy, R.V.; Fetisova, A.M.; Pavlov, V.E. Correlation of the Permian-Triassic ore-bearing intrusions of the Noril'sk region with the volcanic sequence of the Siberian Traps based on the paleomagnetic data. *Econ. Geol.* **2020**, *115*, 1173–1193. [CrossRef]
24. Latyshev, A.V.; Lapkovskii, A.A.; Veselovskiy, R.V.; Fetisova, A.M.; Krivolutskaya, N.A. Paleomagnetism of the Permian–Triassic Siberian traps intrusions from the Kulumbe river valley, northwestern Siberian Platform. *Izvestiya. Phys. Solid Earth* **2021**, *57*, 375–394. [CrossRef]
25. Latyshev, A.V.; Krivolutskaya, N.A.; Ulyakhina, P.S.; Fetisova, A.M.; Veselovskiy, R.V.; Pasenko, A.M.; Khotylev, A.; Anosova, M.B. Paleomagnetism of the Permian-Triassic intrusions from the Noril'sk region (the Siberian Platform, Russia): Implications for the timing and correlation of magmatic events, and magmatic evolution. *J. Asian Earth Sci.* **2021**, *217*, 104858. [CrossRef]
26. Fedorenko, V.A.; Lightfoot, P.C.; Naldrett, A.J. Petrogenesis of the Siberian flood-basalt sequence at Noril'sk, north central Siberia. *Intern. Geol. Rev.* **1996**, *38*, 99–135. [CrossRef]
27. Wooden, J.L.; Czamanske, G.K.; Fedorenko, V.A.; Arndt, N.T.; Chauvel, C.; Bouse, R.M.; King, B.-S.W.; Knight, R.J.; Siems, D.F. Isotopic and trace-element constraints on mantle and crustal contributions to Siberian continental flood basalts, Noril'sk area, Siberia. *Geochim. Cosmochim. Acta.* **1993**, *57*, 3677–3704. [CrossRef]
28. Hawkesworth, C.J.; Lightfoot, P.C.; Fedorenko, V.A.; Blake, S.; Naldrett, A.J.; Doherty, W.; Gorbachev, N.S. Magma differentiation and mineralisation in the Siberian continental flood basalts. *Lithos* **1995**, *34*, 61–88. [CrossRef]
29. Lightfoot, P.C.; Hawkesworth, C.J. Flood basalts and magmatic Ni, Cu and PGE sulfide mineralization: Comparative geochemistry of the Noril'sk (Siberian Traps) and West Greenland sequences. *Geophys. Monogr. Am. Geophys. Union* **1997**, *100*, 357–380.
30. Al'mukhamedov, A.I.; Medvedev, A.Y.; Zolotukhin, V.V. Chemical evolution of the Permian-Triassic basalts of the Siberian platform in space and time. *Petrology* **2004**, *12*, 297–311.
31. Ryabov, V.V.; Shevko, A.Y.; Gora, M.P. *Trap Magmatism and Ore Formation in the Siberian Noril'sk Region*; Springer: Amsterdam, The Netherlands, 2014.
32. Krivolutskaya, N.A. *Siberian Traps and Pt-Cu-Ni Deposits in the Noril'sk Area*; Springer: Berlin/Heidelberg, Germany, 2016; p. 361.
33. Radko, V.A. Model of the Dynamic Differentiation of Intrusive Traps from the Northwestern Siberian Platform. *Geol. Geophys.* **1991**, *11*, 19–27. (In Russian)
34. Radko, V.A. *The Facies of Intrusive and Effusive Magmatism in the Noril'sk Region*; Cartographic Factory VSEGEI Press: St. Petersburg, Russia, 2016; p. 226. (In Russian)
35. Naldrett, A.J.; Fedorenko, V.A.; Lightfoot, P.C.; Kunilov, V.A.; Gorbachev, N.S.; Doherty, W.; Johan, Z. Ni-Cu-PGE deposits of the Noril'sk region, Siberia: Their formation in conduits for flood basalt volcanism. *Trans. Inst. Min. Metall.* **1995**, *104*, B18–B36.
36. Naldrett, A.J. *Magmatic Sulfide Deposits of Nickel-Copper and Platinum-Metal Ores*; St. Petersburg University: St. Petersburg, Russia, 2003; p. 487.
37. Li, C.S.; Ripley, E.M.; Naldrett, A.J. A new genetic model for the giant Ni-Cu-PGE sulfide deposits associated with the Siberian flood basalts. *Econ. Geol.* **2009**, *104*, 291–301. [CrossRef]
38. Dyuzhikov, O.A.; Distler, V.V.; Strunin, B.M.; Mkrtychyan, A.K.; Sherman, M.L.; Sluzhenikin, S.F.; Lurye, A.M. *Geology and Ore Potential of the Noril'sk Ore District*; Nauka: Moscow, Russia, 1988; p. 238.
39. Latypov, R.M. Phase equilibria constraints on relations of ore-bearing intrusions with flood basalts in the Noril'sk region, Russia. *Contrib. Mineral. Petrol.* **2002**, *143*, 438–449. [CrossRef]
40. Krivolutskaya, N.; Gongalsky, B.; Kedrovskaya, T.; Kubrakova, I.; Tyutyunnik, O.; Chikatueva, V.; Bychkova, Y.; Kovalchuk, E.; Yakushev, A.; Kononkova, N. Geology of the Western Flanks of the Oktyabr'skoe Deposit, Noril'sk District, Russia: Evidence of a Closed Magmatic System. *Miner. Depos.* **2019**, *54*, 611–630. [CrossRef]
41. Yao, Z.-S.; Mungall, J.E. Linking the Siberian flood basalts and giant Ni-Cu-PGE sulfide deposits at Noril'sk. *J. Geophys. Res. Solid Earth* **2021**, *126*, e2020JB020823. [CrossRef]
42. Distler, V.V.; Kunilov, V.E. *Geology and Ore Deposits of the Noril'sk Region*; International Platinum Symposium: Moscow, Russia, 4 August 1994; p. 67.
43. Heunemann, C.; Krasa, D.; Soffel, H.; Gurevitch, E.; Bachtadse, V. Directions and intensities of the Earth's magnetic field during a reversal: Results from the Permo-Triassic Siberian trap basalts, Russia. *Earth Plan. Sci. Lett.* **2004**, *218*, 197–213. [CrossRef]
44. Kamo, S.L.; Czamanske, G.K.; Krogh, T.E. A minimum U-Pb age for Siberian flood-basalt volcanism. *Geochim. Cosmochim. Acta* **1996**, *60*, 3505–3511. [CrossRef]
45. Burgess, S.D.; Bowring, S.A. High-precision geochronology confirms voluminous magmatism before, during, and after Earth's most severe extinction. *Sci. Adv.* **2015**, *1*, e1500470. [CrossRef]
46. Pavlov, V.; Fluteau, F.; Veselovskiy, R.; Fetisova, A.; Latyshev, A.; Elkins-Tanton, L.T.; Sobolev, A.V.; Krivolutskaya, N.A. Volcanic pulses in the Siberian Traps as inferred from Permo-Triassic geomagnetic secular variations. In *Volcanism and Global Environmental Change*; Schmidt, A., Ed.; Cambridge University Press: Cambridge, UK, 2015; pp. 63–78.
47. Pavlov, V.E.; Fluteau, F.; Latyshev, A.V.; Fetisova, A.M.; Elkins-Tanton, L.T.; Black, B.A.; Burgess, S.D.; Veselovskiy, R.V. Geomagnetic Secular Variations at the Permian-Triassic Boundary and Pulsed Magmatism During Eruption of the Siberian Traps. *Geochem. Geophys. Geosyst.* **2019**, *20*, 773–791. [CrossRef]
48. Krivolutskaya, N.; Belyatsky, B.; Gongalsky, B.; Dolgal, A.; Lapkovsky, A.; Bayanova, T.B. Petrographical and geochemical characteristics of magmatic rocks in the Northwestern Siberian Traps Province, Kulyumber river valley. part II: Rocks of the Kulyumber site. *Minerals* **2020**, *10*, 415. [CrossRef]

49. Krivolutskaya, N.; Belyatsky, B.; Gongalsky, B.; Dolgal, A.; Lapkovsky, A.; Malitch, K.; Taskaev, V.; Svirskaya, N. Petrography and geochemistry of magmatic rocks in the Northwestern Siberian Traps Province, Kulyumber river valley. Part I: Rocks of the Khalil and Kaya sites. *Minerals* **2020**, *10*, 409. [CrossRef]
50. Zolotolotukhin, V.V.; Ryabov, V.V.; Vasil'ev, Y.R.; Shatkov, V.A. *Petrology of the Talnakh Ore-Bearing Differentiated Trap Intrusion*; Nauka Press: Novosibirsk, Russia, 1975. (In Russian)
51. Masaitis, V.L. Permian and Triassic volcanism of Siberia. *Zap. Vserossiiskogo Mineral. Obs.* **1983**, *4*, 412–425. (In Russian)
52. Simonov, O.N.; Lulko, V.A.; Amosov, Y.N.; Salov, V.M. Geological Structure of the Noril'sk Region. In *The Sudbury—Noril'sk Symposium Ontario Geological Survey Special Publication*; Naldrett, A.J., Lightfoot, P.C., Sheahan, P., Eds.; Ontario Geological Survey: Toronto, ON, Canada, 1994; Volume 5, pp. 161–170.
53. Stekhin, A.I. Mineralogical and geochemical characteristics of the Cu-Ni ores of the Oktyabr'skoe and Talnakh deposits. In Proceedings of the Sudbury-Noril'sk Symposium, Sudbury, ON, Canada, 3–6 October 1992; OGS Special, 1994. Volume 5, pp. 217–230.
54. Zenko, T.E.; Czamanske, G.K. Spatial and Petrologic Aspects of the Intrusions of the Noril'sk and Talnakh Ore Junctions. In *The Sudbury—Noril'sk Symposium Ontario Geological Survey Special Publication*; Naldrett, A.J., Lightfoot, P.C., Sheahan, P., Eds.; OGS: Sudbury, ON, Canada, 1994; Volume 5, pp. 263–282.
55. Lightfoot, P.C.; Zotov, I.A. Geological Relationships between the intrusions, country rocks, and Ni–Cu–PGE sulfides of the Kharaelakh Intrusion, Noril'sk Region: Implications for the roles of sulfide differentiation and metasomatism in their genesis. *Northwestern Geol.* **2014**, *47*, 1–35.
56. Yakubchuk, A.; Nikishin, A. Noril'sk–Talnakh Cu–Ni–PGE deposits: A revised tectonic model. *Miner. Depos.* **2004**, *39*, 125–142. [CrossRef]
57. Pavlov, V.; Courtillot, V.; Bazhenov, M.; Veselovsky, R. Paleomagnetism of the Siberian traps: New data and a new overall 250 Ma pole for Siberia. *Tectonophysics* **2007**, *443*, 72–92. [CrossRef]
58. Latyshev, A.V.; Ulyakhina, P.S.; Krivolutskaya, N.A. Signs of the Record of Geomagnetic Reversal in Permian—Triassic Trap Intrusions of the Ergalakhsky Complex, Noril'sk Region. *Izv. Phys. Solid Earth* **2019**, *55*, 270–286. [CrossRef]
59. Veselovskiy, R.V.; Dubinya, N.V.; Ponomarev, A.V.; Fokin, I.V.; Patonin, A.V.; Pasenko, A.M.; Fetisova, A.M.; Matveev, M.A.; Afinogenova, N.A.; Rud'ko, D.V.; et al. Shared research facilities "Petrophysics, geomechanics and paleomagnetism" of the Schmidt Institute of Physics of the Earth RAS. *Geodyn. Tectonophys.* **2022**, *13*, 0579. (In Russian) [CrossRef]
60. Jelínek, V. Statistical processing of anisotropy of magnetic susceptibility measures on groups of specimens. *Stud. Geophis. Geod.* **1978**, *22*, 50–62. [CrossRef]
61. Jelínek, V. Characterization of the magnetic fabric of rocks. *Tectonophysics* **1981**, *79*, T63–T67. [CrossRef]
62. Day, R.; Fuller, M.; Schmidt, V.A. Hysteresis properties of titanomagnetites: Grain-size and compositional dependence. *Phys. Earth Planet Inter.* **1977**, *13*, 260–267. [CrossRef]
63. Dunlop, D.J. Theory and application of the Day plot (Mrs/Ms versus Hcr/Hc) 1 Theoretical curves and tests using titanomagnetite data. *J. Geophys. Res.* **2002**, *107*, B3.
64. Roberts, A.P.; Pike, C.R.; Verosub, K.L. First-order reversal curve diagrams: A new tool for characterizing the magnetic properties of natural samples. *J. Geophys. Res. Solid Earth* **2000**, *105*, 461–475. [CrossRef]
65. Tarling, D.H.; Hrouda, F. *The Magnetic Anisotropy of Rocks*; Chapman Hall: London, UK, 1993.
66. O'Driscoll, B.; Ferre, E.C.; Stevenson, S.T.E.; Magee, C. The significance of magnetic fabric in layered mafic-ultramafic intrusions. In *Layered Intrusions*; Charlier, B., Namur, O., Latypov, R., Tegner, C., Eds.; Springer: Berlin/Heidelberg, Germany, 2015; pp. 295–329.
67. Andersson, M.; Almquist, B.S.G.; Burchardt, S.; Troll, V.R.; Malehmir, A.; Snowball, I.; Kubler, L. Magma transport in sheet intrusions of the Alnö carbonatite complex, central Sweden. *Sci. Rep.* **2016**, *6*, 27635. [CrossRef]
68. Jelínek, V. *The Statistical Theory of Measuring Anisotropy of Magnetic Susceptibility of Rocks and Its Application*; Geofyzika: Brno, Czech Republic, 1977; p. 88.
69. Hrouda, F. Low-field variation of magnetic susceptibility and its effect on anisotropy of magnetic susceptibility of rocks. *Geophys. J. Int.* **2002**, *150*, 715–723. [CrossRef]
70. Zhu, R.; Liu, Q.; Jackson, M.J. Paleoenvironmental significance of the magneticfabrics in Chinese loess-paleosols since the last interglacial (<130 ka). *Earth Planet Sci. Lett.* **2004**, *221*, 55–69.
71. Varga, J.V.; Gee, J.S.; Staudigel, H.; Tauxe, L. Dike surface lineations as magma flow indicators within the sheeted dike complex of the Troodos Ophiolite, Cyprus. *J. Geophys. Res.* **1998**, *103*, 5241–5256. [CrossRef]
72. Geoffroy, L.; Callot, J.P.; Aubourg, C.; Moreira, M. Magnetic and plagioclase linear fabric discrepancy in dykes: A new way to define the flow vector using magnetic foliation. *Terra Nova.* **2002**, *14*, 183–190. [CrossRef]
73. Shcherbakov, V.P.; Latyshev, A.V.; Veselovskiy, R.V.; Tselmovich, V.A. Origin of false components of NRM during conventional stepwise thermal demagnetization. *Russ. Geol. Geophys.* **2017**, *58*, 1118–1128. [CrossRef]
74. Latyshev, A.V.; Veselovsky, R.V.; Ivanov, A.V. Paleomagnetism of the Permian-Triassic intrusions from the Tunguska syncline and the Angara-Taseeva depression Siberian Traps Large Igneous Province: Evidence of contrasting styles of magmatism. *Tectonophysics* **2018**, *723*, 41–55. [CrossRef]
75. Schwarz, E.J.; Vaughan, D.J. Magnetic phase relations of pyrrhotite. *J. Geomagn. Geoelectr.* **1972**, *24*, 441–458. [CrossRef]

76. Jackson, M. Anisotropy of magnetic remanence: A brief review of mineralogical sources, physical origins and geological applications, and comparison with susceptibility anisotropy. *Pure Appl. Geophys.* **1991**, *136*, 1–28. [CrossRef]
77. Potter, D.K.; Stephenson, A. Single-domain particles in rocks and magnetic fabric analysis. *Geophys. Res. Lett.* **1988**, *15*, 1097–1100. [CrossRef]
78. Dragoni, M.; Lanza, R.; Tallarico, A. Magnetic anisotropy produced by magma flow; theoretical model and experimental data from Ferrar dolerite sills (Antarctica). *J. Geophys. Int.* **1997**, *128*, 230–240. [CrossRef]
79. Ferre, E.C. Theoretical models of intermediate and inverse AMS fabrics. *Geophys. Res. Lett.* **2002**, *29*, 31-1–31-4. [CrossRef]
80. Park, J.K.; Tanczyk, E.I.; Desbarats, A. Magnetic fabric and its significance in the 1400 Ma Mealy diabase dykes of Labrador, Canada. *J. Geophys. Res.* **1988**, *93*, 13689–13704. [CrossRef]
81. Krivolutskaya, N.A.; Latyshev, A.V.; Dolgal, A.S.; Gongalsky, B.I.; Makarieva, E.M.; Makariev, A.A.; Svirskaya, N.M.; Bychkova, Y.V.; Yakushev, A.I.; Asavin, A.M. Unique PGE–Cu–Ni Noril'sk deposits, Siberian Trap Province: Magmatic and tectonic factors in their origin. *Minerals* **2019**, *9*, 66. [CrossRef]
82. Galerne, C.Y.; Neumann, E.-R.; Planke, S. Emplacement mechanisms of sill complexes: Information from the geochemical architecture of the Golden Valley Sill Complex, South Africa. *J. Volcanol. Geotherm. Res.* **2008**, *177*, 425–440. [CrossRef]

minerals

MDPI

Article

Petrology and Age of the Yamaat Uul Mafic Complex, Khangai Mountains, Western Mongolia

Roman Shelepaev [1,2], Maria Shapovalova [1,*], Vera Egorova [1,2], Yaroslav Shelepov [1,2], Tumen-Ulzii Oyunchimeg [3] and Nadezhda Tolstykh [1]

[1] Sobolev Institute of Geology and Mineralogy, Siberian Branch of the Russian Academy of Sciences, Novosibirsk 630090, Russia; rshel@igm.nsc.ru (R.S.); verae@igm.nsc.ru (V.E.); shelepov@igm.nsc.ru (Y.S.); tolst@igm.nsc.ru (N.T.)
[2] Department of Geology and Geophysics, Novosibirsk State University, Novosibirsk 630090, Russia
[3] Institute of Geology, Mongolian Academy of Sciences, Labor Union St., Ulaanbaatar 13330, Mongolia; oyuna22@yahoo.com
* Correspondence: shapovalovam@igm.nsc.ru

Abstract: The Yamaat Uul mafic complex with Cu-Ni mineralization is located in the Khangai Mountains of Western Mongolia. We have received new unique data for mafic rocks of the complex: U-Pb dating (SHRIMP II), mineralogy (WDS) and geochemistry (XRF, ICP-MS), Sm-Nd and Rb-Sr isotope data and sulphur isotopes. The Yamaat Uul mafic complex consists of two intrusions: Intrusion 1 is represented by rocks of plagioclase cumulates and olivine–pyroxene cumulates; Intrusion 2 consists of monzogabbro. Intrusions 1 and 2 are different in composition of minerals such as olivine, plagioclase and biotite. The monzogabbro has higher contents of incompatible elements (REE, K, Ti, P) than rocks of Intrusion 1. Zircon U-Pb dating of the anorthosite and Bt-Am-Ol gabbronorite shows a Late Permian age (255.8 ± 2.9 Ma and 262.6 ± 3.1 Ma, respectively) for the Yamaat Uul mafic complex. All of the rocks of the complex are derived from a unified parental melt due to different amounts of trapped melts in plagioclase and olivine–pyroxene cumulates and without crustal contamination. The Cu-Ni mineralization of the complex has a low degree of evolution of the sulphide melt, similar to PGE-Cu-Ni mafic–ultramafic intrusions of the Khangai Mountains (Nomgon and Oortsog Uul). The Yamaat Uul mafic complex together with other mafic–ultramafic intrusions of the Khangai Mountains is related to the Khangai LIP and can be considered as potential for the PGE-Cu-Ni. The new geological, petrological, geochemical and isotope–geochronological data can later be used to reconstruct the geotectonics of the Khangai Mountains and the Central Asian orogenic belt as a whole.

Keywords: Khangai Mountains; Permian; mineralogy; petrology; geochemistry; Sr-Nd isotope; sulphur; Cu-Ni mineralization; LIP

1. Introduction

Mafic–ultramafic rocks derived from picritic and basaltic magmas are widespread in the orogenic belts of Central and Southeast Asia and are related to large igneous provinces (LIPs) [1]. Recent study of mafic–ultramafic layered intrusions with sulphide mineralization has been undertaken in south-eastern Siberia [2–5], Vietnam [6–9], China [10–14] and Mongolia [15–17]. Such intrusions are derived from mantle magmas and their study contributes significantly to petrological models and reconstruction of the evolutionary history of geological structures.

Such intrusions are also of great interest in the search for associated Cu-Ni-PGE mineralization. Permian large igneous provinces (LIPs) include the Emeishan and Tarim LIPs [4,18–20] and Siberian Traps [1,21].

Early studies of Khangai batholith metallogeny show the role of the mantle plume in the formation of the Late Palaeozoic magmatism of Central Asia, including Mongo-

lia [22]. All granitoid and ultramafic–mafic complexes of the Khangai Mountains can be considered as fragments of the plutonic part of a large igneous province [23], which has been proposed as the Permian Khangai LIP [24]. Granitoids of the Khangai batholith have been studied in detail—divided by age [25,26] and by geochemical and isotopic characteristics [27–29]. Little information has been accumulated about the mafic–ultramafic intrusions in the Khangai region, but some of the Permian intrusions have already been identified (Figure 1) [15,17,30].

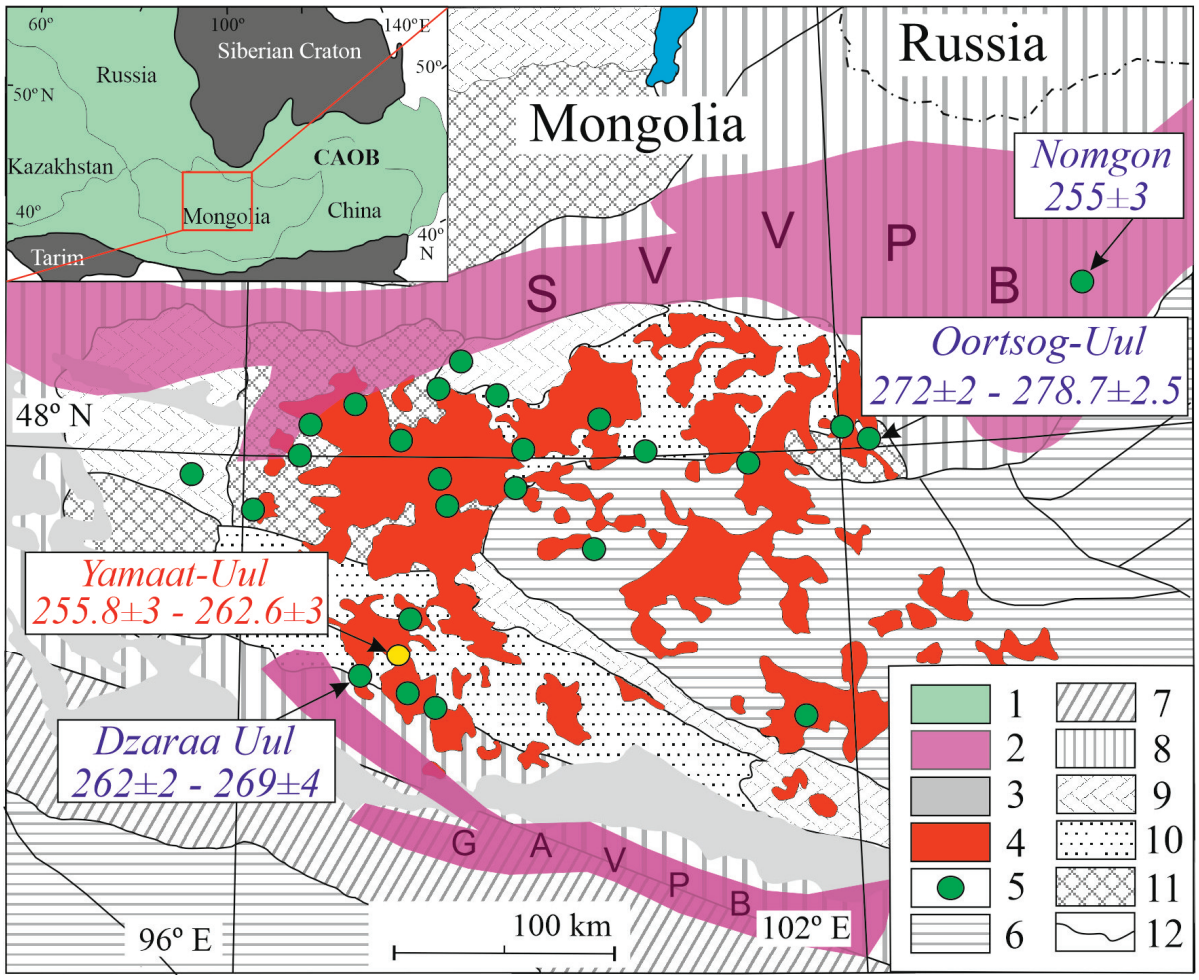

Figure 1. A geologic map of the mafic–ultramafic intrusions location within Khangai batholith (modified after [31,32]). 1—Central Asian orogenic belt (CAOB); 2—volcano–plutonic belt (SVVPB—Selenga–Vitim volcano–plutonic belt, GAVPB—Gobi–Altay volcano–plutonic belt); 3—Mesozoic–Cenozoic troughs; 4—Late Palaeozoic granitoids of the Khangai batholith; 5—Permian gabbros of the Khangai Mountains; 6–9—orogens: 6—Middle–Late Palaeozoic (Hercynides), 7—Early–Middle Palaeozoic (late Caledonides), 8—Vend–Early Palaeozoic (early Caledonides), 9—Neoproterozoic; 10—tectonic blocks with the Early Precambrian basement; 11—tectonic blocks with the Pre-Vend orogenic basement; 12—main tectonic boundaries. Red box—study area.

In this paper, we present new zircon U-Pb ages, Sm-Nd, Rb-Sr isotope data and detailed petrographic, mineralogical and geochemical study of the large Yamaat Uul mafic complex in the Khangai region. The purpose of this research was to identify the typomorphic mineralogical and geochemical features of the Yamaat Uul mafic complex, define the differentiation process of the parental magma and to better understand the tectonic setting of this region during the Permian. In addition, we will consider the sulphide mineralization in the Yamaat Uul complex and the sulphur isotopic composition in comparison with similar Permian intrusions and discuss its PGE-Cu-Ni potential.

2. Geological Setting and Geological Occurrence

The Yamaat Uul mafic complex is located in the Khangai Mountains of Western Mongolia and is part of the CAOB (Figure 1). The Khangai Mountains (Figure 1) are represented by the Khangai batholith, which is bounded by the Selenga–Vitim volcano–plutonic belt in the north and the Gobi–Altay volcano–plutonic belt in the south [33]. Together with other mafic–ultramafic intrusions, they are an early phase of the Khangai batholith [15] according to one of the theories of the Khangai LIP [24].

The CAOB is the largest juvenile Phanerozoic orogenic belt in the world and has developed over about 800 Ma. It is located between the East European, Siberian, North China and Tarim cratons and covers a large area of Russia from the Urals through Altai-Sayan and Transbaikalia to the Sea of Okhotsk, as well as areas of Kazakhstan, Kyrgyzstan, Uzbekistan, Mongolia, Northwest China and Northeast China [34]. The CAOB is composed of fragments of Precambrian continental blocks and Palaeozoic island arcs, ophiolites and volcanic rock assemblages formed by the action of various geodynamic processes [34–38]. The Yamaat Uul complex is located in the southern branch of the Khangai. Structurally and tectonically, it is located in the Baidrig terrane of the Dzavhan–Orkhon block [39], which in turn is part of the Central Mongolian terrane [40,41].

The Yamaat Uul mafic complex is the largest layered intrusion in Western Mongolia with the Cu-Ni mineralization. It is located on the left bank of the Dzavhan River, 25 km from Guulin Som of the Gobi-Altai aimag and 100 km from Altai City. The complex consists of outcrops of several large bodies, 20 × 20 km, which extend from north–west to south–east (Figure 2). The entire complex can be conventionally divided into three parts: Northwestern, Central and Southeastern. The geological map of Mongolia [L-47-VIII] shows only the Central part of the Yamaat Uul complex, but we found outcrops in other parts of the complex during field trips in 2014–2017.

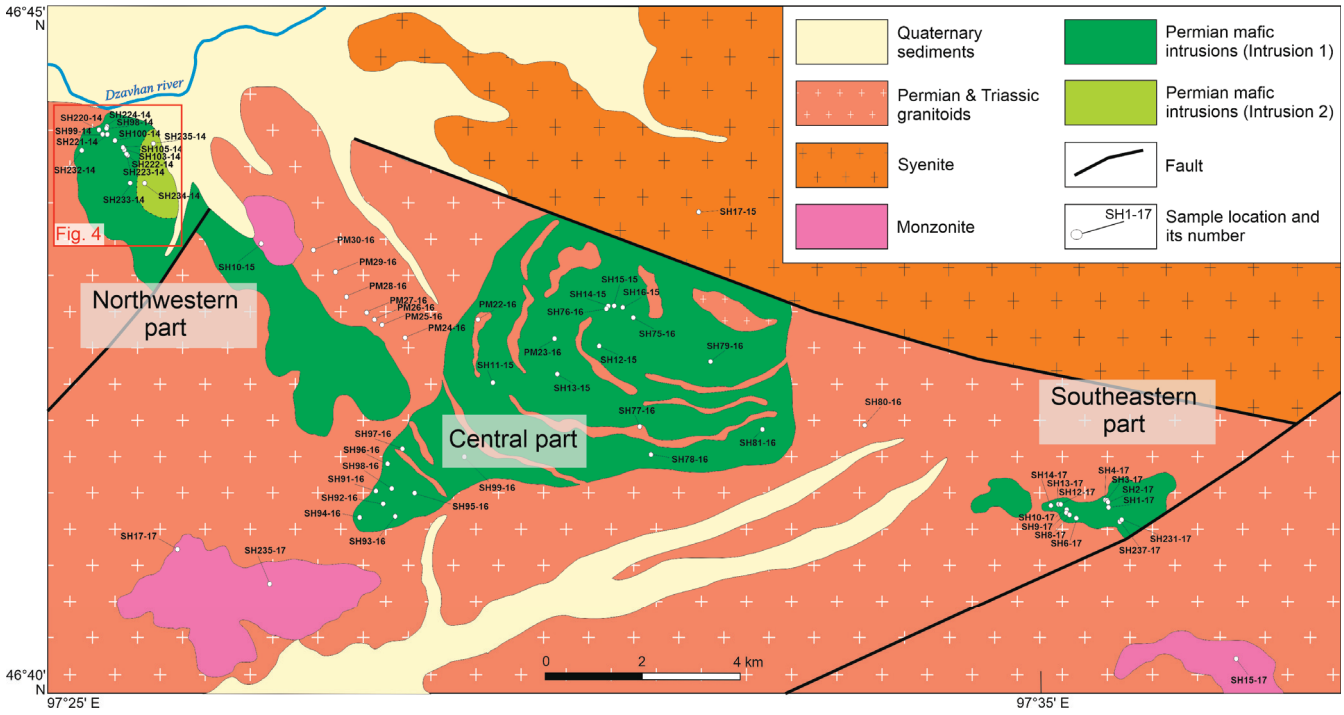

Figure 2. Simplified geological map of the Yamaat Uul mafic complex showing the distribution of lithological unites and sample's location.

The most important part for the reconstruction of the genesis is the Northwestern part of the complex, where we can observe the rock outcrops from two intrusions. Intrusion 1 is mainly represented by two groups of rocks:

(1) leucogabbro and anorthosite (plagioclase cumulate) (Figure 3a–c) and clearly marked in blue on the magnetic anomalies map (Figure 4a);
(2) biotite–amphibole (Bt-Am) gabbro and olivine (Ol) gabbronorite (olivine–pyroxene cumulates), located south of the previous (Figure 3d) and highlighted in yellow and green on the magnetic anomalies map (Figure 4a).

Intrusion 2 is composed of monzogabbro and occurs only in the Northwestern part of the complex; the samples SH234-14 and SH235-14 are involved (Figure 3e), which are marked by a red spot in the Eastern part on the magnetic anomalies map (Figure 4 b,c).

The Southeastern part is characterized by rocks of two groups of Intrusion 1: leucogabbro and gabbro and gabbronorite (without forming separate clusters). The gabbro is characterized by rhythmic layering (Figure 3f,g).

The Central part of the Yamaat Uul complex is composed of leucogabbro, gabbro and gabbronorite. The gabbro is characterized by rhythmic layering (Figure 3f,g); the Central part is a series of rhythmically layered rocks from Bt-Am-Ol gabbronorite to Bt-Am gabbro (Table 1). The layered structure of the mafic complex is clearly visible on the satellite image and in the photos (Figure 3m,n). The thickness of the layers varies from 5 to 20 m. The rocks of the Northwestern and Southeastern parts have subvertical bedding, whereas the Central part lies subhorizontal. Thus, the Yamaat Uul mafic complex is lopolith in plan, as are the major layered intrusions such as the Bushveld in South Africa and Sudbury in Canada [42,43].

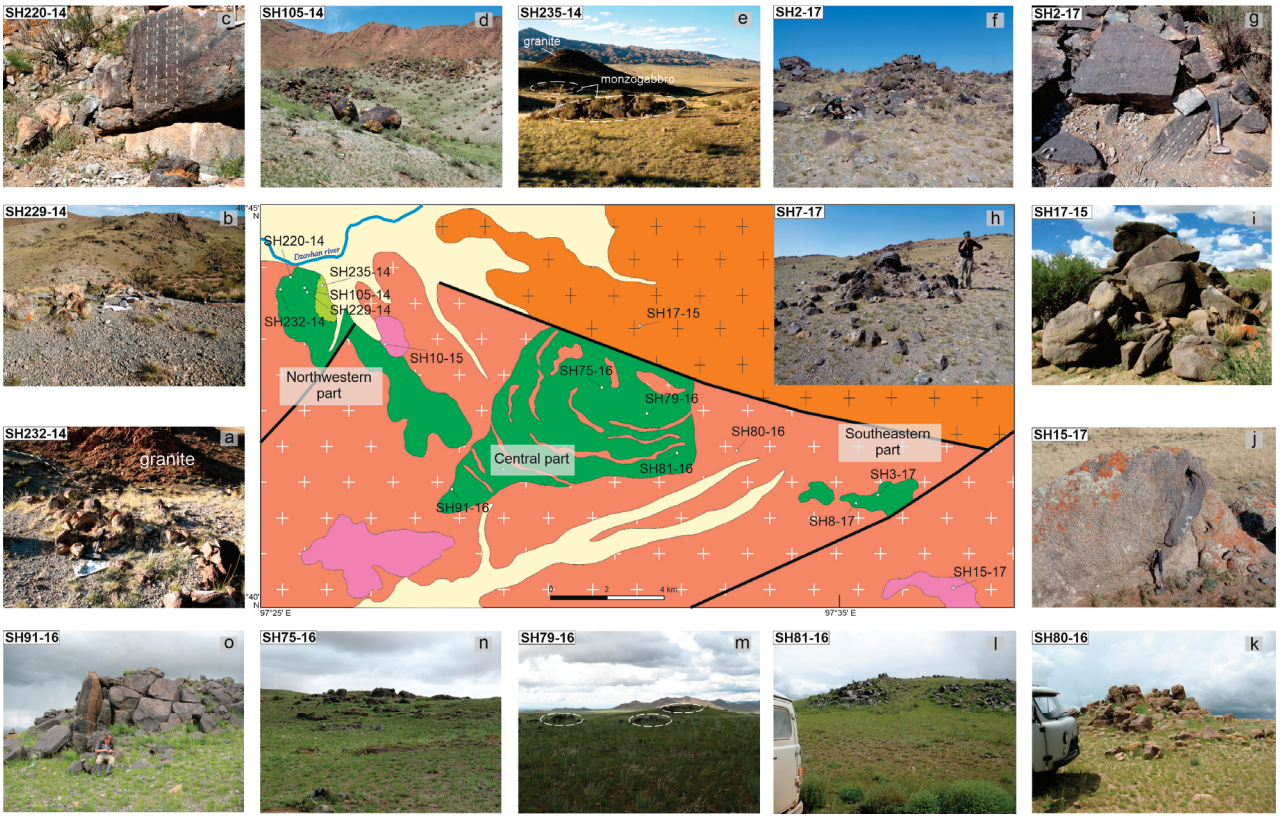

Figure 3. Photos of outcrops of the Yamaa-Uul mafic complex. (**a**–**c**) Plagioclase cumulates of Northwestern part; (**d**) pyroxene cumulates of Northwestern part; (**e**) monzogabbro of Intrusion 2; (**f**–**h**) Bt-Am leucogabbro of Southeastern part; (**i**) quartz syenite; (**j**) quartz monzodiorite; (**k**) Bt monzogranite; (**l**–**o**) gabbroids of Central part. Leucogabbro with fine subvertical layering (**c**,**g**). Names of rocks are in Table 1.

Table 1. Description of representative rock samples from Yamaat Uul mafic complex and surrounding rocks.

	Sample No.	Part of the Complex	Name of Rock	Latitude (N)	Longitude (E)
Intrusion 1					
1	SH100-14	Northwestern	Bt-Am-Ol gabbronorite	46.728381	97.447151
2	SH102-14	Northwestern	Bt-Am-Ol gabbronorite	46.727738	97.447997
3	SH103-14	Northwestern	Bt-Am-Ol gabbronorite	46.727333	97.448625
4	SH105-14	Northwestern	Bt-Am-Ol gabbronorite	46.726724	97.449163
5	SH220-14/2	Northwestern	Anorthosite	46.729082	97.445146
6	SH220-14/10	Northwestern	Leucogabbro	46.729274	97.444686
7	SH225-14	Northwestern	Leucogabbro	46.729533	97.444943
8	SH227-14	Northwestern	Anorthosite	46.729367	97.444792
9	SH228-14	Northwestern	Am gabbro	46.729347	97.444766
10	SH229-14	Northwestern	Bt leucogabbro	46.729296	97.444747
11	SH11-15	Central	Bt-Am-Ol melagabbronorite	46.70177	97.50741
12	SH12-15	Central	Bt-Am-Ol melagabbronorite	46.7058	97.52436
13	SH15-15	Central	Bt-Am gabbro	46.71023	97.52673
14	SH16-15/1	Central	Bt-Am gabbro	46.71004	97.5284
15	SH79-16	Central	Bt-Am gabbro	46.70414	97.54219
16	SH81-16	Central	Bt-Am gabbro	46.69661	97.55044
17	SH94-16/6	Central	Bt-Am gabbronorite	46.68693	97.48623
18	SH97-16	Central	Bt-Am-Ol gabbronorite	46.69443	97.49313
19	SH98-16/1	Central	Bt-Am-Ol gabbro	46.68999	97.49137
20	SH235-17	Central	Bt-Am gabbro	46.679603	97.471888
21	SH2-17	Southeastern	Bt-Am leucogabbro	46.688659	97.605492
22	SH5-17	Southeastern	Bt-Am leucogabbro	46.687670	97.602768
23	SH7-17	Southeastern	Bt-Am leucogabbro	46.687253	97.599314
24	SH14-17	Southeastern	Bt-Am leucogabbro	46.688338	97.596355
25	SH231-17	Southeastern	Bt-Am-Ol gabbronorite	46.686665	97.607608
26	SH232-17	Southeastern	Bt-Am gabbro	46.686665	97.607608
Intrusion 2					
27	SH234-14	Northwestern	Bt-Am-Ol monzogabbro	46.723678	97.451858
28	SH235-14	Northwestern	Bt-Am-Ol monzogabbro	46.728046	97.453226
Felsic and intermediate rocks					
29	SH10-15		Q monzodiorite	46.71689	97.47012
30	SH16-17		Q monzodiorite	46.671505	97.625913
31	SH17-17		Q monzonite	46.683439	97.456712
32	PM30-16		granodiorite	46.716230	97.478799
33	SH80-16		Bt monzonite	46.6971	97.5668
34	SH17-15		Bt-Cpx-Am syenite	46.72047	97.54023

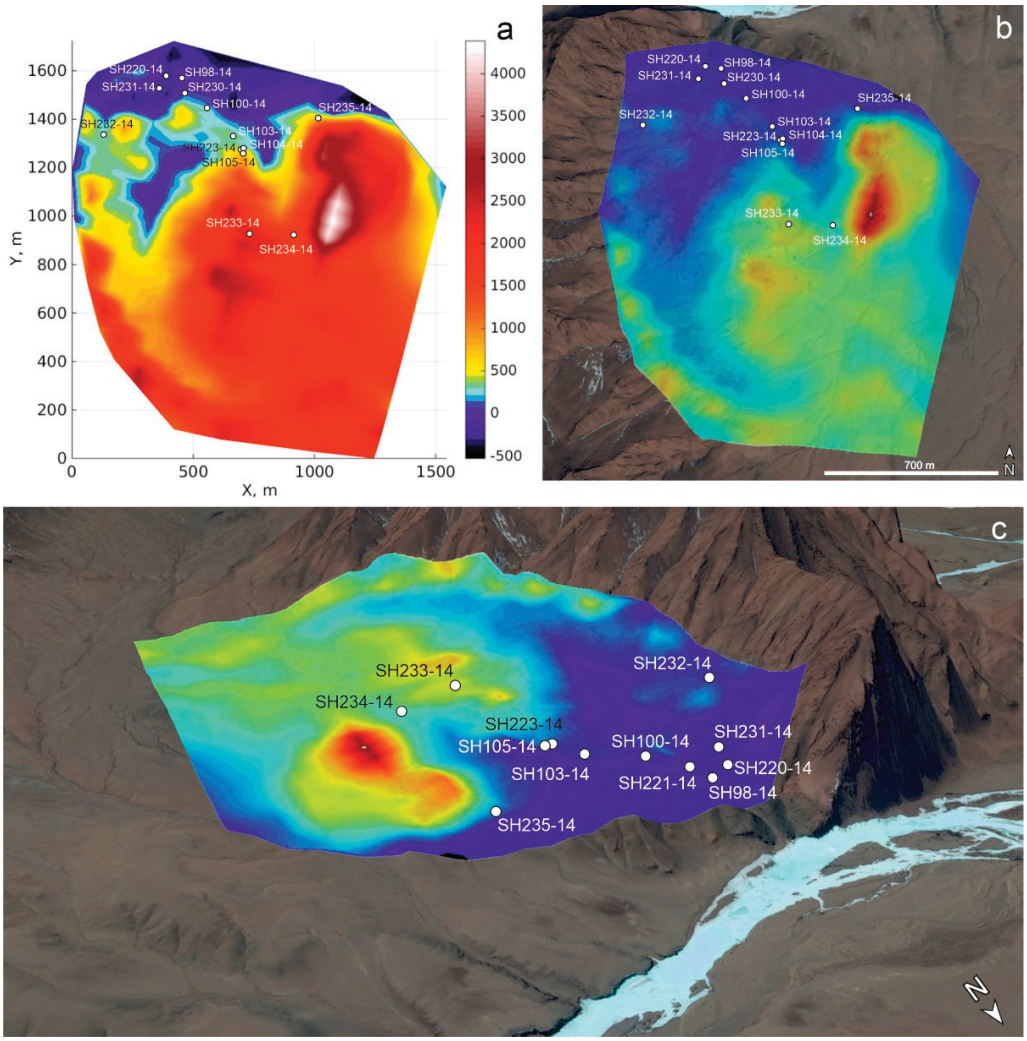

Figure 4. (**a**) Magnetic anomalies map and sample's location of the Northwestern part of the Yamaat Uul mafic complex; (**b**,**c**) shaded-relief magnetic anomaly map of the Northwestern part of the Yamaat Uul mafic complex: view from above (**b**), view from the northeast (**c**).

The boundaries of the Yamaat Uul mafic complex are mostly obscured by Quaternary sediments; outcrops of single round stones are mostly observed (Figure 3a–k). The complex's rocks have intrusive contact with later Permo-Triassic granites in the Northwestern part (Figure 3a); gabbro of the Central part is intensely intruded by granite dikes (Figure 2). There are outcrops of syenite (Figure 3h) to the north of the Central part—the contact with which is also sodded. Outcrops of monzonite and monzodiorite (Figure 3j), probably of a later age than the rocks of the mafic complex, are found in various parts of the complex. In general, the Yamaat Uul complex is surrounded by granitoids of the Khangai batholith [29] (Figure 3k).

The Yamaat Uul mafic complex contains sulphides, which are represented by disseminated and schlieren (droplets, globules) types. The Central part of the complex is characterized by sulphide disseminations only, while in other parts, both sulphide dissemination and sulphide schlieren are found. The sulphide mineralization represented by the chalcopyrite–pentlandite–pyrrhotite composition has been previously described [32].

3. Sampling and Analytical Methods

A collection of about 100 samples of mafic rocks was gathered by authors during the 2014–2017 field works on the Khangai region in Mongolia. Twenty-eight mafic samples of all parts of the Yamaat Uul complex were selected for this study (Table 1). Big-volume

samples of two rock types (SH105-14, SH220-14) were taken for zircon separation and U-Pb dating. Based on petrography, less altered samples were chosen for crushing and grounding to powder for whole-rock analyses. Ten samples were chosen for isotope analyses of Sm-Nd, Rb-Sr and S—systems. Most analyses were carried out in the Analytical Center for multi-elemental and isotope research of the Sobolev Institute of Geology and Mineralogy, Siberian Branch of the Russian Academy of Sciences (IGM SB RAS) in Novosibirsk, Russia.

3.1. Petrography

The Yamaat Uul mafic complex consists of two intrusions. Intrusion 1 is represented by plagioclase cumulates and olivine–pyroxene cumulates. Intrusion 2 consists of monzogabbro, which occurs only in the Northwestern part of the complex. Plagioclase cumulates (Figure 5a,b) are represented by leucogabbro and anorthosite with plagioclase contents of 80–95 vol%, and the interstitials contain anhedral grains of clinopyroxene, amphibole and very rarely biotite. Plagioclase is almost always zoned. Ore mineralization is represented by rare disseminations of chalcopyrite, pyrrhotite, magnetite and pyrite. The structure of the rocks is ophitic, subophitic and poikilophitic. The secondary minerals of chlorite, epidote, actinolite and rutile are common.

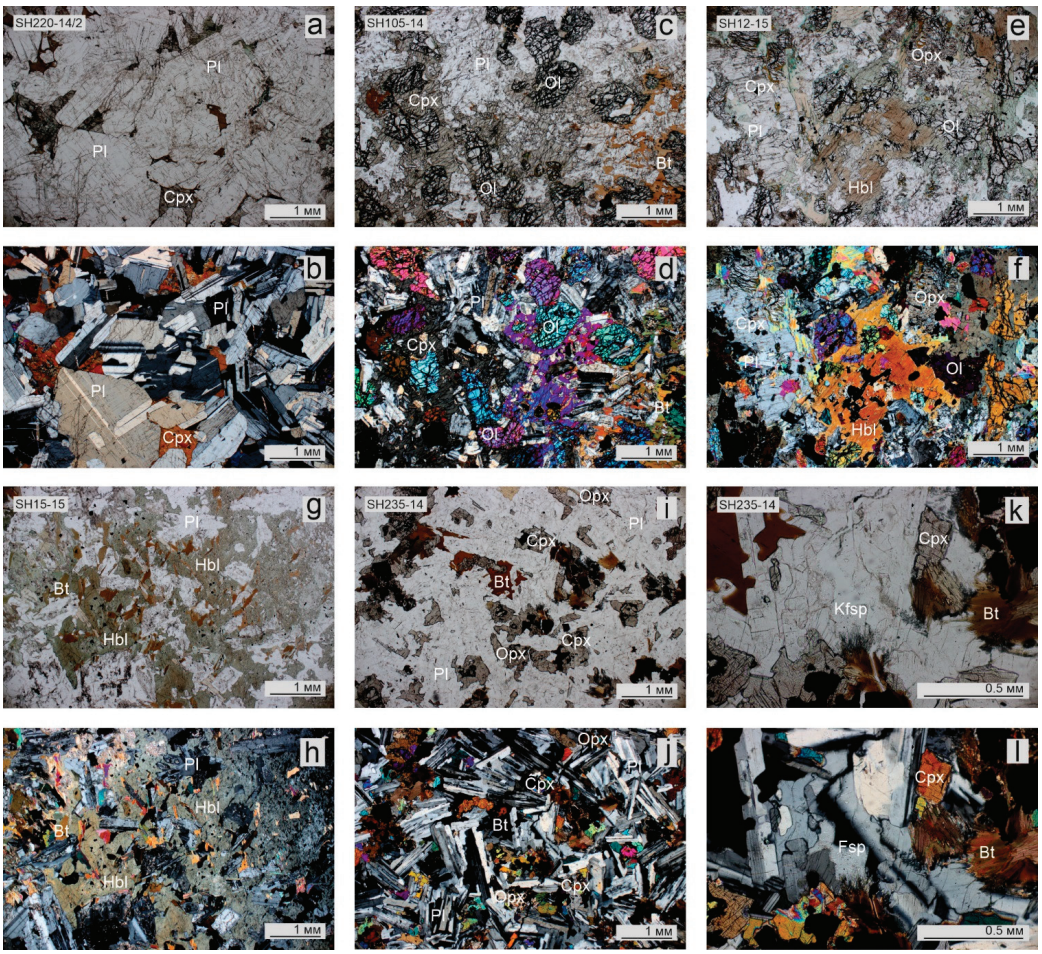

Figure 5. Photos of thin sections of the Yamaat Uul mafic complex: (**a**,**b**) plagioclase cumulate of Intrusion 1; (**c**–**h**) pyroxene cumulate of Intrusion 1: (**c**,**d**) olivine gabbro, (**e**,**f**) Am melagabbronorite, (**g**,**h**) Am gabbro; (**i**–**l**) monzogabbro of Intrusion 2. (**a**,**c**,**e**,**g**,**i**,**k**)—PPL; (**b**,**d**,**f**,**h**,**g**,**l**)—XPL. Ol—olivine, Cpx—monoclinic pyroxene, Opx—rhombic pyroxene, Hbl—hornblende, Bt—biotite, Pl—plagioclase, Fsp—K-Na feldspar.

Olivine–pyroxene cumulates (Figure 5c–h) are represented by amphibole melagabbronorite (Figure 5e,f), amphibole gabbro (Figure 5g,h), olivine gabbro (Figure 5c,d) and

olivine gabbronorite, in which the basic plagioclase content varies from the first percent (in melanocratic varieties) to 50 vol%. Olivine forms relatively large crystals, often surrounded by clinopyroxene (Figure 5c,d), amphibole in gabbroides or only amphibole in hornblende melagabbronorite (Figure 5e,f). The oikocryst of poikilitic clinopyroxene in gabbroids contains zonal distributed chadacrysts of plagioclase, indicating concomitant growth of plagioclase and clinopyroxene. In contrast to plagioclase cumulates, the amount of biotite increases in pyroxene cumulates. Its content is higher in melanocratic rocks than in mesocratic ones. The ore mineralisation is represented by disseminated, drop-shaped or schliere sulphide grains (cubanite, chalcopyrite, pyrrhotite, pentlandite) and schliere titanomagnetite ores. The structure of the rocks is ophitic, subophitic and poikilophitic. The secondary minerals of saussurite, chlorite, actinolite and iddingsite are locally distributed.

Monzogabbro of Intrusion 2 (Figure 5i,j) is leucocratic rocks consisting of plagioclase (60 vol%), olivine (10 vol%), clinopyroxene (5 vol%) and orthopyroxene (5 vol%), amphibole (5 vol%), biotite (10 vol%) and K-Na feldspar (5 vol%). Olivine and plagioclase are euhedral; clinopyroxene and biotite are anhedral. Orthopyroxene forms rims around olivine, and amphibole usually forms rims around clinopyroxene. Feldspar is located between euhedral plagioclase grains (Figure 5k,l). The structure of the rocks is ophitic, gabbro-ophytic and crowned. Monzogabbro contains disseminated oxide mineralization: magnetite and ilmenite.

3.2. Mineral Chemistry

The mineral composition of the Yamaat Uul mafic complex was determined in 24 thin sections previously prepared and polished at the laboratory of the IGM SB RAS. In total, 600 mineral chemistry analyses were conducted with wavelength-dispersive spectroscopy (WDS) in the Analytical Center of multi-elemental and isotope research of SB RAS under a JEOL JXA-8230 electron microprobe with five WDS detectors with LDE, TAP, PET-J, PET-H and LIF-L crystals. The analyses were determined with a current of 20 kV and 30 nA (100 nA for olivine) and 3 μm beam aperture. The analysis time ranged from 20 to 60 s per element, according to the expected abundance.

3.3. Zircon Separation and Analysis

Zircon separation was conducted in the IGM SB RAS with a standard procedure of crushing, panning, heavy-liquid and magnetic separation techniques. Zircon grains were handpicked under a binocular and then mounted in a 6 mm epoxy resin disc. All grains were half-polished to observe the internal structure using cathodoluminescence (CL) and transmitted light. The CL imaging was conducted at the Centre of Isotopic Research of the Russian Geological Research Institute (VSEGEI) using the scanning electron microscope MX2500 S (CamScan, Great Britain, Cambridge) and operated at an accelerating voltage of 12 kV and working distance of 30 mm. The locations for the spot analysis on zircon grains were selected using CL images (Figure 6a,b) and photomicrographs (transmitted light) to avoid mineral inclusions and cracks. Zircons from the samples SH220-14/2 and SH105-14 were analysed for U–Pb ages at the VSEGEI, Russia, with a SHRIMP II, following the standard procedures described in [44]. Prior to each analysis, the rastering of primary beams was applied to minimize contamination by surface Pb. U–Pb ages and concordia diagrams were calculated and plotted using IsoplotR software (ver. 3.75; [45]), respectively; the concordia age of each sample incorporates errors on decay constants and includes evaluation of the concordance of apparent ages. The concordia ages and errors are presented at the two-sigma level. All analyses of zircons are given in Table 2.

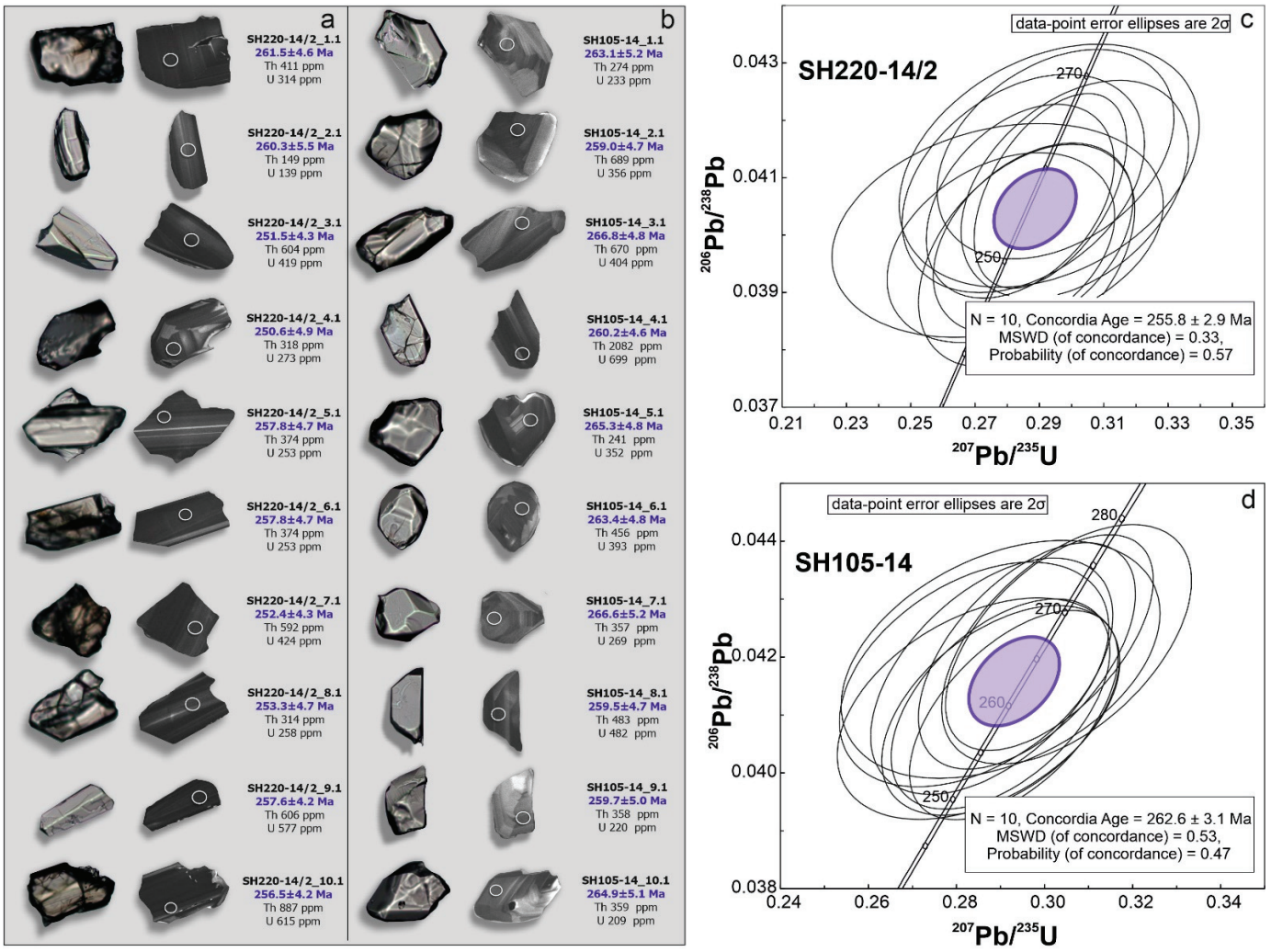

Figure 6. Transmitted light and CL images, U-Pb spot locations and ages for zircons from anorthosite (sample SH220-14/2) (**a**) and Bt-Am-Ol gabbronorite (SH105-14) (**b**). Concordia diagram for zircons from anorthosite (sample SH220-14/2) (**c**) and Bt-Am-Ol gabbronorite (SH105-14) (**d**).

3.4. Whole-Rock Major and Trace Elements

Whole-rock major element oxides were determined with XRF using an ARL 9900 (Thermo Scientific, Basel, Switzerland) according to the method in [46]. Trace elements were analysed with inductively coupled plasma emission-mass spectroscopy (ICP-MS) using an Element-I MAT (Finnigan, Germany) according to the method in [47]. The element abundances and ratios were normalized to chondritic CI and primitive mantle (PM) values, with reference to [48,49], respectively. Representative analyses of major and trace element contents (in wt.% and ppm, respectively) are given in Table 3.

3.5. Whole-Rock Sm-Nd, Rb-Sr and S Isotopic Analyses

Nd isotope compositions were determined at the Institute of Geology and Geochemistry of the Ural Division of the Russian Academy of Sciences in Yekaterinburg. Prepared samples were decomposed with 3% CH3COOH in a Teflon beaker at room temperature. Neodymium was separated during two stages: in the first stage, total REE was isolated with stepwise elution on cationite AG-50 × 8 (200–400 mesh), and then with extraction chromatography on columns filled with KEL-F powder coated with ionite (HDEHP). The isotopic composition was measured on a Finnigan MAT-262 multicollector solid-phase mass spectrometer in the static regime. The measured $^{143}Nd/^{144}Nd$ ratios were normalized to $^{146}Nd/^{144}Nd = 0.7219$. External uncertainty and reproducibility were controlled using

systematic measurements of the JNdi-1 = 0.512115 [50] international standards. The blank contamination for Nd was as low as 90 pg.

Table 2. Isotope parameters and ages of zircons from rocks of the Yamaat Uul mafic complex.

Spot	U	Th	$^{232}Th/^{238}U$	$^{206}Pb_t$, %	$^{206}Pb^*$, ppm	Isotope Parameters						Rho	Age, Ma			
	ppm					$^{207}Pb^*/^{206}Pb^*$	±%	$^{207}Pb^*/^{235}U$	±%	$^{206}Pb^*/^{238}U$	±%		$^{206}Pb/^{238}U$		$^{207}Pb/^{206}Pb$	
Anorthosite (SH220-14/2)																
1.1	314	411	1.35	0.28	11.20	0.0518	4.8	0.295	5.1	0.04141	1.8	0.352	261.5	±4.6	274	±110
2.1	139	149	1.11	0.00	4.92	0.0516	6.1	0.293	6.5	0.04121	2.1	0.330	260.3	±5.5	269	±140
3.1	419	604	1.49	0.35	14.40	0.0507	4.9	0.278	5.2	0.03978	1.7	0.337	251.5	±4.3	226	±110
4.1	273	318	1.20	0.00	9.28	0.0523	4.3	0.286	4.8	0.03964	2.0	0.419	250.6	±4.9	300	± 99
5.1	211	264	1.29	0.00	7.42	0.0506	5.0	0.285	5.4	0.0409	1.9	0.360	258.4	±4.9	221	±120
6.1	253	374	1.53	0.00	8.87	0.0535	4.4	0.301	4.8	0.0408	1.9	0.393	257.8	±4.7	352	± 99
7.1	424	592	1.44	0.21	14.60	0.0523	4.0	0.288	4.4	0.03994	1.7	0.396	252.4	±4.3	298	± 91
8.1	258	314	1.26	0.58	8.93	0.0501	7.4	0.277	7.6	0.04008	1.9	0.250	253.3	±4.7	198	±170
9.1	577	606	1.09	0.00	20.20	0.0522	2.9	0.293	3.3	0.04077	1.7	0.497	257.6	±4.2	294	± 66
10.1	615	887	1.49	0.29	21.50	0.0508	3.9	0.284	4.2	0.04059	1.7	0.395	256.5	±4.2	230	± 89
Bt-Am-Ol gabbronorite (SH105-14)																
1.1	233	274	1.21	0.00	8.36	0.0500	3.4	0.288	3.9	0.04167	2.0	0.511	263.6	±5.2	197	± 78
2.1	356	689	2.00	0.00	12.50	0.0518	2.7	0.293	3.3	0.041	1.8	0.560	258.9	±4.7	278	± 63
3.1	404	670	1.72	0.00	14.70	0.0517	2.6	0.301	3.2	0.04225	1.8	0.581	266.7	±4.8	272	± 59
4.1	699	2082	3.07	0.25	24.80	0.0510	3.0	0.290	3.5	0.04119	1.8	0.507	260.4	±4.6	240	± 70
5.1	352	241	0.71	0.00	12.70	0.0511	2.8	0.296	3.4	0.04202	1.9	0.548	265.5	±4.9	246	± 65
6.1	393	456	1.20	0.30	14.10	0.0494	4.0	0.284	4.4	0.0417	1.9	0.422	264.1	±4.8	164	± 93
7.1	269	357	1.37	0.00	9.77	0.0525	3.2	0.305	3.8	0.04222	2.0	0.531	266.3	±5.3	306	± 73
8.1	482	483	1.04	0.24	17.10	0.0511	3.3	0.290	3.8	0.04108	1.8	0.482	259.6	±4.7	246	± 77
9.1	220	358	1.68	0.00	7.76	0.0503	4.2	0.285	4.6	0.04111	1.9	0.424	260.1	±5.0	208	± 97
10.1	209	359	1.77	0.30	7.57	0.0501	4.7	0.290	5.1	0.04196	2.0	0.386	265.4	±5.2	197	±110

Note. The errors are at the 1σ level. Pbt and Pb *—total and radiogenic Pb, respectively. The error of standard calibration is no more than 0.51%. Correction for total Pb was made with the measured ^{204}Pb. Rho—correlation coefficient for $^{207}Pb^*/^{235}U$ and $^{206}Pb^*/^{238}U$.

The whole-rock Rb-Sr isotope composition was determined in the Analytical Center for multi-elemental and isotope research of IGM SB RAS (Novosibirsk, Russia). The strontium isotopic ratio was measured using the multiple-collector mass-spectrometer MI-1201AT through the double Re-Re tapes. Rb and Sr were extracted with ion chromatography on quartz columns filled with Dowex AG W50x8 resin, the eluent being 2N HCl. The correctness of the $^{87}Sr/^{86}Sr$ ratio was ensured using parallel measurements of each series of water samples according to the VNIIM isotope standard with $^{87}Sr/^{86}Sr = 0.70800 \pm 7$ (2σ, n = 6). The isotope composition of Sr in all of the measured samples was normalized per 0.710248 [51].

Two samples of sulphides (pyrrhotite, chalcopyrite) were analysed for sulphur isotopes. Sulphides were handpicked under a binocular. The separation of SO_2 from the sulphide mineral for the sulphur isotopic analysis followed the method described in [52]. The sulphur isotopic ratios were determined using a mass spectrometer (Finnigan MAT Delta dual inlet mode) at the Analytical Center for multi-elemental and isotope research of IGM SB RAS in Novosibirsk, Russia. The sulphur isotopic composition is expressed as $\delta^{34}S$ (‰) relative to the Canyon Diablo Troilite standard, and its analytical precision is about ±0.2‰.

4. Results

4.1. U-Pb Zircon Dating

The zircons in anorthosite (SH220-14/2) and Bt-Am-Ol gabbronorite (SH105-14) have mostly short prismatic morphologies and euhedral to subhedral crystals. Clear oscillatory zoning, a lack of metamorphic rims and high Th/U ratios indicate a magmatic origin. The locations of the U-Pb spot are shown in Figure 6. The zircons in different samples are similar: the size ranging from 40 to 200 μm, colourless to light yellow or brownish and

transparent to translucent. Isotope parameters and ages of zircons for each sample are shown in Table 2.

Ten zircon grains from SH220-14/2 and ten zircon grains from SH105-14 were analysed with SHRIMP II. These zircons have high U, Th and radiogenic Pb contents of 139–699 ppm, 149–2082 ppm and 5–25 ppm, respectively, with high Th/U ratios of 0.71–3.07. Such Th/U ratios are typical for magmatic rocks [53,54]. SH220-14/2 and SH105-14 yield a mean $^{206}U/^{238}Pb$ age of 255.8 ± 2.9 Ma (MSWD = 0.33) and 262.6 ± 3.1 Ma (MSWD = 0.53), respectively (Figure 6). These zircon U–Pb ages indicate that the mafic rock of the Yamaat Uul complex formed in the Late Permian.

4.2. Mineral Compositions

Olivine occurs in all parts of the Yamaat Uul mafic complex. Its Mg number (Mg#) varies from 68 to 77 in the Central part, from 71 to 72.3 in the Southeastern part and 71–73.6 in the Northwestern part of the complex. Olivine from Intrusion 2 monzogabbro has a lower Mg number of 46–50.3 and higher MnO content than olivine from Intrusion 1 (Figure 7a, Table S1). The CaO and NiO content was rather low: 0.06 to 0.12 wt.% in all rock types.

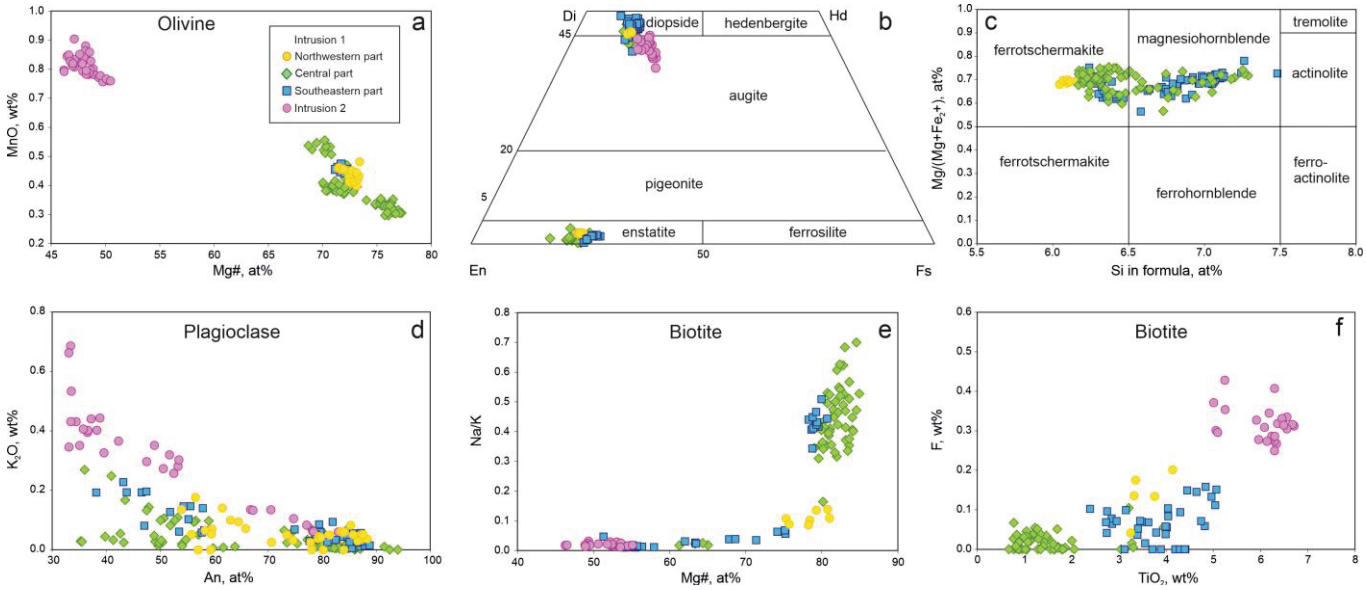

Figure 7. Chemical variation plots of olivine (**a**), clinopyroxene [55] (**b**), amphibole [56] (**c**), plagioclase (**d**) and biotite (**e**,**f**) from the studied rocks.

Clinopyroxenes of all parts of the Yamaat Uul complex show similar compositions in the range $En_{40–45}Fs_{8–16}Wo_{41–49}$ and can be classified as diopside and augite according to the pyroxene nomenclature [55] (Figure 7b, Table S2). Their Mg numbers vary from 73 to 85. Clinopyroxenes are characterized by low TiO_2 (0.28–1 wt.%) and very low Cr_2O_3 (0–0.04%) contents. Al_2O_3 and Na_2O contents vary from 0.7 to 5.0 wt.% and 0.15 to 0.65 wt.%, respectively (Table S2). Clinopyroxenes from Intrusion 2 monzogabbro have the composition range $En_{39–43}Fs_{14–21}Wo_{38–44}$ and are augite [55] (Figure 7b, Table S2). They have a lower Mg number (Mg#, 66–75) and slightly less Al_2O_3 content (0.6–2.8 wt.%) compared with clinopyroxenes of gabbroides from Intrusion 1. The compositions of orthopyroxene from all parts of the intrusion fall in the range $En_{71–79}Fs_{20–27}Wo_{0–2}$ and are classified as enstatite [55] with a Mg# of 72–80 and Al_2O_3 (0.9–2.33 wt.%) (Figure 7b, Table S3).

Brown amphibole of Intrusion 1 rocks ranges from magnesiohornblende to tschermakite [56] (Figure 7c). Its Mg number varies from 57 to 75. The composition of this amphibole usually varies within individual samples, particularly in terms of the Mg number and TiO_2 (0.7–4.6 wt.%) and K_2O (0.3–1.2 wt.%) contents (Table S4).

Plagioclase composition of Intrusion 1 of the Yamaat Uul mafic complex varies within a similar range. It is normally zoned, with An-rich cores gradually passing into An-poor rims (Figure 7d). Cores of plagioclases are generally anorthite–bytownite ($An_{71–94}$) with very low K_2O content (up to 0.09 wt.%). The maximum of An content ($An_{91–94}$) is observed in gabbroides of the Central part. Plagioclase rims show An content varying from labradorite to andesite ($An_{35–66}$) with K_2O up to 0.27 wt.%. Plagioclases from monzogabbro of Intrusion 2 have lower An content and correspond to labradorite–bytownite in cores ($An_{67–83}$) and andesite ($An_{33–53}$) in rims. K_2O content in plagioclase rims is higher than in plagioclase rims from gabbroides and ranges from 0.26 to 0.69 wt.% (Figure 7d, Table S5).

Biotite was observed in all rock types but had different composition in different parts of the complex. In the Central part, it showed a Mg number of 79–85, low T_2O (0.68–2 wt.%), F (0–0.07 wt.%), high Na_2O (1.3–2.62 wt.%) and a high N/K ratio (0.3–0.7), with the exception of a few points. Biotites from Southeastern and Northwestern parts have a wide range in the Mg number from 51 to 81, higher TiO_2 (2.4–5 wt.%) content and slightly higher F (up to 0.16 wt.%) content. More magnesian biotite has high Na_2O (1.55–2.17 wt.%) and a high Na/K ratio (0.3–0.5) like in the Central part; less magnesian minerals have a low Na/K ratio (0.01–0.07) and are richer in K_2O (7.8–9.7 wt.%) (Supplementary Materials Table S5). Biotite from monzogabbro of Intrusion 2 is characterized by the lowest Mg number varying from 46 to 55 and highest K_2O (8.9–9.5 wt.%), TiO_2 (5–6.7 wt.%) and F (0.25–0.43 wt.%) contents (Figure 7e,f and Table S6).

4.3. Whole-Rock Geochemistry

Twenty-eight samples of mafic rocks from the Yamaat Uul complex were selected for detailed description (Table 3). The rocks are characterized by a wide range of MgO at variable SiO_2 (Table 3; Figures 8 and 9): SiO_2 spans 39–52 wt.% and MgO from 0.5 to 24.6 wt.%. The ranges of K_2O, TiO_2 and P_2O_5 are 0.14–1.87, 0.17–2.01 and 0.03–0.43 wt.%, respectively. The concentrations of Al_2O_3 and CaO vary in relatively wide ranges of 8.7–30.7 and 4.15–17.1 wt.%, respectively. According to SiO_2 and total alkali ($Na_2O + K_2O$) contents, i.e., the traditional TAS diagram [57], the Yamaat Uul mafic rocks are dominated by gabbro (Figure 8a). The felsic and intermediate surrounding rocks of the Yamaat Uul mafic complex are dominated by monzonite and granite.

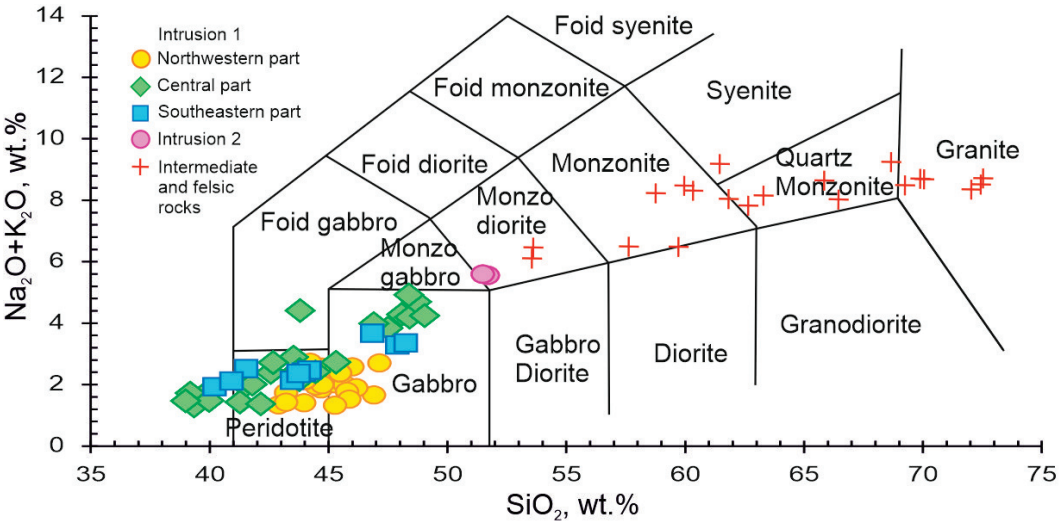

Figure 8. Classification diagram for rocks of the Yamaat Uul mafic complex and surrounding rocks (after [57]).

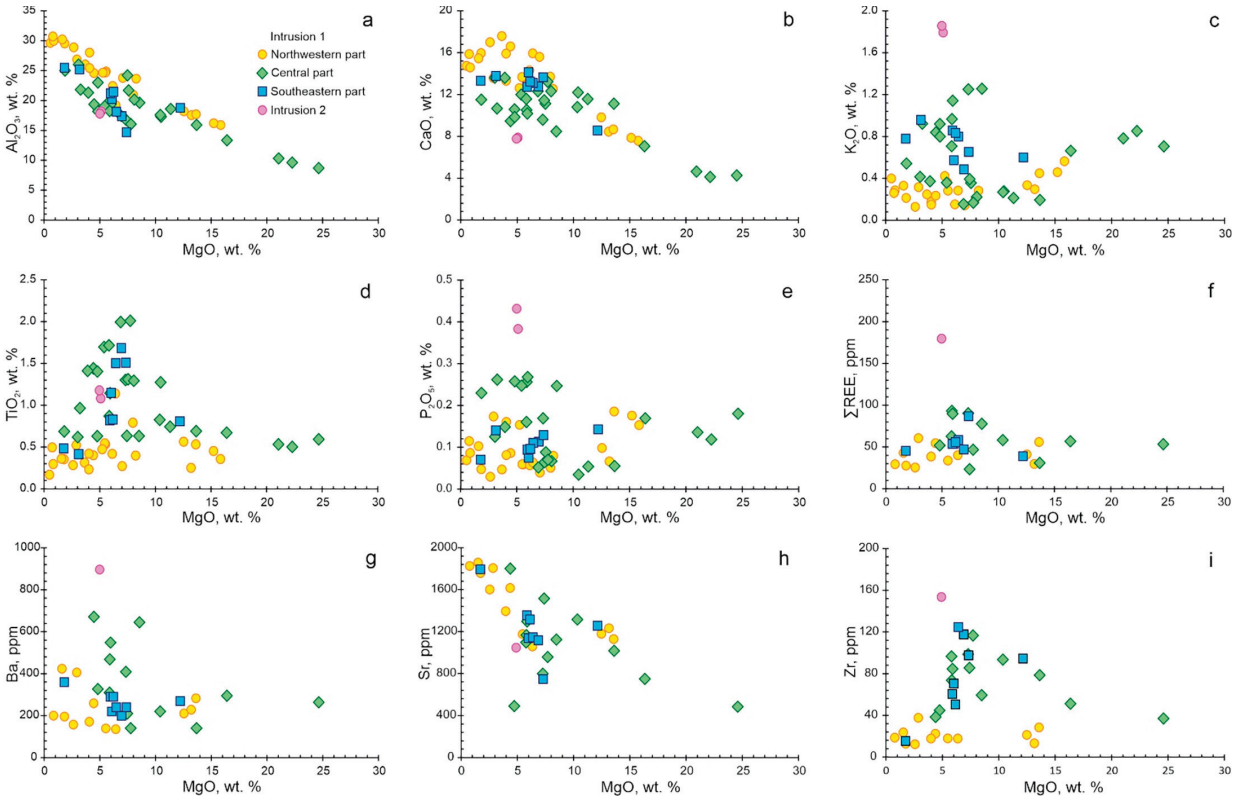

Figure 9. Variation diagrams of MgO vs. (**a**) Al_2O_3, (**b**) CaO, (**c**) K_2O, (**d**) TiO_2, (**e**) P_2O_5, (**f**) ∑REE, (**g**) Ba, (**h**) Sr and (**i**) Zr for the mafic rocks from the Yamaat Uul mafic complex.

The rocks of the Northwestern part form two groups on the binary diagrams (Figure 9). The first group is low-K and high-Sr gabbroides (MgO, 0.51–6.41 wt.%; K_2O, 0.12–0.28 wt.%; Sr up to 1831 ppm) represented by leucogabbro and anorthosite (Figure 5c,h). The second group is high-K and low-Sr gabbroides (MgO, 12.53–15.83 wt.%; K_2O, 0.33–0.56 wt.%; 1061–1236 ppm) that are Bt-Am-Ol gabbros and gabbronorites (Figure 5c,h). The rocks of the Southeastern part from the complex are similar in composition to the first group of the Northeastern part, but with less variability.

Monzogabbro is characterized by a high concentration of K_2O, P_2O_5 and ∑REE: up to 1.87, 0.43 wt.% and 180 ppm, respectively, with 5 wt.% MgO content (Figure 9c,e,f). This is due to the accumulation of incompatible elements during the formation of the mafic complex and the appearance of K-Na feldspar in monzogabbro.

The chondrite-normalized rare-earth element (REE) patterns of the Yamaat Uul complex (Figure 10a,c,e) are flat to moderately enriched in the light REE (LREE): La_n = 5.9–44.6, La/Sm_n = 0.9–4.8 and La/Yb_n = 3.9–16.1 (Table 3). All samples are characterized by medium-fractionated REE patterns that are slightly depleted in heavy REE (HREE): Gd/Yb_n = 1.7–3.0. The level of REE concentrations in the monzogabbro of Intrusion 2 (Figure 10a) is higher than that in the rocks of Intrusion 1 (Figure 10a,c,e) in all parts of the complex. The REE patterns of leucogabbro and anorthosite samples of the Northwestern and Southeastern parts show small positive Eu anomalies (Figure 10a,e), suggesting fractionation of plagioclase.

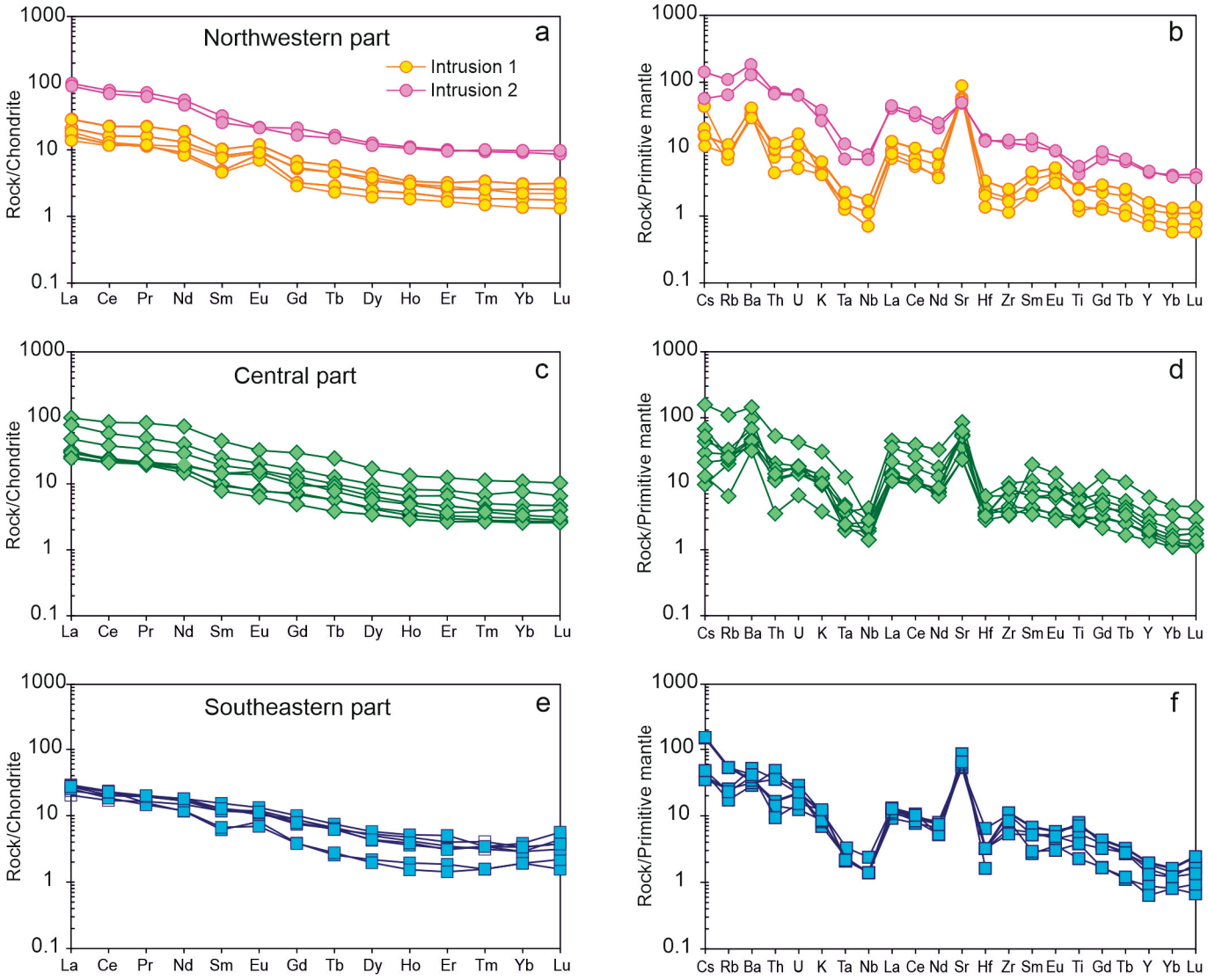

Figure 10. CI-chondrite-normalized [48] REE patterns and primitive mantle-normalized [49] trace element spidergrams for the Yamaat Uul mafic complex: (**a**,**b**) Northwestern part, (**c**,**d**) Central part, (**e**,**f**) Southeastern part.

Table 3. Representative whole-rock major (wt.%) and trace element (ppm) data for the Yamaat Uul mafic complex.

	Intrusion 1									
№	1	2	3	4	5	6	7	8	9	10
Part	NW	NW	NW	NW	NW	NW	NW	NW	NW	NW
Sample	SH100-14	SH102-14	SH103-14	SH105-14	SH220-14/2	SH220-14/10	SH225-14	SH227-14	SH228-14	SH229-14
SiO_2	44.69	44.01	45.50	43.48	47.14	46.00	43.22	44.72	44.23	46.16
TiO_2	0.54	0.57	0.25	0.45	0.17	0.30	1.14	0.36	0.53	0.41
Al_2O_3	24.81	18.16	17.50	16.18	29.61	29.94	19.14	30.19	26.83	24.54
Fe_2O_3	7.37	12.12	10.85	13.33	2.96	4.29	10.91	3.27	5.40	4.24
MnO	0.09	0.16	0.18	0.17	0.02	0.03	0.12	0.06	0.08	0.09
MgO	5.53	12.53	13.20	15.21	0.51	0.84	6.41	1.59	2.91	4.44
CaO	13.70	9.87	8.49	7.90	14.83	14.67	16.02	15.53	13.64	16.69

Table 3. *Cont.*

	Intrusion 1											
Na_2O	1.57	1.80	2.08	1.72	2.31	2.29	1.14	2.24	2.40		1.66	
K_2O	0.28	0.33	0.29	0.46	0.40	0.28	0.28	0.33	0.31		0.23	
P_2O_5	0.06	0.10	0.07	0.18	0.07	0.09	0.06	0.10	0.17		0.09	
LOI	1.07	0.65	1.36	0.86	1.32	1.09	1.05	1.45	2.13		1.54	
Total	99.91	100.59	100.02	100.43	99.55	100.05	99.84	100.05	99.11		100.38	
Rb	3.04	5.38	4.44	8.47	6.18	5.26	2.93	5.65	4.72		4.03	
Cs	0.18	1.00	0.47	0.36	0.32	0.25	0.29	0.29	0.36		0.25	
Ba	138.06	210.14	228.01	267.42	270.44	199.34	134.94	424.08	406.26		259.02	
Sr	1178.36	1181.03	1235.58	955.03	1699.40	1831.18	1060.63	1863.81	1810.73		1620.54	
Th	0.62	0.64	0.38	0.78	1.34	1.02	0.30	0.78	1.24		1.61	
U	0.11	0.16	0.11	0.24	0.39	0.35	0.08	0.24	0.40		0.48	
La	4.26	6.55	4.98	8.61	6.46	5.75	4.09	7.67	9.95		8.98	
Ce	9.32	13.04	9.77	17.76	12.42	10.46	9.76	15.01	20.20		17.74	
Pr	1.45	1.93	1.37	2.23	1.40	1.42	1.61	1.87	2.72		2.31	
Nd	6.72	7.81	5.41	9.04	5.31	4.95	7.85	7.76	11.48		9.46	
Sm	1.47	1.58	0.94	1.88	0.91	0.89	2.07	1.81	2.46		2.18	
Eu	0.67	0.71	0.63	0.67	0.48	0.51	0.81	0.68	0.90		0.82	
Gd	1.41	1.34	0.83	1.53	0.79	0.74	2.02	1.24	1.99		1.81	
Tb	0.21	0.21	0.13	0.21	0.09	0.11	0.30	0.18	0.25		0.26	
Dy	1.23	1.10	0.78	1.04	0.57	0.62	1.77	1.00	1.53		1.49	
Ho	0.22	0.21	0.16	0.21	0.11	0.13	0.32	0.18	0.32		0.30	
Er	0.59	0.54	0.40	0.56	0.34	0.35	0.78	0.40	0.76		0.79	
Tm	0.08	0.08	0.06	0.09	0.05	0.05	0.11	0.06	0.11		0.11	
Yb	0.46	0.54	0.38	0.48	0.34	0.28	0.67	0.34	0.65		0.71	
Lu	0.07	0.08	0.06	0.07	0.05	0.04	0.10	0.05	0.10		0.11	
Zr	17.32	20.69	12.72	35.99	27.48	18.18	17.18	23.01	37.16		21.96	
Hf	0.67	0.72	0.42	0.87	0.77	0.62	0.81	0.67	0.99		0.81	
Nb	0.57	0.82	0.50	1.23	0.83	0.79	0.47	1.25	1.19		0.64	
Ta	<0.05	0.06	<0.05	0.08	0.05	0.06	<0.05	0.05	0.08		<0.05	
Y	5.79	5.54	3.95	6.15	3.19	3.22	8.18	4.93	7.43		7.77	
	Intrusion 1											
№	11	12	13	14	15	16	17	18	19	20	21	22
Part	Central	Central	Central	Central	Central	Central	Central	Central	Central	Central	SE	SE
Sample	SH11-15	SH12-15	SH15-15	SH16-15/1	SH79-16	SH81-16	SH94-16/6	SH97-16	SH98-16/1	SH235-17	SH2-17	SH5-17
SiO_2	43.67	41.50	48.07	43.80	47.49	46.90	41.80	42.66	43.79	46.83	47.88	40.20
TiO_2	0.67	0.59	0.63	1.44	0.87	1.15	0.64	1.72	0.83	1.30	0.49	1.69
Al_2O_3	13.33	8.67	22.98	19.34	19.92	19.29	24.19	18.22	17.55	16.72	25.45	17.36
Fe_2O_3	14.50	15.46	5.95	14.54	8.71	10.44	10.69	15.60	12.43	12.88	6.06	17.74
MnO	0.18	0.20	0.07	0.19	0.12	0.12	0.13	0.14	0.16	0.15	0.07	0.16
MgO	16.39	24.63	4.80	4.45	5.87	5.94	7.44	5.85	10.40	7.32	1.78	6.94
CaO	7.10	4.29	10.64	9.52	10.59	10.24	11.52	11.65	10.87	9.65	13.39	12.84
Na_2O	1.77	1.24	3.35	3.56	2.86	2.83	1.61	2.00	2.21	2.41	2.50	1.44
K_2O	0.66	0.71	0.92	0.84	0.97	1.15	0.39	0.71	0.26	1.25	0.78	0.49
P_2O_5	0.17	0.18	0.26	-	0.26	0.27	0.06	0.16	-	0.17	0.07	0.11
LOI	0.76	1.82	1.69	0.56	1.26	0.99	1.03	1.09	0.61	0.54	0.52	0.48
Total	99.48	99.64	99.47	99.50	99.05	99.46	99.59	99.96	99.79	99.42	99.08	99.64
Rb	12.59	16.26	17.86	14.58	20.70	27.90	16.20	15.90	4.10	46.90	16.00	11.00
Cs	0.22	1.57	0.67	0.48	1.00	1.80	6.40	1.20	0.30	7.70	0.90	1.00
Ba	295.34	263.56	327.25	673.34	470.00	550.00	210.00	310.00	220.00	410.00	360.00	200.00
Sr	751.59	484.82	490.26	1807.09	1170.00	1300.00	1520.00	1100.00	1320.00	800.00	1800.00	1120.00
Th	0.95	1.04	1.73	0.95	1.40	1.80	10.40	1.20	0.30	5.40	3.00	4.10
U	0.30	0.30	0.39	0.30	0.35	0.42	0.10	0.38	0.14	1.15	0.60	0.46
La	9.40	8.02	9.92	30.95	14.80	14.20	4.50	9.10	7.50	14.00	9.00	6.30
Ce	19.66	17.06	18.72	69.11	30.60	28.90	8.20	18.70	16.90	28.90	19.00	13.70
Pr	2.58	2.41	2.35	10.18	4.10	3.91	1.01	2.59	2.52	3.98	1.90	2.00
Nd	10.26	9.84	8.79	44.10	17.30	17.20	4.20	11.40	11.70	15.60	7.00	8.90
Sm	1.82	1.94	1.52	8.66	3.70	3.40	0.80	2.80	2.80	3.80	1.20	2.30
Eu	0.59	0.56	0.47	2.38	1.19	1.26	0.62	1.01	1.14	1.12	0.60	0.88
Gd	1.78	1.88	1.27	7.64	3.32	3.38	0.68	2.46	2.84	3.45	1.00	2.25
Tb	0.27	0.27	0.18	1.13	0.47	0.46	0.08	0.42	0.36	0.53	0.12	0.31
Dy	1.34	1.40	1.10	5.45	2.51	2.49	0.44	2.08	1.83	2.80	0.70	1.61
Ho	0.24	0.27	0.21	0.95	0.47	0.45	0.06	0.37	0.35	0.48	0.14	0.30
Er	0.63	0.69	0.56	2.60	1.39	1.10	0.28	0.97	0.77	1.35	0.39	0.73
Tm	0.09	0.10	0.09	0.36	0.16	0.16	0.05	0.13	0.12	0.20	0.05	0.10

Table 3. *Cont.*

	Intrusion 1											
Yb	0.57	0.63	0.54	2.26	1.00	1.00	0.20	0.80	0.70	1.30	0.40	0.60
Lu	0.09	0.09	0.08	0.33	0.15	0.21	0.12	0.13	0.10	0.18	0.05	0.14
Zr	50.73	36.49	44.32	37.95	73.00	84.00	85.00	96.00	93.00	98.00	15.00	117.00
Hf	1.15	0.87	1.07	1.33	2.00	1.00	5.00	<1	<1	2.00	0.50	2.00
Nb	1.86	1.36	1.50	3.04	2.00	2.00	1.00	1.00	1.00	3.00	1.70	1.00
Ta	0.10	0.08	0.09	0.15	<0.5	<0.5	1.80	<0.5	<0.5	<0.5	0.60	<0.5
Y	7.62	8.27	6.27	28.31	12.20	11.90	2.20	10.00	8.80	12.80	4.00	7.20
	Intrusion 1				**Intrusion 2**		**Felsic and Intermediate Rocks**					
№	23	24	25	26	27	28	29	30	31	32	33	34
Part	SE	SE	SE	SE	NW	NW						
Sample	SH7-17	SH14-17	SH231-17	SH232-17	SH234-14	SH235-14	SH10-15	SH16-17	SH17-17	PM30-16	SH80-16	SH17-15
SiO_2	43.45	43.96	40.91	44.19	51.70	51.50	58.76	60.31	59.95	65.85	69.89	61.45
TiO_2	1.15	1.51	0.81	0.82	1.08	1.18	0.97	0.79	0.81	0.49	0.33	0.76
Al_2O_3	20.21	14.66	18.73	21.17	18.14	17.77	16.76	16.65	16.75	16.44	14.84	17.53
Fe_2O_3	11.60	15.07	15.81	9.83	9.41	9.96	6.57	6.17	5.87	3.47	2.57	4.79
MnO	0.12	0.21	0.16	0.11	0.14	0.15	0.11	0.10	0.09	0.06	0.05	0.10
MgO	6.04	7.36	12.19	5.92	5.09	4.98	2.44	2.38	2.46	1.02	0.64	1.68
CaO	14.20	13.73	8.62	12.80	7.92	7.82	4.39	4.23	4.26	2.58	1.66	3.31
Na_2O	1.56	1.74	1.51	1.60	3.75	3.73	3.99	3.91	4.02	4.45	4.01	4.80
K_2O	0.57	0.65	0.60	0.86	1.80	1.87	4.23	4.39	4.44	4.18	4.69	4.37
P_2O_5	0.07	0.13	0.14	0.09	0.38	0.43	0.31	0.33	0.33	0.16	0.10	0.30
LOI	0.41	0.36	0.07	1.65	0.00	-0.25	0.44	0.26	0.23	0.51	0.52	0.19
Total	99.55	99.59	99.77	99.30	99.63	99.32	99.16	99.68	99.35	99.42	99.47	99.52
Rb	16.00	19.60	14.60	33.80	69.61	41.05	127.14	198.00	226.00	-	-	105.88
Cs	0.80	0.90	1.10	3.50	3.27	1.31	2.58	8.60	9.90	-	-	2.43
Ba	220.00	240.00	270.00	290.00	1283.86	898.84	1231.56	840.00	820.00	-	-	1497.41
Sr	1140.00	750.00	1260.00	1360.00	1023.55	1047.67	697.31	680.00	670.00	-	-	579.05
Th	3.00	1.80	1.20	0.80	5.98	5.65	13.74	25.90	32.00	-	-	13.34
U	0.45	0.89	0.26	0.32	1.37	1.33	1.40	3.85	4.05	-	-	2.39
La	7.40	12.20	7.90	8.80	27.90	30.62	37.00	39.30	43.30	-	-	41.64
Ce	16.20	26.20	14.90	18.20	55.61	62.54	71.89	74.60	84.40	-	-	79.83
Pr	2.36	3.57	1.78	2.38	7.62	8.72	8.99	9.26	10.10	-	-	9.78
Nd	10.00	15.40	7.10	10.00	27.85	33.27	32.28	33.60	36.60	-	-	35.56
Sm	2.50	3.90	1.30	2.30	4.96	6.27	5.41	6.60	6.70	-	-	5.95
Eu	0.76	1.22	0.51	0.82	1.57	1.59	1.20	1.41	1.50	-	-	1.55
Gd	2.28	3.63	0.99	1.92	4.24	5.46	4.85	5.23	5.44	-	-	5.03
Tb	0.29	0.53	0.13	0.30	0.70	0.77	0.72	0.73	0.81	-	-	0.75
Dy	1.71	2.71	0.63	1.37	3.69	4.03	3.97	3.68	3.99	-	-	4.10
Ho	0.34	0.53	0.11	0.26	0.75	0.79	0.72	0.69	0.74	-	-	0.74
Er	0.84	1.51	0.30	0.67	1.99	2.10	2.09	2.02	2.06	-	-	2.27
Tm	0.13	0.19	0.05	0.11	0.32	0.30	0.33	0.30	0.35	-	-	0.36
Yb	0.70	1.20	0.40	0.60	2.02	1.90	1.94	2.10	2.30	-	-	2.15
Lu	0.12	1.19	0.07	0.10	0.31	0.28	0.29	0.34	0.36	-	-	0.33
Zr	70.00	97.00	94.00	60.00	138.36	152.81	213.71	62.00	57.00	-	-	319.27
Hf	1.00	2.00	<1	<1	4.28	4.03	4.90	8.00	8.00	-	-	7.68
Nb	1.00	1.00	1.00	1.00	5.85	4.98	8.82	10.00	13.00	-	-	7.93
Ta	<0.5	<0.5	<0.5	<0.5	0.48	0.28	0.55	<0.5	0.70	-	-	0.51
Y	8.40	13.00	2.90	6.00	20.31	21.32	23.84	19.80	20.40	-	-	22.74

The primitive mantle normalized multi-element patterns for all samples (Figure 10 b,d,f) show a clear Nb, Zr and Hf depletion (Table 3). The presence of the Nb and Hf minimums is a typical feature of rocks formed in a subduction-related setting. All samples are characterized by enrichment in LREE and Sr of varying intensity. The Sr maximum shows fractionation of plagioclase. Generally, the level of the trace element in the monzogabbro of Intrusion 2 (Figure 10b) is higher than that in the rocks of Intrusion 1 (Figure 10b,d,f) in all parts of the complex.

4.4. Whole-Rock Nd, Sr and S Isotopes

Whole-rock Sr-Nd isotopic compositions for selected samples from the mafic rocks of the Yamaat Uul complex and monzodiorite are given in Table 4. The initial $^{87}Sr/^{86}Sr$ ratios (I_{Sr}) and $\varepsilon Nd(t)$ values were calculated on the basis of the zircon U-Pb ages for these rocks

(~260 Ma). The εNd(t) values for the mafic rocks range from −0.05 to +1.79. Their I_{Sr} values range from 0.70458 to 0.70500. In contrast, the εNd(t) values for the quartz monzodiorites range from 0.41 to +5.72, apparently higher than those of mafic rocks (Figure 11). Their I_{Sr} values range from 0.70477 to 0.70497.

Table 4. Sr–Nd isotopic data of mafic rocks from the Yamaat Uul mafic complex and environs.

	Sample №	$^{87}Rb/^{86}Sr$	$^{87}Sr/^{86}Sr$	±2σ	I_{Sr}	$^{147}Sm/^{144}Nd$	$^{143}Nd/^{144}Nd$	±2σ	εNd(0)	εNd(t)
1	SH220-14/10	0.00794	0.704690	0.00002	0.70466	0.10872	0.512550	0.0003	−1.71	1.21
2	SH105-14	0.02233	0.704660	0.00004	0.70458	0.11756	0.512595	0.0003	−0.84	1.79
3	SH225-14	0.00771	0.704650	0.00002	0.70462	0.16622	0.512660	0.0005	0.42	1.43
4	SH12-15	0.09682	0.705170	0.00004	0.70481	0.12964	0.512563	0.0003	−1.46	0.76
5	SH2-17	0.04698	0.705191	0.00002	0.70502	0.11153	0.512505	0.0003	−2.59	0.24
6	SH7-17	0.05247	0.705196	0.00001	0.70500	0.14538	0.512606	0.0004	−0.62	1.08
7	SH231-17	0.03658	0.705136	0.00001	0.70500	0.10104	0.512473	0.0003	−3.22	-0.05
8	SH235-14	0.10768	0.705370	0.00003	0.70497	0.11845	0.512520	0.0003	−2.30	0.30
9	SH10-15	0.61153	0.707030	0.00002	0.70477	0.11150	0.512514	0.0003	−2.42	0.41
10	SH16-17	0.87250	0.708195	0.00001	0.70497	0.10834	0.512781	0.0003	2.78	5.72

Note: the I_{Sr} and εNd(t) values of the Yamaat Uul mafic complex were calculated at the age of 260 Ma.

The sulphide in the rocks of the Yamaat Uul mafic complex have $\delta^{34}S$ values ranging from +0.8 (SH222-14) to +1.1 (SH220-14/10), which are within the typical mantle range [58,59].

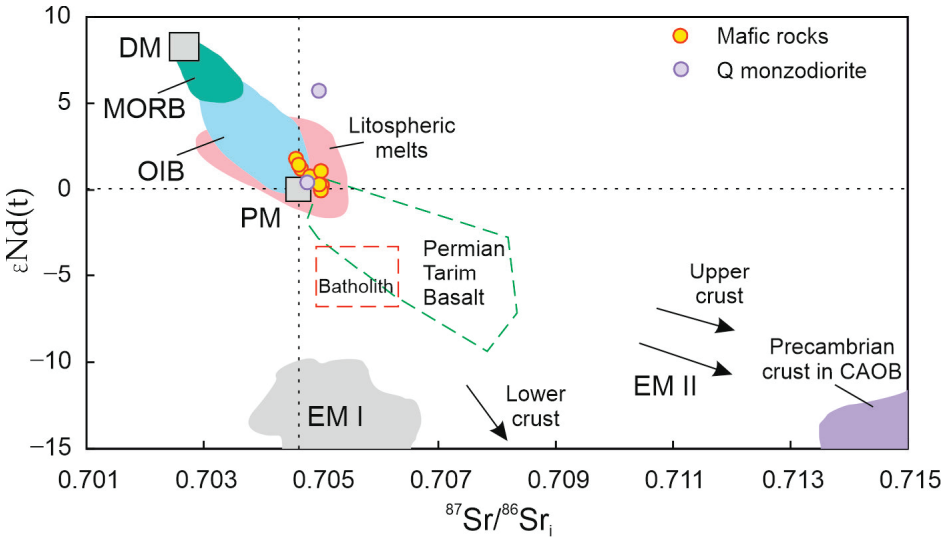

Figure 11. Plot of εNd(t) and initial $^{87}Sr/^{86}Sr$ values for the mafic rocks and Q monzodiorites of the Yamaat Uul mafic complex. DM, depleted mantle; MORB, middle ocean ridge basalt; OIB, ocean island basalt; PM, primitive mantle; EM I and EM II, enriched mantle 1 and 2 sources. Data sources: fields for DM, PM, MORB and OIB are from [60]; field for regional lithospheric melts is based on the data from [61]; Permian Tarim basalt is from [12]; the Precambrian CAOB crust and batholith are from [27].

5. Discussion

5.1. Age of Rock Formation

The geological maps of the Khangai Mountains in previous studies show that all mafic–ultramafic intrusions are of an Early Palaeozoic age [62,63]. All isolated zircons from the rocks of the Yamaat Uul mafic complex are Permian (255–262 Ma), and all zircons are magmatic, while none are xenogenic (Figure 6 and Table 3).

Thus, the data obtained allow us to date the formation of the Yamaat Uul complex to the Permian (255–262 Ma) rather than to the Early Palaeozoic as previously thought [62,63]. The following mafic–ultramafic intrusions of the Khangai Mountains formed during the

same time interval: the Nomgon troctolite–anorthosite–gabbro intrusion (256 ± 2.1 Ma) [30], the Oortsog Uul peridotite–troctolite–gabbro intrusion (257–278 Ma) [32], the Dzaraa Uul monzogabbro intrusion (269 Ma) [15] and the Nariintolburingol intrusion (249–252 Ma) [63]. The rocks of some of them are enriched in PGE [16,32,64]. There is every reason to suggest that the Yamaat Uul complex together with the forenamed intrusions of Mongolia, localized in the single CAOB structure, are the products of Permian magmatism belonging to a single igneous province.

The Yamaat Uul mafic complex is associated with the Early Permian bimodal volcano–plutonic complex [65]. According to [66], such bimodal complexes are the result of riftogenesis initiated by plume activity (Khangai plume), superimposed on the environment of the active continental margin. Thus, the Yamaat Uul complex, as well as other Permian mafic–ultramafic intrusions of Western Mongolia, was formed during the formation of the Khangai batholith (~270–240 Ma) [26], as its earlier intrusion portion [67].

5.2. Source Mantle Characteristics and Crustal Contamination

The Yamaat Uul mafic complex has some unique chemical (geochemical) characteristics compared to other mafic complexes in the world. In our opinion, the MgO-K2O diagram is the most informative. In general, the potassium content in the rocks of the layered complexes increases monotonously as the magnesium content in the rocks increases, for example, in the Skye and Skaergaard mafic complexes [68] (Figure 12). The potassium content in the rocks of the complex does not increase monotonously with decreasing magnesium content in the rocks, but one has a decrease in the plagioclase cumulates in the Yamaat Uul complex on the diagram (Figures 9c and 12). The same distribution of rock compositions is observed in the Oortsog Uul intrusion of the Khangai Mountains [17] and in the Yoko–Dovyren complex of northern Transbaikalia [69]. This distribution can be explained by the following: 1. Two melts (as in the case of the Oortsog Uul complex) and 2. Different contents of trapped melts in plagioclase and olivine–pyroxene cumulates.

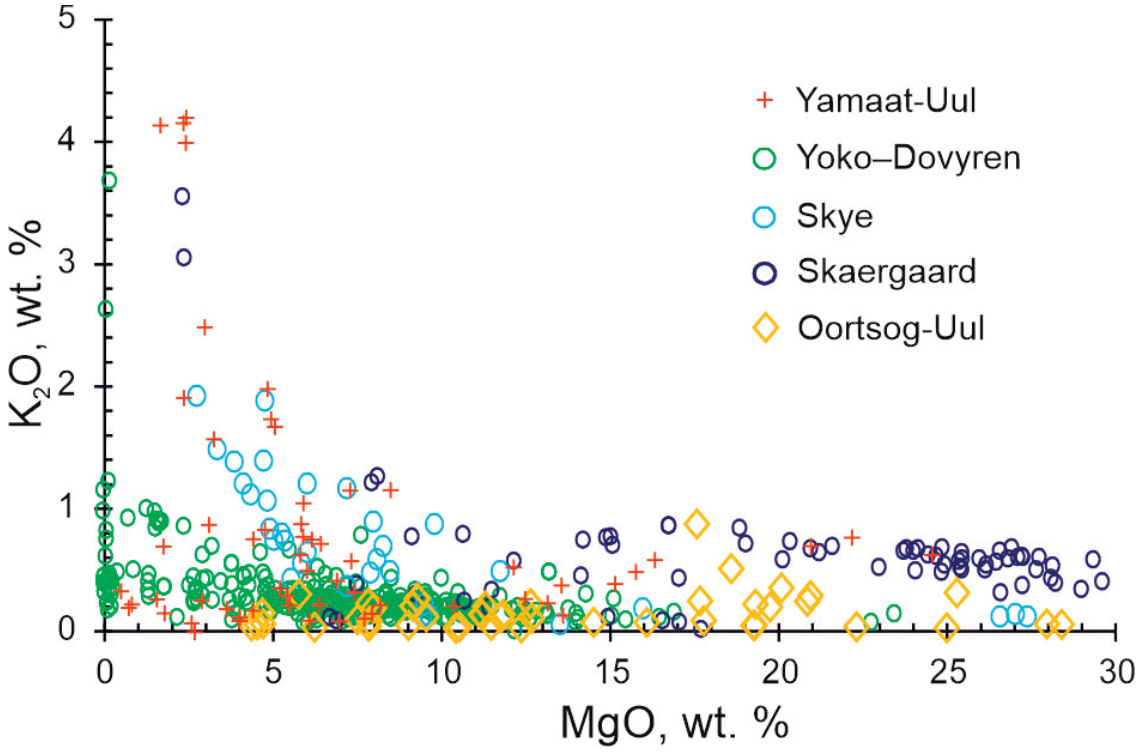

Figure 12. Comparison of MgO vs. K_2O content in the Yamaat Uul mafic complex and layered intrusions: Yoko–Dovyren [69], Skye, Skaergaard [68], Oortsog Uul [17].

The Yamaat Uul mafic complex is similar to the Oortsog Uul peridotite–troctolite–gabbro intrusion [17] in terms of age, mineralogy and geochemistry. Primary amphibole and biotite with high TiO_2 contents (Bt—0.68–5.07 and 3.00–3.01 wt.%, Am—0.23–4.60 and 0.65–3.21 wt.% for Yamaat Uul and Oortsog Uul, respectively) occur in rocks of both intrusions at later stages of formation. Plagioclases have a high An content (75–94% and 81–97%, respectively), and olivine and clinopyroxene have a similar composition. The two intrusions are characterised by rocks with high MgO values: 12.59–25.27 wt.% (Oortsog Uul) and 12.54–25.17 wt.% (Yamaat Uul). These are enriched in K_2O (0.20–0.87 and 0.30–0.87 wt.%, respectively). The same pattern is observed for TiO_2, P_2O_5 and Na_2O + K_2O; there is an enrichment in incompatible elements with an increase in MgO. The rocks of the early intrusions of Oortsog Uul and Yamaat Uul show a gradual increase in the Eu maximum on REE patterns, HFSE (Ta, Nb, Zr, Hf) depletion and LILE (Ba, K) enrichment on spidergrams; therefore, they have typomorphic features of mafic magmas that are subduction-related [70].

Thus, the Permian Yamaat Uul and Oortsog Uul intrusions have similar characteristics. However, Oortsog Uul consists of two intrusions formed from two different melts with different contents of incompatible elements: K, Ti, P and REE. It has been shown that the enriched melt was involved in the formation of Intrusion 1 of the Oortsog Uul, while the depleted melt was involved in the formation of Intrusion 2 [17]. The Sm-Nd isotope composition data (Table 4) confirm the single source of rock formation in the Yamaat Uul complex. The rocks of Intrusions 1 and 2 have close εNd values (0.30 and 1.79, respectively), while for Intrusions 1 and 2 of Oortsog Uul, they have different εNd values (+11 and −3.6, respectively) [17]. Spidergrams of rocks from the Yamaat Uul and Oortsog Uul intrusions show different Sr contents (50.3–88.3 and 1.2–18.6, respectively) at similar MgO contents. This suggests that the Sr content of the mantle is highly variable; there is mantle heterogeneity beneath Khangai in the Permian.

The high Sr content in the rocks of the Yamaat Uul complex (Figure 10, Table 3) may be due to crustal contamination. Since all the zircons are magmatic and xenogenic zircons are absent (see Figure 6a,b), crustal contamination is not typical for the rocks of the Yamaat Uul complex. Furthermore, the $\delta^{34}S$ values of the sulphide mineralization from Yamaat Uul are from 0.8 to 1.1‰, which are within the typical mantle range [58]. Similar δ34S values are typical for disseminated ores of the Gorozubovsky intrusion (2.7‰) [71], and the Zub-Marksheider intrusion (0.39‰) [72] in the Permian–Triassic Noril'sk Province (Russia). These values suggest that "mantle-like" S isotopic composition reflects the primary sulphide assemblage that has not been changed with interaction in a deep-staging chamber, during passage to the surface, or with in situ assimilation, as is frequently suggested [73,74]. The lack of evidence for crustal contamination of the parental magma is also supported with Sr-Nd isotopic data from the Yamaat Uul complex. As shown in Figure 11, the gabbroids show little variation in the isotopic compositions I_{Sr} and εNd(t), and correspond to the field of the lithospheric mantle under the CAOB [61]. Therefore, crustal contamination is not characteristic of the rocks of the Yamaat Uul mafic complex.

5.3. PGE Depletion in Parental Magma

Mantle heterogeneity in the Permian may have influenced the development of metallogeny in the Khangai region. There are mafic–ultramafic intrusions with PGE-Cu-Ni mineralization in the Khangai Mountains, Oortsog Uul and Nomgon [32,63], which, together with the studied intrusion, belong to a single metallogenic province formed above the Khangai plume [24,32].

The different degrees of sulphide melt fractionation of the Nomgon, Oortsog Uul and Yamaat Uul intrusions are clearly shown in the diagram (Figure 13a) and are due to positive correlation or joint enrichment of the melt with copper and PGE (Figure 13b). The sulphide melt fractionates with enrichment of PGE in the Oortsog Uul and Nomgon intrusions, reaching high values that lead to the formation of PGE mineralization that has been detected in these intrusions [32]. On the other hand, no such correlation is found

in the Yamaat Uul complex: PGE does not accumulate with increasing Cu. Therefore, a bornite–cubanite–chalcopyrite association of sulphides appears in the complex, but PGMs are not detected, compared with the Nomgon intrusion.

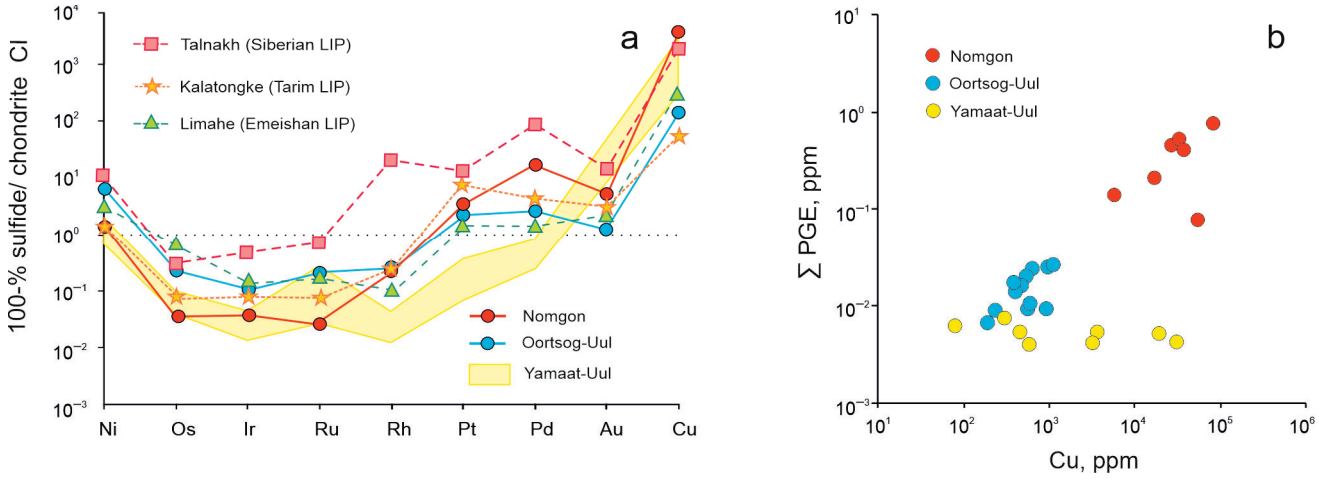

Figure 13. (**a**) Chondrite-normalized [75] chalcophile element distribution patterns for the Yamaat Uul complex in comparison with intrusions of the Khangai Mountains (Nomgon, Oortsog Uul [32]) and disseminated ores of other deposits related to LIPs (Talnakh [43], Kalatongke [76], Limahe [10]). All compositions were recalculated to 100% sulphide. (**b**) Correlation of ∑PGE vs. Cu for Yamaat Uul complex compared to intrusions of the Khangai Mountains (after [32]).

Three possible factors contribute to the PGE depletion in the parental magmas: (1) a PGE-depleted source mantle; (2) a low degree of partial melting of the PGE-undepleted mantle; or (3) previous sulphide removal in the staging magma chamber prior to the emplacement of the parental magmas. The sulphide mineralization from Oortsog Uul and Nomgon shows no obvious PGE depletion [32], suggesting a PGE-undepleted mantle source in the Khangai region.

The IPGE and Ni are more compatible than the PPGE and Cu during partial melting of the mantle [77]. Therefore, a high degree of partial melting of the mantle would result in high Ni/Cu and low Pd/Ir ratios. The sulphide mineralization from the Yamaat Uul complex has moderate Ni/Cu and Pd/Ir ratios, ranging from 0.9 to 10.8 and from 10.7 to 50.5, respectively, and is related to the field of high-Mg basalts and layered intrusions [32]. Sulphide mineralization from the Yamaat Uul complex is apparently depleted in PGE relative to Cu (and Ni) (Figure 13b). In addition, compared to the important Ni-Cu (-PGE) deposits in the LIPs of the Eurasian plate, the sulphide mineralization of the Yamaat Uul complex (in 100% sulphide) has slightly lower Ni contents and significant PGE depletion (Figure 13).

Parental magmas with Cu/Pd ratios higher than the mantle value of ~7000 [78] may reflect the sulphide removal at depth [76,79]. The sulphide mineralization of the Yamaat Uul intrusion has much higher Cu/Pd ratios (10163–1375726) than the mantle value [32], further indicating sulphide removal from primary magmas prior to intrusion emplacement. In conclusion, the PGE depletion of parental magmas in the Yamaat Uul complex may be due to sulphide removal at a deep staging magma chamber or low degrees of partial melting of the mantle source of the Yamaat Uul complex.

6. Conclusions

(1) Zircon U-Pb dating (SHRIMP II) of the anorthosite and Bt-Am-Ol gabbronorite of the Yamaat Uul mafic complex in the Khangai Mountains has a revealed age of 255.8 ± 2.9 Ma and 262.6 ± 3.1 Ma, respectively. Thus, the mafic rocks of the complex were formed in the Late Permian and, together with other mafic–ultramafic intrusions of the Khangai Mountains, are early phases of the Khangai batholith.

(2) The Yamaat Uul mafic complex consists of two intrusions; Intrusion 1 is represented by plagioclase cumulates and olivine–pyroxene cumulates and Intrusion 2 is composed of monzogabbro. All of the rocks of the complex are derived from a unified parental melt due to different amounts of trapped melts in plagioclase and olivine–pyroxene cumulates.
(3) Magmatic zircons, Sm-Nd, Rb-Sr isotope data and sulphur isotopes indicate that crustal contamination did not affect the formation of the Yamaat Uul mafic complex.
(4) The Yamaat Uul mafic complex together with other mafic–ultramafic intrusions of the Khangai Mountains are related to the Khangai LIP and can be considered as potential for the PGE-Cu-Ni. These intrusions have a low degree of evolution of the sulphide melt.

Supplementary Materials: The following supporting information can be downloaded at: https://www.mdpi.com/article/10.3390/min13060833/s1, Table S1: Representative olivine compositions of the Yamaat Uul mafic complex; Table S2: Representative clinopyroxene compositions of the Yamaat Uul mafic complex; Table S3: Representative orthopyroxene compositions of the Yamaat Uul mafic complex; Table S4: Representative amphibole compositions of the Yamaat Uul mafic complex; Table S5: Representative plagioclase compositions of the Yamaat Uul mafic complex; Table S6: Representative biotite compositions of the Yamaat Uul mafic complex.

Author Contributions: Conceptualization, methodology, review and editing, R.S.; writing—original draft preparation, visualization, funding acquisition, M.S.; mineralogy, validation, V.E.; sampling, preparation and description, Y.S.; sampling, field trip, T.-U.O.; editing, N.T. All authors have read and agreed to the published version of the manuscript.

Funding: The reported study was funded by Russian Science Foundation, No. 22-77-00058, https://rscf.ru/en/project/22-77-00058/, accessed on 14 June 2023.

Data Availability Statement: Not applicable.

Acknowledgments: We are grateful to A. Izokh, M. Podlipsky and S. Rudnev for providing samples, assistance in field work and advice. We thank analysts O. Khmelnikova, V. Kiseleva, N. Karmanova and I. Nikolaeva for carrying out analytical procedures, and N. Belkina for technical assistance in preparing the manuscript.

Conflicts of Interest: The authors declare no conflict of interest. The funders had no role in the design of the study; in the collection, analyses or interpretation of data; in the writing of the manuscript; or in the decision to publish the results.

References

1. Ernst, R. *Large Igneous Provinces*, 1st ed.; Cambridge University Press: Cambridge, UK, 2014; p. 666.
2. Mekhonoshin, A.S.; Kolotilina, T.B. Petrological-geochemical features of ultrabasites from the southern framing of the Siberian craton and exploration criteria for Ni sulfide ores. *Ores Met.* **2006**, *6*, 26–30.
3. Tolstykh, N.D.; Orsoev, D.A.; Krivenko, A.P.; Izokh, A.E. *Precious Metal Mineralization in Layered Ultramafic-Mafic Massifs in the South of the Siberian Platform*, 1st ed.; Parallel: Novosibirsk, Russia, 2008; p. 194.
4. Polyakov, G.V.; Izokh, A.E.; Borisenko, A.S. Permian ultramafic-mafic magmatism and accompanying Cu-Ni mineralization in the Gobi-Tien Shan belt as a result of the Tarim plume activity. *Russ. Geol. Geophys.* **2008**, *49*, 455–467. [CrossRef]
5. Polyakov, G.V.; Tolstykh, N.D.; Mekhonoshin, A.S.; Izokh, A.E.; Podlipskii, M.Y.; Orsoev, D.A.; Kolotilina, T.B. Ultramafic-mafic igneous complexes of the Precambrian East Siberian metallogenic province (southern framing of the Siberian craton): Age, composition, origin and ore potential. *Russ. Geol. Geophys.* **2013**, *54*, 1319–1331. [CrossRef]
6. Wang, C.Y.; Wei, B.; Zhou, M.-F.; Minh, D.H.; Qi, L. A synthesis of magmatic Ni-Cu-(PGE) sulfide deposits in the ∼260 Ma Emeishan large igneous province, SW China and northern Vietnam. *J. Asian Earth Sci.* **2018**, *154*, 162–186. [CrossRef]
7. Hoa, T.T.; Izokh, A.E.; Polyakov, G.V.; Borisenko, A.S.; Anh, T.T.; Balykin, P.A.; Phuong, N.T.; Rudnev, S.N.; Van, V.V.; Nien, B.A. Permo-Triassic magmatism and metallogeny of Northern Vietnam in relation to the Emeishan plume. *Russ. Geol. Geophys.* **2008**, *49*, 480–491. [CrossRef]
8. Svetlitskaya, T.V.; Nevolko, P.A.; Ngo, T.P.; Tran, T.H.; Izokh, A.E.; Shelepaev, R.A.; Bui, A.N.; Vu, H.L. Small-intrusion-hosted Ni-Cu-PGE sulfide deposits in northeastern Vietnam: Perspectives for regional mineral potential. *Ore Geol. Rev.* **2017**, *86*, 615–623. [CrossRef]

9. Svetlitskaya, T.V.; Ngo, T.H.; Nevolko, P.A.; Tran, T.A.; Izokh, A.E.; Shelepaev, R.A.; Tran, T.H.; Ngo, T.P.; Fominykh, P.A.; Pham, N.C. Zircon U-Pb ages of Permian-Triassic igneous rocks in the Song Hien structure, NE Vietnam: The Emeishan mantle plume or the Indosinian orogeny? *J. Asian Earth Sci.* **2022**, *224*, 105033. [CrossRef]
10. Tao, Y.; Li, C.; Song, X.; Ripley, E.M. Mineralogical, petrological and geochemical studies of the Limahe mafic–ultramatic intrusion and the associated Ni–Cu sulfide ores, SW China. *Miner. Deposit.* **2008**, *43*, 849–872. [CrossRef]
11. Zhou, M.F.; Arndt, N.T.; Malpas, J.; Wang, C.Y.; Kennedy, A.K. Two magma series and associated ore deposit types in the Permian Emeishan large igneous province, SW China. *Lithos* **2008**, *103*, 352–368. [CrossRef]
12. Tang, D.M.; Qin, K.Z.; Li, C.S.; Qi, L.S.; Su, B.X.; Qu, W.J. Zircon dating, Hf–Sr–Nd–Os isotopes and PGE geochemistry of the Tianyu sulfide-bearing mafic–ultramafic intrusion in the Central Asian Orogenic Belt, NW China. *Lithos* **2011**, *126*, 84–98. [CrossRef]
13. Luo, W.; Zhanga, Z.; Santosha, M.; Houa, T.; Huanga, H.; Zhua, J.; Wanga, X.; Fua, X. Petrology and geochemistry of Permian mafic–ultramafic intrusions in the Emeishan large igneous province, SW China. *Ore Geol. Rev.* **2014**, *56*, 258–275. [CrossRef]
14. Wang, Z.-Z.; Han, B.-F.; Feng, L.-X.; Liu, B. Geochronology, geochemistry and origins of the Paleozoic–Triassic plutons in the Langshan area, western Inner Mongolia, China. *J. Asian Earth Sci.* **2015**, *97*, 337–351. [CrossRef]
15. Izokh, A.E.; Vishnevskii, A.V.; Polyakov, G.V.; Shelepaev, R.A. Age of picrate and picrodolerite magmatism in Western Mongolia. *Russ. Geol. Geophys.* **2011**, *52*, 7–23. [CrossRef]
16. Mao, Y.J.; Dash, B.; Qin, K.Z.; Bujinlkham, B.; Tang, D.M. Comparisons among the Oortsog, Dulaan, and Nomgon mafic-ultramafic intrusions in central Mongolia and Ni-Cu deposits in NW China: Implications for economic Ni-Cu-PGE ore exploration in central Mongolia. *Russ. Geol. Geophys.* **2018**, *59*, 1–18. [CrossRef]
17. Shapovalova, M.O.; Tolstykh, N.D.; Shelepaev, R.A.; Tsibizov, L.V. The Oortsog Peridotite-Troctolite-Gabbro Intrusion, Western Mongolia: New Petrological and Geochronological Constraints. *Russ. Geol. Geophys.* **2019**, *60*, 845–861. [CrossRef]
18. Borisenko, A.S.; Sotnokov, V.I.; Izokh, A.E.; Polyakov, G.V.; Obolensky, A.A. Permo-triassic mineralization in Asia and ist relation with plume magmatism. *Russ. Geol. Geophys.* **2006**, *47*, 170–186.
19. Zhang, C.L.; Li, Z.X.; Li, X.H.; Xu, Y.G.; Zhou, G.; Ye, H.M. A Permian large igneous province in Tarim and Central Asia norogenic belt, NW China: Results of aca. Ma mantle plume? *Geol. Soc. Am. Bull.* **2010**, *122*, 2020–2040. [CrossRef]
20. Xu, Y.-G.; Wei, X.; Luo, Z.-Y.; Liu, H.; Cao, J. The Early Permian Tarim Large Igneous Province: Main characteristics and a plume incubation model. *Lithos* **2014**, *204*, 20–35. [CrossRef]
21. Dobretsov, N.L. 250 Ma large igneous provinces of Asia: Siberian and Emeishan traps (plateau basalts) and associated granitoids. *Russ. Geol. Geophys.* **2005**, *46*, 870–890.
22. Yarmolyuk, V.V.; Kovalenko, V.I. Deep geodynamics and mantle plumes: Their role in the formation of the Central Asian orogenic belt. *Petrology* **2003**, *11*, 504–531.
23. Bryan, S.E.; Ernst, R.E. Revised definition of large igneous provinces (LIPs). *Earth Sci. Rev.* **2008**, *86*, 175–202. [CrossRef]
24. Yarmolyuk, V.V.; Kozlovsky, A.M.; Kuzmin, M.I. Zoned magmatic areas and anorogenic batholith formation in the Central Asian Orogenic Belt (by the example of the Late Paleozoic Khangai magmatic area). *Russ. Geol. Geophys.* **2016**, *57*, 357–370. [CrossRef]
25. Yarmolyuk, V.V.; Kozlovsky, A.M.; Sal'nikova, E.B.; Kozakov, I.K.; Kotov, A.B.; Lebedev, V.I.; Eenjin, G. Age of the Khangai batholith and challenge of polychronic batholith formation in Central Asia. *Dokl. Earth Sci.* **2013**, *452*, 1001–1007. [CrossRef]
26. Yarmolyuk, V.V.; Kozlovsky, A.M.; Travin, A.V.; Kirnozova, T.I.; Fugzan, M.M.; Kozakov, I.K.; Plotkina, Y.V.; Eenzhin, G.; Oyuunchimeg, T.; Sviridova, O.E. Duration of formation and geodynamic nature of the giant batholiths of Central Asia: Data from geological and geochronological studies of the Khangai batholith. *Stratigr. Geol. Correl.* **2019**, *27*, 79–102. [CrossRef]
27. Kovalenko, V.I.; Yarmolyuk, V.V.; Kovach, V.P.; Kotov, A.B.; Kozakov, I.K.; Salnikova, E.B.; Larin, A.M. Isotope provinces, mechanisms of generation and sources of the continental crust in the Central Asian Mobile Belt: Geological and isotopic evidence. *J. Asian Earth Sci.* **2004**, *23*, 605–627. [CrossRef]
28. Savatenkov, V.M.; Smirnova, Z.B.; Yarmolyuk, V.V.; Kozlovsky, A.M.; Sviridova, O.E. Nd and Pb isotopic composition of granitoids in the Khangai batholith as an indicator of crust-forming processes in the terranes of the Central Asian orogenic belt. *Petrology* **2018**, *26*, 351–367. [CrossRef]
29. Yarmolyuk, V.V.; Kozlovsky, A.M.; Savatenkov, V.M.; Kovach, V.P.; Kozakov, I.K.; Kotov, A.B.; Lebedev, V.I.; Enzhin, G. Composition, sources and geodynamic nature of giant batholiths of Central Asia: According to geochemical and Nd isotopic studies of granitoids of the Khangai zoned magmatic area. *Petrology* **2016**, *24*, 468–498. [CrossRef]
30. Izokh, A.E.; Polyakov, G.V.; Gibsher, A.S.; Balykin, P.A.; Zhuravlev, D.Z.; Parkhomenko, V.A. Hich-alumina stratified gabroids of the Central-Asian fold belt: Geochemistry, Sm-Nd isotopic AGE, and geodynamic conditions of formation. *Russ. Geol. Geophys.* **1998**, *39*, 1565–1577.
31. Sal'nikova, E.B.; Yakovleva, S.Z.; Kotov, A.B.; Tolmacheva, E.V.; Plotkina, Y.V.; Fedoseenko, A.M.; Kozlovskii, A.M.; Yarmolyuk, V.V. Crystallogenesis of zircon in alkaline granites and specifics of zircon U-Pb dating: A case study of the Khangai magmatic area. *Petrology* **2014**, *22*, 450–461. [CrossRef]
32. Shapovalova, M.; Tolstykh, N.; Shelepaev, R.; Kalugin, V. PGE-Cu-Ni Mineralization of Mafic-Ultramafic Massifs of the Khangai Upland, Western Mongolia. *Minerals* **2020**, *10*, 942. [CrossRef]
33. Kuzmin, M.I.; Yarmolyuk, V.V. Mantle plumes of Central Asia (Northeast Asia) and their role in forming endogenous deposits. *Russ. Geol. Geophys.* **2014**, *55*, 120–143. [CrossRef]

34. Sengor, A.M.C.; Natalin, B.A.; Burtman, V.S. Evolution of the Altaid Tectonic Collage and Paleozoic Crustal Growth in Eurasia. *Nature* **1993**, *364*, 299–307. [CrossRef]
35. Xiao, W.J.; Zhang, L.C.; Qin, K.Z.; Sun, S.; Li, J.L. Paleozoic accretionary and collisional tectonics of the Eastern Tianshan (China): Implications for the continental growth of Central Asia. *Am. J. Sci.* **2004**, *304*, 370–395. [CrossRef]
36. Windley, B.F.; Alexeiev, D.; Xiao, W.J.; Kroner, A.; Badarch, G. Tectonic models for accretion of the Central Asian Orogenic Belt. *J. Geol. Soc.* **2007**, *164*, 31–47. [CrossRef]
37. Kruk, N.N.; Rudnev, S.N.; Vladimirov, A.G.; Shokalsky, S.P.; Kovach, V.P.; Serov, P.A.; Volkova, N.I. Early-Middle Paleozoic granitoids in Gorny Altai, Russia: Implications for continental crust history and magma sources. *J. Asian Earth Sci.* **2011**, *42*, 928–948. [CrossRef]
38. Safonova, I.; Seltmann, R.; Kroner, A.; Gladkochub, D.; Schulmann, K.; Xiao, W.J.; Kim, J.; Komiya, T.; Sun, M. A new concept of continental construction in the Central Asian Orogenic Belt (compared to actualistic examples from the Western Pacific). *Episodes* **2011**, *34*, 186–196. [CrossRef]
39. Kozakov, I.K.; Kotov, A.B.; Kovach, V.P.; Sal'nikova, E.B. Crust-forming processes in the geological development of the Baidarik block of Central Mongolia: Sm-Nd isotope data. *Petrology* **1997**, *5*, 240–248.
40. Badarch, G.; Cunningham, W.D.; Brian, F.W. A new terrane subdivision for Mongolia: Implications for the Phanerozoic crustal growth of central Mongolia. *J. Asian Earth Sci.* **2002**, *21*, 87–110. [CrossRef]
41. Tomurtogoo, O. Tectonics of Mongolia. In *Tectonics of Northern, Central and Eastern Asia, Explanatory Note to the Tectonic Map of Northern Central Eastern Asia and Adjacent Areas at Scale 1:2500000*; VSEGEI Printing House: Saint Petersburg, Russia, 2014; pp. 110–126.
42. Hamilton, W.B. Form of the Sudbury lopolith. *Can. Miner.* **1960**, *6*, 437–447.
43. Naldrett, A.J. *Magmatic Sulfide Deposits: Geology, Geochemistry and Exploration*, 1st ed.; Springer: Berlin/Heidelberg, Germany, 2004; p. 730.
44. Williams, I.S. U-Th-Pb Geochronology by Ion Microprobe. *Rev. Econ. Geol.* **1998**, *7*, 1–35.
45. Vermeesch, P. Dissimilarity measures in detrital geochronology. *Earth Sci. Rev.* **2018**, *178*, 310–321. [CrossRef]
46. Karmanova, N.G.; Karmanov, N.S. Universal Method of X-ray Fluorescence Silicate Analysis of Rocks on the ARL-9900XP Spectrometer. In Proceedings of the All-Russian Conference on X-ray Spectral Analysis, Novosibirsk, Russia, 19–23 September 2011; p. 126.
47. Nikolaeva, I.V.; Palesskiy, S.V.; Kozmenko, O.A.; Anoshin, G.N. Determination of rare-earth and highly charged elements in standard geological samples by inductively coupled plasma mass spectrometry (ICP-MS). *Geochemistry* **2008**, *10*, 1085–1091.
48. Boynton, W.V. Geochemistry of the rare earth elements: Meteorite studies. In *Rare Earth Element Geochemistry*; Henderson, P., Ed.; Elsevier: New York, NY, USA, 1984; pp. 63–114.
49. McDonough, W.F.; Sun, S.S.; Ringwood, A.E.; Jagoutz, E.; Hofmann, A.W. Potassium, Rubidium and Cesium in the Earth and Moon and the evolution of the mantle of the Earth. *Geochim. Cosmochim. Acta* **1992**, *56*, 1001–1012. [CrossRef]
50. Tanaka, T.; Amakawa, H.; Togashi, S.; Kamioka, H. JNdi-1: A neodymium isotopic reference in consistency with La Jolla neodymium. *Chem. Geol.* **2000**, *168*, 279–281. [CrossRef]
51. Weis, D.; Kieffer, B.; Maerschalk, C.; Barling, J.; Jong, J.D.; Williams, G.A.; Hanano, D.; Pretorius, W.; Mattielli, N.; Scoates, J.S.; et al. High-precision isotopic characterization of USGS reference materials by TIMS and MC-ICP-MS Geochem. *Geophys. Geosyst.* **2006**, *7*, 1525–2027. [CrossRef]
52. Han, L.; Tanweer, A.; Szaran, J.; Halas, S. A modified technique for the preparation of SO2 from sulphates and sulphides for sulfur isotope analyses. *Isot. Environ. Health Stud.* **2002**, *38*, 177–183. [CrossRef]
53. Heaman, L.M.; Bowins, R.; Crocket, J. The chemical composition of igneous zircon suites: Implications for geochemical tracer studies. *Geochim. Cosmochim. Acta* **1990**, *54*, 1597–1607. [CrossRef]
54. Hoskin, P.W.O.; Schaltegger, U. The composition of zircon and igneous and metamorphic petrogenesis. *Rev. Mineral. Geochem.* **2003**, *53*, 25–104. [CrossRef]
55. Morimoto, N.; Fabries, J.; Ferguson, A.K.; Ginzburg, I.V.; Ross, M.; Seifert, F.A.; Zussman, J.; Aoki, K.; Gottardi, G. Nomenclature of pyroxenes. *Can. Miner.* **1989**, *27*, 143–156. [CrossRef]
56. Leake, B.E.; Woolley, A.R.; Birch, W.D.; Burke, E.A.J.; Ferraris, G.; Grice, J.D.; Hawthorne, F.C.; Kisch, H.J.; Krivovichev, V.G.; Schumacher, J.C.; et al. Nomenclature of amphiboles: Additions and revisions to the International Mineralogical Association's amphibole nomenclature. *Can. Miner.* **2003**, *41*, 1355–1370. [CrossRef]
57. Irvine, T.N.; Baragar, W.R.A. A guide to the chemical classification of the common volcanic rocks. *Can. J. Earth Sci.* **1971**, *8*, 523–548. [CrossRef]
58. Chaussidon, M.; Lorand, J.-P. Sulphur isotope composition of orogenic spinel lherzolite massifs from Ariege (North-Eastern Pyrenees, France): An ion microprobe study. *Geochim. Cosmochim. Acta* **1990**, *54*, 2835–2846. [CrossRef]
59. Zhao, Y.; Xue, C.; Zhao, X.; Yang, Y.; Ke, J.; Zu, B. Variable mineralization processes during the formation of the Permian Hulu Ni-Cu sulfide deposit, Xinjiang, Northwestern China. *J. Asian Earth Sci.* **2016**, *126*, 1–13. [CrossRef]
60. Zindler, A.; Hart, S.R. Chemical geodynamics. *Ann. Rev. Earth Planet. Sci.* **1986**, *14*, 493–571. [CrossRef]
61. Zhang, Y.-L.; Liu, C.-Z.; Ge, W.-C.; Wu, F.-Y.; Chu, Z.-Y. Ancient sub-continental lithospheric mantle (SCLM) beneath the eastern part of the Central Asian Orogenic Belt (CAOB): Implications for crust-mantle decoupling. *Lithos* **2011**, *126*, 233–247. [CrossRef]

62. Khosbayar, P.; Byamba, B.; Binderya, T.; Gansukh, Z.; Enkhtuvshin, K.; Bataa, C.; Gaechimeg, Y.; Erdenechimeg, J. *Geological Map, Ugiinuur Region L–48–I, II, Scale: 1:200000. Central Geological Expedition of MG and GRP MPR*; Mineral Resources Authority of Mongolia—Geological Office: Ulaanbaatar, Mongolia, 1987.
63. Izokh, A.E.; Polyakov, G.V.; Krivenko, A.P.; Bognibov, V.I.; Bayarbileg, L. *The Gabbro Formation of Western Mongolia*, 1st ed.; Nauka: Novosibirsk, Russia, 1990; p. 269.
64. Izokh, A.E.; Mayorova, O.N.; Lavrentiev, Y.G. Minerals of the platinum metals in the Nomgon troctolite–anorthozite–gabbro intrusive massif (Mongolia). *Russ. Geol. Geophys.* **1992**, *33*, 104–110.
65. Gavrilova, S.P.; Luchitskaya, A.I.; Frikh-Khar, D.I.; Orolmaa, D.; Badamgarav, J. *Volcano-Plutonic Associations of Central Mongolia*, 1st ed.; Nauka: Moscow, Russia, 1991; p. 229.
66. Yarmolyuk, V.V.; Kovalenko, V.I.; Kozakov, I.K.; Sal'nikova, E.B.; Bibikova, E.V.; Kovach, V.P.; Kozlovsky, A.M.; Kotov, A.B.; Lebedev, V.I.; Eenjin, G.; et al. The age of the Khangai batholith and the problem of batholith formation in Central Asia. *Dokl. Earth Sci.* **2008**, *423*, 1223–1228. [CrossRef]
67. Izokh, A.E.; Vishnevskii, A.V.; Polyakov, G.V.; Kalugin, V.M.; Shelepaev, R.A.; Egorova, V.V.; Oyunchimeg, T. The ureg nuur Pt-bearing volcanoplutonc picrate-basalt association in the Mongolian Altay as evidence for a cambrian-ordovician Large Igneous province. *Russ. Geol. Geopys.* **2010**, *51*, 521–533. [CrossRef]
68. Wager, L.R.; Brown, G.M. *Layered Igneous Rocks*; W.H. Freeman: San Francisco, CA, USA, 1967; p. 588.
69. Kislov, E.V. *The Ioko-Dovyren Layered Massif*, 2nd ed.; RAS SD Buryat Scientific Centre Publishing House: Ulan-Ude, Russia, 1998; p. 264.
70. Izokh, A.E.; Polyakov, G.V.; Hoa, T.T.; Balykin, P.A.; Phuong, N.T. Permian-triassic ultramafic-mafic magmatism of Northern Vietnam and Southern China as expression of plume magmatism. *Russ. Geol. Geophys.* **2005**, *46*, 922–932.
71. Kuz'min, V.K.; Tuganova, E.V. New data on the isotope composition of sulfur in thecopper-nickel sulfide ores of the northwestern part of the Siberian Platform. *Sov. Geol. Geophys.* **1977**, *18*, 98–100.
72. Malitch, K.; Latypov, R.; Badanina, I.; Sluzhenikin, S. Insights into ore genesis of Ni-Cu-PGE sulfide deposits of the Noril'skProvince (Russia): Evidence from copper and sulfur isotopes. *Lithos* **2014**, *204*, 172–187. [CrossRef]
73. Arndt, N.T.; Czamanske, G.K.; Walker, R.J.; Chauvel, C.; Fedorenko, V.A. Geochemistry and origin of the intrusive hosts of the Noril'sk-Talnakh Cu-Ni-PGE sulfide deposits. *Econ. Geol.* **2003**, *98*, 495–515. [CrossRef]
74. Li, C.; Ripley, E.M.; Naldrett, A.J. Compositional variations of olivine and sulfur isotopes in the Noril'sk and Talnakh intrusions, Siberia: Implications for ore forming processes in dynamic magma conduits. *Econ. Geol.* **2003**, *98*, 69–86. [CrossRef]
75. Anders, E.; Grevesse, N. Abundances of the elements: Meteoric and solar. *Geochim. Cosmochim. Acta* **1989**, *53*, 197–214. [CrossRef]
76. Gao, J.F.; Zhou, M.F.; Lightfoot, P.C.; Wang, C.Y.; Qi, L. Origin of PGE−poor and Cu−rich magmatic sulfides from the Kalatongke deposit, Xinjiang, Northwest China. *Econ. Geol.* **2012**, *107*, 481–506. [CrossRef]
77. Barnes, S.-J.; Lightfoot, P. Formation of Magmatic Nickel-Sulfide Deposits and Processes Affecting Their Copper and Platinum-Group Element Contents. In *Economic Geology*; Hedenquist, J., Thompson, J., Goldfarb, R., Richards, J., Eds.; Society of Economic Geology: Littleton, MA, USA, 2005; pp. 179–213.
78. Barnes, S.J.; Maier, W.D. The fractionation of Ni, Cu and the noble metals in silicate and sulfide liquids. *Geosci. Canada* **1999**, *13*, 69–106.
79. Song, X.Y.; Wang, Y.S.; Chen, L.M. Magmatic Ni−Cu−(PGE) deposits in magma plumbing systems: Features, formation and exploration. *Geosci Front.* **2011**, *2*, 375–384. [CrossRef]

minerals

MDPI

Article

Timing of Carbonatite Ultramafic Complexes of the Eastern Sayan Alkaline Province, Siberia: U–Pb (ID–TIMS) Geochronology of Ca–Fe Garnets

Maria V. Stifeeva [1], Ekaterina B. Salnikova [1,*], Valentina B. Savelyeva [2], Alexander B. Kotov [1], Yulia V. Danilova [2], Ekaterina P. Bazarova [2] and Boris S. Danilov [2]

[1] Institute of Precambrian Geology and Geochronology RAS, 199034 St. Petersburg, Russia; stifeeva.maria@yandex.ru (M.V.S.)
[2] Institute of the Earth's Crust SB RAS, 664033 Irkutsk, Russia; vsavel@crust.irk.ru (V.B.S.)
* Correspondence: katesalnikova@yandex.ru

Abstract: In this study, we present the results of U–Pb (ID-TIMS) geochronological studies of calcic garnet from the alkaline ultramafic complexes of Eastern Sayan province (eastern Siberia). New U–Pb ID–TIMS garnet ages obtained from different rocks of Bolshaya Tagna (632 ± 2 Ma) and Srednaya Zima intrusions (624 ± 5 Ma), as well as previously published garnet ages of the Belaya Zima complex (646 ± 6 Ma), allow us to constrain the timing and duration of episodes of alkaline ultramafic magmatism in Eastern Sayan province (619–651 Ma). Variations in the chemical compositions of rocks from three massifs indicate that the parental melts were separated from different magmatic chambers generated during the same episode of mantle melting. This study further highlights garnet U–Pb dating as a potentially robust, high-resolution geochronometer to constrain the evolution of the main pulse of alkaline ultramafic magmatism in the large magmatic provinces.

Keywords: Eastern Sayan magmatic province; garnet U–Pb (ID–TIMS); alkaline rocks; carbonatite; Rodinia; Siberian craton; Belaya Zima; Srednaya Zima; Bolshaya Tagna

1. Introduction

The timing and duration of magmatic events are important factors in understanding the lifespans of plumes and in addressing geodynamic constraints. Alkaline rocks with carbonatites are often temporally and spatially associated with large magmatic provinces (LIP), which are commonly thought to have a very short lifespan (<5 Ma), or to consist of multiple short pulses [1–5] over a longer period of time. However, the problem of timing magmatic events is strongly dependent on the resolution of dating techniques and the quality of the data. The U–Pb zircon method has proven to be of particular usefulness [3,6,7] relative to Rb–Sr, Ar–Ar, and other isotopic systems. Unlike all other chronometers, the U–Pb method is based on two U–Pb decay systems, making it possible to detect even negligible amounts of open system behavior. Zircon demonstrates lattice stability and high U–Pb closure temperatures. Recent studies have focused on the application of the U–Pb system of calcic garnet to precisely date different ages and compositionally diverse alkaline and carbonatitic intrusive rocks and scarns [8–12]. Calcic garnet typically contains enough U for precise age determinations, has a high U–Pb closure temperature (>850 °C) [13], and is resistant to postmagmatic processes. Calcic garnet is a widespread mineral of rocks of the foidolite series, and is therefore a promising source of reliable information about the age of alkaline ultramafic intrusions. The results of a U–Pb (ID–TIMS) geochronological study of calcic garnet from alkaline ultramafic complexes of the Kola Alkaline province (Vuoriyarvi, Sallanlatva, Salmagorsky, and Afrikanda) enable an evaluation of a narrower time span of the main pulse of alkaline ultramafic magmatic activity in Kola province than was previously estimated [14].

This study is an example of attempt to solve the problem of the duration of the Eastern Sayan alkaline magmatic province using a U–Pb system of calcic garnet from ultramafic–alkaline series intrusive rock complexes. The Eastern Sayan rare-metal province is a part of the Neoproterozoic alkaline–carbonatite magmatic area (province) traced for more than 2000 km along the southern margin of the Siberian craton. The alkaline ultrabasic intrusions are concentrated between the southwestern part of the Siberian craton and the Eastern Sayan mountain ridge and distributed along both sides of the Iysko–Urik Graben within the Irkutsk region. The Eastern Sayan province includes the Belaya Zima (Nizhnesayansky), Srednaya Zima (Verkhnesayansky), Bolshaya Tagna, and Bolshezhidosky (Zadoysky) complexes, as well as the Monkresovsky and Yarma fields of dikes of ultrabasic alkaline rocks and carbonatites. The unique Ziminskii rare metal ore district (Nb, Ta, REE, U, Pb, Zn, and P) is related to Eastern Sayan province [15,16]. One of the largest niobium deposits of the province is linked with the Belaya Zima complex, which is the most well-studied complex within the province. Within the past decade, numerous geochronological data have been obtained concerning the age of the Eastern Sayan province complexes, with estimates ranging from 645 to 622 Ma. Thus, available geochronological data (ID–TIMS U–Pb garnet and phlogopite $^{40}Ar/^{39}Ar$) have been obtained only for the Belaya Zima complex, with estimates ranging from 622 to 645 Ma (according to ID–TIMS U–Pb analysis [12], $^{40}Ar/^{39}Ar$ dating [17,18], and ID–TIMS U–Pb analysis of zircon [19]). An Sm–Nd isochron age of 640 ± 11 Ma was obtained for rocks of the Bolshaya Tagna complex [20]. $^{40}Ar/^{39}Ar$ dating of phlogopites from rocks of the dike series provided two plateaus, with ages of 644 ± 9 and 646 ± 9 Ma [18].

Available geochronological data were obtained using different isotope methods ($^{40}Ar/^{39}Ar$, Sm–Nd, and U–Pb) with different closure temperatures, making it difficult to determine whether this time span corresponds to the real duration of Neoproterozoic intrusive alkaline magmatism in the province during the interval of ~620–650 Ma, or whether it reflect the effects of isotope system behavior. Therefore, additional geochronological data obtained using modern and precise techniques are required to solve this problem.

The formation of Neoproterozoic alkaline complexes in the southern part of the Siberian platform is associated with the breakup of Rodinia [19]. Hence, determining the duration of the Eastern Sayan magmatic alkaline process is important for the paleogeographic reconstruction of the Siberia–Laurentia connection.

2. Analytical Techniques

2.1. Whole-Rock Geochemistry

The major elements of whole rock were analyzed at the "Geodynamics and Geochronology Center" at the Institute of the Earth's crust of the Siberian Branch of the Russian Academy of Sciences (Irkutsk, Russia). Crushed sample was mixed with a combination of soda and boron at a temperature of 950 °C. The resulting alloy was dissolved in hydrochloric acid, the volume was brought to 500 mL with distilled water, and the major elements were determined in aliquots of the resulting solution [21]. The Genesys 10S spectrophotometric complex was used to determine SiO_2, TiO_2, Al_2O_3, Fe_2O_3, FeO, and P_2O_5, whereas a Solaar M6 atomic absorption spectrophotometer was used to determine MnO, CaO, MgO, K_2O, and Na_2O [22,23]. F was determined using the potentiometric method, H_2O and calcination losses were determined via a gravimetric method, and CO_2 was determined using the titrimetric method [21]. The accuracy of the analysis of petrogenic oxides was 0.5%–1.0%.

Trace elements and rare earth elements were analyzed using inductively coupled plasma mass spectrometry (ICP-MS) on an Agilent 7900ce analyzer at the "Geodynamics and Geochronology Center" of the Institute of the Earth's Crust SB RAS (Irkutsk, Russia). The samples were fused with $LiBO_2$ using the method developed by the authors of [24]. Calibration was performed according to national and international standards, including G-2, GSP-2, JG-2, and RGM-1. The accuracy of the analysis of the rare and rare earth elements was up to 5%.

2.2. Major-Element Garnet Analysis

For a major-element analysis study, we selected three samples of garnet from two alkaline complexes. The garnet crystals were mounted in epoxy, and polished and analyzed at the Geomodel Research Center (Saint-Petersburg State University, Saint-Petersburg, Russia) using a Hitachi S-3400N electron microscope with an Oxford X-Max 20 energy-dispersive analysis attachment. The instrument was operated at 20 kV and 17 nA, with a spectrum-counting time of 30 s. The WDS data were converted to mineral formulas, and the Fe^{2+}/Fe^{3+} ratio was calculated assuming the ideal garnet stoichiometry, i.e., 12 oxygen atoms and 8 cations. The chemical formulas of the garnets and components were calculated according to the method described in [25].

2.3. U–Pb ID–TIMS

Geochronological studies of garnets using ID–TIMS-based U–Pb were undertaken at the Isotope Geology Laboratory of the Institute of Precambrian Geology and Geochronology (IPGG RAS, Saint-Petersburg, Russia). For this study, we hand-picked the most visually homogeneous single-crystal fragments measuring <200 μm in size (2–15 fragments were used for analysis). The selected garnet fractions were subjected to preliminary ultrasonic cleaning with 1 N HCl followed by acid treatment to dissolve calcite and apatite inclusions (6 N HCl at 80 °C for 15–30 min) [26]. Then, the samples were washed in warm water for 20 min, placed in a pressure vessel for digestion [27], spiked with a ^{202}Pb–^{235}U tracer, and dissolved in a mixture of 29 N HF and 15 N HNO_3 (in a proportion of 10:1) at 220 °C for 24–48 h. The Pb and U were separated using a single-stage upgrading technique, which involves the elimination of interfering elements (Ca, Fe, Ti, Al, etc.) with a stepwise combination of 3.1 N HCl and 0.5 N HBr prior to the separation of lead and uranium with 6 N HCl and H_2O, respectively [28]. Furthermore, the U was purified with UTEVA resin [29]. The blanks were 10 pg for Pb and 1 pg for U. The accuracy of the U/Pb ratios and the U and Pb contents was 0.5%, and these used to plot the data points on the concordia diagram and any age calculations. In cases where the error exceeded the established value, the calculated analysis uncertainties were used directly. The data were reduced using PbDAT [30], and visualized using ISOPLOT 3.0 [31] software. A correction for common Pb was applied according to the model developed by Stacey and Kramers [32]; all of the errors are reported here as 2σ.

According to research teams, to arbitrarily cut off between young and old ages ranges from 800 Ma to 1600 Ma, we used the $^{206}Pb/^{238}U$ geochronometer for age averaging for the slightly discordant analyses, along with the concordia ages for concordant ones.

3. Geological Background, Rock Composition, and Geochemical and Mineralogical Characteristics

The Eastern Sayan province comprises several alkaline–ultrabasic complexes located within the joint zone between the southwestern part of the Siberian Platform and the East Sayan mountain ridge (Figure 1a), and distributed along both sides of the Iysko–Urik Graben [15,16].

The locations of complexes are controlled by the fault system of the northwest strike. Massifs intrude into the Paleoproterozoic shales, and greenshists compose the graben. The intrusive complexes of the Eastern Sayan magmatic province are steeply or vertically oriented as tube-shaped or stock-shaped bodies with oval or round sections. Carbonatite rock occupies about 70% of the total area of some complexes in Eastern Sayan province. The ultramafic–alkaline rock series are represented by pyroxenites and melanocratic series of foidolite (melteigite and ijolite). Most ultramafic alkaline rocks were significantly reworked by carbonatite melt. Due to strong secondary alteration, identification of the primary mineral composition of the alkaline rock series is a complicated task [15,16]. The degree of secondary alteration also depends on the locations of intrusion relative to the controlled structures. The Belaya Zima and Srednaya Zima complexes are located directly in the ridge zone, and the carbonatite magmatic stage in these intrusions is more pronounced [15].

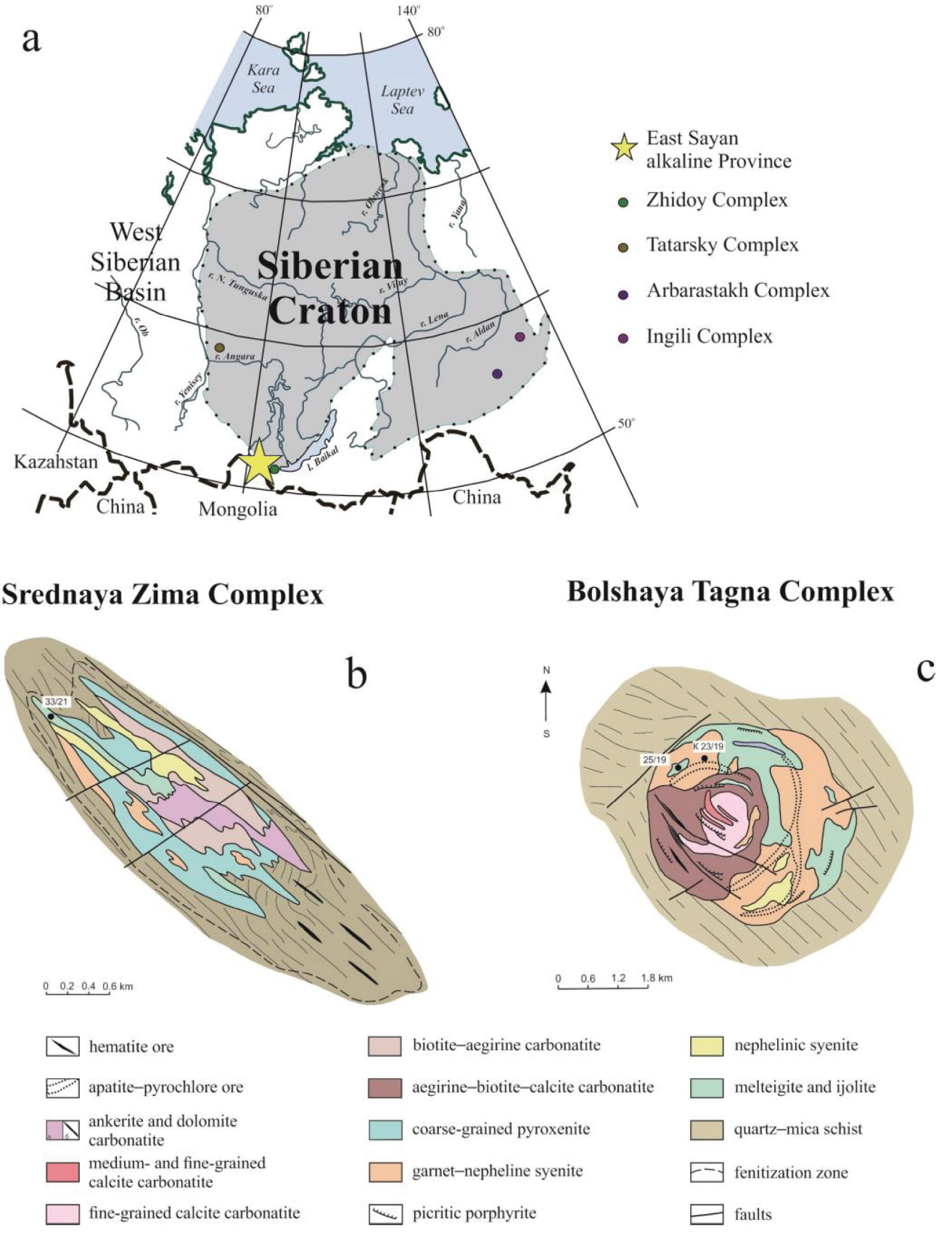

Figure 1. (**a**) The schematic geological maps and locations of the ultramafic–alkaline complexes in the south part of the Siberian craton; (**b**,**c**) schematic geological maps of the Srednaya Zima (53°27′ N; 100°25′ E) and Bolshaya Tagna (53°38′ N; 100°28′ E) intrusions. The localities of samples for U–Pb study are demonstrated on maps [33].

This province includes several complexes of alkaline ultramafic rocks and dikes of aillkites, mica picrites, kimberlite-like pyroxene-free picrites, lamproites, and rare explosion pipes. These complexes are associated with a rich rare metal Ziminskii ore district.

The Belaya Zima (Beloziminsky) Complex is located on the left bank of the Zima River at the intersection of the Iysko–Urik Graben and the Taimyr–Angara paleo rift. The intrusion crops out over an area of 18 km^2. Its country rocks are Neoproterozoic schists, quartzites, and dolerite sills [33]. The alkaline intrusive series includes ijolite and nepheline syenites that form arcuated bodies arranged concentrically around a central carbonatite stock. The nepheline syenite has a U–Pb ID–TIMS zircon age of 643 $\pm$ 4.0 Ma [19]. The U–Pb ID–TIMS garnet age of calcite-bearing ijolite is 645 $\pm$ 6 Ma [12], and the age of an ankerite carbonatite Ar–Ar phlogopite is 645 $\pm$ 6.0 Ma [16].

The Sredhaya Zima Complex is located in the Iysko–Urik Graben area, not far from the Belaya Zima Complex. Its country rocks comprise Neoproterozoic sandstones and schists, which are intensively fenitized and complicated in a northwest- and northeast-trending fracture system. The complex has a lenticular form of 2.6 km^2 at the current level of exposure (Figure 1b). The formation of the complex was a multistage process [34]. The earliest intrusion phases are fine-grained pyroxenite, which are preserved as a xenolith in the carbonatitic rocks. The second phase formed series of veins and lenticular bodies of ijolite and melteigite. The rocks of the next phase comprise medium-grained porphyric varieties of syenite. The last alkaline series of rocks is subalkaline massive coarse- and fine-grained syenite. Carbonatitic rocks ended the magmatic evolution of the Srednaya Zima intrusive complex. They occupy more than half the area of the massif. The carbonatite series includes biotite–calcite, aegirine–calcite, aegirine–biotite–calcite, amphibole–calcite, and ankerite–dolomite varieties of rocks, with carbonatitic rocks associated with betafite (main type), pyrochlore, apatite, zircon, burbankite–ancylite, and magnetite mineralization.

The Bolshaya Tagna Complex is surrounded by early Proterozoic metasedimentary rocks. The complex has a circular form with a diameter of approximately 4 km, and is characterized by a concentric zonal structure (Figure 1c) [15,16]. The Bolshaya Tagna intrusion is located away from the East Sayan mountain ridge. The ultramafic–alkaline rocks of this intrusion are relatively less jointed and carbonanatized to those in the Belaya Zima and Srednaya Zima intrusions [16]. The alkaline intrusive series is represented by ijolite–melteigite, nepheline syenite, subalkaline feldspathoidal syenite, picrite–porphyrite, and carbonatite (Figure 1c). The most prominent rock variety is ijolite. The less common varieties include nepheline and aegirine syenite. Carbonatite rocks form a large stock body in the western part of the complex and vein-shaped bodies within the alkaline rocks. Carbonatite rock types are standout coarse-grained; porphyritic with aegirine, riebeckite, and pyrochlore; and fine-grained calcite–dolomite. Hematite ore in carbonatite and syenite is the final stage of the complex formation.

Jjolite–melteigites from all massifs demonstrate wide variations in chemical composition, whereas alkaline intrusive rocks of the Srednaya Zima complex are very similar in composition to those from the Belaya Zima complex (Figure 2). Most of studied rocks are characterized by relatively low total alkalies due to the presence of calcite in the rocks, which can be both primary magmatic and postmagmatic.

Geochemical studies show that rocks of the alkaline ultramafic complexes are generally characterized by a high content of rare earth elements (Supplementary Materials Table S2). Foidolite series rocks contain 281 to 495 ppm REE, alkaline syenites (81 to 688 ppm REE). The studied rocks demonstrate LREE enrichment, with LREE (La–Eu)/HREE(Gd–Lu) ranging from 5.4 to 94. REE in the spectra, and rock from the Bolshaya Tagna and Srednya Zima are generally similar to Belya Zima alkaline silicate rocks (Figure 3) [33].

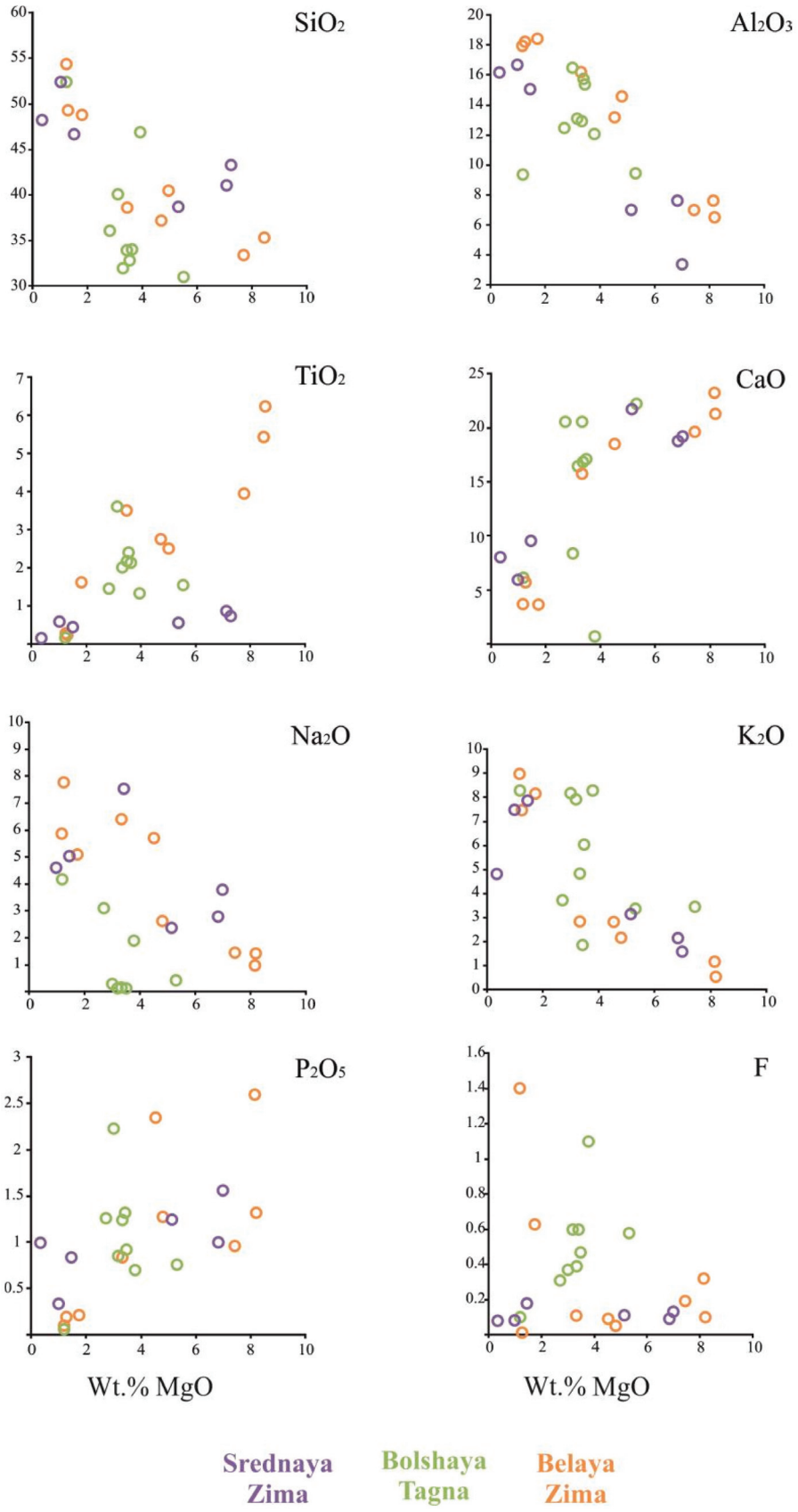

Figure 2. MgO variation diagrams for ultramafic–alkaline rock series of Srednaya Zima, Bolshaya Tagna (author's data), and Belaya Zima complexes [33].

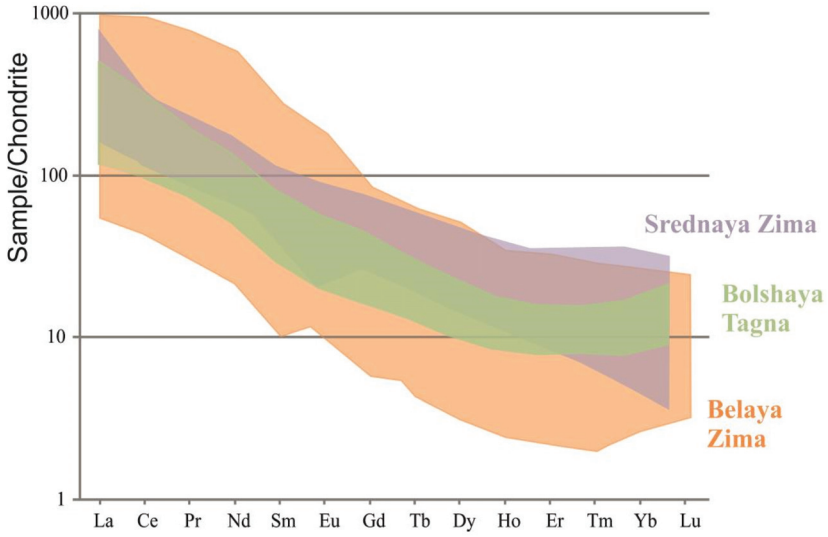

Figure 3. Chondrite-normalized REE distribution pattern of ultramafic–alkaline rock series from Srednaya Zima, Bolshaya Tagna (author's data), and Belaya Zima [33]. Normalized values are from [34].

4. Sample Descriptions

4.1. The Srednaya Zima Complex

Garnet is a rare mineral in the Srednaya Zima complex. A garnet sample from calcite–garnet pyroxenite (33/21) was selected for a detailed study. The studied rock contained diopside (60%–65%), calcite (15%–20%), and cancrinite formed on altered nepheline (15%–20%). Biotite (5%–7%), garnet (3%–5%), and aegirine (1%–2%) were less common (Figure 4a). The accessory minerals included fluorapatite, titanite, magnetite, baddeleyite, zircon, Mn–ilmenite, and pyrite.

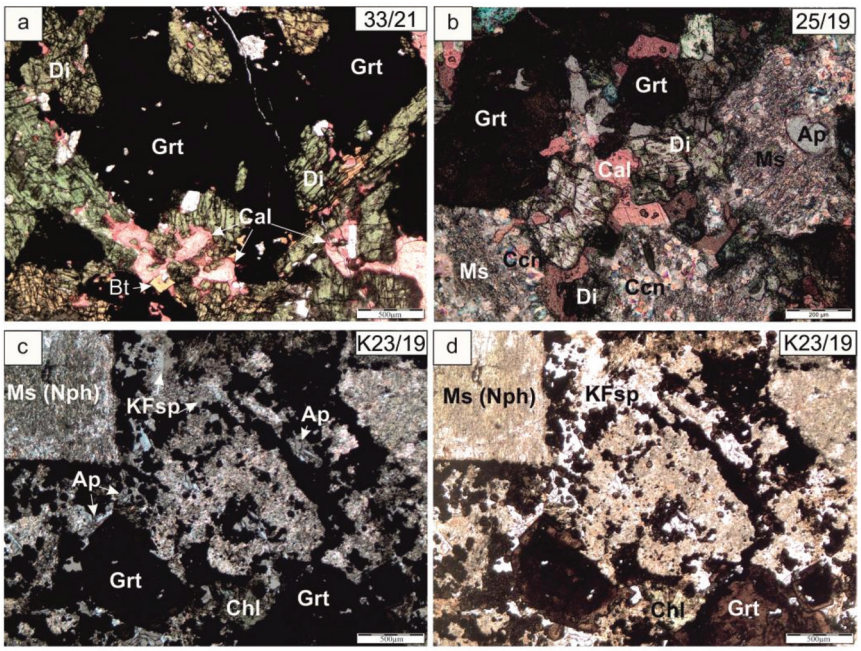

Figure 4. Photomicrographs of mineral textures, with polarizing (**a**,**b**,**d**) and crossed (**c**) nicol; (**a**) subhedral encrustations of garnet in calcite–garnet pyroxenite Srednaya Zima complex (33/21); (**b**) garnet crystals from altered diopside–garnet ijolite–melteigite (25/19) and zoned garnet (**c**,**d**) in altered garnet–nepheline syenite (K23/19) from Bolshaya Tagna complex; Grt—garnet, Ap—apatite, Cal—calcite, Chl—chlorite, Nph—nepheline, KFsp—potassic feldspar, Di—diopside, Ms—muscovite, Bt—biotite, Ccn—cancrinite.

Garnet occurs as subhedral encrustations between diopside, calcite, and pyroxene grains. Some garnet crystals contain single inclusions of apatite and rutile that are located in fractures. The relations between garnet and other rock-forming minerals imply that the garnet formed during the late magmatic stage after diopside, calcite, and biotite.

The color of garnet crystal fragments varies from dark brown to brown. The compositional range of garnet is $Adr_{33–48}Mmt_{21–32}Htn_{10–15}Sch_{2–14}Mg\text{-}Mmt_{2–6}$, with minor proportions of kimzeyite (<3%), Na–Ti garnet (<2.3%), and calderite (<1.3%) (Supplementary Materials Table S1; Figure 5b). No visible zoning was detected in single crystals. The chemical composition of single garnet crystals was found to vary within a narrow range.

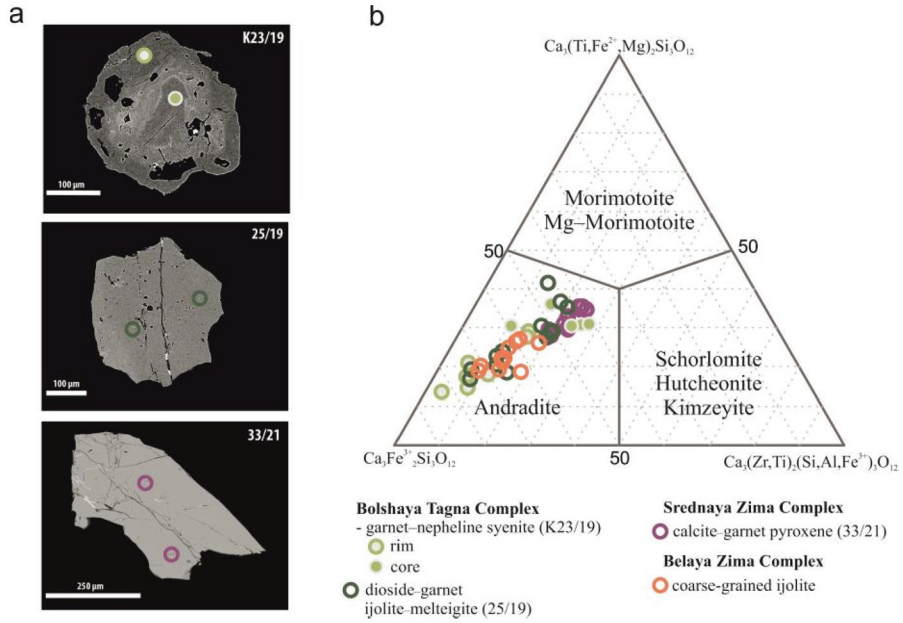

Figure 5. (**a**) Back-scattered electron (BSE) images of garnet crystal from studied rock samples; (**b**) chemical composition of calcic garnets from the present study and garnet from ijolite from Belaya Zima complex [12], expressed in terms of the principal end-member components (mol.%).

4.2. The Bolshaya Tagna Complex

Garnet samples from altered diopside–garnet, ijolite–melteigite (25/19), and garnet–nepheline syenite (K23/19) were selected for a geochronological study. The ijolite was composed mainly of nepheline (30%–35%), pyroxene (25%–30%), garnet (25%–30%), and calcite (10%–15%) (Figure 4b). The accessory minerals included cancrinite, potassic feldspar, and muscovite. Garnet forms single crystals, and presents as an inclusion in pyroxene grains. Some garnet crystals contain rare inclusions of calcite, apatite, and magnetite. The relationship between minerals in ijolite–melteigite rock indicates that the crystallization of garnet was a synchronous process with diopside that finished after the formation of nepheline, with an average composition of $Adr_{45–67}Htn_{8–14}Mmt_{15–30}$ (calderite (<1.3%) (Supplementary Materials Table S1; Figure 5b).

Garnet–nepheline syenite is a porphyritic rock composed of large (0.3–0.6 cm) porphyritic crystals of nepheline (30%–35%) and xenomorphic grains of potassic feldspar (20%–25%), garnet (25%–30%), and pyroxene (10%–15%) (Figure 4c,d). Nepheline crystals are replaced by fine-grained sericite. Garnet forms crystals of a dark brown color up to 1 mm. The composition of garnet ranges from $Adr_{38}Mmt_{13}Sch_2$ to $Adr_{78}Mrt_{33}Sch_{23}$, and the contents of other components (calderite, goldmanite, Na–Ti garnet, kimzeyite, and hutcheonite) do not exceed 5% (calderite (<1.3%) (Supplementary Materials Table S1; Figure 5b). The garnet crystals are zoned; the abundances of Ti and Zr decrease, whereas Fe and Mn contents increase from the core outward. Some crystals contain inclusions of biotite, calcite, and magnetite. Garnet is partly replaced by Mn–ilmenite.

5. Results of U–Pb ID–TIMS Garnet Geochronological Study

5.1. The Srednaya Zima Complex

Andradite from Srednaya Zima calcite–garnet pyroxenite was used for a U–Pb geochronological study. In total, three garnet fractions were selected for analysis (analyses 1–3, Table 1; Figure 6a). The studied samples were characterized by high U contents (8–10 ppm) and low levels of common Pb (Pb_c/Pb_t = 0.1–0.2). The data points were concordant (#2 and 3, Table 1) or slightly discordant (#1, Table 1), and yielded a concordia age of 624 ± 5 Ma (MSWD = 0.31, the probability of concordance = 0.58). The weighted average of $^{206}Pb/^{238}U$ ages of all analyzed garnet fractions (#1–3, Table 1) corresponded to an age of 623 ± 5 (MSWD = 1.6), which is close to the concordia age (Figure 6c). However, the obtained U–Pb garnet age is the first geochronological data to be reported for the Srednaya Zima complex.

Table 1. U–Pb ID–TIMS isotopic data [a] for garnets from ultramafic–alkaline rocks of the Eastern Sayan province.

No.	Garnet Characteristic; Treatment Type	Weight, mg	Pb, ppm	U, ppm	Pbc/Pbt	$^{206}Pb/^{204}Pb$ [b]	Isotopic Ratios Corrected for Blank and Common Pb				Rho	Age, Ma		
							$^{207}Pb/^{206}Pb$	$^{208}Pb/^{206}Pb$	$^{207}Pb/^{235}U$	$^{206}Pb/^{238}U$		$^{207}Pb/^{235}U$	$^{206}Pb/^{238}U$	$^{207}Pb/^{206}Pb$
						Srednaya Zima Complex								
						calcite-garnet pyroxenite (33/21)								
1	Fragments; 6-8 N HCl	0.44	1.87	9.99	0.13	202	0.0611 ± 2	0.8311 ± 1	0.8537 ± 34	0.1013 ± 2	0.60	627 ± 2	622 ± 1	644 ± 7
2	Fragments; 6-8 N HCl	0.42	1.77	8.71	0.20	135	0.0608 ± 2	0.7986 ± 1	0.8537 ± 42	0.1019 ± 3	0.58	627 ± 3	625 ± 2	632 ± 9
3	Fragments; 6-8 N HCl	1.20	1.43	8.28	0.07	368	0.0604 ± 3	0.7775 ± 1	0.8439 ± 48	0.1013 ± 2	0.46	621 ± 4	622 ± 1	619 ± 11
						Bolshaya Tagna Complex								
						altered garnet-nepheline syenite (23/19)								
4	Fragments; 6-8 N HCl	0.94	0.89	5.24	0.42	88	0.0614 ± 3	0.0457 ± 1	0.8752 ± 51	0.1033 ± 2	0.48	638 ± 4	634 ± 1	655 ± 11
5	Fragments; 6-8 N HCl	0.95	0.93	4.71	0.50	76	0.0617 ± 3	0.0499 ± 1	0.8783 ± 46	0.1032 ± 2	0.55	640 ± 3	633 ± 2	664 ± 9
6	Fragments; 6-8 N HCl	0.78	0.61	3.18	0.49	71	0.0607 ± 5	0.0324 ± 1	0.8633 ± 93	0.1031 ± 6	0.60	632 ± 7	632 ± 4	630 ± 19
						altered diopside–garnet ijolite–melteigite (25/19)								
7	Fragments; 6-8 N HCl	0.34	0.70	4.64	0.29	77	0.0617 ± 11	0.1377 ± 1	0.8757 ± 183	0.1029 ± 9	0.50	639 ± 13	631 ± 5	665 ± 39
8	Fragments; 6-8 N HCl	0.40	0.64	2.70	0.53	60	0.0609 ± 5	0.2009 ± 1	0.8643 ± 86	0.1029 ± 3	0.45	632 ± 6	632 ± 2	635 ± 19
9	Fragments; 6-8 N HCl	0.55	0.73	4.58	0.33	106	0.0631 ± 5	0.1414 ± 1	0.8999 ± 92	0.1033 ± 4	0.51	652 ± 7	634 ± 3	713 ± 19

[a] All measured values are given to the last significant digit (based on the corresponding 2σ). [b] Measured isotopic ratios.

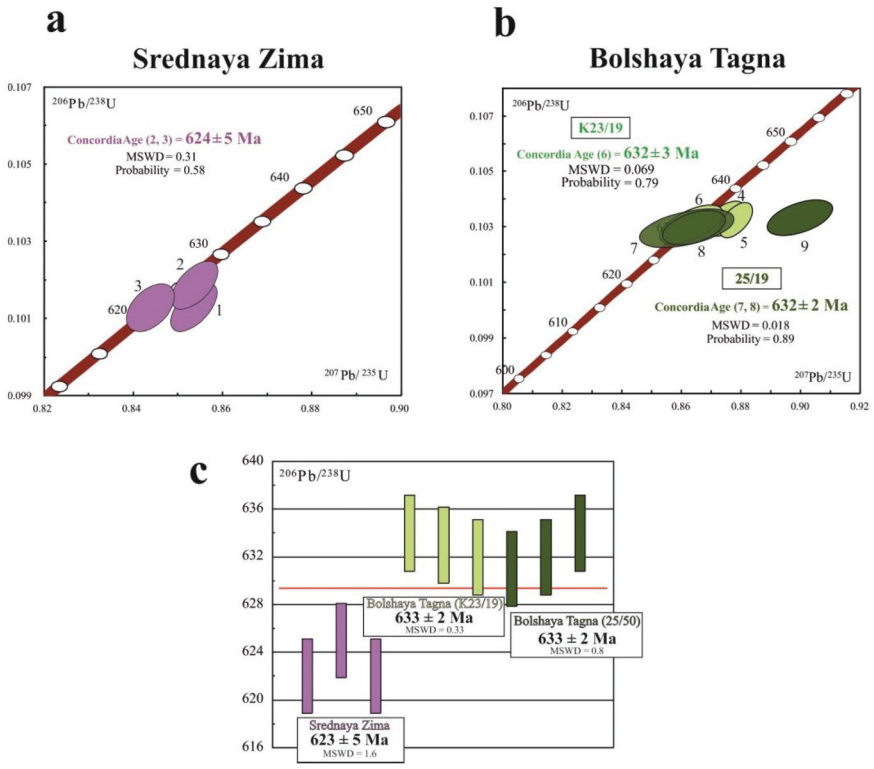

Figure 6. Concordia diagrams showing U–Pb ID–TIMS data for calcic garnet from (**a**) Srednaya Zima and (**b**) Bolshaya Tagna complexes; (**c**) weighted average $^{206}Pb/^{238}U$ for all data points. For the source data, see Table 1. Error ellipses are 2σ.

5.2. The Bolshaya Tagna Complex

For the U–Pb geochronological studies, we used visually homogeneous and clean fragments (0.10–0.15 mm) of andradite crystals from altered diopside–garnet ijolite–melteigite (sample 25/19) and altered garnet–nepheline syenite (sample 23/19). The garnet from both samples (analyses 4–9 in Table 1) is characterized by moderate U and low Pb contents (2.7–5.2 and 0.6–0.9 ppm, respectively). The data points of andradite from the ijolites (sample 23/19) were plotted on the concordia (analysis 6, Table 1) or slightly to the right, and yield a weighted average ($^{206}Pb/^{238}U$) age of 633 ± 2 (MSWD = 0.33) (#4–6, Table 1; Figure 6c) and a concordia age of 632 ± 3 (MSWD = 0.07, probability = 0.79).

As shown in Figure 6b, two points of the andradite from the nepheline syenite are located on the concordia (analyses 7,8; Table 1), providing a reasonably well-constrained age of 632 ± 2 (MSWD = 0.02; probability of concordance = 0.89). One analysis (#9) is discordant, and reveals some degree of inheritance ($^{207}Pb/^{206}Pb$ = 713 Ma). However, the $^{206}Pb/^{238}U$ age of the discordant data point coincides with the concordia age. The weighted average ($^{206}Pb/^{238}U$) age of the analyzed garnet fractions from this sample is 633 ± 2 (MSWD = 0.8), which perfectly coincides to the age of the garnet from the ijolite (Figure 6c).

These values reported above are in agreement with (but with more precision) the Sm–Nd age determinations (640 ± 11 Ma) for the rocks of the Bolshaya Tagna.

6. Discussion and Conclusions

Within the southern and southwestern margins of the Siberian craton, the final stages of the breakup of Rodinia are marked by the generation of alkaline ultramafic complexes from 650 to 621 Ma. These complexes trace for more than 3000 km [35] from the Aldan Shield (Arbarastakh and Ingili complexes) through the Altai–Sayan (Bolshaya Tagna, Belaya Zima, Srednaya Zima, and Zhidoy complexes) to the Tatrsky complex (Figure 1a), and are mostly characterized by similar types of rare metal deposits. The timing of Neoproterozoic magmatic events that occurred along the Siberian craton margin is an important point for the geodynamic correlation of the ultimate phase of Rodinia and the early stages of the Paleo-Asian Ocean. The main factors limiting these correlations are geochronological data obtained by different isotopic systems ($^{40}Ar/^{39}Ar$, K–Ar, U–Pb, and Sm–Nd) for intrusions with carbonatites and ultrabasic dikes.

Numerous recent studies have convincingly shown that Ca–Fe–Ti garnets offer unique opportunities for the timing of magmatic events, with a temporal resolution comparable to that of zircon dating. In this study, we presented new U–Pb (ID–TIMS) geochronological and geochemical data for Ca–Fe–Ti garnets from two complexes of the Eastern Sayan magmatic province and whole-rock geochemistry. Combining new geochronological data with those previously published for the Belaya Zima complex (645 ± 6 Ma), we provide information on the duration of the main magmatic event and the timing of alkaline ultrabasic complexes of the Ziminsky ore district of emplacement (Figure 1a). The new data provide an age range (ca. 650–624 Ma) with the possible relative age order Belaya Zima (ca. 650 Ma), Bolshaya Tagna (ca. 633 Ma), and Srednaya Zima (ca. 624 Ma). No geochronological data for the latter complex were available before our study. As demonstrated in Figure 7, the precision and accuracy of our U–Pb garnet geochronological study are similar to those using U–Pb zircon age determination, allowing us to evaluate the pulses of magmatic activity within the Eastern Sayan province.

Variations in the chemical composition of rocks from three complexes indicate that the parental melts were separated from different magmatic chambers that were generated during the same episode of mantle melting. According to the $^{40}Ar/^{39}Ar$ phlogopite data obtained for aillikite, damtjernite, and picrite from basic dikes from the northern part of the Eastern Sayan province (650–620 Ma), the rock formation in the dike complex of the region was related to the same stage.

This time span of about 25 Ma is also related to the emplacement of other massifs of biotite pyroxenite, ijolite, urtite, alkaline syenite, and carbonatites within the southern and southwestern marginal parts of the Siberia and Zhidoy complexes (632 ± 2 Ma [19]),

the Arbarastakh complex (650–638 Ma [36]), the Ingili complex (654 ± 7 Ma [19]), and the Tatarsky complex (630 Ma [37,38]). At the same time, Neoproterozoic mafic dike swarms within the southeastern and southern parts of the Siberian craton were emplaced about 100 Ma earlier, between 725 and 710 Ma [35,39,40], and demonstrated that at 720 Ma, the center of the Irkutsk plume occurred within the studied area, providing very good correlations with the 720 Ma Franklin plume center of northern Laurentia. The 720 Ma Franklin–Irktusk LIP event marks an attempted initial separation of southern Siberia from northern Laurentia during the breakup of Rodinia.

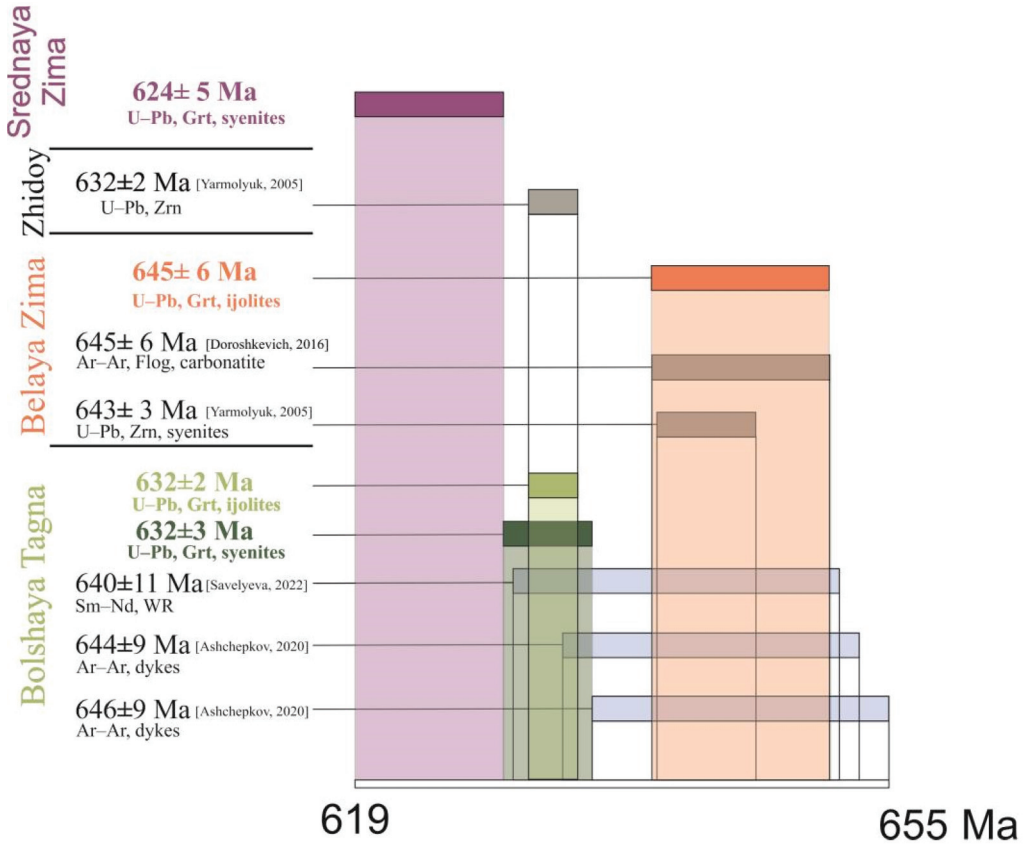

Figure 7. Summarized geochronological data for complexes of the Eastern Sayan magmatic province. Used own results and data from [17–20].

Accordingly, basic dikes indicate the early stage of Neoproterozoic extension, while alkaline–ultramafic carbonatitic complexes and potassium dikes record the late stages of extension of the lithosphere, and mark the early stages of the creation of the Paleo-Asian Ocean.

Supplementary Materials: The following supporting information can be downloaded at: https://www.mdpi.com/article/10.3390/min13081086/s1, Table S1: Chemical analyses of garnets from studied alkaline rocks; Table S2: Chemical composition of ultramafic-alkaline rock series of Srednaya Zima and Bolshaya Tagna complexes.

Author Contributions: Conceptualization and writing, M.V.S., E.B.S. and V.B.S.; investigation and U–Pb dating, M.V.S. and E.B.S.; geological background and geochemical study, Y.V.D., E.P.B. and B.S.D.; supervision, A.B.K. All authors have read and agreed to the published version of the manuscript.

Funding: This research was supported financially by the Russian Science Foundation (projects nos. 22–17–00211; IPGG theme nos. FMUW-2022-0003) and the "Geodynamic and geochronology" Collective Use Center of the Institute of Earth Crust SB RAS (project nos. 075-15-2021-682).

Data Availability Statement: Data will be made available on request.

Acknowledgments: We would like to thank the anonymous reviewers and academic editors for their constructive and thorough comments which greatly helped improve the manuscript.

Conflicts of Interest: The authors declare no conflict of interest.

References

1. Ernst, R.E.; Buchan, K.L. Large mafic magmatic events through time and links to mantle plume heads. In *Mantle Plumes: Their Identification through Time*; Ernst, R.E., Buchan, K.L., Eds.; Geological Society of America: Boulder, CO, USA, 2001; Volume 352, pp. 483–575. ISBN 9780813723525.
2. Hofmann, C.; Féraud, G.; Courtillot, V. $^{40}Ar/^{39}Ar$ Dating of Mineral Separates and Whole Rocks from the Western Ghats Lava Pile: Further Constraints on Duration and Age of the Deccan Traps. *Earth Planet. Sci. Lett.* **2000**, *180*, 13–27. [CrossRef]
3. Courtillot, V.E.; Renne, P.R. On the Ages of Flood Basalt Events. *Comptes Rendus Geosci.* **2003**, *335*, 113–140. [CrossRef]
4. Jerram, D.A.; Widdowson, M. The Anatomy of Continental Flood Basalt Provinces: Geological Constraints on the Processes and Products of Flood Volcanism. *Lithos* **2005**, *79*, 385–405. [CrossRef]
5. Blackburn, T.J.; Olsen, P.E.; Bowring, S.A.; McLean, N.M.; Kent, D.V.; Puffer, J.; McHone, G.; Rasbury, E.T.; Et-Touhami, M. Zircon U-Pb Geochronology Links the End-Triassic Extinction with the Central Atlantic Magmatic Province. *Science* **2013**, *340*, 941–945. [CrossRef] [PubMed]
6. Heaman, L.M.; LeCheminant, A.N. Paragenesis and U-Pb Systematics of Baddeleyite (ZrO_2). *Chem. Geol.* **1993**, *110*, 95–126. [CrossRef]
7. Söderlund, U.; Ibanez-Mejia, M.; El Bahat, A.; Ernst, R.E.; Ikenne, M.; Soulaimani, A.; Youbi, N.; Cousens, B.; El Janati, M.; Hafid, A. Reply to Comment on "U–Pb Baddeleyite Ages and Geochemistry of Dolerite Dykes in the Bas-Drâa Inlier of the Anti-Atlas of Morocco: Newly Identified 1380Ma Event in the West African Craton" by André Michard and Dominique Gasquet. *Lithos* **2013**, *174*, 101–108. [CrossRef]
8. Salnikova, E.B.; Stifeeva, M.V.; Chakhmouradian, A.R.; Glebovitsky, V.A.; Reguir, E.P. The U–Pb System in Schorlomite from Calcite–Amphobole–Pyroxene Pegmatite of the Afrikanda Complex (Kola Peninsula). *Dokl. Earth Sci.* **2018**, *478*, 148–151. [CrossRef]
9. Stifeeva, M.V.; Salnikova, E.B.; Samsonov, A.V.; Kotov, A.B.; Gritsenko, Y.D. Garnet U–Pb Age of Skarns from Dashkesan Deposit (Lesser Caucasus). *Dokl. Earth Sci.* **2019**, *487*, 953–956. [CrossRef]
10. Salnikova, E.B.; Stifeeva, M.V.; Nikiforov, A.V.; Yarmolyuk, V.V.; Kotov, A.B.; Anisimova, I.V.; Sugorakova, A.M.; Vrublevskii, V.V. Andradite–Morimotoite Garnets as Promising U–Pb Geochronometers for Dating Ultrabasic Alkaline Rocks. *Dokl. Earth Sci.* **2018**, *480*, 778–782. [CrossRef]
11. Stifeeva, M.V.; Vladykin, N.V.; Kotov, A.B.; Salnikova, E.B.; Sotnikova, I.A.; Adamskaya, E.V.; Kovach, V.P.; Plotkina, Y.V.; Tolmacheva, E.V.; Alymova, N.V. Formation Age of Early Precambrian Carbonatites in the Southeastern Part of the Chara–Olyokma Geoblock, Aldan Shield. *Dokl. Earth Sci.* **2022**, *507*, S247–S250. [CrossRef]
12. Salnikova, E.B.; Chakhmouradian, A.R.; Stifeeva, M.V.; Reguir, E.P.; Kotov, A.B.; Gritsenko, Y.D.; Nikiforov, A.V. Calcic Garnets as a Geochronological and Petrogenetic Tool Applicable to a Wide Variety of Rocks. *Lithos* **2019**, *338–339*, 141–154. [CrossRef]
13. Mezger, K.; Hanson, G.N.; Bohlen, S.R. Contributions to Mineralogy and Petrology U-Pb Systematics of Garnet: Dating the Growth of Garnet in the Late Archean Pikwitonei Granulite Domain at Cauchon and Natawahunan Lakes, Manitoba, Canada. *Contrib. Mineral. Petrol.* **1989**, *101*, 136–148. [CrossRef]
14. Stifeeva, M.V.; Salnikova, E.B.; Arzamastsev, A.A.; Kotov, A.B.; Grozdev, V.Y. Calcic Garnets as a Source of Information on the Age of Ultramafic Alkaline Intrusions in the Kola Magmatic Province. *Petrology* **2020**, *28*, 62–72. [CrossRef]
15. Frolov, A.A.; Belov, C.V. The Complex Carbonatite Deposits of the Ziminski Ore District (Eastern Sayan, Russia). *Geol. Ore Depos.* **1999**, *41*, 94–113.
16. Frolov, A.A.; Tolstov, A.P.; Belov, C.V. *Carbonatite Deposits of Russia*; NIA-Priroda: Moscow, Russia, 2003.
17. Doroshkevich, A.G.; Veksler, I.V.; Izbrodin, I.A.; Ripp, G.S.; Khromova, E.A.; Posokhov, V.F.; Travin, A.V.; Vladykin, N.V. Stable Isotope Composition of Minerals in the Belaya Zima Plutonic Complex, Russia: Implications for the Sources of the Parental Magma and Metasomatizing Fluids. *J. Asian Earth Sci.* **2016**, *116*, 81–96. [CrossRef]
18. Ashchepkov, I.; Zhmodik, S.; Belyanin, D.; Kiseleva, O.N.; Medvedev, N.; Travin, A.; Yudin, D.; Karmanov, N.S.; Downes, H. Aillikites and Alkali Ultramafic Lamprophyres of the Beloziminsky Alkaline Ultrabasic-Carbonatite Massif: Possible Origin and Relations with Ore Deposits. *Minerals* **2020**, *10*, 404. [CrossRef]
19. Yarmolyuk, V.V.; Kovalenko, V.I.; Salnikova, E.B.; Nikiforov, A.V.; Kotov, A.B.; Vladykin, N.V. Late Riphean Rifting and Breakup of Laurasia: Data on Geochronological Studies of Ultramafic Alkaline Complexes in the Southern Framing of the Siberian Craton. *Dokl. Earth Sci.* **2005**, *3*, 400–406.
20. Savelyeva, V.B.; Danilova, Y.V.; Letnikov, F.A.; Demonterova, E.I.; Yudin, D.S.; Bazarova, E.P.; Danilov, B.S.; Sharygin, I.S. Age and Melt Sources of Ultramafic Dykes and Rocks of the Bolshetagninskii Alkaline Carbonatite Massif (Urik-Iya Graben, SW Margin of the Siberian Craton). *Dokl. Earth Sci.* **2022**, *505*, 452–458. [CrossRef]
21. Sizykh, Y.I. *Complex Scheme of Chemical Analysis of Rocks and Minerals*; Institute of Crustal Research, Russian Academy of Sciences: Irkutsk, Russia, 1985.

22. Revenko, A.G. Physical and Chemical Methods of Researching Rocks and Minerals in the Analytical Centre of the Institute of the Earth's Crust, SB RAS. *Geodyn. Tectonophys.* **2014**, *5*, 101–114. [CrossRef]
23. Ivanov, A.V.; Demonterova, E.I.; Revenko, A.G.; Sharygin, I.S.; Kozyreva, E.A.; Alexeev, S.V. History and Current State of Analytical Research at the Institute of the Earth's Crust SB RAS: Centre for Geodynamics and Geochronology. *Geodyn. Tectonophys.* **2022**, *13*, 0582. [CrossRef]
24. Panteeva, S.V.; Gladkochoub, D.P.; Donskaya, T.V.; Markova, V.V.; Sandimirova, G.P. Determination of 24 Trace Elements in Felsic Rocks by Inductively Coupled Plasma Mass Spectrometry after Lithium Metaborate Fusion. *Spectrochim. Acta Part B At. Spectrosc.* **2003**, *58*, 341–350. [CrossRef]
25. Bulakh, A.G. *Calculation of Mineral Formulas*, 2nd ed.; Nedra: Moscow, Russia, 1964.
26. Dewolf, C.P.; Zeissler, C.J.; Halliday, A.N.; Mezger, K.; Essene, E.J. The Role of Inclusions in U-Pb and Sm-Nd Garnet Geochronology: Stepwise Dissolution Experiments and Trace Uranium Mapping by Fission Track Analysis. *Geochim. Cosmochim. Acta* **1996**, *60*, 121–134. [CrossRef]
27. Krogh, T.E. A Low-Contamination Method for Hydrothermal Decomposition of Zircon and Extraction of U and Pb for Isotopic Age Determinations. *Geochim. Cosmochim. Acta* **1973**, *37*, 485–494. [CrossRef]
28. Corfu, F.; Andersen, T.B. U–Pb Ages of the Dalsfjord Complex, SW Norway, and Their Bearing on the Correlation of Allochthonous Crystalline Segments of the Scandinavian Caledonides. *Int. J. Earth Sci.* **2002**, *91*, 955–963. [CrossRef]
29. Horwitz, E.P.; Dietz, M.L.; Chiarizia, R.; Diamond, H.; Essling, A.M.; Graczyk, D. Separation and Preconcentration of Uranium from Acidic Media by Extraction Chromatography. *Anal. Chim. Acta* **1992**, *266*, 25–37. [CrossRef]
30. Ludwig, K.R. *ISOPLOT for MS-DOS, a Plotting and Regression Program for Radiogenic-Isotope Data, for IBM-PC Compatible Computers, Version 1.00*; US Geological Survey: Reston, VA, USA, 1988.
31. Ludwig, K.R. *User's Manual for Isoplot/Ex Version 3.00, a Geochronological Toolkit for Microsoft Excel*; Berkeley Geochronology Center Special Publications: Berkeley, CA, USA, 2003; Volume 4.
32. Stacey, J.S.; Kramers, J.D. Approximation of Terrestrial Lead Isotope Evolution by a Two-Stage Model. *Earth Planet Sci. Lett.* **1975**, *26*, 207–221. [CrossRef]
33. Doroshkevich, A.G.; Veksler, I.V.; Klemd, R.; Khromova, E.A.; Izbrodin, I.A. Trace-Element Composition of Minerals and Rocks in the Belaya Zima Carbonatite Complex (Russia): Implications for the Mechanisms of Magma Evolution and Carbonatite Formation. *Lithos* **2017**, *284–285*, 91–108. [CrossRef]
34. Sun, S.-s.; McDonough, W.F. *Chemical and Isotopic Systematics of Oceanic Basalts: Implications for Mantle Composition and Processes*; Geological Society, London, Special Publications: London, UK, 1989; Volume 42, pp. 313–345. [CrossRef]
35. Yarmolyuk, V.V.; Kuzmin, M.I.; Ernst, R.E. Intraplate Geodynamics and Magmatism in the Evolution of the Central Asian Orogenic Belt. *J. Asian Earth Sci.* **2014**, *93*, 158–179. [CrossRef]
36. Prokopyev, I.R.; Doroshkevich, A.G.; Ponomarchuk, A.V.; Kruk, M.N.; Izbrodin, I.A.; Vladykin, N.V. Geochronology of the Alkaline-Ultra-Basic Carbonatite Complex Arbarastakh (Aldan Shlied, Yakutia): New Ar-Ar and U-Pb Data. *Geosfernye Issled.* **2022**, *4*, 48–66. [CrossRef]
37. Nozhkin, A.D.; Turkina, O.M.; Bayanova, T.B.; Berezhnaya, N.G.; Larionov, A.N.; Postnikov, A.A.; Travin, A.V.; Ernst, R.E. Neoproterozoic Rift and Within-Plate Magmatism in the Yenisei Ridge: Implications for the Breakup of Rodinia. *Russ. Geol. Geophys.* **2008**, *49*, 503–519. [CrossRef]
38. Vernikovskaya, A.E.; Vernikovsky, V.A.; Sal'nikova, E.B.; Kotov, A.B.; Kovach, V.P.; Travin, A.V.; Wingate, M.T.D. *A* -Type Leucogranite Magmatism in the Evolution of Continental Crust on the Western Margin of the Siberian Craton. *Russ. Geol. Geophys.* **2007**, *48*, 3–16. [CrossRef]
39. Gladkochub, D.P.; Mazukabzov, A.M.; Stanevich, A.M.; Donskaya, T.V.; Motova, Z.L.; Vanin, V.A. Precambrian Sedimentation in the Urik-Iya Graben, Southern Siberian Craton: Main Stages and Tectonic Settings. *Geotectonics* **2014**, *48*, 359–370. [CrossRef]
40. Ernst, R.E.; Gladkochub, D.P.; Soderlund, U.; Donskaya, T.V.; Pisarevsky, S.A.; Mazukabzov, A.M.; Bilali, H.E. Identification of the ca. 720Ma Irkutsk LIP and its plume centre in southern Siberia: The initiation of Laurentia-Siberia separation. *Precambrian Res.* **2023**, *394*, 107111. [CrossRef]

minerals

MDPI

Article

Origin of Redbeds in the Neoproterozoic Socheong Formation and Their Relation to the Dashigou Large Igneous Province

Hawon Yun [1], Seung Hwan Lee [2] and Inah Seo [1,3,*]

[1] Department of Environment and Energy, Jeonbuk National University, Jeonju 54896, Republic of Korea; yunhawon@jbnu.ac.kr
[2] Geology and Space Division, Korea Institute of Geoscience and Mineral Resources, Daejeon 34132, Republic of Korea; lsh07@kigam.re.kr
[3] Department of Earth and Environmental Sciences, Jeonbuk National University, Jeonju 54896, Republic of Korea
* Correspondence: inahseo@jbnu.ac.kr

Abstract: During the latest Mesoproterozoic–Early Neoproterozoic era, extensional regimes generated a number of sedimentary basins in various regions in the Sino-Korean Craton. Mantle-plume emplacements are widely recognized in the sedimentary strata as mafic dikes and sills of the Dashigou Large Igneous Province (LIP). The occurrence of Fe-rich redbeds is first reported in the Neoproterozoic Socheong Formation of the Sangwon Supergroup in the Pyeongnam Basin. Their geochemical and mineralogical characteristics indicate basin-wide Fe enrichment due to hydrothermal fluid input. The episodic yet repetitive hydrothermal injection into the basin generated short-lived anoxia, recorded as greenish-gray coloration in the ferruginous beds. This hydrothermal fluid was likely sourced from the mafic igneous activities involved in the Dashigou LIP. The redbeds can be utilized as key beds for intra- or inter-basinal stratigraphic correlation and to study the negative carbon isotope excursions that occurred in the genetically related basins in the region (e.g., the Sangwon, Xu-Huai, and Dalian basins).

Keywords: Socheong Formation; Sangwon Supergroup; Neoproterozoic; redbed; Large Igneous Province

1. Introduction

During the Late Paleoproterozoic–Neoproterozoic period (1800–541 Ma), an extensional tectonic regime generated multiple rifts in the Sino-Korean Craton (SKC) [1]. A number of sedimentary basins, including the Dalian, Pyeongnam (Pyongnam), and Xu-Huai basins (Figure 1A), developed simultaneously in the SKC during the Early Neoproterozoic period (ca. 1000–800 Ma). Although these basins were generated by a common rifting system, namely the Xu-Huai Rift System, the sedimentary successions (represented by the Qingbaikou System in North China) in the basins have been studied separately, largely owing to their ambiguous inter-basin relationship (e.g., [1–4]). A few comparative studies have analyzed the geologic affinities between these basins, particularly to analyze their common detrital provenances and contemporaneous igneous activities [5–9]. However, the geological history of the Sangwon Supergroup of the Pyeongnam Basin remains relatively unexplored, owing to the limited geologic information about the region.

The sedimentary strata deposited in these extensional basins, which are affected by the Xu-Huai Rift System, are commonly intruded by mafic sills or dike swarms shared by a common mantle-plume source [4,10]. This plume-related igneous activity is thought to have caused a large mafic extrusion, covering an area of 50,000 km^2, referred to as the Dashigou Large Igneous Province (LIP) [11–13]. The emplacement of the LIP had dramatic effects on the regional and/or global environment during the Phanerozoic, e.g., warming, cooling, ocean acidification, marine anoxia, and mass extinction [14]. However, the influence of this enormous magmatic activity on the semi-enclosed sedimentary basins

of the Xu-Huai Rift System remains uncertain. Recently, negative carbon isotope excursions (nCIEs) have been identified in the Xu-Huai, Dalian, and Pyeongnam basins, suggested to be the earliest-known nCIE events attributed to the formation of the Dashigou LIP [15–17]. However, their concurrent causation is not well-understood, partly because of the lack of knowledge of the environmental and biotic responses to the emplacement of the LIP.

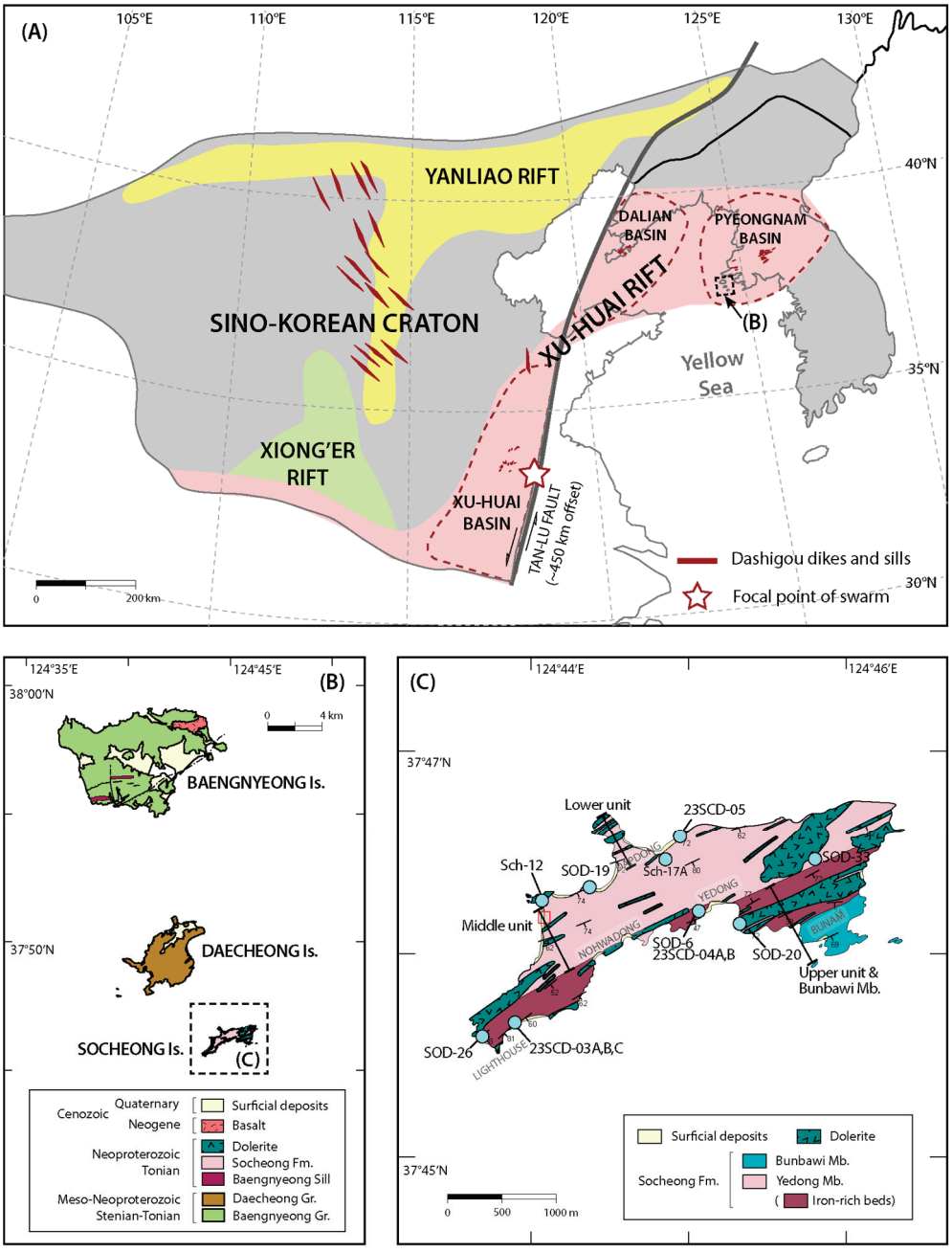

Figure 1. (**A**) Simplified tectonic map of Sino-Korean Craton, portraying three representative sedimentary basins, namely, the Pyeongnam (Pyongnam), Dalian, and Xu-Huai basins, during the latest Mesoproterozoic–Early Neoproterozoic period (modified after [4,6,12,18]); also shown are 940-890 Ma Dashigou dike swarms and their focal point (star) to mark the plume center [12]. (**B**) Simplified geologic map of the Baengnyeong, Daecheong, and Socheong islands (modified after [19]). (**C**) Geologic map of Socheong Island, presenting the locations of the redbeds and the sampling sites. The locations of representative sections are indicated as solid lines.

In this study, we report the occurrence of redbeds in the Socheong Formation, Socheong Island, South Korea, which is part of the Sangwon Supergroup of the Pyeongnam Basin. The origins of the redbeds and the co-occurring iron-rich greenish beds were determined from their geochemistry and mineralogy, and their relation to the region mafic igneous activity was also assessed. The hydrothermal activity associated with the Dashigou LIP and the relevant mafic igneous activities supplied Fe, while triggering local anoxia in the basin. The results of this study support the existing hypothesis that the formation of the LIP had a great influence on the biosphere and seawater chemistry, even during the Proterozoic [14,20].

2. Geological Settings

The sedimentary strata in the Baengnyeong, Daecheong, and Socheong islands have long been regarded as southwestern extensions of the Sangwon Supergroup in the Pyeongnam Basin in North Korea [21]. The Sangwon Supergroup is a (meta)sedimentary succession that corresponds to the Qingbaikou System (1000–780 Ma) in North China. The Sangwon Supergroup in mainland North Korea is subdivided into the Jikhyeon (Jikyon), Sadangu, Mukcheon (Mukchon), and Myeoraksan (Myoraksan) groups (in stratigraphically ascending order) [22].

Socheong Island is situated in the Yellow Sea, approximately 14 km from Jangsan Cape in South Hwanghae Province of North Korea (Figure 1). Kim and Kim [23] suggested that the sedimentary strata are related to the Mukcheon and Myeoraksan groups of the upper Sangwon Supergroup of North Korea, based on the stromatolite morphotypes discovered on Socheong Island. Lee et al. [24] reported bacterial microfossils as supporting evidence for the Neoproterozoic ages of the stromatolite. However, owing to the wide stratigraphic range of the Precambrian bacterial microfossils, a precise stratigraphic framework could not be established for the Socheong, Daecheong, and Baengnyeong islands.

Precise geological surveying and mapping of the Socheong, Daecheong, and Baengnyeong islands were carried out by Cho et al. [19], who developed a lithostratigraphic framework of the Proterozoic strata of the three islands. The Proterozoic sedimentary strata distributed in the Baengnyeong, Daecheong, and Socheong islands are called the Baengnyeong and Daecheong groups and the Socheong Formation, respectively (Figure 1B). The Baengnyeong and Daecheong groups are subdivided into the Nampori, Junghwadong, and Dumujin formations and the Jiduri and Dokbawi formations, respectively, in ascending stratigraphic order [19]. The Socheong Formation, the only formal lithostratigraphic unit on Socheong Island [19], is subdivided into two members (in ascending stratigraphic order): the Yedong and Bunbawi members (Figures 1C and 2A). The Yedong Member consists mainly of alternating sandstone–siltstone–shale layers, with partially intercalated limestone layers. The Bunbawi Member consists of thick limestone strata, with thin shale layers containing stromatolite fossils from the Neoproterozoic Era [23].

The depositional ages of the Baengnyeong, Daecheong, and Socheong formations were constrained by Cho, Lee, and Park [19], based on the maximum depositional ages of the strata determined by the igneous ages of the detrital zircons within, and the intrusion ages of, the mafic sills. Cho, Lee, and Park [19] reported the detrital zircon U-Pb ages of the Socheong Formation, with the youngest age peak estimated to be 900 Ma (Figure 2B,C). The U-Pb ages of the zircons (884 $\pm$ 4 Ma) and baddeleyites (888 $\pm$ 5 Ma) of the intruding dolerite (SOD-20 in Figure 2A) indicate that the depositional age of the Socheong Formation is the Tonian Period of the Neoproterozoic Era. Similarly, the depositional ages of the Daecheong and Baengnyeong groups range from 1040 Ma to 940 Ma, corresponding to the Mesoproterozoic (Stenian)–Neoproterozoic (Tonian) period [19].

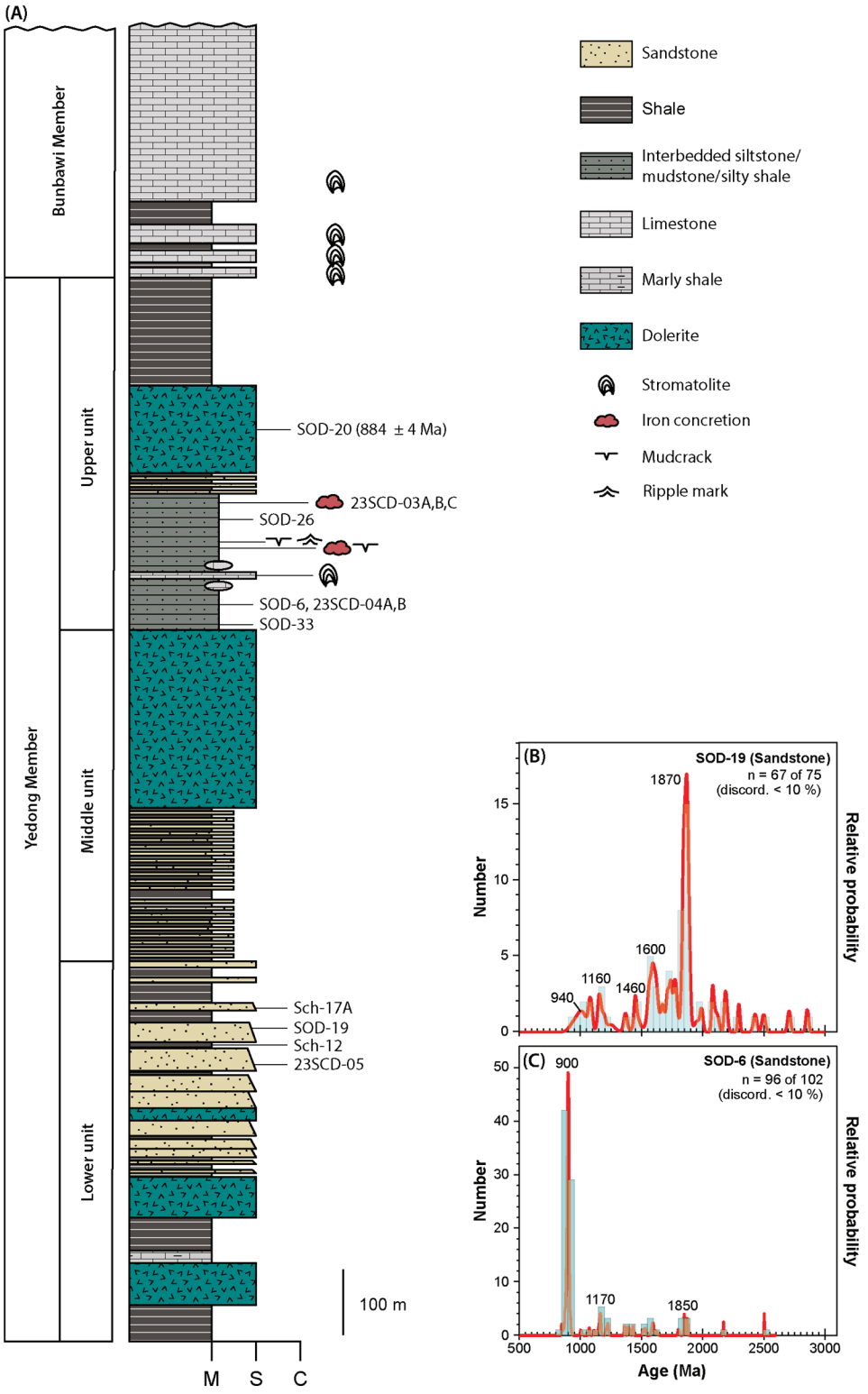

Figure 2. (**A**) Schematic illustration of the columnar section of Socheong Formation and positions of samples collected. (**B**,**C**) LA-MC-ICP-MS U-Pb isotopic analyses results for samples of Socheong Formation (data from [10]).

3. General Lithology of Socheong Formation and Redbed Occurrences

A schematic of the columnar section of the Socheong Formation is shown in Figure 3. The lower part of the Yedong Member is best exposed in the Dapdong area at the northern cape of the island, near the port. The lower part is mainly characterized by fine-grained

gray sandstone intercalated with thin dark gray mudstone (Figure 3A), dark gray shale, and light gray marly shale (Figure 3B,C). The thicknesses of the individual sandstone-mudstone couplets are 2–10 cm, sometimes exceeding several decimeters. The monotonous repetition of fine sandstone with graded bedding overlain by thin mudstone beds and remarkable lateral continuity (>10 m) are typical of low-density turbidite facies (Figure 3D). As shown in the figures, the dark gray shale and light gray marly shale exhibit parallel and laterally continuous laminae, indicating suspension settling. The lower part of the Yedong Member indicates a distal hemipelagic depositional process. Notably, in the Dapdong area, dolerites are frequently found as sills that are parallel to bedding planes.

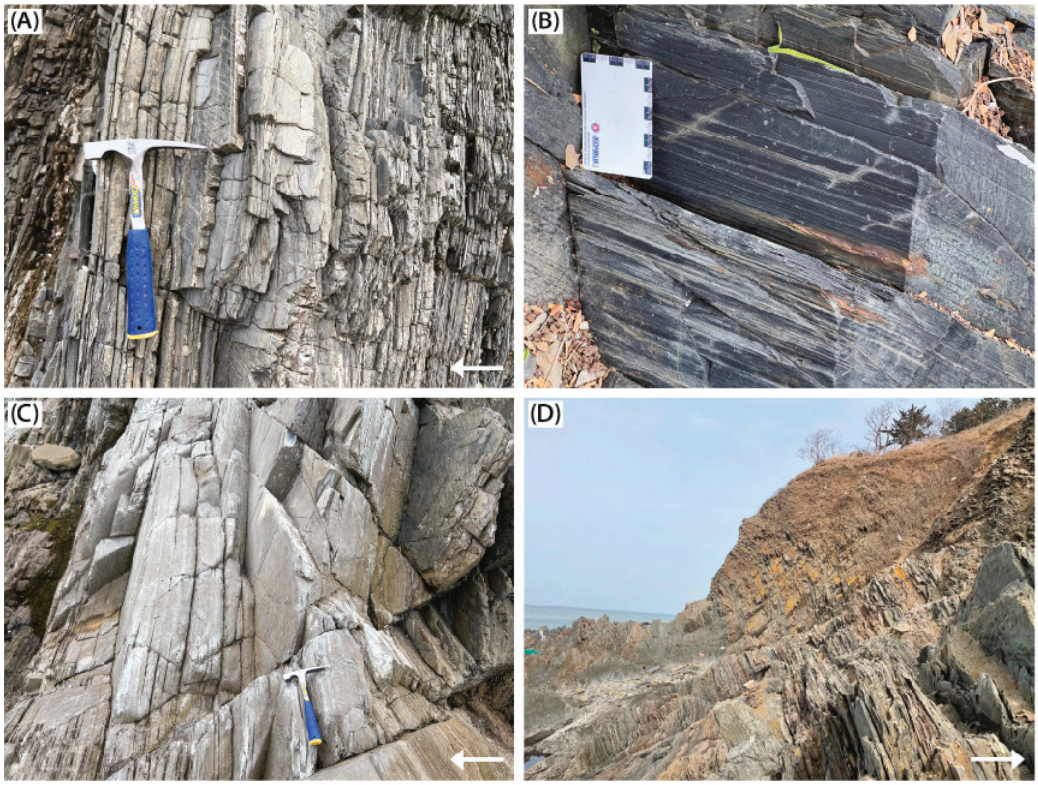

Figure 3. Outcrop photographs of the representative lithologies of the lower unit of Yedong Member, Socheong Formation. (**A**) Fine-grained gray sandstone intercalated with thin dark gray mudstone; (**B**) dark gray shale; (**C**) light gray marly shale; and (**D**) intercalated sandstone–mudstone exhibiting remarkable lateral continuity.

The middle part of the Yedong Member was well-exposed along the western coast of the island; a detailed columnar section of this strata has been provided by [19]. It is characterized by thick (>50 cm) bedded sandstone, interbedded mudstone–siltstone, and laminated dark gray shale. The most dominant lithology is interbedded mudstone–siltstone couplets with parallel/horizontal bedding (Figure 4A), occasionally occurring with thick laminated shale (Figure 4B). The outer shelf environment is presumed to be based on the lateral continuity of mudstone–siltstone beds, without any tidal or wave-generated substructures, such as mudstone rip-ups or internal cross-lamination. The intermittent invasion of the coarse-grained sandstone layer may indicate the occurrence of storm events.

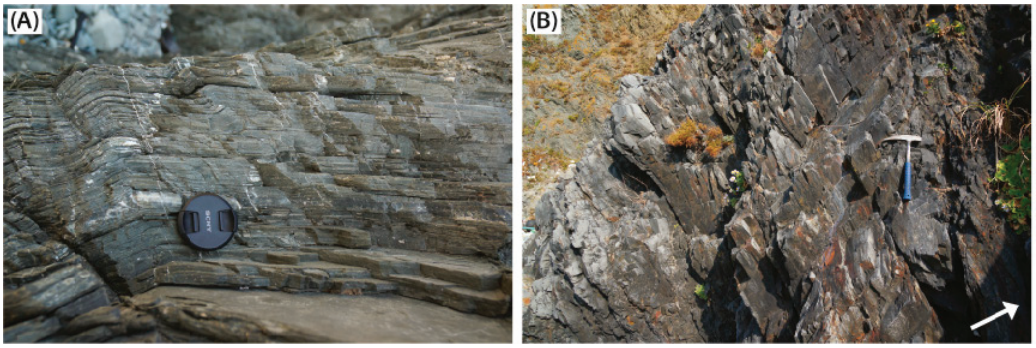

Figure 4. Outcrop photographs of middle unit of Yedong Member, Socheong Formation: (**A**) interbedded mudstone–siltstone with parallel/horizontal bedding and (**B**) thick dark gray shale exhibiting parallel bedding.

The upper part of the Yedong Member consists of plane or wavy laminated shale that is occasionally intercalated with tabular or lenticular-shaped limestone (Figure 5A), interbedded mudstone, and siltstone, exhibiting flaser, wavy, and lenticular bedding patterns (Figure 5B), and thick sandstone (Figure 5C). The siltstone–mudstone interbeds are very-thin to thin-bedded, with planar to undulated bedding planes, and cross-laminations within the siltstone can be noted. Mudcracks (Figure 5D,E) and symmetrical wave-ripple marks (Figure 5F) were observed on the bedding planes of the mudstone, for which raindrop imprints were reported [25]. These characteristics suggest a tidally influenced marginal marine environment above the wave base, which was occasionally exposed subaerially.

The upper boundary of the Yedong Member is marked by the thick development of a white–grayish-white limestone bed of the Bunbawi Member in the Bunam area (Figure 1C). The limestone in the lower unit exhibits a lenticular or tabular form, generally <1 m in thickness, being intercalated with purple or dark gray shale (Figure 6A), whereas the upper unit is almost entirely composed of stromatolitic limestone (Figure 6B). In the upper unit, the limestones are strongly deformed and partly metamorphosed into marble; thus, their bedforms and internal structures are sometimes amalgamated and thus difficult to discern [26]. Kong and Lee [26] provided a more detailed morphological description of the stromatolites.

The interbedded mudstone–siltstone and laminated shale of the upper Yedong Member exhibited a wide range of colors, including light and dark-gray, purple, red, and greenish-gray. The redbeds occur as ferruginous red-purple shale and interbedded siltstone–mudstone in the upper part of the Yedong Member (Figure 7A,B). They can be traced along the southeastern coast of Socheong Island, from the Deungdae (Socheong Lighthouse) to Yedong ports, and along the boundary between the Yedong and Bunbawi members (Figure 1C). The redbeds are often intercalated with greenish-gray beds that have similar lithologies; in some localities, the color changes from greenish-gray at the base to a reddish color in the upper section (Figure 7C). Some localities that exhibited hydrothermal vein injection were greenish-gray in color, indicating the reducing effect of the hydrothermal fluids (Figure 7D). The Fe concretions (ranging from mm to cm in diameter) were occasionally found in the greenish-gray beds (Figure 7E), but not in the purple-red beds. The purple shale underlying the upper boundary of the Yedong Member (Figure 7F) had thickness of >100 m.

Figure 5. Outcrop photographs of upper unit of Yedong Member, Socheong Formation: (**A**) Shales with tabular or lenticular limestone; (**B**) interbedded mudstone and siltstone with wavy beddings; (**C**) thick sandstone; (**D**,**E**) Mudcracks; and (**F**) wave-ripple marks on the mudstone bedding planes.

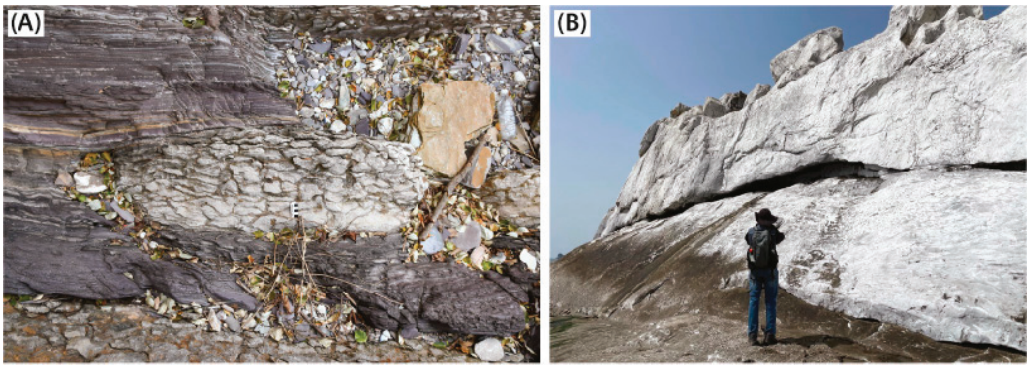

Figure 6. Outcrop photographs of Bunbawi Member of Socheong Formation: (**A**) lenticular limestone interbedded with purple shale (photo courtesy: Jeong-Hyun Lee) and (**B**) thick strata of stromatolitic limestone.

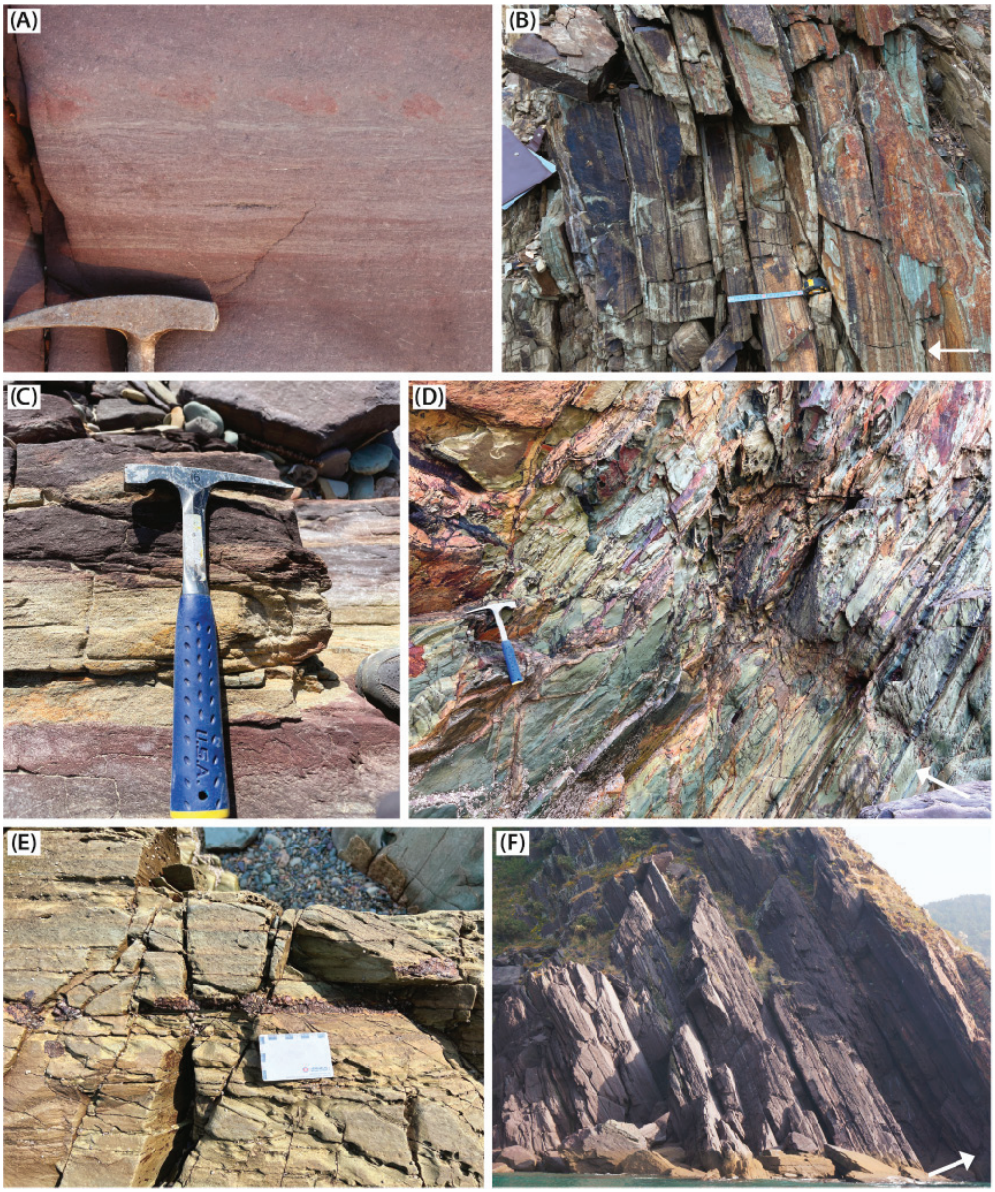

Figure 7. Photographs of the outcrops of redbeds and associated lithologies of Yedong Member, Socheong Formation. (**A**,**B**) Siltstone–mudstone couplets in (**A**) purple and (**B**) greenish-gray shales;

(**C**) siltstone–shale bed exhibiting gradual upward color change, from greenish-gray to purple, separated from the underlying purple shale by a sharp boundary; (**D**) hydrothermal veins in greenish-gray silty shale; (**E**) iron concretions in greenish-gray mudstone; (**F**) thickly developed purple shale beds below the upper boundary of Yedong Member.

4. Analytical Methods

4.1. Samples

Twelve rock samples were obtained from both the upper and lower units of the Yedong Member, Socheong Formation (Figure 1C, Table 1). Within the lower unit, four samples were collected, encompassing various lithologies such as sandstone, mudstone, silty shale, and others. In the upper unit, distinct color variations, including purple, red, greenish-gray, and dark gray, were observed in the beds, showcasing more pronounced differences compared with those in the lower unit of the Yedong Member. Consequently, the sampling process aimed to investigate the geochemical and mineralogical variances associated with these color differences. Notably, certain beds in the upper unit, particularly those exhibiting a greenish-gray color, contain metallic concretions. To thoroughly assess these features, a separate sample was taken from the beds with metallic concretions for further analysis (23SCD-03B).

Table 1. Major element compositions of the 12 samples analyzed in this study.

Analyte Symbol	SiO_2	Al_2O_3	$Fe_2O_{3(T)}$	MnO	MgO	CaO	Na_2O	K_2O	TiO_2	P_2O_5	LOI	Total	Lithology
Unit Symbol	%	%	%	%	%	%	%	%	%	%	%	%	
Detection Limit	0.01	0.01	0.01	0.005	0.01	0.01	0.01	0.01	0.001	0.01		0.01	
Analysis Method	FUS-ICP	FUS-ICP	FUS-ICP	FUS-ICP	FUS-ICP	FUS-ICP	FUS-ICP	FUS-ICP	FUS-ICP	FUS-ICP	GRAV	FUS-ICP	
Lower Unit													
23SCD-05	80.06	8.04	3.84	0.022	0.89	0.54	1.18	1.44	0.497	0.09	1.69	98.28	Sandstone
Sch-12	70.93	13.53	6.36	0.027	1.64	0.2	1.06	2.94	0.675	0.06	2.71	100.1	Mudstone
Sch-17A	65.3	17.64	4.81	0.024	1.64	0.05	0.84	4.86	1.217	0.04	3.55	99.97	Silty shale
SOD-19	74.2	9.09	4.95	0.082	1.48	2.89	0.91	1.86	0.459	0.04	4.12	100.1	Sandstone
Upper Unit													
23SCD-03A	50.32	20.68	16.19	0.114	1.78	0.29	0.44	3.63	2.121	0.21	4.12	99.9	Dark greenish–gray silty shale
23SCD-03B	36.76	16.98	29.36	0.361	4.45	0.36	0.25	0.58	2.214	0.21	9.3	100.8	Part of 23SCD-03A with metallic concretions
23SCD-03C	48.95	22.37	15.75	0.042	0.88	0.36	0.62	4.52	2.23	0.29	3.73	99.75	Purple shale
SOD-33	57.2	18.36	12.92	0.072	2.05	0.2	0.27	2.86	1.542	0.13	4.07	99.67	Purple shale
SOD-26	39.8	18.41	27.58	0.067	1.37	0.37	1.39	2.49	3.646	0.22	3.25	98.6	Purple shale
SOD-6	51.09	22.04	15.48	0.139	0.97	1.54	0.16	0.76	3.609	1.23	3.18	100.2	Greenish-gray silty shale
23SCD-04A	47.63	25.37	11.66	0.17	0.32	0.05	0.79	1.54	5.069	0.1	5.7	98.39	Greenish-gray silty shale
23SCD-04B	51.86	22.49	16.83	0.133	1.1	0.19	0.14	0.67	3.01	0.23	3.25	99.89	Greenish-gray silty shale

4.2. Bulk-Rock Geochemistry

We analyzed the bulk-rock geochemistry for 12 rock samples obtained from the Socheong Formation (Figure 1C). The analyses were performed at Activation Laboratories Ltd., in Ontario (Canada), using the 4LITHO (11+) QOP WRA/QOP WRA 4B2 package. The rock powders were fused with lithium metaborate/tetraborate, diluted with nitric acid, and analyzed using inductively coupled plasma optical emission spectroscopy (ICP-OES) and inductively coupled plasma mass spectrometry (ICP-MS). The accuracy of the results was evaluated by repeated analyses of the standard materials NIST 694, GBW07113, NOD-A-1, NOD-P-1, SY-4, BIR-1a, ZW-C, OREAS 101b, NCS DC86318, USZ 25-2006, DNC-1a, BCR-2,

USZ 42-2006, REE-1, and W-2b (Supplementary Table S1). Additional information about the procedure, precision, and accuracy of the analyses can be found at www.actlabs.com.

4.3. Mineralogy

The mineralogy of the representative lithologies was analyzed using a PANalytical X'pert Pro X-ray diffractometer at the Korea Institute of Ocean Science and Technology, using Cu-Kα radiation generated at 45 kV and 30 mA. The powdered samples of the rocks were scanned from 3° to 55°, with a step size of 0.02° and a measuring speed of 1°/min, at room temperature. Data reduction was performed using the PANalytical Highscore Plus software version 4.1 (Malvern PANalytical) for pattern processing.

5. Analytical Results

The analytical results for the bulk-rock geochemistry of the 12 samples are listed in Tables 1 and 2. There is a notable distinction in the geochemical composition between the samples from the lower and upper units. Two sandstones (23SCD-05 and SOD-19) and two mudstones (Sch-12 and Sch-17A) from the lower, non-redbed unit of Socheong Formation exhibited SiO_2 contents of 65.30–80.06 wt %, Al_2O_3 contents of 8.04–17.64 wt %, and $Fe_2O_{3(T)}$ contents of 3.84–6.36 wt %, indicating their ordinary siliciclastic origin. The siltstone and mudstone samples from the redbeds (23SCD-03C, SOD-33, and SOD-26) and intercalated greenish-gray beds (23SCD-03A, 23SCD-03B, SOD-6, 23SCD-04A, and 23SCD-04B) exhibited SiO_2 contents of 36.76–51.86 wt %, Al_2O_3 contents of 16.98–25.37 wt %, and $Fe_2O_{3(T)}$ contents of 11.7–29.36 wt %. Figure 8 portrays the major elemental composition normalized to that of the upper continental crust. The rare earth element and yttrium (REY) compositions of the samples were normalized with respect to the post-Archean Australian Shale (PAAS; Taylor and McLennan, 1985) (Figure 9); Y was inserted between Dy and Ho according to its ionic radius [27].

Table 2. Rare earth element and yttrium contents of the 12 samples analyzed in this study.

Analyte Symbol	La	Ce	Pr	Nd	Sm	Eu	Gd	Tb	Dy	Ho	Er	Tm	Yb	Lu	Y
Unit Symbol	ppm	ppm	ppm	ppm	ppm	ppm	ppm	ppm	ppm	ppm	ppm	ppm	ppm	ppm	ppm
Detection Limit	0.1	0.1	0.05	0.1	0.1	0.05	0.1	0.1	0.1	0.1	0.1	0.05	0.1	0.01	1
Analysis Method	FUS-MS	FUS-MS	FUS-MS	FUS-MS	FUS-MS	FUS-MS	FUS-MS	FUS-MS	FUS-MS	FUS-MS	FUS-MS	FUS-MS	FUS-MS	FUS-MS	FUS-ICP
Lower Unit															
23SCD-05	25.3	52	5.84	21.8	4.5	0.75	4.2	0.6	3.8	0.8	2.2	0.32	2	0.31	22
Sch-12	36.2	73.1	8.54	31.9	6.4	1.13	5.5	0.9	5.7	1.1	3.2	0.47	3.2	0.51	32
Sch-17A	46.6	91.4	10.4	39.2	7.5	1.36	6.1	1.1	6.8	1.4	4.2	0.64	4.3	0.7	41
SOD-19	24	49.3	5.78	22	4.5	0.79	3.9	0.6	3.9	0.8	2.2	0.31	2.1	0.34	22
Upper Unit															
23SCD-03A	31	47.7	8.31	30.9	6.5	1.87	5.9	1	6.5	1.3	3.5	0.5	3.2	0.48	32
23SCD-03B	96.2	371	21.4	81.5	16.4	4.49	14.3	1.8	9.1	1.5	4	0.53	3.3	0.51	38
23SCD-03C	120	251	28.9	109	19.5	4.63	14.7	1.9	10.6	2	5.6	0.79	5.2	0.79	53
SOD-33	46.8	93.9	10.8	39.9	7.5	1.21	5.9	1	6.7	1.4	4.4	0.67	4.4	0.7	36
SOD-26	24.7	53.4	6.1	24.8	5.5	2.18	6.1	1.1	7.3	1.4	3.9	0.54	3.4	0.56	33
SOD-6	63.3	130	15	59.7	12	4.02	11	1.7	9.6	1.7	4.7	0.65	4	0.63	49
23SCD-04A	70.6	153	18.2	72.8	13.8	3.54	10.4	1.4	8.1	1.6	4.5	0.63	4.2	0.66	44
23SCD-04B	77.9	176	21	84.9	15.2	3.71	11.2	1.5	9.1	1.8	4.8	0.67	4.5	0.66	47

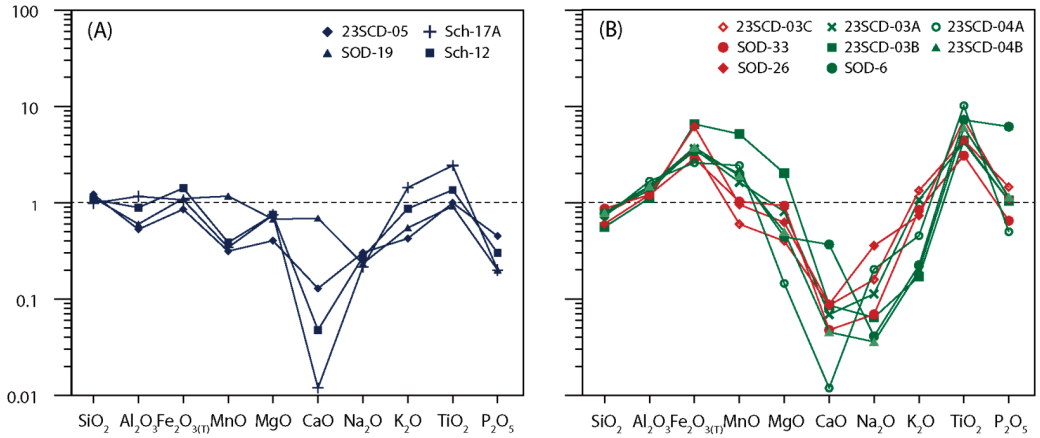

Figure 8. Major elemental compositions of the samples normalized to that of the upper continental crust of Socheong Formation (**A**: lower unit; **B**: upper unit). The symbols in panel B are color-coded to correspond with the bed colors; e.g., red represents red or purple beds, and green represents greenish-gray or dark greenish-gray beds.

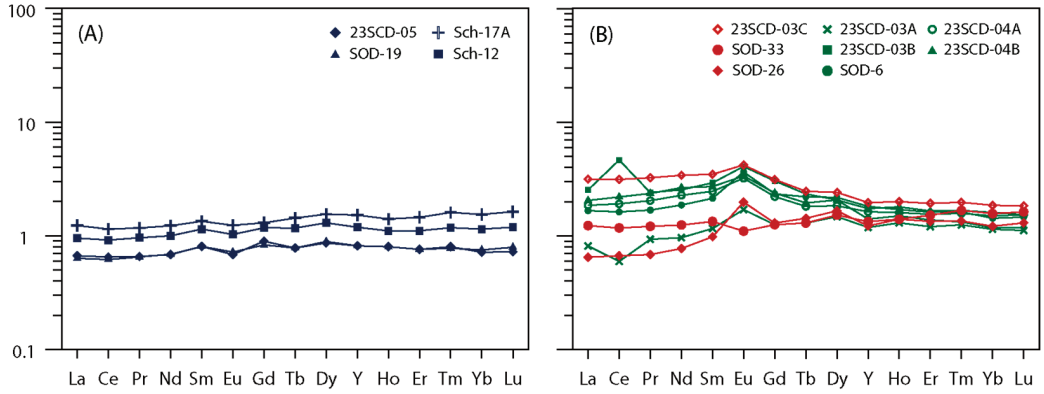

Figure 9. Rare earth element (REE) composition normalized to the post-Archean Australian Shale for (**A**) lower unit and (**B**) upper unit of Yedong Member, Socheong Formation.

X-ray diffraction (XRD) patterns and petrographic thin-section photos of the Socheong Formation are shown in Figures 10 and 11, respectively. The dark gray mudstone (Sch-12) from the lower unit exhibited characteristic quartz peaks, with the small peaks being hardly identifiable (Figure 10A). The thin section of the dark greenish-gray silty shale sample (23SCD-03A) from the upper unit is shown in Figure 11A; with respect to the XRD analysis, the sample exhibited peaks at ~14.1, ~7.1, ~4.7 and ~3.56 Å, which could be attributed to the (001), (002), (003), and (004) basal reflections of chlorite (Figure 10B). The relative intensities of the (001) and (003) reflections were considerably lower than those of the (002) and (004) reflections, indicating that chamosite, an Fe-rich end-member of chlorite, was the dominant component of the sample. The purple shale sample (SOD-26) of the upper unit exhibited the characteristic peaks of hematite (Figure 10C), indicated in the thin section by a dark color (Figure 11B), in addition to the characteristic peaks of quartz and muscovite/illite (Figure 10C). The greenish-gray siltstone samples (23SCD-04A and 23SCD-04B) of the upper unit exhibited characteristic peaks of chloritoid at ~4.45 Å (~20° 2θ), pyrophyllite at ~9.2, ~4.6, and ~3.1 Å (~9.6°, 19.3° and 29.1° 2θ), and chlorite (Figure 10D,E); these minerals were observed in the petrographic thin-section analysis as well (Figure 11C,D).

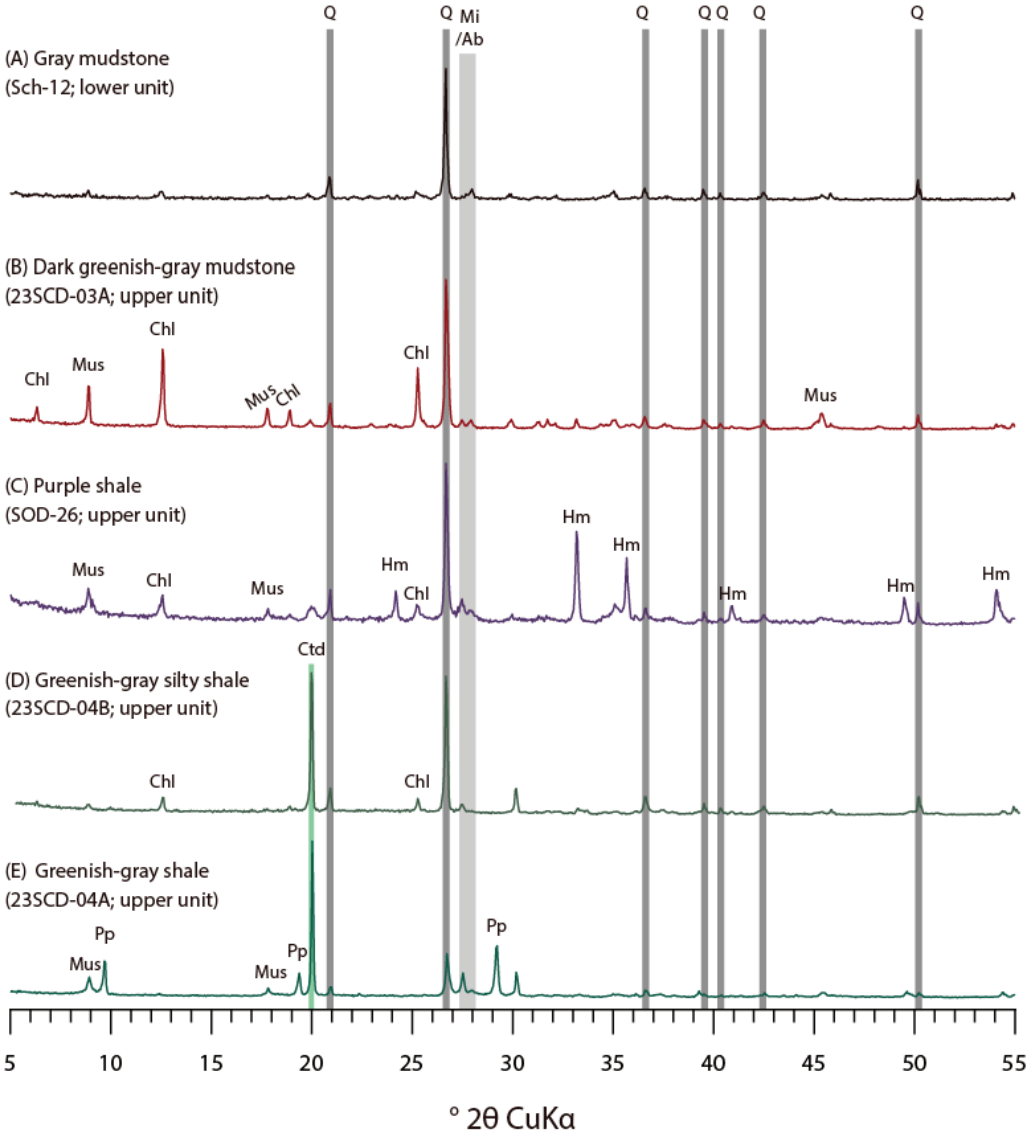

Figure 10. X-ray diffraction (XRD) results of the representative samples of Socheong Formation: (**A**) Gray mudstone sample (Sch-12) of lower unit; (**B**–**E**) representative samples of Fe-rich upper unit for (**B**) 23SCD-03A, (**C**) SOD-26, (**D**) 23SCD-04B, and (**E**) 23SCD-04A. Q = quartz, Mi/Ab = microcline/albite, Chl = chlorite, Mus = muscovite and illite, Hm = hematite, Ctd = chloritoid, and Pp = pyrophyllite.

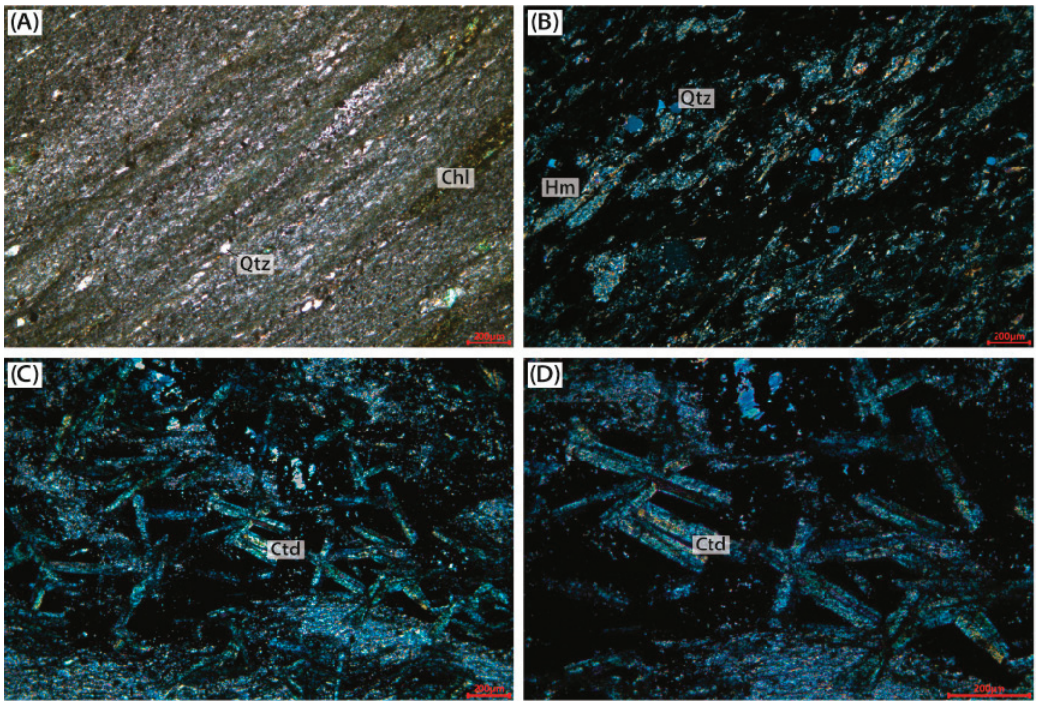

Figure 11. Photographs of thin sections of Fe-enriched upper unit samples: (**A**) dark greenish-gray silty shale (23SCD-03A, PPL); (**B**) purple shale (SOD-26); and (**C**,**D**) greenish-gray silty shale (23SCD-04A), after magnification. Q = quartz, Chl = chlorite, Hm = hematite and Ctd = chloritoid.

6. Discussion

6.1. Hydrothermal Input of Fe

The redbeds and co-occurring greenish-gray siltstone–mudstones of the upper unit contained 18.2% $Fe_2O_{3(T)}$ on average (with 12.7% Fe) (Table 1), which is significantly enriched compared with those of UCC (Figure 8). The purple shale sample (SOD-33) contained 29.4% of $Fe_2O_{3(T)}$ (19.29% Fe); thus, the rock can be termed "ironstone," based on the definition proposed in previous studies [28,29]. The high $Fe_2O_{3(T)}$ contents (Table 1, Figure 8B) and Fe/Al ratios (Figure 12A) for the samples obtained from the upper unit suggest an additional input of Fe, other than from the detrital source. The positive Eu anomalies [$Eu/Eu^*_{SN} = (Eu_{SN}/(0.67Sm_{SN} + 0.33Tb_{SN})$] for most samples of the Fe-rich upper unit indicated a hydrothermal source of Fe (Figure 12B), supported by the general covariance of the Eu anomaly and $Fe_2O_{3(T)}$. In contrast, the Fe content of the lower unit of the Yedong Member is similar to that of the upper continental crust (Figure 8A). The small negative Eu anomalies and Fe/Al ratios, similar to those observed for the PAAS, indicate a negligible influence of the hydrothermal fluid.

A conceivable detrital source of Fe is the mafic sills reported in the Baengnyeong and Daecheong islands; in particular, the source can be the Baengnyeong Sill strata [10], because the intrusion age of the Baengnyeong Sill (ca. 940 Ma) is largely concurrent with the maximum ages of the detrital zircons found in the Socheong Formation (ca. 930–880 Ma; Figure 2B,C). However, the total Fe content, represented as $Fe_2O_{3(T)}$, of the Baengnyeong Sill sample was 13.8–16.9 wt % [10], generally lower than those of the Fe-rich units of Socheong Formation. The Eu anomaly was not apparent in the Baengnyeong Sill [10], either, negating its possibility as a direct detrital source for the Fe-rich upper unit of the Socheong Formation.

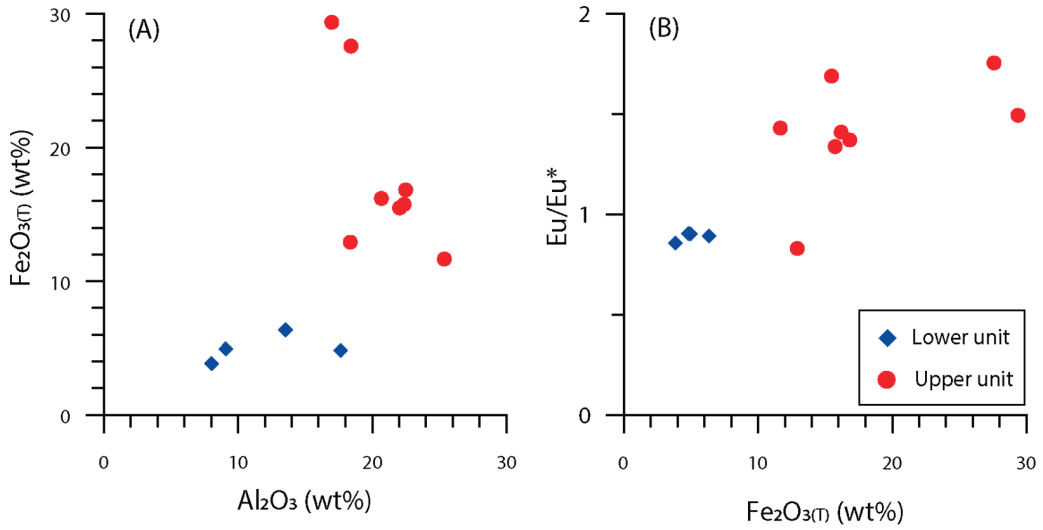

Figure 12. Cross-plots of (**A**) $Fe_2O_{3(T)}$ versus Al_2O_3 and (**B**) Eu/Eu* versus Fe_2O_3 of upper and lower units of Yedong Member, Socheong Formation.

In the greenish-gray shale samples (SOD-6, 23SCD-04A and 23SCD-04B) of the upper unit, chloritoid porphyroblasts were detected in the XRD patterns and observed in the petrographic thin sections as well (Figure 10D,E and Figure 11C,D, respectively). Chloritoid, a neosilicate mineral represented by the general formula $(Fe,Mg,Mn)_2Al_4Si_2O_{10}(OH)_4$, is generally found in metamorphic rocks of various grades ranging from sub-greenschist to amphibolite facies [30]. The Socheong Formation is considered to have undergone sub-greenschist facies metamorphism, indicated by the absence of textural schistosity or high-grade metamorphic minerals. The chloritoids in the Socheong Formation can be associated with chamosite and white mica (presumably pyrophyllite or muscovite) (Figure 10), indicating low-grade metamorphism. Although chloritoids are more commonly associated with higher-grade metamorphic index minerals, such as andalusite, kyanite, and staurolite [31], hydrothermal activity has been reported to induce the growth of chloritoid minerals [32]. The low-grade metamorphic ensemble of chloritoid, chlorite, and muscovite of the upper unit of the Yedong Member, Socheong Formation indicates Fe enrichment and high contents of Al [30,33–35], which can be explained by the addition of hydrothermal iron to Al-rich pelitic rocks.

6.2. Bottom Redox Conditions

The differential redox sensitivities and ionic radii of REY compositions result in the relative enrichment and/or depletion of light rare earth elements (LREEs), Ce, and Y in the bulk sediment. The negative Ce anomaly, $[Ce/Ce^*_{SN} = Ce_{SN}/(0.5La_{SN} + 0.5Pr_{SN})]$, and the depletion of LREEs over heavy rare earth elements (HREEs) is typical for modern oxidized ocean water, because of the preferential incorporation of Ce^{4+} and the scavenging of LREEs by rapidly oxidized Fe–Mn oxyhydroxides [36,37]. The behavior of Y was somewhat inverse to those of the LREEs and Ce. Notably, Ho, the geochemical analog of Y, is more reactive than Y; thus, Y is enriched in seawater when normalized to the average shale composition [38]. In the redox-stratified ocean, a negative Ce anomaly and positive Y anomaly and LREE depletion are expected to occur above the redoxcline, where the oxidizing environment prevails; the opposite is expected to occur below the redoxcline [37]. Significant variabilities in LREE depletion and Ce and Y anomalies are apparent in Fe-rich beds, suggesting that the beds have been deposited near the redoxcline, where the adsorption–remobilization reactions are the most active. Such characteristics in the REY are similar to those of hydrothermally influenced sediments near the redox boundary deposited after the Late Paleoproterozoic [37]. In contrast, flat REY patterns and a lack of

Ce and Y anomalies were observed for the samples of the lower unit of the Yedong Member (Figure 10A).

The repetitive occurrence of greenish-gray and purple strata (Figure 7) in the upper unit of the Yedong Member also indicates episodic hydrothermal activity and the consequent variation in the redox state of the basin. During the deposition of the upper unit, an overall oxygenated bottom water condition is inferred, as evidenced by the presence of thickly developed red or purple shale overlain by the substantial limestone unit (i.e., Bunbawi Member). Episodic hydrothermal fluids may have contributed to brief periods of anoxia that dissipated rapidly. There is a gradual change in color from the greenish-gray bottom to the purple top of the bed (Figure 7C), sharply underlain by another greenish-gray colored bed. This can be explained by intermittent hydrothermal activity, which not only supplied Fe^{2+}, but also generated short-lived anoxia in the basin, resulting in a greenish-gray or dark gray mudstone layer. The green color of the rock can be attributed to the presence of ferrous clay minerals (chamositic chlorite). After the anoxia dissipated, Fe^{2+} was oxidized at the water–sediment interface; the red-purple color of the mudstones could be attributed to the presence of hematite (Figure 10C). The alteration of purple and greenish-dark gray mudstone beds disappeared upward, and the purple shale developed thickly in the uppermost strata of the Yedong Member (Figure 7F). Notably, in the uppermost strata of the Yedong Member of the Socheong Formation, purple shale diminishes progressively, alternating with stromatolite-bearing limestone beds (Figure 6A) and eventually transforming into thick limestone (Bunbawi Member). This indicates that the hydrothermally driven anoxia ceased to exist, because the deposition of redbed and stromatolite-bearing limestone occurred in photic, oxygenated, yet Fe-enriched surface water. One may suggest that the colors of the beds only reflect the water depths of deposition; however, this possibility is negated by their similarity in sedimentary structures and the development of mudcracks (Figure 5D,E), in both the greenish-gray and purple shales. Thus, the color transition in the shale unit can only be explained by Fe addition, and the relevant bottom redox condition changes can be attributed to intermittent hydrothermal activity.

6.3. Genetic Linkage of Fe-Rich Beds and the Dashigou Large Igneous Provinces (LIP)

Because Fe is easily precipitated in an oxic environment, the excess Fe supplied by hydrothermal activity in the modern, nearly fully oxidized open ocean basin would be accumulated near the vents in the form of oxyhydroxides. However, under anoxic conditions (e.g., below the redoxcline), excessive Fe can be mobilized as Fe^{2+} or only partly deposited in the sulfide phases. Such mobilization of Fe would result in the enrichment of dissolved Fe in the basin, which would eventually lead to the deposition of iron-rich formations or ironstones, if sufficiently oxidized. In Archean and Early Paleoproterozoic oceans, wherein anoxia prevailed, iron oxygenation was largely mediated by microbes or photochemical reactions in reducing conditions, resulting in the deposition of banded iron formations [20,37,39]. In the Late Neoproterozoic and modern Phanerozoic ocean, after the rise of atmospheric oxygen during the Neoproterozoic Oxygenation Event (~850–540 Ma), a sufficient amount of Fe^{2+} delivery was achieved in small semi-isolated basins, favoring the formation of ironstones [20,39]. Consequently, their formation can be likely linked to anoxic events in several cases, as exemplified by the Snowball Earth events [40]. During the Mesoproterozoic–Early Neoproterozoic (~1.85–0.75 Ga), the ocean redox condition is assumed to be between these two extremes, which was less reducing than the Archean and the Early Paleoproterozoic but notably more reducing than the Phanerozoic Ocean [20,37,39]. Even after the Great Oxygenation Event, at 2.32 Ga [39], deep-ocean anoxic conditions might have been preserved in isolated–semi-isolated basins, even if the surface ocean was oxygenated [20]. Notably, differential oxygenation generates a redox stratification and developed a "redoxcline" in the water column, which is favorable for the formation of Fe-rich beds in the presence of large hydrothermal fluxes of Fe [20,37,39].

The delivery of an excessive amount of Fe^{2+} into these semi-isolated redox-stratified basins may have been achieved through mafic igneous activities. Iron-rich formations

and ironstones are often genetically linked to an excessive Fe supply from volcanic and hydrothermal activities [20,39,41,42]. The deposition of large and economically important iron formations commonly coincides with mantle-plume breakout events, as recorded by the occurrence of LIPs, dike swarms, and submarine mafic volcanic rocks [20,41]. In the study area, relevant mafic igneous activity was recorded at ~890 Ma in a doleritic sill on Socheong Island, corresponding to the Sariwon Sill of the Pyeongnam Basin [10,12]. Its intrusion age is vaguely discernible from the maximum depositional age of the Socheong Formation (~900 Ma), based on the youngest detrital zircon ages of the upper unit of the Yedong Member (SOD-6, Figure 2C), with respect to the precision of $^{207}Pb/^{206}Pb$ ages [10]. The age distribution of the SOD-6 sample was characterized by a predominant 930–880 Ma peak, devoid of any other age peaks identified in the lower unit of the Yedong Member (SOD-19, Figure 2B), exhibiting similar age distribution patterns to those of the Baengnyeong and Daecheong groups [19]. This difference indicates a significant change in the provenance of the detritus during the deposition of the Yedong Member, involving syn- or near-depositional extrusive magmatism that could have supplied the zircons (of age 900 Ma). Although no mafic extrusive rocks have been found on Socheong Island, it is likely that magmatic events accompanying hydrothermal activity occurred during the deposition of the Socheong Formation before the sill intrusion.

In the southern Pyeongnam Basin of mainland North Korea, reddish-purple sericite-chlorite phyllite has been reported in the upper Seolhwasan (Solhwasan) Formation, which is underlain by the limestone-dominated Okhyeonri (Okhyonri) Formation of the Mukcheon (Mukchon) Group [22]. The similarity in the lithologic associations between the Yedong and Bunbawi members of the Socheong Formation and the Seolhwasan and Okhyeonri formations is consistent with the existing hypothesis of their stratigraphic affinity [23]. The deposition of Fe-rich beds was presumably widespread, at least in the southern Pyeongnam Basin, during the deposition of the Socheong and Okhyeonri formations, which can be attributed to mafic igneous activities in the region.

6.4. Regional Concurrency of the Formation of the Redbeds and Dashigou Large Igneous Province (LIP) and the Stratigraphic Implications

The mafic sill intrusions in the Pyeongnam Basin are thought to have originated from the mantle plume involved in the formation of the Dashigou LIP, as evidenced by the widespread intrusions of mafic dikes and swarms in the Xu-Huai, Dalian, and Pyeongnam basins [1,4,7,10,12]. Although there should have been some degree of inter-basinal differences with respect to the timings of mafic igneous activities, the intensity of hydrothermal activity and sensitivity to the changes in redox states, as evidence of Fe enrichment in sedimentary strata, was noted in various regions of the eastern SKC. For instance, red or purple shales have been reported in the Shisanlitai Formation of the Jinxian Group in the Dalian Basin [17,43] and the Shijia Formation of the Huaibei Group in the Xu-Huai Basin [16]. The occurrence of red limestones in the eastern and southern SKC during the Tonian Period was also reported by Kuang et al. [44], supporting the theory of the occurrence of basin-wide hydrothermal Fe-enrichment.

Given the paucity of precise age-determination methods for Proterozoic strata, the extensive occurrence of redbeds indicates their potential as marker beds for regional stratigraphic correlation. However, previous studies recognize at least three different magmatic activities involved in the Dashigou LIP, at 940, 920, and 890 Ma [10], in the Pyeongnam, Dalian, and Xu-Huai basins, respectively, corroborating that the repetitive occurrences of redbeds may be due to magmatic Fe supply. For instance, the Obongri Formation of the Jikhyeon Group, which has a correlation with the Baengnyeong and Daecheong groups, contains reddish-purple shale or phyllite [22]. The timing of this redbed deposition was estimated to be 1000–940 Ma, preceding the formation of the Socheong Formation by at least 60 million years [10]. Although the field investigation searching for the further presence of the redbeds in the individual basins is beyond the aims of this study, and thus not attempted in this work, their synchroneity can be supplemented by carrying out $\delta^{13}C$ chemostratigra-

phy analysis. Interestingly, the Majiatun anomaly at approximately 950–920 Ma, suggested to be the oldest known Neoproterozoic nCIE event in eastern SKC [17], can be identified within the red stromatolite-bearing dolostone and limestone associated with the abovementioned red shale beds [44]. Likewise, a nCIE has been documented in the Seolhwasan and Okhyeonri formations of Mukcheon Group in southern Pyeongnam Basin, presumably correlated to the Socheong Formation. This occurrence aligns with the presence of red-purple shale and limestone layers [15]. Therefore, the correspondence of $\delta^{13}C$ negative excursion event in the redbeds can be a stratigraphically diagnostic feature. The genetic relationship between redbed occurrence and $\delta^{13}C$ negative excursion events can be an interesting topic for future studies in marine biology, paleontology, and/or related fields, as Fe addition and bottom anoxia induced by hydrothermal activities may have a significant influence on the microbial community.

7. Conclusions

Our study is the first to report the occurrence of redbeds in the Early Neoproterozoic Socheong Formation. The geochemical and mineralogical characteristics of the redbeds indicated that the source of Fe was hydrothermal fluids from mafic igneous activities. Hydrothermal inputs generated episodic temporal anoxia in the redox-stratified semi-isolated basins in the study area, even though the surface waters of the basins were oxygenated, resulting in the intercalation of chamositic and hematitic ferruginous ironstone beds. The Fe-enriched hydrothermal fluids likely originated from the mafic igneous activities involved in the emplacement of the Dashigou LIP in the Sangwon Supergroup. With a strong correlation with nCIE events, the occurrence of redbeds has been reported in various strata of the Sangwon, Xu-Huai, and Dalian basins; thus, the redbeds can be used as a diagnostic feature for stratigraphic correlation. The occurrence of hydrothermally driven anoxia and Fe addition further supports the existing hypotheses that the formation of the Dashigou LIP had a great influence on the biosphere and seawater chemistry in the region, even during the Proterozoic period.

Supplementary Materials: The following supporting information can be downloaded at: https://www.mdpi.com/article/10.3390/min14010059/s1, Table S1. Quality control details of geochemical analyses.

Author Contributions: Conceptualization, H.Y. and I.S.; investigation, H.Y. and S.H.L.; formal analysis, H.Y. and S.H.L.; writing—original draft preparation, H.Y.; writing—review and editing, I.S.; visualization, H.Y.; supervision, I.S.; funding acquisition, I.S. and S.H.L. All authors have read and agreed to the published version of the manuscript.

Funding: This study was supported by the Marine Environment Division of the Incheon Metropolitan City, Republic of Korea and the Basic Research Project of KIGAM (GP2020-003) funded by the Ministry of Science and ICT, Republic of Korea.

Data Availability Statement: Data are contained within the article.

Acknowledgments: The authors would like to thank Jae Yong Jeong, Jun Hyuk Seo, and Euijong Lee for their assistance in fieldwork and experimental setup, and Jeong-Hyun Lee, Hyojong Lee, and Deung-Lyong Cho for their informative discussions and photo courtesy.

Conflicts of Interest: The authors declare no conflicts of interest.

References

1. Peng, P. Late Paleoproterozoic–Neoproterozoic (1800–541 Ma) Mafic Dyke Swarms and Rifts in North China. In *Precambrian Geology of China*; Zhai, M., Ed.; Springer: Berlin/Heidelberg, Germany, 2015; pp. 171–204.
2. Hu, B.; Zhai, M.; Li, T.; Li, Z.; Peng, P.; Guo, J.; Kusky, T.M. Mesoproterozoic magmatic events in the eastern North China Craton and their tectonic implications: Geochronological evidence from detrital zircons in the Shandong Peninsula and North Korea. *Gondwana Res.* **2012**, *22*, 828–842. [CrossRef]
3. Hu, J.; Li, Z.; Gong, W.; Hu, G.; Dong, X. Meso-Neoproterozoic Stratigraphic and Tectonic Framework of the North China Craton. In *Main Tectonic Events and Metallogeny of the North China Craton*; Zhai, M., Zhao, Y., Zhao, T., Eds.; Springer: Singapore, 2016; pp. 393–422.

4. Peng, P. Precambrian mafic dyke swarms in the North China Craton and their geological implications. *Sci. China Earth Sci.* **2015**, *58*, 649–675. [CrossRef]
5. Peng, P.; Zhai, M.-G.; Li, Q.; Wu, F.; Hou, Q.; Li, Z.; Li, T.; Zhang, Y. Neoproterozoic (~900 Ma) Sariwon sills in North Korea: Geochronology, geochemistry and implications for the evolution of the south-eastern margin of the North China Craton. *Gondwana Res.* **2011**, *20*, 243–254. [CrossRef]
6. Peng, P.; Hu, B.; Zhang, Z.Y.; Zhang, Y.B.; Guo, J.H.; Zhai, M.G. Review on geological evolution of the Pyongnam basin in Korean Peninsula. *Acta Petrol. Sin.* **2021**, *37*, 129–142. [CrossRef]
7. Su, X.; Peng, P.; Foley, S.; Teixeira, W.; Zhai, M.-G. Initiation of continental breakup documented in evolution of the magma plumbing system of the ca. 925 Ma Dashigou large igneous province, North China. *Lithos* **2021**, *384-385*, 105984. [CrossRef]
8. Sun, F.; Peng, P.; Zheng, D.; Zuo, P. Reappraising the Provenance of Early Neoproterozoic Strata in the Southern–Southeastern North China Craton and Its Implication for Paleogeographic Reconstruction. *Minerals* **2022**, *12*, 510. [CrossRef]
9. Zhai, M.; Zhang, X.-H.; Zhang, Y.-B.; Wu, F.-Y.; Peng, P.; Li, Q.-L.; Li, Z.; Guo, J.; Li, T.-S.; Zhao, L.; et al. The geology of North Korea: An overview. *Earth Sci. Rev.* **2019**, *194*, 57–96. [CrossRef]
10. Cho, D.-L.; Peng, P.; Hwan Lee, S.; Park, J.-Y.; Seo, I.; Sun, F.; Li, Q.; Zhang, Y. Identify vestiges of large igneous provinces in deep time: A 0.9 Ga case from North China (Sino-Korean) craton. *Precambrian Res.* **2023**, *398*, 107220. [CrossRef]
11. Ernst, R.E. *Large Igneous Provinces*; Cambridge University Press: Cambridge, UK, 2014.
12. Peng, P.; Bleeker, W.; Ernst, R.E.; Söderlund, U.; McNicoll, V. U–Pb baddeleyite ages, distribution and geochemistry of 925Ma mafic dykes and 900Ma sills in the North China craton: Evidence for a Neoproterozoic mantle plume. *Lithos* **2011**, *127*, 210–221. [CrossRef]
13. Zhao, H.; Zhang, S.; Ding, J.; Chang, L.; Ren, Q.; Li, H.; Yang, T.; Wu, H. New geochronologic and paleomagnetic results from early Neoproterozoic mafic sills and late Mesoproterozoic to early Neoproterozoic successions in the eastern North China Craton, and implications for the reconstruction of Rodinia. *GSA Bull.* **2020**, *132*, 739–766. [CrossRef]
14. Ernst, R.E.; Youbi, N. How Large Igneous Provinces affect global climate, sometimes cause mass extinctions, and represent natural markers in the geological record. *Palaeogeogr. Palaeoclimatol. Palaeoecol.* **2017**, *478*, 30–52. [CrossRef]
15. Park, H.U.; Zhai, M.G.; Yang, J.H.; Peng, P.; Kim, J.N.; Zhang, Y.B.; Kim, M.C.; Park, U.; Feng, L.J. Deposition age of the Sangwon supergroup in the Pyongnam Basin (Korea) and the Early Tonian negative carbon isotope interval. *Acta Petrol. Sin.* **2016**, *32*, 2181–2195.
16. Xiao, S.; Shen, B.; Tang, Q.; Kaufman, A.J.; Yuan, X.; Li, J.; Qian, M. Biostratigraphic and chemostratigraphic constraints on the age of early Neoproterozoic carbonate successions in North China. *Precambrian Res.* **2014**, *246*, 208–225. [CrossRef]
17. Zhang, Z.; Peng, P.; Feng, L.; Gong, Z.; Mitchell, R.N.; Li, Y. Oldest-known Neoproterozoic carbon isotope excursion: Earlier onset of Neoproterozoic carbon cycle volatility. *Gondwana Res.* **2021**, *94*, 1–11. [CrossRef]
18. Kim, S.W.; Kwon, S.; Santosh, M.; Cho, D.-L.; Kee, W.-S.; Lee, S.-B.; Jeong, Y.-J. Detrital zircon U-Pb and Hf isotope characteristics of the Early Neoproterozoic successions in the central-western Korean Peninsula: Implication for the Precambrian tectonic history of East Asia. *Precambrian Res.* **2019**, *322*, 24–41. [CrossRef]
19. Cho, D.-L.; Lee, S.H.; Park, J.-Y. *Geological Report of the Baengnyeongdo·Daecheongdo·Socheongdo sheets (1:50,000)*; Korea Institute of Geoscience and Mineral Resources: Daejeon, Republic of Korea, 2021; p. 73.
20. Bekker, A.; Planavsky, N.J.; Krapež, B.; Rasmussen, B.; Hofmann, A.; Slack, J.F.; Rouxel, O.J.; Konhauser, K.O. 9.18—Iron Formations: Their Origins and Implications for Ancient Seawater Chemistry. In *Treatise on Geochemistry*, 2nd ed.; Holland, H.D., Turekian, K.K., Eds.; Elsevier: Oxford, UK, 2014; pp. 561–628.
21. Lim, S.-B.; Choi, H.-I.; Kim, B.C.; Kim, J.C. *Depositional systems of the sedimentary basins (I): Depositional systems and their evolution of the Proterozoic Paegryeong Group and Taean Formation*; KIGAM Annual Report; Korea Institute of Geoscience and Mineral Resources: Daejeon, Republic of Korea, 1999; p. 116.
22. Paek, R.J.; Kang, H.G.; Jon, G.P.; Kim, Y.M.; Kim, Y.H. *Geology of Korea*; Foreign Languages Books Publishing House: Pyongyang, Republic of Korea, 1993; p. 631.
23. Kim, J.-Y.; Kim, T.-S. Occurrence and Geological Significance of Stromatolites from the Precambrian Strata in the Socheong Island, Incheon, Korea. *J. Korean Earth Sci. Soc.* **1999**, *20*, 111–125.
24. Lee, S.J.; Kim, J.; Lee, K.C. Bacterial microfossils from Precambrian sedimentary rocks, Socheong Island, Korea. *J. Geol. Soc. Korea* **2003**, *39*, 171–182.
25. Kim, J.-Y.; Kim, K.-S.; Kim, T.-S. Raindrop imprints from the Late Proterozoic Sangwon System of the Socheong Island of Ongjin-gun, Incheon, Korea. *J. Korean Earth Sci. Soc.* **1999**, *20*, 55–60.
26. Kong, D.-Y.; Lee, S.-J. Possibility for Heliotropism from Inclined Columns of Stromatolites, Socheong Island, Korea. *J. Korean Earth Sci. Soc.* **2013**, *34*, 381–392. [CrossRef]
27. Bau, M.; Dulski, P. Distribution of yttrium and rare-earth elements in the Penge and Kuruman iron-formations, Transvaal Supergroup, South Africa. *Precambrian Res.* **1996**, *79*, 37–55. [CrossRef]
28. Gross, G.A. A classification of iron formations based on depositional environments. *Can. Mineral.* **1980**, *18*, 215–222.
29. James, H.L. Sedimentary facies of iron-formation. *Econ. Geol.* **1954**, *49*, 235–293. [CrossRef]
30. Castellanos-Alarcón, O.M.; Ríos-Reyes, C.A.; García-Ramírez, C.A. Occurrence of chloritoid-bearing metapelitic rocks and their significance in the metamorphism of the Silgará Formation at the Central Santander Massif. *Bol. Cienc. Tierra* **2016**, 5–15. [CrossRef]

31. Spear, F.S. *Metamorphic Phase Equilibria and Pressure-Temperature-Time Paths/Frank S. Spear*, 2nd ed.; Mineralogical Society of America: Washington, DC, USA, 1995; p. 799.
32. Ochoa, M.; Arribas, J.; Mas, R.; Goldstein, R.H. Destruction of a fluvial reservoir by hydrothermal activity (Cameros Basin, Spain). *Sediment. Geol.* **2007**, *202*, 158–173. [CrossRef]
33. Johnson, T.E.; Brown, M.; Solar, G.S. Low–pressure subsolidus and suprasolidus phase equilibria in the MnNCKFMASH system: Constraints on conditions of regional metamorphism in western Maine, northern Appalachians. *Am. Mineral.* **2003**, *88*, 624–638. [CrossRef]
34. Primmer, T.J. A transition from diagenesis to greenschist facies within a major Variscan fold/thrust complex in SW England. *Mineral. Mag.* **1985**, *49*, 365–374. [CrossRef]
35. Turner, F.J.; Verhoogen, J. *Igneous and Metamorphic Petrology*, 2nd ed.; McGraw-Hill: New York, NY, USA, 1960.
36. German, C.R.; Elderfield, H. Application of the Ce anomaly as a paleoredox indicator: The ground rules. *Paleoceanography* **1990**, *5*, 823–833. [CrossRef]
37. Planavsky, N.; Bekker, A.; Rouxel, O.J.; Kamber, B.; Hofmann, A.; Knudsen, A.; Lyons, T.W. Rare Earth Element and yttrium compositions of Archean and Paleoproterozoic Fe formations revisited: New perspectives on the significance and mechanisms of deposition. *Geochim. Cosmochim. Acta* **2010**, *74*, 6387–6405. [CrossRef]
38. Bau, M.; Möller, P.; Dulski, P. Yttrium and lanthanides in eastern Mediterranean seawater and their fractionation during redox-cycling. *Mar. Chem.* **1997**, *56*, 123–131. [CrossRef]
39. Bekker, A.; Slack, J.F.; Planavsky, N.; Krapez, B.; Hofmann, A.; Konhauser, K.O.; Rouxel, O.J. Iron Formation: The Sedimentary Product of a Complex Interplay among Mantle, Tectonic, Oceanic, and Biospheric Processes*. *Econ. Geol.* **2010**, *105*, 467–508. [CrossRef]
40. Kump, L.R.; Seyfried, W.E. Hydrothermal Fe fluxes during the Precambrian: Effect of low oceanic sulfate concentrations and low hydrostatic pressure on the composition of black smokers. *Earth Planet. Sci. Lett.* **2005**, *235*, 654–662. [CrossRef]
41. Isley, A.E.; Abbott, D.H. Plume-related mafic volcanism and the deposition of banded iron formation. *J. Geophys. Res. Solid Earth* **1999**, *104*, 15461–15477. [CrossRef]
42. Klein, C.; Beukes, N.J.; Holland, H.D.; Kasting, J.F.; Kump, L.R.; Lowe, D.R. Proterozoic Atmosphere and Ocean. In *The Proterozoic Biosphere: A Multidisciplinary Study*; Klein, C., Schopf, J.W., Eds.; Cambridge University Press: Cambridge, UK, 1992; pp. 135–174.
43. Wu, Z.; Zhang, G.; Gao, F.; Wang, H.; Qiu, L.; Sun, Q.; Yu, F.; Zhong, M. Sequence stratigraphic division of the Shisanlitai Formation of Neoproterozoic in Southern Liaoning, China. *IOP Conf. Ser. Earth Environ. Sci.* **2020**, *558*, 032010. [CrossRef]
44. Kuang, H.; Bai, H.; Peng, N.; Qi, K.; Wang, Y.; Chen, X.; Liu, Y. Temporal and spatial distribution of Precambrian red beds and their formation mechanisms. *Geosyst. Geoenviron.* **2022**, *1*, 100098. [CrossRef]

MDPI AG
Grosspeteranlage 5
4052 Basel
Switzerland
Tel.: +41 61 683 77 34

Minerals Editorial Office
E-mail: minerals@mdpi.com
www.mdpi.com/journal/minerals

Academic Open
Access Publishing

mdpi.com

ISBN 978-3-7258-6046-3